JOURNAL OF THE

Electrochemical Society

ol. 114, No. 2 February 1967 In Two Parts—Part I

Part II, 1966 Index—See Inside Back Cover

IN THE LONG RUN...

You'll be ahead with GLC Anodes for chlor-alkali production.

PRODUCTS YOU CAN TRUST ® GLC

GRAPHITE PRODUCTS DIVISION

GREAT LAKES CARBON CORPORATION

18 East 48th Street • New York, N. Y. 10017

OFFICES AND AGENTS FROM COAST-TO-COAST AND AROUND THE WORLD

Great Lakes Carbon Corporation is one of the world's largest manufacturers of graphite for electrochemical and electrothermic processes—and for aerospace, nuclear, metallurgical and other industrial uses.

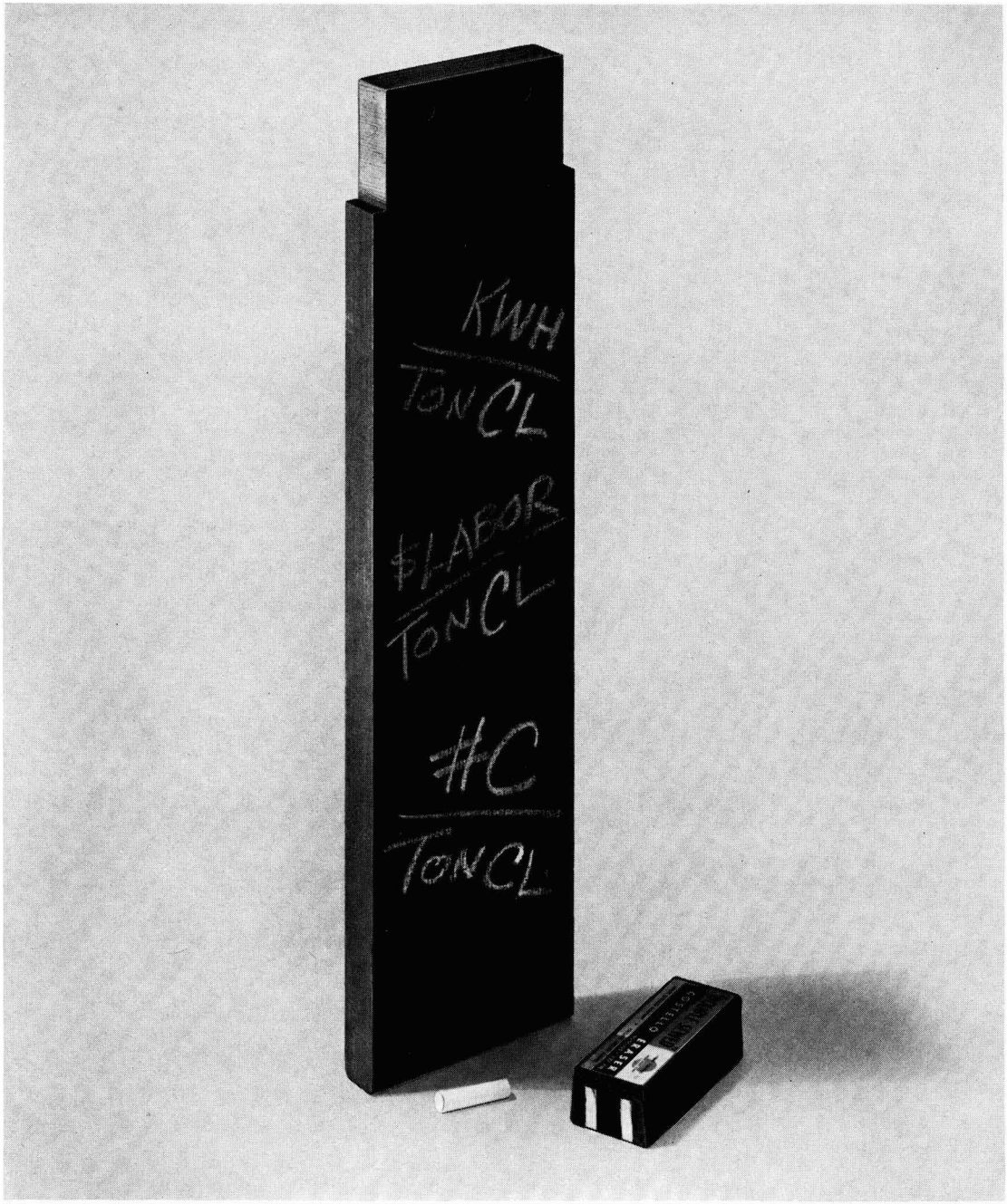

Any way you figure it...

Stackpole GraphAnodes® save you money. That's the way they are made.

When you place your next order for anodes, investigate the savings you could be getting from Stackpole GraphAnodes.® Why not write for the full story today: Stackpole Carbon Company, Carbon Division, St. Marys, Pennsylvania. Phone: 814-781-8463; TWX: 510-693-4511.

STACKPOLE
CARBON DIVISION

JOURNAL OF THE

FEBRUARY 1967

ELECTROCHEMICAL SOCIETY

VOL. 114 • NO. 2

ELECTROCHEMICAL SOCIETY NEWS

Manuscripts submitted to the Journal should be sent, in triplicate, to the Editorial Office at 30 East 42 St., New York, N. Y., 10017. They should conform to the revised Instructions to Authors published on pp. 299C-300C of the Nov. 1966 issue. Manuscripts so submitted become the property of The Electrochemical Society and may not be published elsewhere, in whole or in part, unless permission is requested of and granted by the Editor.

The Electrochemical Society does not maintain a supply of reprints of papers appearing in its Journal. A photoprint copy of any particular paper, however, may be obtained by corresponding direct with the Engineering Societies Library, 345 E. 47 St., New York, N. Y., 10017.

Inquiries re positive microfilm copies of volumes should be addressed to University Microfilms, Inc., 313 N. First St., Ann Arbor, Mich.

Walter J. Johnson, Inc., 111 Fifth Ave., New York, N. Y., 10003, have reprint rights to out-of-print volumes of the Journal, and also have available for sale back volumes and single issues, with the exception of the current calendar year. Anyone interested in securing back copies should correspond direct with them.

Published monthly by The Electrochemical Society, Inc., at 215 Canal St., Manchester, N. H.; **Executive Offices, Editorial Office and Circulation Dept.,** and **Advertising Office** at 30 East 42 St., New York, N. Y., 10017, combining the JOURNAL and TRANSACTIONS OF THE ELECTROCHEMICAL SOCIETY. Statements and opinions given in articles and papers in the JOURNAL OF THE ELECTROCHEMICAL SOCIETY are those of the contributors, and The Electrochemical Society assumes no responsibility for them.

Claims for missing numbers will not be allowed if received more than 60 days from date of mailing plus time normally required for postal delivery of JOURNAL and claim. No claims allowed because of failure to notify the Circulation Dept., The Electrochemical Society, 30 East 42 St., New York, N. Y., 10017, of a change of address, or because copy is "missing from files." Subscription to members as part of membership service; subscription to nonmembers $24.00 plus $1.50 for postage outside U.S. and Canada. Single copies $1.70 to members, $2.25 to nonmembers.

Entered as second-class matter at the Post Office at Manchester N. H., under the act of August 24, 1912. Postage paid at Manchester, N. H.

Report from

BELL LABORATORIES

Photodiodes with gain

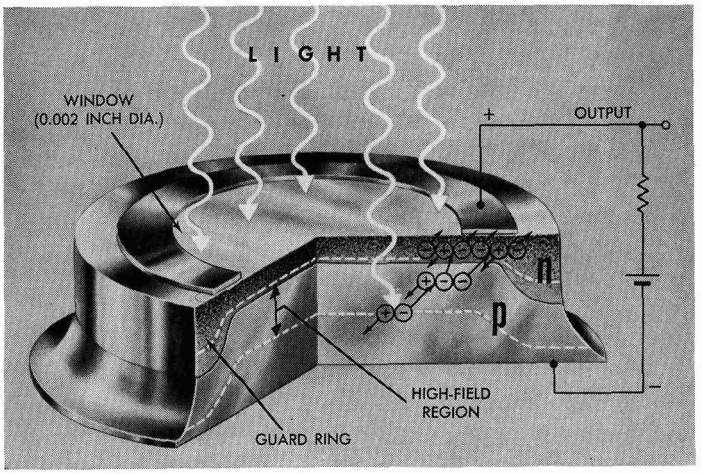

Cross-section of one form of the new photodiode. For the avalanche effect, positive voltage is applied to the n region and negative to the p (i.e., against the direction of easy current flow).

A photon, in being absorbed, creates an electron-hole pair. Electrons, formed in this way within the high-electric-field region of the junction, move toward the n-side. In so doing, they pick up energy, strike other atoms and create more pairs of electrons and holes. (A similar but opposite process occurs for the holes.) This "chain reaction"—the avalanche effect—produces relatively large currents and gives the diode its gain.

It is important that the avalanche multiplication factor be uniform over the entire window area . . . that no small area exhibit a particularly high multiplication factor. To achieve this, we start with homogeneous germanium and create a "guard ring" in which the density of charge-carrying impurities is relatively low. This low density results in a reduced electric field where the p-n junction meets the circumference . . . where breakdown currents would otherwise occur.

Because the time required for avalanche is very short, the diode responds to modulation frequencies as high as 60 GHz.

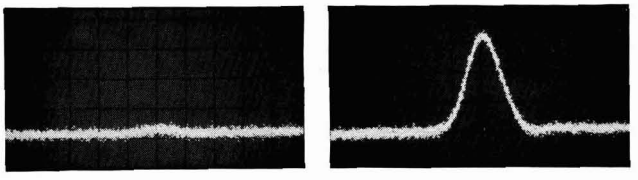

Performance of Bell Laboratories' germanium avalanche photodiode (right) compared with that of an otherwise identical non-avalanche type. Under a weak light signal (40 μW) the output of the ordinary diode is lost in noise. High gain of the new avalanche type, however, permits the signal pulse to be clearly seen.

In a typical photodiode, a negative and a positive charge carrier—called an electron-hole pair—are created for each photon that penetrates the diode's surface. Now, Bell Laboratories scientists W. T. Lynch and H. Melchior have made experimental germanium photodiodes that have gain, developing up to 250 such electron-hole pairs per photon. And the new photodiodes respond to light of wavelengths from the visible region well into the infrared . . . to 1.6 microns.

The gain in these diodes stems from the "avalanche" effect (left). This requires carefully selected germanium and a special construction feature—a "guard ring"—developed here some years ago.

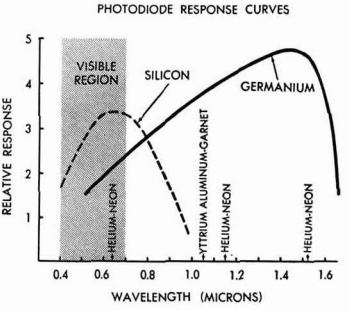

In opto-electronic systems using infrared light from helium-neon or yttrium-aluminum-garnet lasers, for instance, the response of the new diode (above right) could be used in detecting modulation signals, and its high output would permit omission of some stages of amplification. (The "avalanche effect" was discovered at Bell Laboratories; the first avalanche photodiodes were of silicon and cut off below 1 micron in the "near" infrared.)

Bell Telephone Laboratories
Research and Development Unit of the Bell System

EDITORIAL

The Naming of Names

SCIENCE and technology require the frequent invention of new words and terminology. In the past, many new terms have been adapted from Greek and Latin origins; Michael Faraday thus obtained *ion, electrode, etc.* Electrical and magnetic units are named after famous researchers, as *volt, ohm, coulomb,* and *oersted.* In general such names have been adopted only when the definitions of the units do not permit simple description in terms of fundamental quantities. Men's names are also applied to much-used multiples or fractions of established units: *angstrom* (or the correct Swedish name) for 10^{-8} cm, debye for 10^{-18} esu-cm, *faraday* for the chemical unit of charge.

The logical cgs pressure unit is the dyne/cm^2, but since this is so small, 10^6 dynes/cm^2 is used as the practical unit, especially by physicists (the *bar*, same origin as barometer). Unfortunately the *bar* and the *millibar* are not useful to the experimentalist. The height of a mercury column has traditionally been used to measure gas pressure (and tubes containing mercury were mounted in the Eiffel Tower and in deep mine shafts for high-pressure studies). The *mm Hg* is an easily visualized experimental unit and the term is highly descriptive; nevertheless great effort is expended to induce authors to call it the *torr.* J. R. Partington (*An Advanced Treatise on Physical Chemistry,* 1949) said "The mm. Hg unit is quite unnecessarily called a *torr* (after Torricelli) in some German works." In high vacuum work perhaps the *microtorr,* the *nanotorr,* even the *picotorr* will find application; neither the Vacuum Society nor the Cryogenic Society has insisted on uniformity, and their advertisers seem to prefer the *mm Hg* and the *micron* (10^{-6} meter Hg) as nomenclature units.

In radio engineering it has become common to dub the simple cycle-per-second (*cps*) the *hertz. This Journal* does so, in conformance with the National Bureau of Standards practice. Unfortunately a practice perhaps sound is spreading from use in the *hertzian wave* region to low frequency electric current on the one hand, to the microwave and infrared regions of molecular structure studies on the other. Is it simpler to write *GHz* than 10^9 cps? A radio magazine feature writer even uses the *hertz* to express sound frequencies; he describes a signal device which "puts out a continuous tone of 2800 Hz $\pm$ 300 Hz." The manufacturer in his advertisement in the same magazine says 2800 cps.

A popular method of coining new names is to use *acronyms*: the initial letters of a descriptive phrase. Happy scientific examples are *maser* and *laser.* Contractions of two or more words into one can be effective, as for the Madmen (Madison Avenue ad-men) or the Modfash columns. D. P. Boden of The Electric Storage Battery Co. (which in some way acquired the name Exide) tells us he does not approve of contractions like *cursity* (current density) or *anector, cathector* (anode, cathode current collectors). We agree, but note that *adatom, adion* are widely used (adsorbed atom, ion); and what about *anolyte, catholyte*?

On this page we can only briefly explore what seems to be a great confusion of terminology and nomenclature. We fear that no important Standards Committee, or Journal Policy, can enforce uniformity. The important thing is that authors and editors make sure that whatever is published be understandable to its intended audience; don't, without warning, use *nm* (nanometer) for the mμ (millimicron) reader, or λ for the μ*l* audience. As for new words and terms, time serves to establish the most useful ones; the others are forgotten.

—CVK

If you're an analytical chemist...

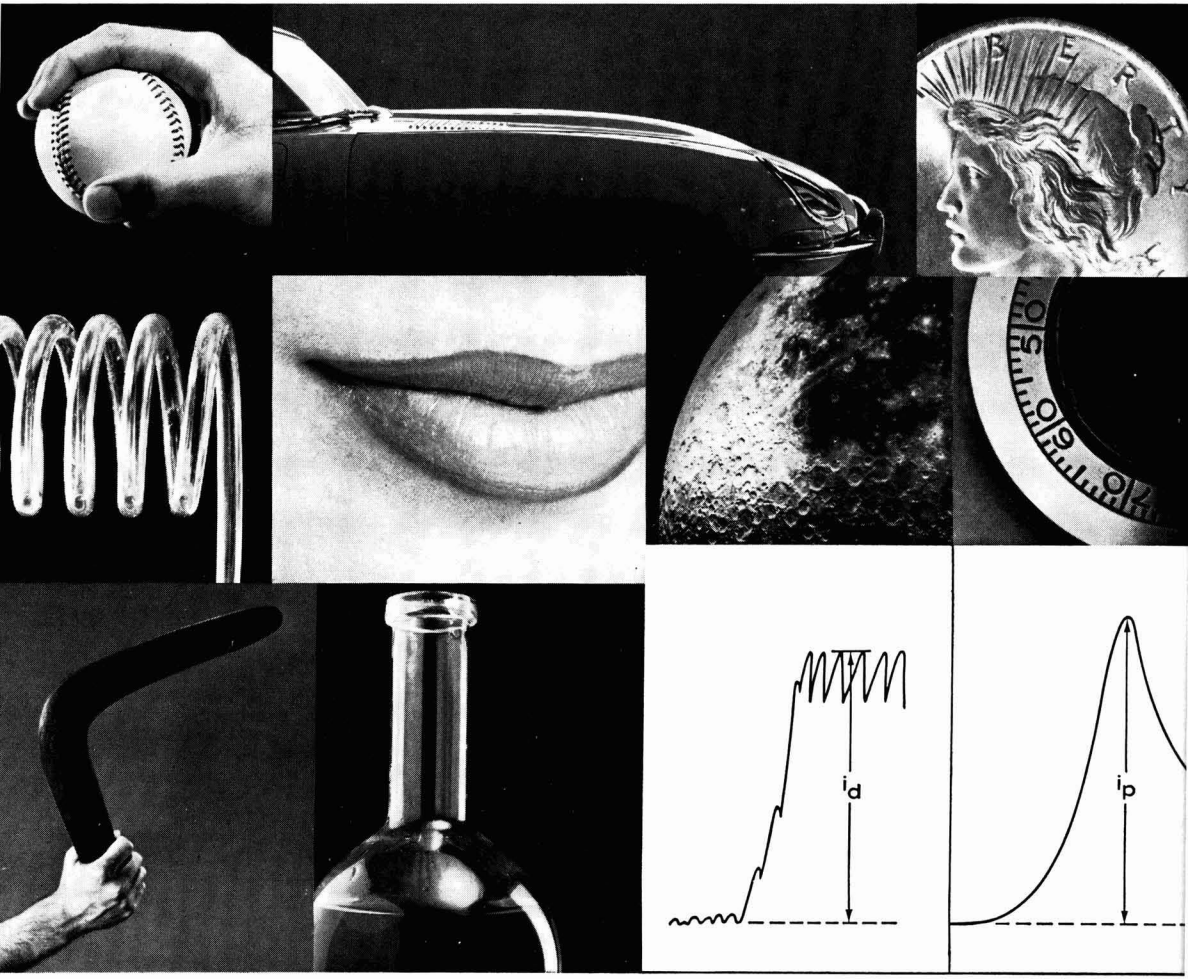

these curves should turn you on

With the Beckman Electroscan 30™ Electroanalytical System, you can perform either polarographic analysis or potential sweep chronoamperometric analysis (PSCA). Both are valuable techniques for quantitative analysis at low concentrations, with measurement current directly proportional to concentration.

Studies on cadmium, zinc, and nickel have shown that PSCA has these advantages over polarography: (1) *Speed*. Utilizing a rapid voltage sweep, analysis takes only a few seconds—30 to 40 times faster than polarography. (2) *Sensitivity*. Measurements can be made down to 10^{-5} M (approximately 1 ppm) — a tenfold increase in sensitivity over polarography which has a practical limit of only 10^{-4} M. (3) *Broader application*. By utilizing other electrodes, PSCA eliminates the polarographic limitation of using only the dropping mercury electrode. This makes possible analysis of those organic analytes that cannot be measured by polarography.

If your application demands polarography, you owe it to yourself to investigate the superior qualities of the Electroscan 30 that make it the best polarographic analyzer you can buy. You may also need it for PSCA and the other 13 electroanalytical techniques it can perform. For more information to turn you on, write for Data File LES-266-36.

Beckman™ INSTRUMENTS, INC.
SCIENTIFIC AND PROCESS INSTRUMENTS DIVISION
FULLERTON, CALIFORNIA • 92634

INTERNATIONAL SUBSIDIARIES: GENEVA; MUNICH; GLENROTHES, SCOTLAND; TOKYO; PARIS; CAPETOWN; LONDON; MEXICO CITY

ELECTROCHEMICAL SCIENCE

A Coulogravimetric Study of the Sintered Silver Electrode in 1 Molar Potassium Hydroxide

A. Langer and J. T. Patton

Research Laboratories, Westinghouse Electric Corporation, Pittsburgh, Pennsylvania

ABSTRACT

Weighing of a sintered silver electrode while immersed in electrolyte during cathodic and anodic reaction reveals breaks in the weight change-coulomb curves. The different slopes can be explained by the volume change during phase transformation, affecting the buoyancy of the electrode. These breaks coincide with the potential changes of the plate, measured against a reference electrode.

The silver electrode in alkali electrolyte has gained considerable prominence in the construction of batteries offering high discharge rates and high energy densities per unit weight and volume. The outstanding properties of this electrode have long been recognized (1-4), but a complete understanding of its behavior is still lacking (5,6). Moreover, since efficient electrodes are usually of the porous type, an exhaustive interpretation of their behavior requires an understanding of the many factors affecting this type of electrode. Among these are the expansion and contraction of the active mass.

This volume change affecting the buoyancy is studied by weighing continuously the porous silver electrode in 1.0M potassium hydroxide as electrolyte during the complete cathodic and anodic cycle. Simultaneously, the corresponding number of coulombs involved is determined, and the potential of the electrode is recorded against a suitable reference electrode and correlated with the change in weight. A similar procedure was used by Schoop (7) at the turn of the century, but it has not been practiced frequently since (8, 9).

Theory

If a silver plate suspended in the electrolyte is oxidized anodically to silver oxide, the change in the weight of the immersed electrode is the algebraic sum of several related effects, principally (*i*) a weight increase due to the added mass of reacted oxygen, and (*ii*) an altered buoyancy lift due to the volume change of the electrode by the newly formed compound. There is still another factor affecting the buoyancy of the sample considered to be minor. The density of the electrolyte around the electrode is changing, due to the consumption of ions at the interface and the heat that is generated by the passage of the current.

In the following discussion we assume that minor effects can be neglected, provided low current densities are used, so that concentration differences in the electrolyte are small since equalized by diffusion. Additionally, for these conditions, the density gradients are not large enough to produce convection of the electrolyte which may still further influence the weight of the sample. The reaction must be carried out at potentials where no gas evolution will occur since small bubbles formed in or adhering to the electrode will alter its true weight. We also assume that the reaction products are only sparingly soluble in the electrolyte.

Under these conditions we can derive an equation for the weight change of the electrode in the electrolyte. Let a mass of silver m_{Ag} and density d_{Ag} be immersed in a liquid electrolyte of density d_s. The weight of the silver in the solution $m_{Ag}{}^s$ will be

$$m_{Ag}{}^s = m_{Ag}\left(1 - \frac{d_s}{d_{Ag}}\right) \qquad [1]$$

If the silver is converted to an oxide, for example AgO, the weight of the oxide in the electrolyte will be

$$m_{AgO}{}^s = m_{AgO}\left(1 - \frac{d_s}{d_{AgO}}\right) \qquad [2]$$

If the metal were oxidized and weighed in air, the weight increase would be

$$m_{AgO} - m_{Ag} = m_O \qquad [3]$$

or simply the mass of oxygen reacted with the specimen. In the electrolyte we will register a change m^s due to both mass increase and volume change, given by the equation

$$m^s = m_{AgO}\left(1 - \frac{d_s}{d_{AgO}}\right) - m_{Ag}\left(1 - \frac{d_s}{d_{Ag}}\right) \qquad [4]$$

In an electrochemical process without any side reaction, the mass of the reaction products produced by a current I in a time t is given by Faraday's law

$$m = \frac{It\,M}{nF} = Eq \cdot Q \qquad [5]$$

Here $Q = It$ is the number of coulombs passed, $Eq = (M/nF)$ is the electrochemical equivalent of the species of molecular weight M, F is the Faraday, and n is the number of electrons per molecule taking part in the reaction. A line should result if the weight change m^s of the electrode in the electrolyte is plotted against the number of coulombs used. The slope of this line can be expressed by substituting [5] into [4]

$$\frac{m^s}{Q} = Eq_{AgO}\left(1 - \frac{d_s}{d_{AgO}}\right) - Eq_{Ag}\left(1 - \frac{d_s}{d_{Ag}}\right) \qquad [6]$$

If a constant reaction rate is maintained by charging (or discharging) the electrode with a constant current, then Q is calculated by measuring the elapsed time.

In cases where the density of the electrolyte is not altered, a change in the slope of m^s *vs.* Q represents a variation in the density of the active mass formed. Information can be obtained concerning the density of the products by utilizing Eq. [6] and the experimentally determined value of the slope.

Electrode Reactions

Ever since the earliest investigations on the silver electrode, it has been apparent that charging and discharging processes in an alkaline solution proceed in steps that have been associated with the formation of the oxides Ag_2O and AgO.

The formation of these oxides seems to be well established and verified by x-ray diffraction (10-13)

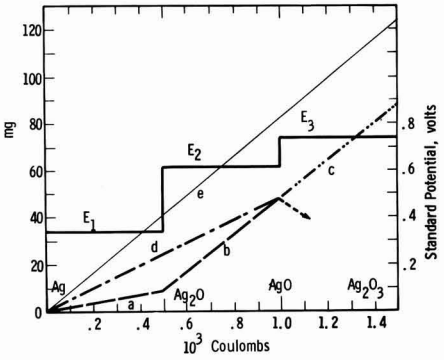

Fig. 1. Ideal weight change-coulomb relations, silver electrode of 10^3 coulomb total capacity.

Reaction	Weighing in electrolyte $d_s = 1.050$ line	slope mg/kQ	Weighing in air line	slope mg/kQ
$2Ag + ½ O_2 \rightarrow Ag_2O$	a	18.4	e	82.9
$Ag_2O + ½ O_2 \rightarrow 2AgO$	b	78.2	e	82.9
$Ag + ½ O_2 \rightarrow AgO$	d	48.0	e	82.9
$2AgO + ½ O_2 \rightarrow Ag_2O_3$	c	—	e	82.9

although the true nature of the AgO is still disputed (14). It has been shown that AgO can take up additional oxygen electrochemically (15). However, in the charging process, oxygen gas is liberated on the electrode after the AgO level has been reached. Other reactions of the silver electrode have been advanced (16, 17), especially the direct conversion of silver to AgO, but their importance is not well established. The main reactions are accompanied by definite potential plateaus.

Using the density of the involved species, $d_{Ag} = 10.5$, $d_{Ag_2O} = 7.14$, and $d_{AgO} = 7.44$ g/cm^3 (18), in Eq. [6], and assuming that silver will convert first completely to the Ag_2O oxide of bulk density and then completely again to AgO, we can calculate the weight change curves. Figure 1 represents the idealized theoretical behavior of a silver plate of 10^3 coulombs (1 kQ) total capacity up to the AgO level. The plate is immersed in approximately 1.0M KOH electrolyte of density $d_s = 1.050$ at room temperature.

Line a represents the weight increase of the electrode for formation of Ag_2O. Because of the large difference in density between silver and this oxide, there is a considerable buoyancy correction, causing the slope m^s/Q to be 18.4 mg/kQ, rather than the 82.9 mg/kQ slope that would be obtained if the weighing were performed in air. The weight change curve in air is represented by line e. As the oxidation proceeds from Ag_2O to AgO, the change in density should be relatively small, resulting in only a minor buoyancy influence. The calculated slope of 78.2 mg/kQ, as represented by line b, is therefore almost parallel to the line representing the weighing in air. The possible weight change curve for formation of Ag_2O_3 cannot be predicted with any certainty since the density of the compound is unknown. In case silver is directly converted to the AgO, the weight increase should follow line d with a slope of 48 mg/kQ.

The potential-coulomb curve should follow lines E_1-E_3, representing the standard potentials of the reactions. In actual charging E_c and discharging E_d, the effect of overvoltage for the particular current density must be considered.

How an actual sintered electrode follows this predicted scheme was tested on the following experimental arrangement.

Experimental

The apparatus used is shown schematically in Fig. 2. It consists of an analytical balance, with small mercury-filled cups attached to the balance support and to one of the pans. Platinum wires, fastened to the middle and end of the balance beam, were bent to dip very slightly into the mercury. In this way, electrical connection could be maintained through the balance arm without impairing its free movement. The automatic weighing was done with a permanent magnet and solenoid restoring element, balanced by a dual photocell (19). The weight change was recorded on a pen recorder. The speed of the recording paper (1 in. in 10 min) gave the time base for the reactions studied. The sensitivity was adjusted so that 1 mg gave ½ in. on the chart. Weight fluctuations due to amplifier noise were about 0.2 mg.

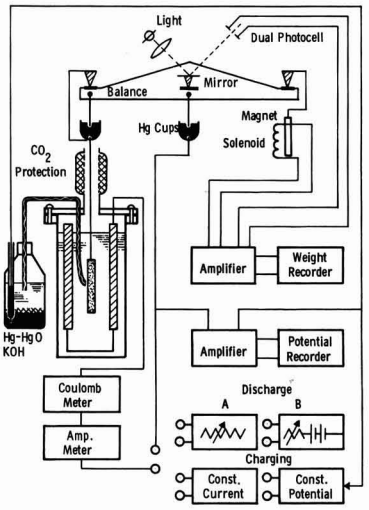

Fig. 2. Continuous coulogravimetric arrangement

The electrodes were enclosed in a plastic box with a small opening for the wire suspending the working electrode. The wire was also passed through an attached perforated tube surrounded by solid KOH. It was hoped to minimize in this way the influence of atmospheric CO_2 on the electrolyte, as carbon dioxide seems to affect adversely the extended operation of silver electrodes. As the negative electrodes, two commercial sintered cadmium plates were used; each was about 5 times the physical size of the silver electrode. The cadmium electrodes were wrapped in two layers of wettable cellophane of the type used to wrap silver electrodes. This was done to retard the possible deposition of silver on these plates. An external 1.0M KOH mercury-mercury oxide electrode was used as reference. The capillary was made of polyethylene tubing filled with a purified asbestos string. The potential was recorded by a high impedance chart recorder driven synchronously with the weight recorder.

The current passed through the cell was registered on a calibrated multirange ampere meter. An ampere-hour meter (Danubia-Wien, Austria), accurate to 0.001 amp-hr, was used as a check, to record the total number of coulombs. Reversing switches were used to operate these instruments during charge and discharge cycles.

The electronically regulated, constant-current power supply allowed charging currents up to 400 ma. The constant current discharges were made by manually regulating the current with a decade resistance box. To obtain very deep discharge, or to help stabilize the discharge current, a 12v storage battery was sometimes used in series with the test cell.

The working electrode consisted of a piece of sintered silver plate, cut to about 3.1 x 3.1 cm and 0.05 cm thick, and attached to the balance by a silver wire. As an electrolyte, a 1M solution was prepared from

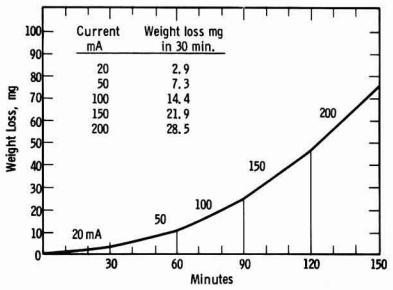

Fig. 3. Weight loss-time relation, porous silver electrode of 16 cm^2 area; electrolyte 1.0M KOH d_s = 1.05 g/cm^3. Discharge at the Ag_2O level at different current densities.

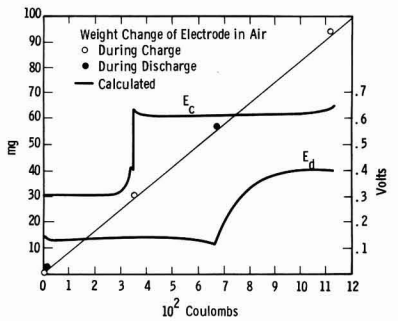

Fig. 4. Efficiency test of silver electrode reactions. Weight change-coulomb relations.

chemically pure KOH and boiled water that had been cooled under N_2. Although the solution was handled as little as possible in air, it could have absorbed unknown amounts of CO_2. All experiments were performed at about 25°C with some shielding against light.

Results

Before proceeding with the experiments, the validity of Eq. [1] was tested by electroplating copper from a copper sulfate solution onto a copper strip. The corrected weight in the electrolyte, the weight in air after washing and drying, and the weight calculated from the number of coulombs all agreed within 2%.

The assumption that the electrolyte in the pores and around the electrode interchanges rapidly with the bulk of the solution was tested in the following way. An approximately 4 x 4 cm, 0.05 cm thick, sintered and previously cycled silver plate was first fully charged and then drained at the Ag_2O voltage plateau, using discharge rates ranging from 20 to 200 ma for the whole plate. Figure 3 shows straight sections of different slopes in the weight loss-time coordinate system. For the same number of coulombs passed, the weight loss was equal for all of the current densities used. This result indicates that no appreciable concentration polarization could occur at these current densities, and that there was no deficiency in transport of the proper ions to sustain the reaction. This conclusion was also substantiated by the observation that the different rates were established without any noticeable time delay on the graphs.

To verify that the Faradic efficiency of the reactions was close to 100% under the prevailing conditions, direct weighings of the electrode were performed in air at different stages in the charge and discharge cycle (11). The electrode was removed from the electrolyte and soaked in fresh water four times for a period of at least 1 hr each. After rinsing with alcohol, the electrode was dried to a constant weight in a desiccator. The weighings were made in the region where the potential plateaus changed. The results are shown in Fig. 4. These points coincide quite well with the calculated values for m_0. We conclude, in addition, that the compounds formed in the reaction are stable enough to withstand this analytical procedure.

The actual weighings of the electrode during the charge-and-discharge cycle has indicated that the silver electrode behaves similarly to predictions from the theoretical equation. Typical experimental results are plotted on Fig. 5.

When an unused, sintered silver electrode is charged at constant current, the measured potential settles down to an almost constant value E_1 after an initial potential rise in the first few seconds. This steady potential is designated as the Ag-Ag_2O level. With the 10 cm^2, 0.05 cm thick electrode charged at a 100 ma total current rate, the measured weight-change/coulomb slope was 36 mg/kQ as shown in dashed line

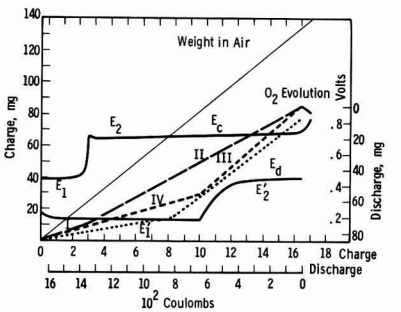

Fig. 5. Weight change-coulomb relations, first cycle; porous silver electrode 3.1 x 3.1 cm, 0.5 mm thick, in KOH electrolyte of d_s = 1.050 g/cm^3 at 25°C; charge and discharge current 100 ma; slope of segments in mg/kQ. Charging I = 36, II = 56, discharge III = 83, IV = 29.

segment I. This slope is almost twice as large as the predicted 18.4 mg/kQ (dotted line), but it is much lower than would be expected if no volume change had taken place. One can conclude that the density of the compound formed in the experiment must be around 8 g/cm^3.

At a later stage, the potential-coulomb curve starts to rise, slowly at first and then suddenly, until a new higher level E_2 is reached. This level is assigned to the formation of AgO. Figure 5 shows that more silver is oxidized on this level than on the previous one. It is interesting to observe that the point of sudden increase in potential coincided with a change in the slope of the weight-change/coulomb curve, the new slope being close to 56 mg/kQ as shown by dashed line segment II. This value is not as high as the predicted 78.2 mg/kQ for the conversion of Ag_2O to AgO and indicates that the active mass is expanding more than expected, so that a larger buoyancy correction is still in play. Actually, the slope of 56 mg/kQ is closer to the value of 48 mg/kQ that would indicate the direct conversion of silver to AgO.

Whether these data represent a gradual expansion of the existing lattice, or the formation of new distinct crystals as revealed by some x-ray diffraction studies (19) cannot be decided.

After a lengthy plateau region, during which the potential rises only slightly, there is a sudden increase with a corresponding change in the weight-change curve. The curve becomes erratic, levels for a short period, and then decreases quite rapidly. An inspection of the electrode at this point reveals that the gassing stage has been reached and the decrease in weight is caused by gas bubbles clinging to the surface of the electrode.

Several minutes are allowed for the gas to be dispelled before starting the discharge process. At the same current density of 100 ma/plate, one finds that

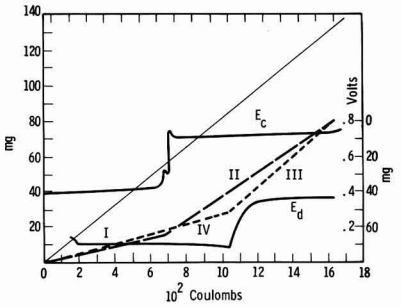

Fig. 6. Weight change-coulomb relations, second cycle; slope of segments in mg/kQ. Charging I = 23, II = 68, discharge III = 83, IV = 29.

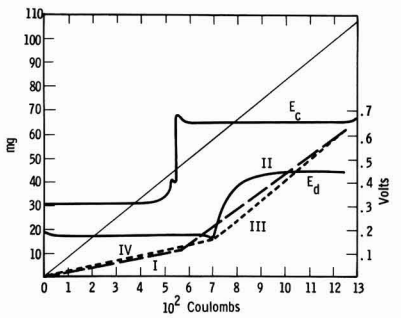

Fig. 7. Weight change-coulomb relations, fourth cycle; slope of segments in mg/kQ. Charging I = 20, II = 74, discharge III = 82, IV = 22.

the discharge proceeds at a potential E_2'. This potential decreases slowly at first, then gradually faster, but never is the change as rapid as during the charging process. The weight decreases rather fast at a rate of 83 mg/kQ, as shown by shortly dashed line III. (The discharge curves on all the graphs are plotted backwards from the charge curves. The new origin for the weight-change and number of coulombs is the maximum value reached during charging as indicated by the double scale in Fig. 5 but omitted in succeeding graphs.) This rapid change in weight is nearly what the plate would suffer if the weighings were made in air. This may mean that the volume of the electrode remains unchanged during the higher potential plateau of the discharge cycle. The slight contraction that should occur in this region should give a slope of 78.2 mg/kQ.

After the potential reaches the second discharge plateau, E_1', the potential remains almost constant until the silver oxide is close to exhaustion. In a self-sustained discharge, the potential begins to rise with the rapidly falling current output. In most cases tested, the current sank so low, even with the resistance box shorted, that a complete exhaustive discharge was not achieved. Shorting of the cell for many hours was not attempted. In this region, the weight curve followed the line IV with a slope of 29 mg/kQ, as compared to a slope of 36 mg/kQ in the charging portion, but not as low as the expected slope of 18.4 mg/kQ.

The data clearly show the large "hysteresis loop" created by the weight-change, coulomb charge and discharge curves. The rather short charging branch on the Ag_2O level represents only 18% of the total charge taken up, while the corresponding branch on discharge amounts to about 60% of the total charge released.

As early as the second cycle, Fig. 6, the Ag_2O charging branch becomes considerably extended. The slope was now 23 mg/kQ. Assuming a start from the silver level, this slope would represent the formation of an oxide of 7.3 g/cm^3 density. This density is very close to 7.25, the x-ray density of Ag_2O.[1] The weight change for the AgO plateau was 78 mg/kQ on charging, and again 83 mg/kQ during discharge. Figure 6 also shows that a slope of 29 mg/kQ was obtained during discharge at the Ag_2O level. The difference between the charge and discharge behavior became less pronounced.

A potential overshoot is usually noticed on charging during the transition from the Ag_2O to the AgO level. This overshoot has been the subject of several investigations, and different causes have been assigned for its appearance (16, 21). It can be seen in Fig. 6 that an additional small peak preceded the main one. In other runs, such peaks sometimes followed the main one.

Figures 7 and 8 represent the response of the same

[1] Data of x-ray density were kindly indicated by one of the reviewers.

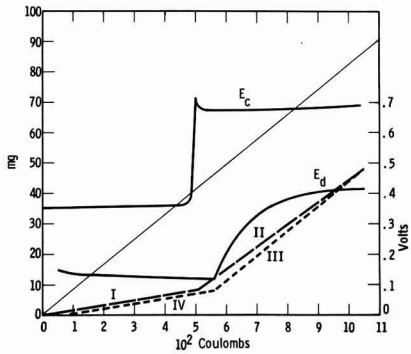

Fig. 8. Weight change-coulomb relations, sixth cycle; slope of segments in mg/kQ. Charging I = 16, II = 72, discharge III = 80, IV = 17.

electrode in the fourth and sixth cycle. The cathodic and anodic behavior become even more similar, with weight change per coulomb values approaching the predicted values, and both plateaus in the charging and discharging cycle of almost the same length. But another factor became more apparent, namely, the total capacity of the plate decreased progressively during cycling. The first cycle gave 1650 coulombs, and the sixth only about 1050 coulombs. Taking into account the weight of the active silver in the electrode, by subtracting the weight of the reinforcing grid, the electrode was about 50% efficient in the first cycle, considering the conversion to AgO. The departure from higher efficiencies obtained in actual batteries might be attributed to the difference in electrolyte concentration. The decrease in capacity represents a calculated loss of 335 mg of active silver.

These experiments were repeated with new electrodes and electrolyte several times. The behavior was not completely identical although the general features were the same. One factor became disturbing during cycling. The electrolyte acquired a dark brown color, and some sediment appeared at the bottom of the cell, indicating considerable solubility of the active compounds in the electrolyte. Taking the solubility of the silver oxides in 1M KOH as 2.10^{-4}M Ag (22, 23), the silver in the 200 ml of electrolyte amounts to only 4.3 mg. The residue formed in cycling which settled at the bottom of the cell was less than 50 mg. The combined weight loss and solubility alone cannot account for the large loss in capacity of the silver electrode.

Conclusions

The coulogravimetric experiments confirm the proposition that the silver electrode undergoes a large volume change, mainly during the transition from Ag to Ag_2O phase. This change occurs in both the

cathodic and anodic reaction. Changes in the weight-coulomb relation coincide with the changes in potential-coulomb curves. Differences in coulombic efficiencies of the two potential-coulomb plateaus were found mainly during the first few charging and discharging cycles. More silver was being oxidized on the second AgO plateau than the amount converted in the initial step. On the contrary more oxide was reduced on the Ag_2O level than at the higher oxide one. These differences became less pronounced during repeated cycling.

The loss of electrode capacity during cycling cannot be explained solely by the dissolution of the silver oxides in the electrolyte or shedding of the active mass. The loss in capacity might be due to sealing up of capillary passages in the sintered electrode, reducing the available active area in the next cycle or the influence of increasing carbonate concentration.

Manuscript received March 30, 1966; revised manuscript received Nov. 10, 1966.

Any discussion of this paper will appear in a Discussion Section to be published in the December 1967 JOURNAL.

REFERENCES

1. E. W. Junger, DPR, 110210, 1899.
2. W. Morrison, U. S. Pat. 978,980 (1910).
3. F. Jirsa, *Z. Elektrochem.* **33**, 129 (1927).
4. H. Andre, *Bull. soc. franc. electriciens*, **1**, 132 (1941).
5. T. P. Dirkse, *This Journal*, **106**, 453 (1959).
6. J. A. McMillan, *Chem. Rev.*, **62**, 65 (1962).
7. M. U. Schoop, *Electrochem. Industry*, **2**, 279 (1904).
8. G. W. Vinal and L. M. Ritchie, *Technol. Papers Bur. Stand.*, **17**, 117 (1922).
9. H. Winkler, *Elektrotechnik*, **6**, 355 (1952); **9**, 300 (1955).
10. R. Luther and F. Pokorny, *Z. anorg. u. allgem. chem.*, **57**, 290 (1908).
11. T. P. Dirkse, *This Journal*, **106**, 920 (1959).
12. I. A. Denison, *Trans. Electrochem. Soc.*, **90**, 387 (1946).
13. C. P. Wales and J. Burbank, *This Journal*, **106**, 885 (1959).
14. V. Scatturin and P. L. Bellon, *ibid.*, **108**, 819 (1961).
15. B. D. Cahan, J. B. Ockerman, R. F. Amlie, and P. Rüetschi, *ibid.*, **107**, 725 (1960).
16. T. P. Dirkse and G. J. Werkena, *ibid.*, **106**, 88 (1959).
17. T. P. Dirkse and D. B. DeVries, *J. Phys. Chem.*, **63**, 107 (1959).
18. N. A. Lange, "Handbook of Chemistry," p. 304, Handbook Publ. Inc., 1956.
19. F. A. Mauer, *Rev. Sci. Instr.*, **25**, 598 (1954).
20. P. Jones, H. R. Thirsk and W. F. K. Wynne-Jones, *Trans. Faraday Soc.*, **52**, 1003 (1956).
21. P. C. Wales and J. Burbank, *This Journal*, **112**, 13 (1965).
22. R. F. Amlie and P. Rüetschi, *ibid.*, **108**, 813 (1961).
23. T. P. Dirkse and B. Wiers, *ibid.*, **106**, 284 (1959).

A Kinetic Study of the Heterogeneous Reactions of Metallic Sodium with Chlorine and Bromine

M. J. Dignam and D. A. Huggins[1]

Department of Chemistry, University of Toronto, Toronto, Ontario, Canada

ABSTRACT

Data on the chlorination and bromination of sodium in the temperature range of 238°-323°K have beeen obtained for evaporated sodium films by following the change in optical density of the metal films. The chlorination data corresponding to the first few minutes of reaction have been found to be in accord with an equation of the form of that predicted by Mott and Cabrera for the growth of very thin oxide films on metals, while the bromination data for 273°K and below are in accord with a direct logarithmic law. Following longer reaction periods for chlorination, and above 273°K for bromination, the behavior is complex, being influenced in the case of bromination, for example, by illumination with light.

Stimulated by the practical problems of corrosion, fundamental research in the field of anodic and air oxidation of metals has gained increasing attention in recent years. Whereas early studies were concerned primarily with the formation of thick films (>1000Å) recent studies have examined more closely the kinetics and morphology of thin film formation. The material reported herein falls into this latter category.

Many metals, perhaps all which oxidize readily, show very similar behavior when exposed to oxygen at sufficiently low temperatures. The oxidation rate is initially very rapid, but drops off to a low or negligible value, a stable film of the order of 20-200Å being formed (1). Theories which have been applied to these low-temperature, thin film conditions have been based on a model involving a continuous adherent and homogeneous film. The rate-controlling process has been assumed variously to be electron transport (1-5); ion transport under the influence of the high electrostatic field produced by equilibration of electrons between the metal and surface levels at the film-oxidant interface (6, 7); chemisorption or incorporation of the oxidant at the film oxidant interface (8); combinations of some of the above allowing for space charge in the film; and finally film recrystallization and related phenomena (9, 10).

Differentiation between some of these theoretical approaches from experimental data is difficult, since many of them lead to the same or a similar form for the rate law. It is for this reason that we chose to investigate the halogenation of the alkali metals, which apart from providing a unique series of reactions, involves reactants and products which are sufficiently simple to make possible calculations of the rate constants from other data. In this manner, an unequivocal choice between alternate theories should be possible. At present one cannot say what information, if any, gained in the study of these systems may be readily related to more conventional metal oxidation reactions. It appears almost certain, however, that a thorough experimental and theoretical investigation of these systems will provide considerable insight into conventional oxidation studies. In addition, the investigation has intrinsic interest.

The present paper presents data on the reactions of metallic sodium with chlorine and bromine in the temperature range 230°-320°K. The chlorination reaction appears to be in accord with the Mott-Cabrera (7)

[1] Present address: J. Roy Gordon Research Laboratories, Sheridan Park, Clarkson, Ontario, Canada.

mechanism for film growth in the very thin film region. Good agreement between the data and the theoretical equation has been obtained over five decades of time and for up to a sevenfold increase in the film thickness.

The bromination data show some very interesting effects. The rate law is not that obeyed for the chlorination reaction, but instead takes the form

$$X = K \log t + K'^{2}$$

where for the lower temperatures, K is independent of temperature. Limitations of the data prevented the temperature coefficient of K' from being ascertained. It appears, however, to be fairly small or zero. At higher temperatures the value of K is smaller, the change in K' being once again uncertain. Irradiation with light of wavelength 5461Å has no effect on the rate at low temperatures, but at the higher temperatures it increases K to the value observed at low temperatures.

Experimental

As the apparatus employed for the present investigation is now being replaced, the description of it will be kept to a minimum. An outline of the experimental procedure follows, with further details given in subsequent sections.

Distilled sodium metal was evaporated in a stainless steel system at a rate of about 4 Å/sec, to form a film approximately 1000Å thick on a quartz slide cooled to near liquid nitrogen temperatures. The evaporation process was stopped by introducing purified argon to a pressure of about 1 atm.

The quartz slide was mounted on the end of a stainless steel tube which could be manipulated through a double "o" ring vacuum seal. Following film deposition the sample was transferred into the reaction chamber, which was then isolated from the evaporation unit.

The film was annealed at 60°C, the argon pumped out of the reaction chamber, and a predetermined pressure of halogen introduced through a pneumatically operated valve. The rate of the reaction was then followed by measuring the change in the intensity of the beam of monochromatic light (Hg 5461Å line) transmitted through the film. This change arises from the decrease in optical density of the film, since the metal with a high extinction coefficient reacts to give an essentially transparent halide layer. The output from the photocell unit, to be described later, was connected to an oscilloscope with camera and to a recording potentiometer.

The switch that controlled the pneumatic valve also triggered the oscilloscope, and thus the course of the reaction could be followed from times as short as a few milliseconds up to many hours or even days. It is primarily the speed of measurement which recommends this optical method for the study of thin film formation.

Evaporation unit and reaction vessel.—Figure 1 is a scale drawing, somewhat simplified, of the apparatus labelled to indicate the function of the various components. It was constructed entirely from stainless steel, the vacuum seals being formed with "o" rings of compound number 17507, Precision Rubber Products (a fluorocarbon polymer of high chemical inertness and stable to temperatures in excess of 150°C). As the diagram is largely self-explanatory, little will be added except to point out the various functions of the sample support tube which supports at one end the quartz slide on which the metallic sodium was deposited. Its principal function was to transport the slide from the sodium evaporation chamber to the reaction chamber while maintaining high vacuum or controlled atmosphere conditions. At the same time, however, a flange on this tube sealed the evaporation chamber from the reaction chamber when the slide

[2] By log y shall be meant $\log_{10} y$.

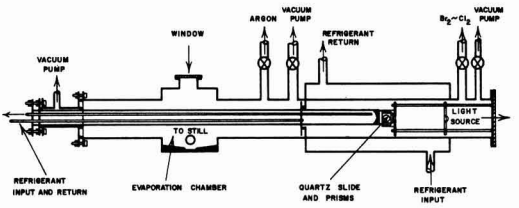

Fig. 1. Evaporation unit and reaction vessel

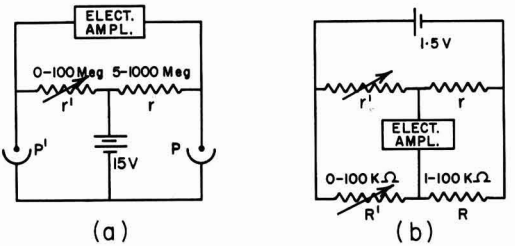

Fig. 2. Photometer circuit diagram and related circuit

was positioned in the latter, thus preventing contamination of the sodium in the evaporation chamber during the reaction. Within the main sample support tube were smaller tubes through which thermostated fluids or liquid nitrogen could be circulated to control the temperature of the quartz slide. The window in the evaporation chamber was used to observe the sodium film during deposition.

Following bakeout at about 150°C, the apparatus could be evacuated to a pressure of better than 3×10^{-7} Torr.

Photometric measurements.—A mercury arc lamp (General Electric AH100A) in conjunction with filters to isolate the 5461Å line (Kodak interference filter 540 and gelatin filter number 77), collimating lenses, first surface mirrors, and prisms made up the optical part of the photometric equipment. A beam splitter was used, and the intensity of the beam transmitted through the metal film was compared to that of the reference beam using circuits (Fig. 2) similar to those described by Dignam, Forbes, and Le Roy (11). Figure 2a consists of a Wheatstone bridge in which two adjacent resistance elements are replaced by 1 P37 vacuum photocells (P and P') whereas Fig. 2b is a simple Wheatstone bridge used to obtain the value of the resistance ratio r/r' in terms of the precision resistors R and R'. The electrometer amplifier was a Keithley Model 603 instrument (input impedance 10^{15} ohms), the output for which was connected to a recording potentiometer and to an oscilloscope with camera.

In addition to the circuits illustrated in Fig. 2, two other circuits could be selected which enabled the voltages across the resistors r' and r to be measured independently. Under experimental conditions the photocell dark currents were about 2×10^{-11} amp, with the lowest value for the light current being about 5×10^{-10} amp. In some runs, therefore, correction for the dark current was required.

Changes in the optical density of the metal film were measured as follows. The experimentally determined quantities are the voltages across the resistors r and r' and the ratio R/R' when circuit b is in balance. Associating P' with the reference beam, and P with the transmitted beam, the following symbols are defined in connection with the transmitted beam: V, voltage across r; i, total photocurrent; i_d, dark current; i_L, $i - i_d$; I, light intensity incident on photocell P. An identical set of primed symbols are defined in connection with the reference beam.

From Fig. 2a, $i = V/r$ and $i' = V'/r'$, and from Fig. 2b, at balance, $r/r' = R/R'$ so that

$$i/i' = (R'/R)\,(V/V')$$

or

$$\frac{i}{i'} = \frac{R'}{R}\left[1 + \frac{\Delta V}{V'}\right] \qquad [1]$$

where $\Delta V = V - V'$.

The dark current could always be neglected in connection with the reference beam, but not always in connection with the transmitted beam. Therefore $i = i_L + i_d$ and $i' = i'_L + i'_d \simeq i'_L$ so that [1] becomes

$$\frac{i_L}{i'_L} = \rho - \rho_d \qquad [2]$$

where

$$\rho = \frac{R'}{R}\left[1 + \frac{\Delta V}{V'}\right] \qquad [3]$$

and ρ_d is the value of ρ when $i = i_d$ (*i.e.*, the value of ρ measured with $I = 0$). Since $I \propto i_L$ and $I' \propto i'_L$[3] we may write

$$I/I' \propto (\rho - \rho_d)$$

The change in optical density from time zero to time t

$$\Delta\alpha = \log \frac{I(t=0)}{I(t)} \qquad [4]$$

is therefore given by

$$-\Delta\alpha = \log\left(\frac{\rho(t) - \rho_d}{\rho(t=0) - \rho_d}\right) \qquad [5]$$

During any given run, the value of r was held constant, as was the intensity of the lamp, so that I' remained constant. Thus $V' \propto I'r' = I'r(R'/R)$ so that we may set $V' = v(R'/R)$ where v is a constant for any given run.

The equation for ρ now becomes

$$\rho = \frac{R'}{R} + \frac{\Delta V}{v} \qquad [6]$$

Prior to beginning a run, r and r' were adjusted to make ΔV close to zero, and v was determined. ΔV was then recorded continuously during the run, with r' (and hence the ratio R'/R) adjusted from time to time to keep ΔV within the recorder scale. In Eq. [6], the second term, $\Delta V/v$, arises from the off-balance of the bridge circuit (Fig. 2a). By maintaining $\Delta V/v$ small compared with R'/R, fluctuations in the lamp intensity have only a small effect on the values of ρ determined. With this circuit it was possible to detect changes in the transmitted light intensity as small as 1 part in 3000, although such sensitivity was rarely required.

The thickness of the halide film may now be related to the change in optical density, $\Delta\alpha$, in the following way. If we let I_o be the light intensity incident on an element of area, dA, of the metal film system, then on neglecting multiple reflections within the films the element of transmited light, dI, is given by

$$dI = dA\, I_o\, 10^{-\epsilon X_m} \qquad [7]$$

where ϵ and X_m are the decadic extinction coefficient and thickness of the metal film. We shall assume that I_o and X_m are in general dependent on the position on the surface, but that ϵ and the halide film thickness, or thickness of metal consumed, ΔX_m, are independent of position. Substituting $X_m = X^o_m - \Delta X_m$ in the above equation, where X^o_m is the metal film thickness before reaction, and integrating over the entire illuminated surface, we obtain the following expression

$$I = \int_{\text{Area}} dA\, I_o\, 10^{-\epsilon(X^o_m - \Delta X_m)} \qquad [8]$$

[3] In the intensity range employed, 1P37 vacuum photocells have a linear response according to tube specifications.

Since ΔX_m is constant at any given time, and is zero at time zero, it follows immediately from [8] that

$$\frac{I(t)}{I(t=0)} = 10^{\epsilon\Delta X_m} \qquad [9]$$

and hence from [4], [5], and [9]

$$\Delta X_m = \frac{1}{\epsilon}\log\frac{\rho(t) - \rho_d}{\rho(t=0) - \rho_d} \qquad [10]$$

The thickness of the halide film, X, can be calculated from [10] and the relation

$$X = (\Omega/\Omega_m)\,\Delta X_m \qquad [11]$$

where Ω and Ω_m are the volumes per metal atom in the halide and metal, respectively.

The extinction coefficient, ϵ, was calculated from the optical constants[4] for evaporated sodium films measured by Ives and Briggs (12), the value for 5461Å radiation being given by $\epsilon = 2.32 \times 10^{-3}$ Å^{-1}.

The effect of neglecting multiple internal reflections within the metal and halide films will now be examined. Multiple reflections within the metal film can, of course, be entirely neglected because of the extremely high rate of attenuation of amplitude in this medium. Interference effects arising from multiple reflections within the halide film are, however, significant. Thus, a NaBr film (refractive index 1.62) 500Å thick, will cause a reduction in the transmitted intensity of about 6%, which in turn corresponds to an error in the halide film thickness determination of about 10Å. For thinner films, the error is less, going to zero at zero film thickness. The errors for NaCl films are somewhat less for the same thickness owing to the smaller value for the refractive index (1.50). In both cases, the errors introduced by neglecting multiple reflections, although not insignificant, are of the same order or smaller than random errors arising from other sources, principally light scattering, a phenomenon which is discussed later.

As the properties of thin metal film are known to depend appreciably on film thickness for sufficiently thin films, care was taken to make sure that the metal film thickness never fell below about 300Å during the run.

Materials.—Analar grade sodium was melted in a Pyrex vessel under vacuum, filtered, then outgassed, and finally transferred in an argon atmosphere to a stainless steel still connected to the sodium evaporation chamber. It was further outgassed here under high vacuum conditions and finally distilled at about 375°C into the evaporation chamber, the background pressure being never higher than 10^{-5} Torr. According to Horsley (13) this should produce sodium of 99.9995% purity, apart from gas content.

Argon was purified as required by bubbling it through a column of liquid sodium.

Commercial tank chlorine was condensed into a Pyrex trap and subjected to ten trap-to-trap distillations while pumping. On the final distillation, the background pressure did not rise above 2×10^{-6} Torr.

Bromine was treated in a similar manner.

Results

Chlorination.—Chlorination results obtained for metal films deposited under conditions where the background pressure during deposition was much in excess of 10^{-6} Torr were irreproducible. Only results obtained for films deposited at background pressures of 7×10^{-7} Torr or less are reported herein. The apparatus is being replaced by an ultrahigh vacuum system, capable of sustaining vacuums of the order of 10^{-10} Torr, in order to overcome the above difficulty.

For a number of runs, the expected behavior of the transmitted light intensity with time was not ob-

[4] The familiar chemical extinction coefficient is related to the fundamental optical extinction coefficient k' (which is the imaginary part of the complex refractive index) by the equation $\epsilon = 4\pi k'/\lambda_o$ 2.303, where λ_o is the wavelength of the light *in vacuo*.

served. Instead, the transmitted light first appeared to decrease in intensity, followed ultimately by the expected increase with time. The anomalous behavior arose almost certainly as a result of the scattering of the light beam at the sodium-halide-halogen interfaces, brought about presumably by the roughening of the surface during the initial period of reaction. This extremely undesirable effect was reduced very substantially by having the light beam incident on the bare surface of the quartz slide rather than on the halide surface. The effect appeared to be entirely absent for several runs, suggesting that the initial roughening of the surface probably took place as a result of surface contamination prior to introducing the halogen gas. However, no reaction could be detected prior to introducing the halogen, despite the fact that reaction of about 1/10 of the sodium atoms on the surface should produce a detectable change in optical transmission.

The above problem constitutes the major limitation of the data and the principal incentive to abandon the apparatus in favor of one which overcomes this difficulty. Nevertheless, the present data, despite this limitation, provide some interesting information concerning the kinetics of halogenation of sodium.

The chlorination data, plotted as chloride film thickness *vs.* the logarithm of the reaction period, are presented in Fig. 3 to 6, the circles representing the experimental values. The runs at 237° and 255°K (Fig. 3) were the only ones which showed no evidence of the light scattering effect mentioned above. The points for these two runs were calculated using Eq. [10] and [11], no correction for scattering being applied. Five further runs, (Fig. 4-6) although they showed a light scattering effect, were otherwise acceptable in that the background pressure during film deposition was less than 7×10^{-7} Torr. Of these five, all but one (curve a, Fig. 5) gave results reasonably consistent with the above two for reaction periods greater than 10 sec on applying an additive correction, X_o, to the film thickness calculated from [10] and [11]. If the fraction of light scattered remained constant after about 10 sec of reaction, such an additive correction should indeed apply. The method of choosing the values for the correction thickness, X_o, will be dealt with shortly.

An experiment to determine the pressure dependence of the reaction rate, although not entirely conclusive, indicated that the rate was proportional to the chlorine pressure to the power of approximately 0.3 (see Fig. 7).

Bromination.—As the data for the bromination of sodium were found under certain conditions to be affected by the 5461Å radiation used in the optical transmission measurements, the majority of these runs were carried out under conditions of intermittent illumination, the sample being illuminated only long enough to make the individual measurements (about 1 sec).

As was the case for the chlorination, only results for metal films deposited at background pressures of 7×10^{-7} Torr or less are reported. Furthermore, all

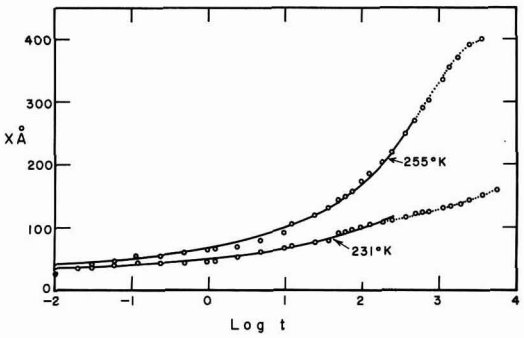

Fig. 3. Results for the chlorination runs which showed no evidence of the light scattering effect. Time in sec; chlorine pressure 3.86 Torr at 331°K, 3.90 Torr at 255°K.

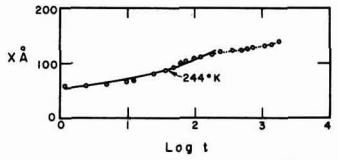

Fig. 4. Results for the chlorination runs which showed light scattering, corrected for light scattering as discussed in paper. Time in sec; chlorine pressure 4.60 Torr.

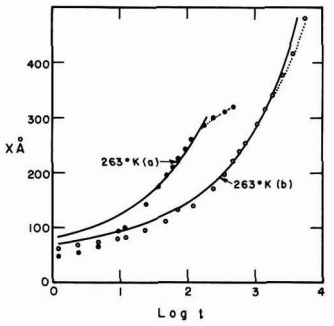

Fig. 5. Results for the chlorination runs which showed light scattering, corrected for light scattering as discussed in paper. Time in sec; chlorine pressure 5.48 Torr curve a, 6.90 Torr curve b.

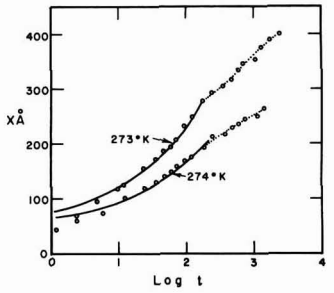

Fig. 6. Results for the chlorination runs which showed light scattering, corrected for light scattering as discussed in paper. Time in sec; chlorine pressure 4.61 Torr at 273°K, 4.90 Torr at 274°K.

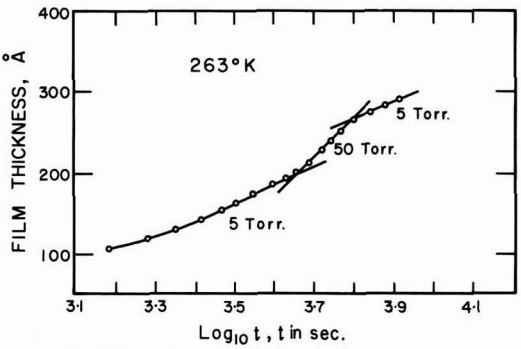

Fig. 7. Dependence of chlorination rate on pressure

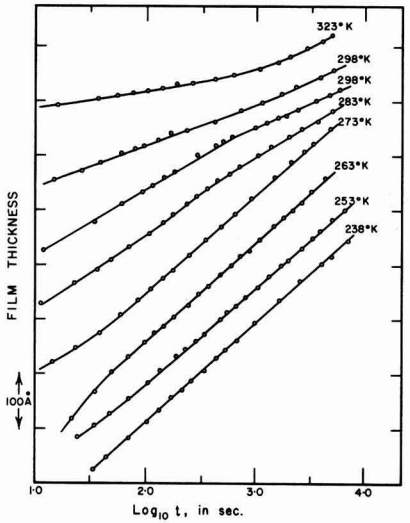

Fig. 8. Bromination results

the runs showed the light scattering effect, making it impossible to determine the absolute thicknesses of the bromide films. The change in thickness following the first few seconds of reaction could be determined as before, however, provided the fraction of scattered light remained independent of film thickness and time (*i.e.*, provided the degree of roughness of the halide-halogen interface remained essentially constant).

The data are presented in Fig. 8, the positioning of the curves with respect to translation along the "Film Thickness" axis being arbitrary. As far as could be determined, however, there appeared to be no systematic change in intercept with temperature for the temperature range 238°-273°K, indicating only a small or zero temperature coefficient for the reaction rate in this temperature range. It is clear from Fig. 8 that above 273°K, the behavior is somewhat different.

Illumination with 5461Å radiation was found to have an effect on the rate only for runs at the higher temperatures (*i.e.*, above 273°K). The influence of continuous irradiation on the rate is illustrated in Fig. 9.

Combined bromination, chlorination runs.—A few runs were carried out under conditions of intermittent illumination in which the sodium film was first reacted with bromine, then the bromine removed and chlorine

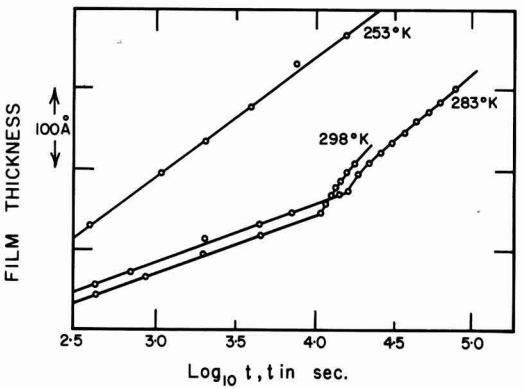

Fig. 9. Effect of illumination with 5461Å radiation on bromination rate.

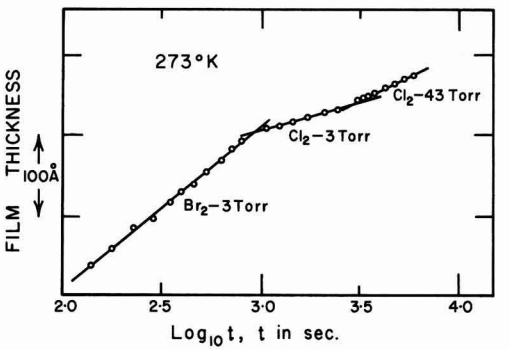

Fig. 10. Effect on rate of metal consumption of replacing bromine with chlorine following bromination.

introduced. The results for one such run are presented in Fig. 10.

Discussion

Chlorination results.—The data for the chlorination of sodium were fitted to a slightly modified form of the Mott-Cabrera theory (10) for the growth of thin and very thin films. The equation, which is discussed in some detail by Dignam, Fawcett, and Böhni (14), is given below

$$dX/dt = 2A \sinh (B/X) \qquad [12]$$

$$A = \Omega\nu\, a \exp(-U/kT) = A_o \exp(-Q/kT) \qquad [13]$$

$$B = \mu^* V/kT \qquad [14]$$

where the symbols are defined as follows: n, volume concentration of mobile species, in general a function of temperature; U, zero field activation energy associated with movement of the species; ν, usual frequency term associated with the movement of the species; a, distance travelled per activation, or the jump distance; Ω, volume of product per cation or anion (depending on whether transport is cationic or anionic); μ^*, charge-activation distance produced (activation dipole) associated with movement of the species; V, potential drop across the product film arising from equilibration of electrons in the metal with those in surface states at the film-gas interface. Equation [12] may be re-written in the following integrated form

$$\int_{B/X}^{\infty} \frac{(1/2)\ \mathrm{csch}\ u}{u^2}\, du = \frac{A}{B}\, t \qquad [15]$$

where the boundary condition $X = 0$ at $t = 0$ has been used. The data in Fig. 3 where fitted to Eq. [15] using a 7094 IBM computer and a procedure outlined previously. The solid curves shown were calculated for values of B and A which minimized the variance in each case. From the values of B, μ^*V was calculated to be $7.2_2 \pm 0.3_3$ and $7.7_7 \pm 0.2_6$ eÅv for the runs at 231° and 255°K, respectively. Since the two values agree within their combined standard deviations, μ^*V was taken to be temperature independent, the weighted mean value and the standard deviation of the mean being given by: $\mu^*V = 7.5_7 \pm 0.2_1$.

As the remaining data (Fig. 4-6) involve light scattering effects, as mentioned previously, they were analyzed in a slightly different manner. In Eq. [15], X was replaced by $X' + X_o$ where X' is the apparent film thickness calculated from [10] and [11], and X_o the correction term to allow for the attenuation of light arising from scattering. If the fraction of light scattered remains constant after a short period of time, then X_o will be constant following this transition period. For these runs, therefore, B was assumed to be given by [14], using the above value for μ^*V, and

A and X_o chosen to minimize the variance. The computed curves for these runs are also shown as solid lines in Fig. 4-6.

It is clear from the data that following chlorination for a period in the neighborhood of 100-1000 sec, a more or less abrupt break occurs in the plot of film thickness *vs.* log (time), the direction of the break suggesting a fairly sudden decrease in the reaction rate. Apart from this effect, however, which will be discussed later, fairly good agreement between the data and calculated curves is obtained.

Thus, the only two fully reliable chlorination runs (Fig. 3) fit Eq. [12] or [15] over about 4 decades in the chlorination period, and in the case of the run at 255°K, over a factor of 7 in the chloride film thickness. Furthermore, the fit is obtained for essentially the same value of μ^*V. Of the remaining five runs which may be considered, all of which involve light scattering, two (Fig. 4 and 5b) are brought into excellent accord, and two (Fig. 6) into fair accord with [12] or [15] after correcting for scattering on the assumption of a constant fraction of light scattered. Furthermore, the accord is achieved for the same value of μ^*V as above. Again, the values of A determined for the seven runs show the expected temperature dependence (Fig. 11) within experimental scatter. It therefore appears that the chlorination of sodium in the temperature range 231°-273°K takes place initially in accord with [12] (*i.e.*, essentially the Mott-Cabrera theory), a "break-away" occurring to lower rates after a certain period.

Before the Mott-Cabrera theory or any minor modification of it can be accepted even tentatively, however, other common rate laws must be examined. To this end, the data of Fig. 3 (255°K), which do not involve light scattering, and furthermore are the most extensive, were fitted to the most general form of the parabolic and direct logarithmic equations (*i.e.*, $X = K_p(t + t_o)^{1/2}$ and $X = K \log (t + t_o) + K'$, respectively). The results are summarized in Table I, in which the standard deviation of X, σ_X, from the most probable curve is given for the three rate laws. In order that the statistical significance of differences in σ_X can be ascertained, the standard deviation of σ_X, σ_σ, is also given.[5] From these values one can conclude that the chances against the improved fit for the Mott-Cabrera law being accidental are about 20 to 1 on comparison with the logarithmic law and 100 to 1 for the parabolic law. An even more pronounced decision in favor of the Mott-Cabrera law is obtained for run b, Fig. 5. As this run involved light scattering, however, the result is perhaps less convincing than the above. For the remaining runs, the total per cent change in film thickness is insufficient to provide a basis for distinguishing between the three rate laws. On the present evidence we conclude, therefore, that the chlorination data for the initial reaction period are in accord with the Mott-Cabrera law, rather than either the direct logarithmic or parabolic law.

[5] σ_σ was calculated from the relationship $\sigma_\sigma = \sigma_X/[2(n - i)]^{1/2}$ where n is the number of experimental points and i the number of disposable constants in the equation being fitted.

Table I. Comparison of the fit of the data of Fig. 3 (255°K) to the Mott-Cabrera, direct logarithmic and parabolic rate laws

	Mott-Cabrera	Logarithmic	Parabolic
σ_X, Å	6.0	10.6	13.4
σ_σ, Å	0.9	1.6	2.0

From Fig. 11, the temperature dependence of A is given by [13] with log (A_o in Å/sec) = 7.9 ± 2.4, Q = 0.48 ± 0.12 ev where the limits represent one standard deviation. We note that Q is smaller than the activation energy for migration of a cation vacancy in sodium chloride (about 0.8 ev) suggesting that the concentration of cation vacancies in the present case has a negative temperature coefficient. Although a detailed mechanism can support such a proposition, the difference in the activation energies is not sufficiently large compared with the standard deviation in Q, to rule out chance disagreement.

Any explanation of the "break-away" phenomena offered at this stage must be regarded as highly speculative. Bearing this in mind, the accumulation, as the film thickens, of the space charge due to the mobile ionic species would have the effect of reducing the rate below that predicted by [12]. Although this postulate has been tested quantitatively and successfully, further development of the thesis will be delayed until more extensive data are available.

Bromination results.—From Fig. 8 it is clear that for runs at temperatures of 273°K and below, the data are in accord with a direct logarithmic law (*i.e.*, film thickness linear in log time). This is in contrast with the chlorination results which appear to fit the Mott-Cabrera theory of metal oxidation, an approximate integrated form of which is sometimes referred to as the inverse logarithmic law. That reactions which are so very similar in nature should follow different kinetic rate laws is somewhat surprising. We note, however, that the chlorination data fit the Mott-Cabrera theory only for sufficiently short time periods. It is possible that the bromination data for sufficiently short time periods would also fit this law. The light scattering effect mentioned previously thwarted attempts to obtain such data.

A further interesting result is that the decadic rate constant is temperature-independent below 273°K (although it cannot be said with any degree of certainty that the intercept on a thickness *vs.* log t graph is likewise temperature-independent) and decreases as one proceeds to higher temperatures (see Fig. 8). Furthermore, illumination with 5461Å radiation, while having no measurable effect on the decadic rate below 273°K, above this temperature it causes the decadic rate to increase to the value found below 273°K (see Fig. 9). A tentative explanation for these observations follows.

It is possible that for sufficiently thin films the rate is controlled by ion transport through the film. In the absence of space charge effects this will lead to data in accord with the Mott-Cabrera theory (*i.e.*, inverse logarithmic law). If space charge effects are important, however, then a kinetic law approximating to a direct logarithmic law might perhaps be expected (15). As the film thickens, the rate might become controlled by

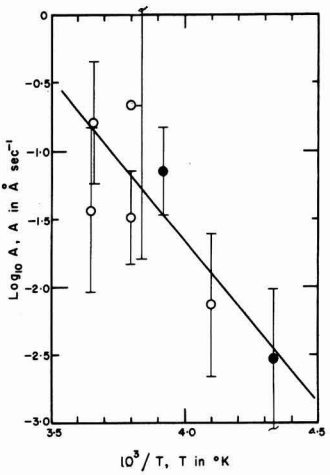

Fig. 11. Temperature dependence of the factor A for chlorination of sodium. The vertical lines represent 95% confidence limits, the diagonal line being the weighted least squares regression line for A. The solid circles represent the results for the runs which did not involve light scattering.

electron transport through the film rather than ion transport. Assuming the mechanism of electron transport to involve Schottky emission, this mechanism will also lead to a kinetic rate law approximating to a direct logarithmic law (16). Illumination of the brominating sample with light would be expected to have little if any effect on the rate of ion transport through the film, but would alter very substantially the rate of emission of electrons. Thus, at the higher temperatures where the electron transport mechanism is presumably operative, illumination with 5461Å radiation could stimulate electron transport through the film to such an extent that the rate-controlling process becomes ion transport once more. No such effect is expected at the lower temperatures where the rate-controlling process is presumably already ion transport. These considerations must be regarded at present as highly speculative.

Results for combined bromination chlorination runs. —The significance of these results (Fig. 10) concerns the fact that most of the reaction conditions remain unaltered as one proceeds from a point just before that at which the bromine was removed to a point immediately after the reaction was recommenced with chlorine present. In particular, the temperature, metal, and film materials are the same in both cases as well as the film thickness. The only change in the system, therefore, concerns the nature of the film-gas interface. We note that the rate of reaction on replacing the bromine with chlorine is reduced very substantially despite the fact that the free energy decrease for the reaction of sodium with chlorine is greater than that with an equivalent pressure of bromine at the same temperature. We must conclude, therefore, that the detailed structure of the film-gas interface is extremely important in the over-all kinetic process. Presumably the reduction in rate arises from the fact that chlorine atoms can be less readily chemisorbed on sodium bromide than can bromine atoms. Further investigation along these lines should provide interesting results.

Summary and Conclusions

Preliminary data on the chlorination and bromination of sodium have been obtained in the temperature range 238°-323°K. The results may be summarized as follows.

The initial chlorination data are in accord with an equation of the form

$$dX/dt = p^m\gamma \sinh (B/X)$$

where

$$m \approx 0.3,\ \gamma \simeq 2 \times 10^8 \exp (0.5/kT \text{ (ev)})$$

$$B = \mu^*V/kT,\ \mu^*V = 7.6 \text{ eÅv}$$

After a few minutes reaction time, however, the rates fall below those predicted by this equation. At 255°K, the results adhered to this equation over a range corresponding to more than 4 decades in the time and to an increase in the film thickness of more than a factor of 7. The film thicknesses achieved after about 1 hr reaction time range from about 150 to 420Å over the temperature range 231°-273°K.

For temperatures of 273°K and below, the data which correspond to bromination periods of 10 sec or more are in accord with an equation of the form

$$X = K \log t + K'$$

where K, the decadic rate constant, is independent of temperature in this region and has a value of 180Å per decade of time. The temperature dependence of the intercept, K' is uncertain, but appears to be small. Above 273°K, the decadic rate constant decreases with increasing temperature, however on illumination with 5461Å radiation, the decadic rate is increased to match that found below 273°K.

On interrupting a bromination run by replacing the bromine with chlorine at the same pressure, the rate is found to decrease very substantially, indicating that the processes occurring at the film oxidant interface play an important role in the over-all kinetic behavior.

The present data, though preliminary in nature, already show promise in providing information for the critical evaluation of mechanisms of growth of thin continuous films on metals. Further calculations will be postponed, however, until more extensive and more precise data are available.

Acknowledgments

The authors are grateful to the National Research Council of Canada for supporting this research and for a scholarship (D.A.H.). They also wish to express their thanks to Miss W. Y. Shiu and Mr. D. Goad for assistance in carrying out the calculations.

Manuscript received July 18, 1966; revised manuscript received Nov. 10, 1966. This paper was presented at the Philadelphia Meeting, Oct. 9-13, 1966.

Any discussion of this paper will appear in a Discussion Section to be published in the December 1967 JOURNAL.

REFERENCES

1. N. F. Mott, *Trans. Faraday Soc.*, **35**, 1175 (1939).
2. N. F. Mott, *ibid.*, **36**, 472 (1940).
3. H. H. Uhlig, *Acta Met.*, **4**, 541 (1956).
4. A. T. Fromhold, Jr., *Nature*, **200**, 1309 (1963).
5. A. T. Fromhold, Jr., *J. Phys. Chem. Solids*, **24**, 1309 (1963).
6. T. B. Grimley, *Discussions Faraday Soc.*, **28**, 223 (1959).
7. N. Cabrera and N. F. Mott, *Rep. Prog. Phys.*, **12**, 163 (1948).
8. D. D. Eley and P. R. Wilkinson, *Proc. Roy. Soc. (London)*, Ser. A, **254**, 326 (1960).
9. R. W. Bartlett, *This Journal*, **111**, 903 (1964).
10. M. J. Dignam and W. R. Fawcett, *This Journal*, **113**, 663 (1966).
11. M. J. Dignam, W. G. Forbes, and D. J. Le Roy, *Can. J. Chem.*, **35**, 1341 (1957).
12. H. E. Ives and H. B. Briggs, *J. Opt. Soc. Amer.*, **27**, 181 (1936).
13. G. W. Horsley, A.E.R.E. Report M/R 1152 (1953).
14. M. J. Dignam, W. R. Fawcett, and H. Böhni, *This Journal*, **113**, 656 (1966).
15. M. J. Dignam, *ibid.*, **109**, 192 (1962).
16. E. L. Cook and A. T. Fromhold, Jr., Paper presented at Southeastern Sectional Meeting of the American Physical Society, November, 1965.

Oxide Growth and Capacitance on Preirradiated Zircaloy-2 and Zirconium

R. J. Davis

Reactor Chemistry Division, Oak Ridge National Laboratory, Oak Ridge, Tennessee

ABSTRACT

Previous work has demonstrated a large enhancement of corrosion of Zircaloy-2 by oxygenated aqueous solution during bombardment by fast neutrons. Measurements of oxide growth and of film impedance were made on specimens preirradiated with fast neutrons in order to determine whether the irradiation damage important to corrosion occurs in the oxide film or in the metal substrate. A small enhancement of corrosion was observed with some specimen pretreatments. The results indicate that some corrosion enhancement results from irradiation of the substrate metal and that dissolved oxygen is required for the effect.

It has been demonstrated that corrosion of Zircaloy-2 in oxygenated aqueous media under heavy particle irradiation occurs at constant rates. If the heavy particles are fission fragments, the corrosion rate R (mils per year) depends on the fission power density in solution, P (watts per ml). At high power densities (greater than several w/ml) the rates also depend on temperature according to (1-3)

$$1/R = 2.3/P + 2.25 \times 10^{-11} \exp^{11,500/T} \qquad [1]$$

If the heavy particles are fast neutrons and the flux, ϕ is 10^{13} (n/cm^2/sec $>$ 1 Mev) or less, the rate increases with fast neutron flux according to (4)

$$R = 4.3 \times 10^{-13} \phi \qquad [2]$$

It was hypothesized that the radiation damage which affected corrosion, with both types of heavy particles, was the production of interstitials and vacancies (4). The rate equations were roughly correlated (*i.e.*, as well as the uncertainty of the estimation of the number of defects per fission would allow). This indicated that in terms of the rates of atom displacement D (no/cm^3/sec)

$$R \cong 10^{-15} D$$

These efforts did not establish the mechanism of the radiation effect. It is the purpose of this study to determine one feature of the mechanism, namely, where the important damage occurs.

Experimental

In outline the experimental proposal was to prepare pairs of specimens with and without oxide film, to irradiate one specimen of each pair and retain the other for a control and to corrode both specimens in an oxygen-steam environment and compare rates of weight gain and film impedance. The weight gain data were to provide a measure of corrosion rates and the film impedances an empirical indication (5) of the protective quality of the film. It can be shown that such data would in principle distinguish between three conceivable situations: (*i*) the primary radiation damage is in the oxide; (*ii*) the primary damage is in the metal which results in inferior oxide; or, (*iii*) the damage is in the metal, but the oxide is not changed.

Two sets of prefilmed specimens were prepared as indicated in Table I; one set was preoxidized for 1 hr and the other set for four days. Two sets of film-free Zr-2 specimens were also prepared (Table I); the 500°C heating in helium was employed to dissolve into the metal (6) the small amount of oxide left by pickling. (In the film-free specimen experiment, number 2, the interior of the autoclave was pickled; in all other experiments the autoclave interiors were as machined.)

The results of the first experiments led to other specimen preparations as indicated below. There was some indication of an effect due to fluoride left in pickling; also the possibility was raised that the effect found was due to the additive elements in Zircaloy-2. For these reasons a set of crystal-bar zirconium specimens was prepared to be film-free and fluoride-free but in a manner to provide some dissolved oxygen in the substrate metal. This is the film-free, fluoride-free preparation in Table I. The 700°C vacuum anneal was done in a large, zirconium foil-lined, quartz furnace. Any fluoride was expected to be volatilized as ZrF_4 by the treatment.

A set of specimens was prepared, as indicated in Table I, in a way to provide not only a film-free surface but a surface with a low dissolved oxygen content in the substrate metal. The low oxygen content was achieved by heating in helium at 800°C which is expected to dissolve into the metal the small amount of oxide left by pickling and disperse it almost uniformly through the metal (6).

The irradiations were made with the specimens still in the autoclaves which were canned as shown in Fig. 1, with a layer of boron-10 around them to reduce the thermal neutron flux and hence the activation of the zirconium. The irradiations were done at 100°C at a fast flux (>1 Mev) of 10^{13} for ten days. The control specimens were held at 100°C in an oven for a similar period.

The postirradiation oxidations were made in a furnace which provides a stream of a 50-50 mixture of oxygen and steam at 300°C and 1 atm. This environment was chosen for two reasons: (*i*) it contains water and oxygen, the chemical constituents of the media in which irradiation enhancement of corrosion has been seen (1, 2), and (*ii*) it is a convenient system. The notable feature of this furnace is the rapid heat-up device. By appropriate manual interchanges of the two portable furnaces shown on the left (Fig. 2), specimens were heated to 300°C in 30 sec and

Table I. Preirradiation treatments

Prefilmed:	Pickle in HF-HNO_3; oxidized in 300°C H_2O-O_2 (50-50 volume % mixture at 1 atm); seal in He-filled Zr-2 autoclave.
Film free:	Pickle in HF-HNO_3; seal in He-filled Zr-2 autoclave;[1] heat at 500°C 16 hr.
Film-free, fluoride-free:	Pickle in HF-HNO_3, vacuum anneal at 700°C 4 hr; oxidize in 300°C H_2O-O_2 (50-50 volume % mixture at 1 atm) for 1 hr; seal in He-filled Zr-2 autoclave; heat at 500°C 16 hr.
Low oxygen content:	Pickle in HF-HNO_3; seal in He-filled Zr-2 autoclave; heat at 800°C 16 hr.

[1] In one experiment the interior of the autoclave was pickled. (In all other experiments the autoclave surfaces were as machined.)

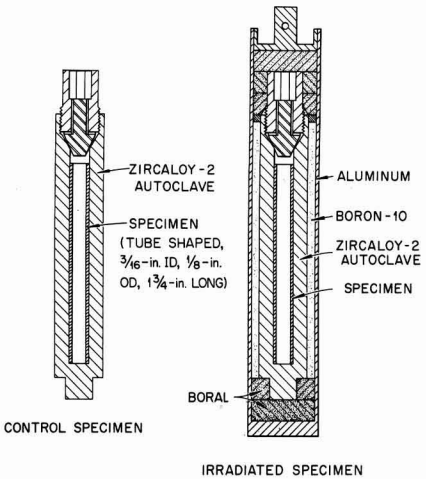

Fig. 1. Specimen autoclaves

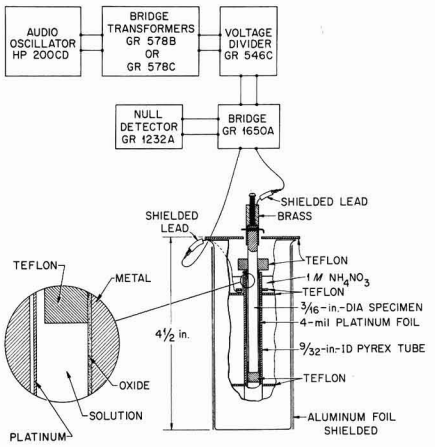

Fig. 3. Capacitance cell

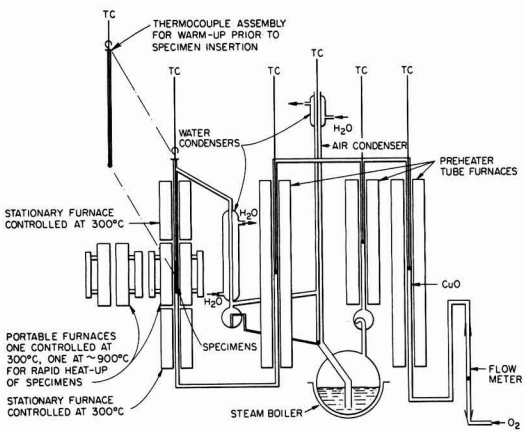

Fig. 2. Steam-oxygen furnace

meaningful exposures of as short as 5 min were made. Periodic rapid heat-ups were shown not to affect subsequent corrosion.

The impedance measuring devices are shown in Fig. 3. All but the cell are conventional equipment. The electrolyte was 1M NH_4NO_3. NH_4NO_3 was chosen because it decomposes at 210°C to volatile products; therefore traces of the electrolyte should not affect subsequent corrosion.

The measured impedances include the impedance of the platinized platinum surface, the electrolyte, and the ZrO_2 film. The impedance of the platinum surface is negligible, the electrolyte resistance is small and is known both by observation and calculation and can therefore be subtracted out. The impedance of the ZrO_2 film can therefore be measured (9).

The novel feature of this cell is the use of Teflon sleeves to demark the area over which the impedance is observed. Previous workers have used various sealing waxes (10). The important advantage of Teflon is that the impedance measurements do not affect the specimen weight or subsequent corrosion.

Several measurements were made to demonstrate the reliability of the impedance measurements. Reported film capacities on anodized films (10) have been reproduced. It was demonstrated that the same impedance is measured using Teflon as using Apiezon *W* sealing wax. It was also shown that a γ-field of intensity similar to that from induced radioactivity in an irradiated specimen does not affect the measured impedance. The impedances reported were all measured at 1 kc. Weight gains were measured on a microbalance with a precision of about 0.3 $\mu g/cm^2$.

Results

The weight-gain *vs.* time data for the film-free specimens (Fig. 4) show that a small increase (x 1.5-2 in corrosion rates occurred due to the irradiation. (The film-free specimen which was pretreated and irradiated in the autoclave which had been pickled showed a smaller radiation effect.) The corrosion of the irradiated specimen was continuously faster than the controls from essentially the start to the end of the postirradiation exposures. The crystal-bar specimen with the minimized surface fluoride showed the same behavior as the others.

The weight-gain data for the prefilmed specimens (Fig. 5) show no acceleration of corrosion due to irradiation; in fact the data suggest a small and temporary retardation of corrosion. [The prefilmed control specimens corroded more rapidly than the film-free controls. This is attributed to the 100°C treatment in He for 10 days. Others (7, 8) have found that heating a corrosion film in an inert environment at as low as 150°C (8) enhances subsequent corrosion.]

The low-oxygen specimen (Fig. 6) showed no effect as a result of irradiation.

The impedance data are given in Fig. 7-9. The data taken from the impedance bridge were equivalent series capacitance and loss tangent (tan δ) across the cell for about 0.5 cm^2 areas. The observed values were corrected for the solution resistance (~1 ohm-cm) and

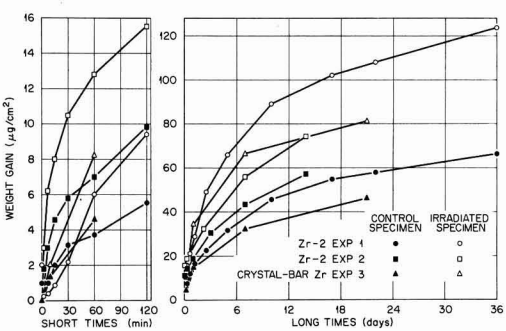

Fig. 4. Weight gains of film-free specimens

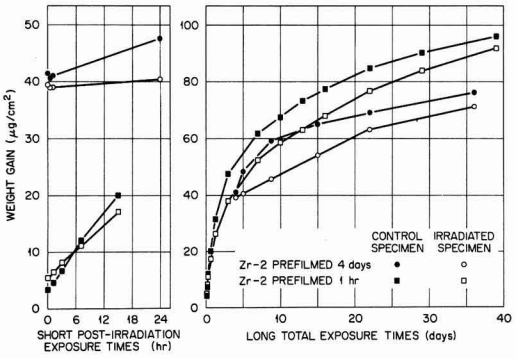

Fig. 5. Weight gains of prefilmed specimens

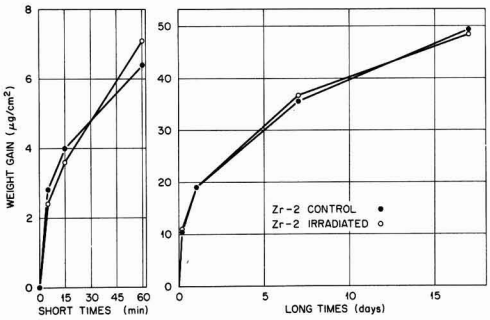

Fig. 6. Weight gains of low-oxygen specimens

the capacitances were converted to equivalent parallel capacitances per unit area. Both corrections are small. The data are plotted as reciprocal of capacitance per unit area and tan δ, both as a function of weight gain. For uniform growth of a homogeneous oxide film, reciprocal capacitance *vs.* weight gain should plot as a straight line through the origin. The slope of the line is inversely proportional to the dielectric constant of the oxide. Tan δ, for a homogeneous insulating material, is a property of the material, independent of thickness.

The impedance data (Fig. 7-9) generally show two deviations from the simple behavior expected for uniform growth of homogeneous material. In some cases the reciprocal capacitance (Fig. 7) remained very low up to weight gains as high as 20 μg/cm². In most cases (Fig. 7, 8, and 9), tan δ was lower (in one case higher) during the first 20 μg/cm² of weight gain than the approximately constant value observed thereafter. Neither of these effects were peculiar to irradiated specimens.

The impedance data for film grown on film-free specimens (Fig. 7) show no significant effect due to irradiation on either tan δ or reciprocal capacitance. (A possible exception is the reciprocal capacitance of the crystal-bar specimen, however neglecting the first 20 μg/cm² weight gain) the slopes of these two plots on Fig. 7, are similar.)

The impedances of the prefilmed specimen, after postirradiation oxidation are given in Fig. 8. Here we find no significant effect on tan δ but the reciprocal capacitances were less (or the dielectric constant greater) for the irradiated specimens. The differences were about 15% for the four day prefilmed specimens and almost 30% for the 1-hr prefilmed specimen.

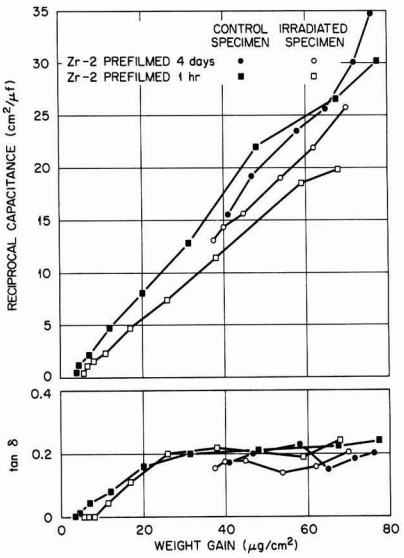

Fig. 8. Film impedances of prefilmed specimens

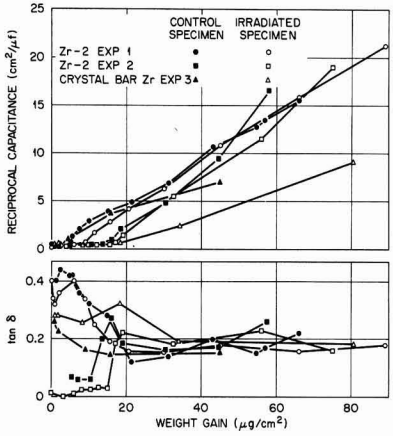

Fig. 7. Film impedance of film-free specimens

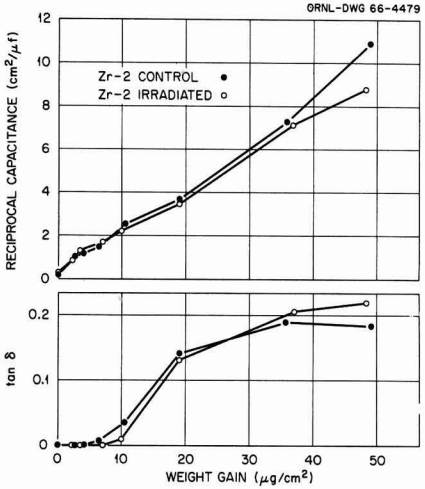

Fig. 9. Film impedances of low-oxygen specimens

The low oxygen specimen (Fig. 9) showed no effects due to irradiation.

Discussion

A small and continuing enhancement of postirradiation corrosion due to irradiation was found with certain pretreatments and not with others. Corrosion enhancement due to irradiation was observed with specimens pretreated to be free of oxide film, showing that the irradiation damage was in the metal. The pretreatments which would provide an oxygen-rich layer of metal at the surface resulted in irradiation enhancement of corrosion. These pretreatments included: (*i*) the Zr-2 pickled then heated in helium at 500°C and (*ii*) the X-bar Zr pickled, annealed, briefly prefilmed, then heated in helium at 500°C. The pretreatments which would lead to a nearly oxygen-free metal layer at the surface resulted in no enhancement of corrosion by irradiation. These include the pickle followed by heating in helium at 800°C, and prefilming at 300°C. These results indicate that the irradiation damage in the metal, which affects corrosion, is associated with dissolved oxygen although other interpretations, related to effects in the metal as a result of the various heat treatments, may be possible. The small irradiation enhancement was observed with the fluoride-free X-bar Zr, which is taken to indicate that neither fluoride nor the additive elements in Zr-2 are required for the irradiation effect.

The film impedances were measured to provide an empirical indication of protective quality. It was presumed that oxide of lower apparent dielectric constant would be more protective. (In terms of the weight gain, w, and reciprocal capacitances, $1/c$, and where K is an appropriate constant, the apparent dielectric constant is given by: $\epsilon = K\dfrac{d(w)}{d(1/c)}$. In the case of an irradiation effect in the metal, it was anticiated that film impedances would distinguish between two possibilities: first, that the damaged metal was more chemically reactive, and second, the metal damage resulted in poor quality oxide.

The apparent dielectric constants of film grown on those specimens which show the small corrosion enhancement, was not significantly different from the controls. However, it is not clear how the apparent dielectric constant relates to protective quality. In the case of the prefilmed specimens, the slight retardation of corrosion was accompanied by a significant increase in apparent dielectric constant, which is opposite to the relation expected (5). The film impedances therefore do not distinguish between the possibility that poor oxide grows on irradiated metal from the possibility that the damaged metal is more chemically reactive.

As indicated in the introduction, simultaneous exposure of Zircaloy-2 to oxygenated aqueous media at 300°C with irradiation to a fast neutron flux of 10^{13} n/cm^2/sec results in linear corrosion at a rate of 4.3 mils/year (metal consumption) or about 3 μg/cm^2/hr (weight gain). The question of whether this phenomenon and the enhancement of postirradiation corrosion reported in this paper are indeed ramifications of the same kind of irradiation damage cannot be completely resolved.

Although not related to irradiation effects, it is of incidental interest to take note of the two phenomena regarding the impedances of thin films. Up to 20 μg/cm^2 weight gain, very low reciprocal capacitances were observed for several specimens, perhaps due to short circuits through the film. Also low (and in one case high) tan δ values were observed for thin films on Zr-2 specimens; this indicates a change in the nature of the material at about 20 μg/cm^2 weight gain.

It is concluded that a small enhancement of corrosion of Zircaloy-2 results from prior irradiation of film-free surfaces prepared in certain ways. The data indicate that the damage occurs in the metal and is probably related to dissolved oxygen.

Cox (11) has found that Zircaloy-2 corrosion in steam is accelerated by inhomogeneously distributed oxygen in the metal surface, and particularly in the limiting case where oxygen is present as particles of ZrO_2 in the metal. Fast neutron irradiation has been found to precipitate carbon (12) and nitrogen (13) in iron as the carbide and nitride, respectively. A possible mechanism of the irradiation effect on corrosion is therefore suggested: during the process of corrosion the outermost layers of metal are supersaturated with dissolved oxygen. Fast neutrons cause the precipitation of this dissolved oxygen as zirconium oxide particles, and these precipitated particles enhance corrosion.

Manuscript received July 1, 1966; revised manuscript received Oct. 17, 1966. This research was sponsored by the United States Atomic Energy Commission under contract with the Union Carbide Corporation.

Any discussion of this paper will appear in a Discussion Section to be published in the December 1967 JOURNAL.

REFERENCES

1. G. H. Jenks, "Fluid Fuel Reactors," pp. 232-245, J. A. Lane, H. G. MacPherson, and Frank Mason, Editors, Addison-Wesley Co., Inc., Reading, Mass. (1958).
2. G. H. Jenks, "Corrosion of Zirconium Alloys," ASTM Special Tech. Pub. No. 368, Philadelphia, Pa., 1963, pp. 101-117.
3. B. Cox, K. Alcock, and F. W. Derrick, *This Journal*, **108**, 129 (1961).
4. G. H. Jenks and R. J. Davis, To be published.
5. J. N. Wanklyn and D. R. Sylvester, *This Journal*, **105**, 647 (1958).
6. J. P. Pemsler, *ibid.*, **105**, 315 (1958).
7. S. Kass and D. B. Scott, *ibid.*, **109**, 92 (1962).
8. D. W. Shannon, *Corrosion*, **19**, 414 (1963).
9. L. Young, "Anodic Oxide Films," pp. 150 *et seq.*, Academic Press, Inc., London and New York, (1961).
10. A. B. Reidinger, "The Corrosion Behavior of Zircaloy," MS Thesis, Union College, Schenectady, N. Y., May 1958.
11. B. Cox and B. R. Harder, *This Journal*, **110**, 1110 (1963).
12. F. E. Fujita and A. C. Damask, *Acta Meta.*, **12**, 331 (1964).
13. J. T. Stanley, "Diffusion in Body Centered Cubic Metals," J. A. Wheeler and F. R. Winslow, Editors, Chap. 26, p. 349, ASM, Metals Parks, Ohio (1965).

Electrodeposition of Tc^{99} from Aqueous Solution

Roger E. Voltz[1] and M. L. Holt

Chemistry Department, University of Wisconsin, Madison, Wisconsin

ABSTRACT

A study has been made to determine the optimum conditions necessary for the electrodeposition of macro amounts of technetium (Tc^{99}) from an aqueous bath containing about 0.018 mole of NH_4TcO_4 and 1 mole of $(NH_4)_2SO_4$ per liter of solution with H_2SO_4 added to pH about 1. Electrolysis of this solution at 1 to 2 amp/dm^2 and room temperature gives a bright, metallic appearing deposit of Tc with a cathode current efficiency of up to 30%. Included in this study are the effects on CCE of such factors as current density, bath pH, concentrations of the various reagents, temperature, and the colored cathode reduction product. Tests made to determine the nature of the deposit showed it to be essentially metallic; however, annealing is necessary to produce metallic crystals. During electrolysis a light pink reduction product forms in the bath; as electrolysis continues this reduction product becomes darker and appears to poison the bath. Addition of small amounts of H_2O_2 to the bath during electrolysis can prevent the colored reduction products from forming.

Technetium, the first artificial element to be synthesized (1), can be purchased from Oak Ridge National Laboratory as the salt NH_4TcO_4 for about $90 per gram of activity. This availability suggested to the authors that a study of the electrodeposition of technetium on a macro scale from aqueous solution would be a worthwhile addition to the already extensive literature dealing with the electrochemistry of the element and its compounds. An excellent review article by Boyd (2) and a book by Colton (3) gives information about the production and properties of Tc so detailed information will not be repeated here.

Tc^{99} has a half life of about 2.12×10^5 years and emits weak beta rays with a maximum energy of 0.32 Mev (4); thus the walls of ordinary laboratory glassware give sufficient radiation protection when Tc and its compounds are being used. Since information about the physiological effects of Tc is still incomplete, great care should be taken to protect the worker as well as the laboratory from contamination. Several sources of information describing the handling of Tc and its salts (3, 5) are available. Use of rubber gloves, protective clothing, a "film badge," a well-ventilated hood [$HTcO_4$ is fairly volatile (6)], and a covered plating cell are mandatory protections for the laboratory worker.

A number of reports of the electrodeposition of technetium from aqueous solutions have appeared in the literature, but most of them necessarily deal with dilute baths in the order of 10^{-12} to 10^{-5} m/l (mole per liter). The discoverers of Tc, Perrier and Segré, reported the deposition of a thin layer on a platinum wire from a very dilute acid solution (7). Other investigators (8) obtained bright cathode deposits from solutions of NH_4TcO_4 in 2*N* H_2SO_4 and NH_4HF_2. Black or brown cathode deposits were obtained when various pertechnetate salts in H_2SO_4 were electrolyzed (9, 10). Lietzke and Stoughton (11) obtained semi-quantitative data on the electrodeposition of Tc on Pt and Hg cathodes indicating that up to 97% of the Tc could be removed from an acid bath but not necessarily as the pure metal. An alkaline bath containing a Tc salt in 2*N* NaOH produced dark deposits (12). Polarographic studies have indicated the reduction of TcO_4^- to the metal or even to the hydride (13-15).

A survey of the literature suggested that two plating baths producing macro electrodeposits of Tc should be tried before further work was undertaken. The first was the bath reported by Eakins and Humphries (16) which contained NH_4TcO_4 in 2*N* H_2SO_4 with H_2O_2 added to prevent formation of a colored reduction product. We found that electrolysis of this bath at the conditions recommended by the authors gave a metallic appearing plate with a CCE of about 10%. The second macro bath developed by Box (17) uses various minimum amounts of H_2SO_4 (depending on the metal used as a cathode) with ammonium pertechnetate in 0.7M ammonium oxalate and a specially designed electrolysis cell. Plates up to 18 mg/cm^2 were reportedly obtained from this bath at a current density of 130 amp/dm^2, and no H_2O_2 was needed. We were not able to duplicate exactly these results in our electrolysis set-up which consisted of small (1 cm^2) cathodes and anodes in 50-100 ml of plating solution contained in a 150 ml beaker. We found that a light green reduction product formed when the NH_4TcO_4 concentration was about 1 g/l although the bath continued to plate at a low efficiency (about 2%). The extremely high C.D. makes it necessary to take special precautions, and apparently it is necessary to use the plating cell described in the article in order to operate this bath effectively.

Both of these reports indicate that virtually 100% of the Tc can be removed from the plating solutions as what appears to be metallic Tc. Neither of these baths was studied in detail. The first seemed unsuitable for our purpose because of the variation in CCE with each addition of H_2O_2 and the rapidity with which the bath darkened if H_2O_2 was not added. The second was unsuitable for our purpose because of the low CCE and because we were unable to obtain consistent results in our electrolysis set-up. For example, five different baths containing 1-2 g/l of NH_4TcO_4, made according to directions (17), were electrolyzed using both gold and copper cathodes. The deposits on the gold were very loose but metallic gray in appearance whereas those on copper were dark and obviously heavily oxided. All of these baths containing 1-2 g/l of NH_4TcO_4 turned light green after 15 min of electrolysis.

Experimental Methods

The source of Tc in all plating solutions was NH_4TcO_4. Boiled, distilled water was used for making the solutions. One hundred ml of bath was used for each plating run. The electrolysis cell, a 150 ml beaker, was fitted with two 3 x 3 cm Pt anodes and either a gold, copper, or stainless steel cathode of the same size. Direct current was supplied by a variable voltage rectifier. Cells were covered during electrolysis by specially fitted hard plastic plates, and all runs were made in a well ventilated hood. All pH determinations were made with a Beckman, battery operated pH meter. When semi-quantitative results were required a copper coulometer was used in series with the plating cell. The bus bars were arranged so that the coulometer electrodes and the plating cell elec-

[1] Chemistry teacher, East High School, Wauwatosa, Wisconsin. National Science Foundation Fellow.

trodes could be removed simultaneously from their respective cells. In cathode current efficiency calculations, the equivalent weight of Tc was assumed to be 14.4g (99/7). Shielding and possible spillage or spattering were monitored with a model 107C Professional Geiger Counter.

Preliminary observations.—A number of different plating solutions each containing 0.006 mole of NH_4TcO_4 per liter of solution were electrolyzed at room temperature for about 15 min with a cathode current density (CCD) of about 4 amp/dm², and the results are given in Table I.

The results given in Table I indicated that the sulfuric acid bath containing $(NH_4)_2SO_4$ was quite promising. Hull cell tests showed a plating range of approximately 0.6 to 15 amp/dm² for a pH 1.0 solution of this bath compared to about 0.1 to 4.0 amp/dm² for the acid solutions without $(NH_4)_2SO_4$. Also, this bath had a higher CCE (about 18%) than a comparable bath containing NH_4HF_2 (about 12%). Both the K_2SO_4 and Na_2SO_4 baths gave CCE's (16 and 17%, respectively) comparable to the ammonium sulfate bath, but the solubilities of these salts limited a study of their concentration effects. Thus all additional experimental results were obtained using the NH_4TcO_4-$(NH_4)_2SO_4$-sulfuric acid bath.

Experimental Results

The bath used to obtain the following experimental results contained (unless otherwise stated) 1 mole of $(NH_4)_2SO_4$ and 0.006 mole of NH_4TcO_4 per liter of solution with H_2SO_4 added to give the desired pH. Electrolysis resulted in a pink or brown solution; this was shown to be a cathode reduction product when the cathode was placed in a porous cup during electrolysis runs. The solution in the cup became black and heavy with precipitate while the solution outside the cup remained clear and colorless. The effect of this precipitate on the electrolysis is indicated by the low CCE of these runs (about 3%). Addition of small amounts of H_2O_2 removed the color and dissolved the precipitate. If the bath was to be restored to its former plating efficiency, it was necessary to decompose the excess H_2O_2 by heating with Pt black. Failure to do so resulted in a plating solution that gave a lower CCE.

Cathode current density and CCE.—The results of this study are given in Table II and show that CCE decreased as CCD increased and that a CCD of about 1-2 amp/dm² was satisfactory.

Bath pH and CCE.—H_2SO_4 was used to vary the pH. The results given in Table III indicate that a pH range of 0.5-1.5 is satisfactory for producing metallic appearing plates, and thus a bath pH of 1.0 was used for additional work.

Bath temperature and CCE.—Although most electrolyses were made at room temperature, the results given in Table IV show that a higher CCE is obtained at elevated temperatures.

It was noted that the plate taken from the bath at 90°C was much duller and darker than those from lower temperature baths, probably indicating deposit of some oxide and accounting for the apparently much higher CCE. It was also noted that the baths darkened much faster at elevated temperatures than they did at room temperature.

NH_4TcO_4 *concentration and CCE.*—A series of runs were made with baths containing larger amounts of NH_4TcO_4. Table V shows that at about 0.018M NH_4TcO_4 the CCE begins to level off.

All plates were bright and metallic in appearance. Two further runs were later made on fresh baths at 0.030 and 0.036M NH_4TcO_4 concentration. They produced CCE's of 32 and 33%, respectively, again showing the tendency for the CCE to level off at a maximum near 30%.

$(NH_4)_2SO_4$ *concentration and CCE.*—The results, shown in Table VI, indicate that any concentration of $(NH_4)_2SO_4$ above 1 m/l produces a darker plate. For all subsequent studies, the concentration of $(NH_4)_2SO_4$ was 1 m/l.

Table I. Electrolysis of 0.006M NH_4TcO_4 solutions; room temperature; 15-min runs at 4 amp/dm²

Solution	pH	Appearance of cathode deposit	Remarks
NH_4TcO_4 aqueous	6.0	Shiny, metallic	Poor conductivity
NH_4TcO_4 + H_2SO_4	2.0	Dark, loose	Bath darkened
NH_4TcO_4 + H_2SO_4	1.0	Shiny, metallic	Bath darkened
NH_4TcO_4 + 1M H_2SO_4	—	Shiny, metallic	Bath darkened
NH_4TcO_4 + 2M H_2SO_4	—	Shiny, metallic	Bath darkened
NH_4TcO_4 + H_2SO_4 + NH_4HF_2	1.0	Shiny, metallic	Bath darkened
NH_4TcO_4 + citric acid + H_2SO_4 or NH_4OH	2 to 9	All black	Bath darkened
NH_4TcO_4 + $(NH_4)_2SO_4$ + H_2SO_4	0.5 to 1.5	Shiny, metallic	Bath turned light pink
NH_4TcO_4 + Na_2SO_4 + H_2SO_4	1.0	Shiny, metallic	Light pink
NH_4TcO_4 + K_2SO_4 + H_2SO_4	1.0	Shiny, metallic	Light pink
NH_4TcO_4 + NaOH	12.0	Black	Bath dark

Table II. Effect of CCD on CCE; pH 1.0; room temperature; fresh bath for each 15-min run

CCD, amp/dm²	Wt of deposit,* g	CCE, %
1	0.0050	27
2	0.0075	18
3	0.0103	14
4	0.0101	11

* All deposits were shiny and metallic in appearance.

Table III. Bath pH and CCE; room temperature; 2 amp/dm²; fresh bath for each 15-min run

Bath pH	Wt of deposit, g	CCE, %	Deposit appearance
0.5	0.0080	13	Bright
1.0	0.0075	18	Bright
1.5	0.0096	21	Bright
2.0	—	—	Dark, loose

Table IV. Bath temperature and CCE; pH 1.0; 2 amp/dm²; fresh bath for each 15-min run

Bath temperature, °C	Wt of deposit, g	CCE, %	Deposit appearance
25	0.0075	18	Bright
40	0.0089	19	Bright
55	0.0101	24	Bright
70	0.0145	26	Bright
90	0.0166	37	Dull

Table V. Effect of NH_4TcO_4 concentration on CCE: room temperature; pH 1.0; 2 amp/dm²; fresh bath for each 15-min run

NH_4TcO_4, mole/liter	Wt of deposit, g	CCE, %
0.006	0.0075	18
0.012	0.0126	27
0.018	0.0153	30
0.024	0.0163	32

Table VI. Effect of $(NH_4)_2SO_4$ concentration on CCE; room temperature; pH 1.0; 2 amp/dm²; fresh bath for each 15-min run

Concentration of $(NH_4)_2SO_4$, m/l	Wt deposit, g	CCE, %	Deposit appearance
0.0	0.0062	14	Bright
0.5	0.0065	14	Bright
1.0	0.0077	18	Bright
2.0	0.0096	20	Dark on edges
3.0	0.0076	17	Dark on edges
4.0	0.0080	17	Dark and dull

Table VII. Effect of consecutive runs on CCE; 0.012 m/l NH_4TcO_4 in first 15-min run; room temperature; pH 1

Consecutive run	Wt deposit, g	CCE, %
1	0.0126	27
2	0.0095	21
3	0.0078	17
4	0.0062	12
5	0.0055	11

Continued electrolysis and CCE.—A plating solution originally containing 0.012 m/l of NH_4TcO_4 was used in a series of 15-min runs with no treatment between consecutive runs. A dark precipitate gradually formed in the bath and, as shown in Table VII, the CCE decreased. All plates, however, remained shiny and metallic in appearance.

After this series of runs, a small amount of H_2O_2 was added to the solution to oxidize the black reduction product back to the colorless TcO_4^-. The solution was then warmed with Pt black to decompose the excess H_2O_2. The resulting solution, made up to 100 ml and pH 1.0, on electrolysis gave a CCE only slightly (2%) less than the original solution. A bath originally containing 0.03 m/l of NH_4TcO_4 gave similar results with 12 consecutive 15-min runs, and H_2O_2 treatment also restored this bath so that on electrolysis it gave almost its original CCE (29 instead of 32%).

Nature of the Cathode Deposit

The cathode deposit obtained from the ammonium pertechnetate-ammonium sulfate-sulfuric acid bath at pH 0.5-1.5 appeared very metallic. It was not attacked by HCl and only slowly by concentrated H_2SO_4. It was attacked readily by HNO_3 of various concentrations and also by H_2O_2 in either sulfuric acid or ammonium hydroxide, as others have reported (18). When the bath pH was 2.0 or higher, the deposit became dark and quite loose. Accordingly, the possibility that the deposit was an oxide of technetium existed. Three series of tests were developed to explore this possibility. These were hydrogen reduction studies, precipitation studies, and x-ray diffraction studies. Other methods for quantitative determination of Tc are summarized by Colton (3).

Cathode deposits for these studies were obtained from 100 ml of the $(NH_4)_2SO_4$-H_2SO_4 bath containing 0.012 mole of NH_4TcO_4 per liter (pH 1.0, C.D. 2 amp/dm^2) on gold, platinum, and stainless steel cathodes. Before electrolysis, cathodes were rinsed with distilled water and then alcohol and dried to constant weight in an evacuated dessicator and after the plating run was completed, the plated cathodes were treated in the same manner.

Hydrogen reduction.—Ten plated cathodes, along with the control plates (unused stainless steel cathodes), were heated in a hydrogen atmosphere at 350°-400°C (10, 15) for 2 hr. They were then allowed to cool to room temperature, with the hydrogen still passing over them, before reweighing. Calculations, based on the stoichiometry: $Tc + TcO_2 \cdot 2H_2O + 2H_2 \rightarrow 2Tc + 4H_2O$, showed the deposit to be 92 ± 5% metallic Tc. Allowance was made for standard weighing deviations and control plate weight loss (average 0.0001g), but there was no way to measure the weight loss involved in the mere handling of this deposit that was not very adherent. Hence the evidence from this study can only be interpreted as indicating that the plate is essentially Tc metal.

Precipitation studies.—Three cathode deposits, whose weights had been previously determined, were dissolved in HNO_3 to remove the deposit from the gold cathodes and the solution adjusted to pH 8.0 with NH_4OH. Tetraphenylarsonium chloride was then used as the precipitating agent using the procedure described in the literature (19). Preliminary tests on this procedure had indicated a recovery of Tc was 98-100% which was in accord with the results of other investigators (20) and well within our standard weighing deviations. After drying the tetraphenylarsonium pertechnetate to constant weight, calculations were made based on the stoichiometry: $Tc + TcO_2 \cdot 2H_2O + 10\ HNO_3 + 2NH_4OH + 2(C_6H_5)_4AsCl \rightarrow 2(C_6H_5)_4AsTcO_4 + 2NH_4Cl + 10\ NO_2 + 8H_2O$. The results obtained showed the deposit to be 100 ± 2% Tc metal.

X-ray diffraction studies.—It was felt that three comparison values were needed in order to pursue this investigation: (*i*) A diffraction study of pure Tc metal. The Tc metal was prepared by electrodepositing Tc on stainless steel cathodes and subjecting these deposits to hydrogen reduction at 400°C until no further weight loss was noted. The deposits were then scraped (with great difficulty) from the stainless steel. (*ii*) A diffraction study of technetium dioxide. The oxide was deposited from a high pH (9.0) bath and dried to constant weight at 100°C. (*iii*) A diffraction study of the cathode deposit taken from the bath being studied. The cathode deposit taken from the bath described above was dried and easily scraped from the stainless steel cathode. Each of these prepared samples was then submitted for an x-ray diffraction study. The pure Tc metal prepared as above, showed only the lines of Tc, as reported in the literature (21), and no other lines; but neither the oxide nor the cathode deposit scrapings showed any lines capable of evaluation. Both were judged as being amorphous. A search of the literature revealed that others had experienced the same difficulty in evaluating a plate taken from a slightly acid ammonium sulfate-ammonium pertechnetate bath (22) and found that further annealing was necessary to develop the crystalline nature of the plate. Their study showed that from their higher pH bath, both Tc and Tc in an oxidation state of 4 were present.

We obtained several more cathode plates and collected more oxide and annealed both in an argon atmosphere for 2 hr. It was found that a temperature in excess of 200°C was needed to bring out the lines in the oxide while a temperature of 350°-400°C was required to anneal the plate material.

Seven fresh cathode plates were then prepared from the bath and the weights determined as described previously. The plates, along with control plates, were then annealed in an argon atmosphere for 2 hr at 400°C and the weight loss noted. In all cases, the weight losses were well within the standard weighing deviation. Annealing made the deposit extremely adherent and difficult to remove from the basis metal.

The scrapings from the plates were submitted to x-ray and in all cases showed only the lines of Tc and no other lines. At the annealing temperature we would expect any hydrated technetium oxide to have released its water of hydration with the stoichiometry:

$$Tc + TcO_2 \cdot 2H_2O \xrightarrow{400°C} Tc + TcO_2 + 2H_2O \quad (23).$$

Since the weight losses were well within the standard weighing deviations and since no lines other than pure Tc metal were discernible in the x-ray diffraction pattern, it appears that the amorphous plates, produced under the bath conditions described, were metallic within the limits of our investigation. Thus, all three studies tend to support the conclusion that the plate is certainly not oxide and is probably about 100% metallic.

Alloys

Attempts to electrodeposit a Ni-Tc (TcO_4^- added to a Watts bath) and a W-Tc alloy (TcO_4^- + Na_2WO_4 solution) were not successful. There was some evidence, however, that it might be possible to codeposit Re and Tc from a solution containing ReO_4^- and TcO_4^-.

Conclusions

The results presented show that Tc can be deposited in macro amounts as the bright metal from various

aqueous solutions. The $(NH_4)_2SO_4$-NH_4TcO_4-H_2SO_4 bath described here gives good CCE, is reasonably stable, can be readily rejuvenated by H_2O_2, and with reasonable precautions can be used safely in ordinary laboratory equipment. A bath containing 1M $(NH_4)_2SO_4$ and from 0.006 to 0.024M NH_4TcO_4 with H_2SO_4 added to give a *p*H of about 1.0, can be electrolyzed at 1-2 amp/dm^2 to produce a metallic cathodic deposit of Tc with a CCE range of 18-30%.

Electrodeposited Tc metal has few uses at the present time outside of medicine (24). However, its superconductivity at low temperatures as a metal (25) and as an alloy may find value in the rocket guidance systems and computer systems at a future time (26). Certainly, the possibility of plating an alloy of Tc deserves consideration.

Acknowledgment

The authors express their thanks to Dr. Chin-Hsuan Wei, of this department, who gathered and interpreted the x-ray diffraction data. One of us (REV) is grateful to NSF for financial support that made this work possible.

Manuscript received Sept. 8, 1964; revised manuscript received Sept. 9, 1966.

Any discussion of this paper will appear in a Discussion Section to be published in the December 1967 JOURNAL.

REFERENCES

1. C. Perrier and E. Segré, *J. Chem. Phys.*, **5**, 712 (1937).
2. G. Boyd, *J. Chem. Ed.*, **36**, 3 (1959).
3. R. Colton, "The Chemistry of Rhenium and Technetium," John Wiley & Sons, Inc., London (1965).
4. S. Fried, A. Jaffey, N. Hall, and L. Glendenin, *Phys. Rev.*, **81**, 741 (1951).
5. U. S. Dept. of Commerce, Nat. Bur. of Stand. Handbook 42, Sept. 1949, "Safe Handling of Radioactive Isotopes."
6. W. Smith, Jr., J. Cobble, and G. Boyd, *J. Am. Chem. Soc.*, **75**, 5773 (1953).
7. C. Perrier and E. Segré, *J. Chem. Phys.*, **7**, 155 (1939).
8. E. Motta, Q. Larson, and G. Boyd, ORNL Declassified Report, Mon-C-99, April, 1947, p. 22., (cited from ref. 2).
9. G. Cartledge and W. Smith, Jr., *J. Phys. Chem.*, **59**, 1111 (1955).
10. J. Cobble, C. Nelson, G. Parker, W. Smith, Jr., and G. Boyd, *J. Am. Chem. Soc.*, **74**, 1852 (1952).
11. M. Lietzke and R. Stoughton, Private communication.
12. N. Matuura and M. Yumoto, *Radioisotopes*, **8**, 28 (1959); *C. A.*, **53**, 21272 (1959).
13. G. Salaria, C. Rulfs, and P. Elving, *J. Chem. Soc.*, **1963**, 2479.
14. G. Salaria, C. Rulfs, and P. Elving, *Anal. Chem.*, **35**, 979 (1963).
15. R. Colton, J. Dalziel, W. Griffith, and G. Wilkinson, *J. Chem. Soc.*, **1960**, 71.
16. J. Eakins and D. Humphries, *J. Inorg. Nucl. Chem.*, **25**, 737 (1963).
17. W. Box, *Nucl. Applic.*, **1/2**, 155 (1965).
18. R. Colton and R. Peacock, *Quart. Rev.*, **16**, 299 (1962).
19. F. Jasim, R. MaGee, and C. Wilson, *Talanta*, **4**, 17 (1960).
20. C. Parker and W. Martin, U.S. At. En. Com. Document, ORNL-1116, 26 (1952).
21. R. Mooney, *Acta. Cryst.*, **1**, 160 (1948).
22. V. Spitsyn, A. Kuzina, N. Zamoshnikova, and A. Oblova (USSR), A/Conf. 28/p. 349, May 1964. Nuc. Abs. 18: 37108 (1964).
23. C. Nelson, G. Boyd, and W. Smith, Jr., *J. Am. Chem. Soc.*, **76**, 348 (1954).
24. W. Box, *Nucl. Applic.*, **1/2**, 157 (1965). Private communications of E. Christenberry.
25. J. Daunt and J. Cobble, *Phys. Rev.*, **92**, 507 (1953).
26. A. Pozdnyakov, *Rus. Chem. Rev.*, **2**, 129 (1965).

Determination of the Composition of Complexes and Their Instability Constant by Calorimetry

II. The Complex in Fused Potassium Chloride and Cadmium Chloride

William H. Metzger, Jr., Abner Brenner, and Harry I. Salmon

National Bureau of Standards, Washington, D. C.

ABSTRACT

A new method of determining the composition of complexes in solution and their equilibrium constant has been developed which is based on the determination of the partial molal heat effect developed when a small increment of each salt is added in turn to a series of mixtures covering the range of composition from 0 to 100%. The method was applied to the molten KCl-$CdCl_2$ system. The data show that the system contains the 1:1 complex with an instability constant of 0.32 at temperatures of 600° and 780°C. A calorimeter is described which permits the addition of the increments of salt to the molten mixture while the latter is stirred continually.

In a previous publication (1) a general method was described for determining the composition of complexes and their instability constant by calorimetric measurements. The experimental procedure consisted in adding a small amount of one reactant to a mixture of the reactants and determining the heat effect. From the latter the partial molal heat effect was obtained. The purpose of adding only a small amount of reactant was to determine the resultant heat effect without changing the composition of the mixture by more than a per cent. Thus, the heat effect is a function of the composition of the mixture. This procedure was repeated with one or preferably with both reactants over the range of composition of mixtures from 0 to 100%. In the aforementioned paper the method was applied to the determination of the composition and instability constant of two of the copper cyanide complexes. These measurements involved the addition of about 1g of sodium cyanide to solutions of cuprocyanide covering a range of composition.

The partial molal heat effect can be considered as the heat effect resulting from the addition of one mole of reactant to an infinite amount of mixture. It can be seen qualitatively that the heat effect is a function of the composition of the mixture by the following example: Let the complex formed from the two reactants A and B be AB_2. If small increments of A are added to a series of mixtures, starting with pure B

and then proceeding through intermediate steps to the composition AB_2 and beyond to pure A, it would be found that the maximum heat effect would occur when the addition of A is made to pure B. If the instability constant is small (less than 10^{-2}), the molal heat effect would be approximately equal to the heat of formation of the compound AB_2. The heat effect would diminish only slightly with succeeding mixtures until the composition AB_2 is approached. At the stoichiometric point the partial molal heat effect would rapidly decrease and beyond this point would have a small value. The partial molal heat effect of adding pure B to an infinite amount of pure A would be only half of that obtained by adding A to an infinite amount of B because only ½ mole of complex is formed per mole of B.

Assume that almost complete reaction occurs when a small amount of A is added to an infinite amount of B, and let this maximum heat effect (which is approximately the heat of reaction) be designated by θ_A per mole of A. Then the ratio of the partial molal heat effect $\Delta\overline{H}$ (obtained by adding a mole of A to an infinite amount of a mixture of A and B) to θ_A represents the fraction of a mole of AB_2 formed. For example, if θ_A is 10 kcal and $\Delta\overline{H}$ for a mixture just beyond the stoichiometric point is 0.5 kcal, this would mean that the addition of one-mole of A to an infinite amount of mixture of that composition results in the formation of only 1/20 mole of complex. This ratio, which is the fraction of a mole formed in the reaction, will be called the "fraction of reaction."

The fraction of reaction is the quantity which is experimentally determined. It can vary from zero to unity. This fraction is a partial derivative and is related to the mass action expression. If dy is the increment of A added to a mixture of any composition and $d\bar{a}$ is the amount of the product AB_2 formed, then the fraction of reaction is $\partial\bar{a}/\partial y$. Similarly, if dx denotes the increment of B that is added to a mixture, then $\partial\bar{a}/\partial x$ also is the fraction of reaction, and it cannot be larger than ½.

The two partial derivatives will be denoted by $\bar{a}'_x$ and $\bar{a}'_y$ or simply $\bar{a}'$ when only one independent variable is used throughout the discussion. They are derived mathematically from the expression for the mass action law by differentiation. If the reaction is $rA + sB \rightarrow A_rB_s$, the general expression for the mass action law for fused salts written in terms of mole fraction is

$$\frac{\left[\frac{y-r\bar{a}}{f}\right]^r\left[\frac{x-s\bar{a}}{f}\right]^s}{\frac{\bar{a}}{f}} = k \qquad [1]$$

where y and x represent the initial moles of A and B, respectively, used in making up the mixture, $\bar{a}$ represents the moles of A_rB_s formed at equilibrium. r and s are the coefficients of A and B in the chemical reaction, and f is the total number of moles present, $f = x + y + \bar{a}(1-r-s)$.

The formulas and the methods of determining the composition and the instability constant of a complex were derived in a former publication (1).

The cadmium chloride-potassium chloride system was chosen for study mainly to explore the applicability of the partial molal heat method to a fused salt system. This system had received extensive investigation (3-17) but the complexes present in the molten mixture had not been determined with certainty. We studied the system at a temperature of about 780°C so that it would be above the melting point of the highest melting component, potassium chloride (mp 772°C). This permits the introduction of increments of either salt in the molten form, hence there is no complication owing to heat of fusion of a solid. This temperature was higher than that used by most of the previous workers.

Apparatus

The determination of the heats of reaction in the fused salt bath requires the construction of a calorimeter which is operable at temperatures up to 900°C. The literature contains descriptions of several high temperature calorimeters, but experience with them has been so limited that no one design has emerged as the best. A description of the various high temperature calorimeters which have been constructed would be too much of a digression here. However, none of them have the two features which we consider essential for the success of the measurements. The two features are (*i*) continuous stirring of the reaction mixture while an increment of a reactant is added, and (*ii*) the complete submersion of the ampoule containing the increment below the surface of the fused salts, so that it is exactly at the temperature of the reaction mixture at the time that the ampoule is broken. Otherwise the construction of the furnace and calorimeter is conventional.

The construction of the calorimeter is shown in Fig. 1. It consists of a stainless steel jacket about 40 cm in diameter and 75 cm high, surrounded by a 5 cm thick layer of thermal insulation. Internally, the loss of heat is diminished by seven radiation shields made of stainless steel. The heating system consists of two wire wound concentric heaters and a third flat heater placed horizontally on the bottom below the other two. The outer and the bottom heaters are operated at a con-

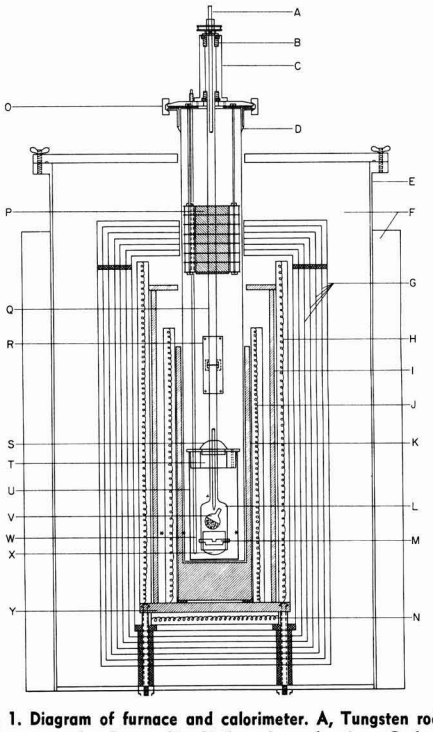

Fig. 1. Diagram of furnace and calorimeter. A, Tungsten rod for breaking ampoule; B, graphite-Teflon sleeve bearing; C, bearing holder; D, silicone adhesive; E, furnace jacket, stainless steel; F, zirconia wool-filled space; G, radiation barrier shields, stainless steel; H, outer circumferential heater; I, heat sink, silver; J, inner circumferential heater; K, heat sink, silver; L, perforated dispenser device, Pt-Ir alloy; M, bar against which ampoule is crushed; N, bottom heater; O, split-ring clamp; P, middle bearing; Q, dispenser-stirrer shaft, nickel tube; R, shaft coupling, nickel; S, bottom bearing, Vycor; T, calorimeter cap, machined of fused silica; U, calorimeter, Pt-Rh alloy; V, loaded ampoule of fused silica; W, Vycor tube containing the platinum heater used for calibrations; X, retainer cup, Pt-Ir alloy; Y, heat sink, silver. * Thermocouple locations.

stant current, such that a temperature slightly below the desired temperature is maintained in the center of the furnace. The inner heater is controlled by an automatic device which obtains its input signal from two chromel alumel thermocouples connected in series and located in the heart of the furnace near the reaction vessel. Most of the emf of these thermocouples is annulled by a potentiometer as the controller can handle a maximum input of only 7 mv. This method of obtaining the emf-change only as a difference increases the sensitivity of the control system. Over a period of 10 min the temperature of the inner vessel holds constant to about 0.01°C, but over a period of a day the temperature varies about 0.5°C. However, since the reaction is complete in about 15 to 30 sec, constancy for only a short time is adequate. The heaters have a total maximum power capacity of 5 kva.

To improve the uniformity of temperature, the furnace is provided with two concentric cylinders of silver about 1 cm thick, having a total weight of about 30 kg.

The inner vessel consists of a mullite tube, 8 cm in diameter and 60 cm long which is closed at the lower end. The upper end carries a brass flange which is cemented to the tube by an air cured silicone plastic material. The end projects sufficiently above the furnace so as not to be heated higher than 200°C. Another reason for having the open end of the tube project above the level of the furnace is to prevent corrosive halide vapors from damaging the heating elements.

The fused salt is contained in a platinum-rhodium vessel measuring 6.5 cm in diameter and 14 cm high. About 600 to 800g of salt are used for an experiment and the liquid level generally comes to within 5 cm of the top of the vessel. It is essential to construct the vessel of a platinum alloy as ceramic vessels frequently break when the fused salts solidify in them.

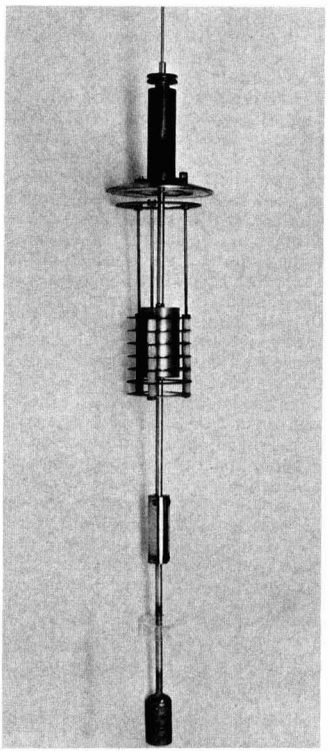

Fig. 2. Dispenser-stirrer unit, fully assembled with bearings and removable radiation shields.

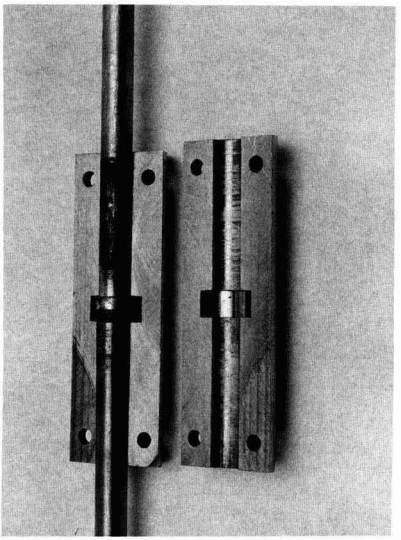

Fig. 3. Shaft coupling of the dispenser-stirrer; open view.

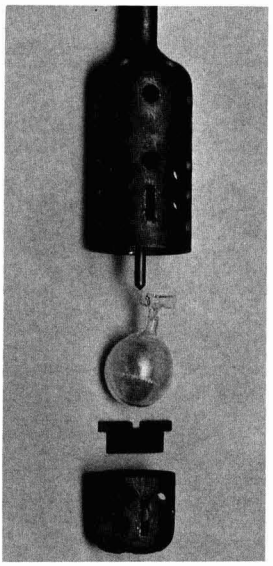

Fig. 4. Dispenser-stirrer: exploded view of the dispenser with loaded ampoule.

The most time-consuming part of the investigation was the development of a satisfactory device hereafter referred to as "dispenser-stirrer" for stirring the molten salt and for adding the increment. This part of the apparatus is shown in Fig. 2-4 in both an assembled and exploded photographic view. The dispenser-stirrer body is constructed of a platinum-iridium alloy, as ceramic vessels which were tried were not rugged enough and caused the loss of many experiments through breakage. The platinum alloy basket holds the ampoule, retains the broken fragments of the ampoule, and prevents them from catching in the thermocouples or the heater used for calibration. The notched platinum alloy bar with tabs holds the basket and ampoule in place and in addition acts as an anvil for breaking the ampoule. The pointed tungsten rod located inside of the shaft is used for breaking the ampoule containing the increment of salt. The stirring shaft is a nickel tube connected to the

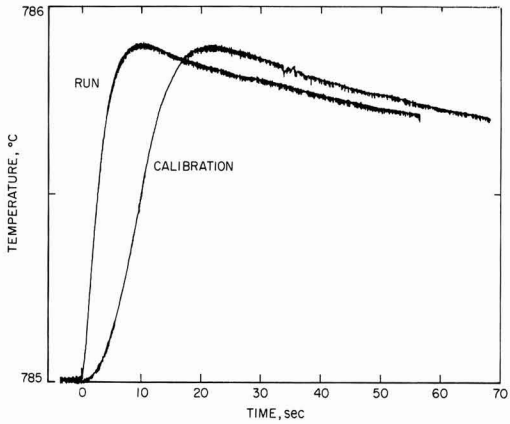

Fig. 5. Typical curves of temperature vs. time obtained with the recording potentiometer.

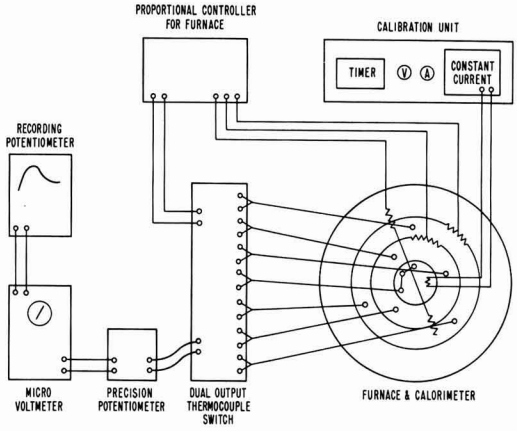

Fig. 6. Block diagram of apparatus

upper tubular part of the dispenser-stirrer by the coupling shown in Fig. 3. This construction allows for interchange of parts and permits the tungsten rod to move freely up and down in the shaft while the assembly is rotating.

The ampoules are made of fused silica. They are thin-walled and about 2 cm in diameter. They are easily broken by punching with the tungsten rod while stirring is in progress. The end of the neck of the ampoule is either bent or enlarged with a piece of fused silica to prevent the neck from protruding through the holes in the dispenser and snagging a thermocouple.

The temperature rise in the reaction vessel is measured by three commercial chromel alumel thermocouples connected in series. These are only 1.5 mm in diameter and require very little space. Furthermore, because of their small size they react to the temperature changes in a second. A temperature change of 0.01°C gives an indication slightly more than 1 μv. The average temperature rise in the experiments is about 1°C and the largest temperature rise is about 3°C.

The temperature increase during an experiment is measured by a microvoltmeter in series with an output voltage from a microvolt potentiometer. This arrangement made it posible to balance the thermocouple emf with the potentiometer immediately prior to the breaking of the ampoule and thus read the emf change on the microvoltmeter. The temperature rise is measured on the microvoltmeter, usually on the 100 μv scale. The voltage *vs.* time trace is recorded on a recording potentiometer connected to the microvoltmeter shown in Fig. 5. Readings are made to 1 μv.

For purposes of accurate temperature measurement and stability, the thermocouples used in the body of the furnace consist of platinum, platinum-10% rhodium alloy. These thermocouples are placed in tubes of pure aluminum oxide. At a temperature of 800°C the resistance between a thermocouple and ground is about 20 megohms. The proper insulation of the thermocouples is a matter of considerable importance.

In our first experiments the thermocouples were placed in mullite tubes, and they operated satisfactorily up to a temperature of about 600°C. But at 800°C the mullite tubes became too conductive and the thermocouples picked up stray voltages which prevented accurate readings being taken with the microvoltmeter. The block diagram for the thermocouples and associated measuring instruments is shown in Fig. 6.

Procedure

The furnace is allowed to come almost to temperature by being left on at a steady current over night. The furnace is put on automatic temperature control in the morning. The salt mixture is placed in the platinum-rhodium reaction vessel and melted in a pot furnace. It is then quickly transferred to the calorimeter furnace. The preliminary heating of the mixture reduces the time required for the setup to come to thermal equilibrium, and in so doing also reduces the loss of cadmium chloride by volatilization.

Next, the dispenser-stirring device is loaded with an ampoule of salt, the latter weighing usually from 1 to 3g (usually about 0.02 mole of salt is added to about 4 moles of salt mixture). The entire unit shown in Fig. 2 is locked into place with a split ring-clamp at the top of the ceramic tube. Stirring is started and after about ½ hr thermal equilibrium attained. This is considered to be the case when the temperature does not change more than 0.01°C/min. On breaking the ampoule, the reaction is completed in about 15 sec, as indicated by the maximum in the temperature rise.

The calibration of the calorimeter is performed at least twice for each determination, usually before and after the introduction of the increment of salt. An electric current of about 4 amp at 14v is passed through the platinum alloy heater coil (the latter being enclosed in a fused silica tube) for 10 to 20 sec. The high current and short period of heating is necessitated by the need to duplicate the heating rate of the chemical reaction. This is not achieved exactly, as the time of heating would have to be too short and the current too large for convenience in measuring. Although the interval of calibration may vary from 10 to 20 sec, it is accurately read on an electric timer accurate to 0.01 sec. The current is delivered by a constant current device, consequently, only one reading of current needs to be made during the calibration. The voltage, however, varies from about 13 to 14v during the calibration. Readings are therefore taken at intervals of about 2 or 3 sec on a voltmeter accurate to 0.5% and averaged. The heat capacity of the calorimeter, including the fused salt, is about 1 cal/μv or about 120 cal/degree.

In calculating the heats of reaction, no correction is made for the heat leak. The temperature rise is taken as the peak of the curve. This probably does not represent the true equilibrium temperature, but since the calibration is made in the same manner, most of the error is annulled. Since the heat leak is mostly a result of radiation, a simple correction cannot be made, as in calorimetry which is done at room temperature. This is because the rate of heat leak is not directly proportional to the temperature head. A graphical method of correcting for heat leak, which is based on the cooling curve, is given in the appendix. This correction for heat leak was not considered to be practicable in our work, because the calorimeter did not maintain a sufficiently constant temperature over

the period of 10-30 min that would be required to establish the cooling curve.

The filling of the ampoule presented a special problem, because the presence of a trace of moisture in the salt caused some of them to explode in the furnace. The following procedure is successful. After the required amount of salt is placed in the ampoule, it is placed in a furnace at 650°C for an hour to remove moisture. Then after cooling in a desiccator the ampoule is evacuated and sealed.

To expedite the measurements, two complete dispenser-stirring units are used. This permits another run to be made as soon as one unit is removed from the calorimeter. Four complete runs can be made in one day, including the necessary number of calibrations. The largest amount of time is spent in waiting for the system to come to thermal equilibrium.

Results

Although the precision of measuring the temperature rise in most of the experiments was about 1%, the precision of the measurements of the heat capacity of the system was about 3%. The over-all precision of the measurement of the partial molal heat effects was about 5% or 200 cal, whichever was the larger.

As an over-all check on the accuracy of the measurements, the heat of fusion of potassium chloride was measured. This was done by adding about 3g of potassium chloride to 450g of a melt consisting of about 95 mole % potassium chloride and 5 mole % cadmium chloride. Additions of solid potassium chloride were made at about 8° below its melting point. We found that the heat of solution (cooling) of the solid potassium chloride was 6380 cal/mole (1 cal = 4.18 Joules). The heat of mixing of the molten potassium chloride, determined at 780°C in the same melt, was small and positive, about 180 cal/mole. The heat of fusion of potassium chloride was 6560 ± 160 cal/mole. This result is about 5% higher than the value of 6274 cal/mole obtained by the drop method of calorimetry (2).

The experimental results for the $CdCl_2$-KCl system were obtained in the form of a heat effect for the increment of potassium chloride or cadmium chloride added to the melt. From this effect was computed the heat effect per mole of added salt, that is, the partial molal heat effect, $\Delta\bar{H}$. These data are graphed in Fig. 7 and 8 against mole per cent of potassium chloride in the melt.

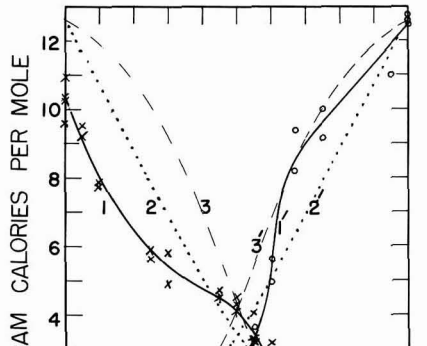

Fig. 7. Partial molal heat effects obtained at 780°C by adding either potassium chloride (curve 1) or cadmium chloride (curve 1') in the molten state to molten mixtures of potassium and cadmium chloride. Curves 2 and 3 represent theoretical curves for the addition of potassium chloride and curves 2' and 3' represent the corresponding curves for cadmium chloride.

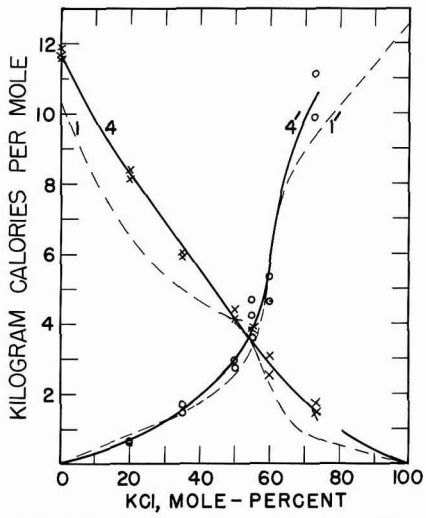

Fig. 8. Partial molal heat effects obtained by adding either potassium chloride (curves 1 and 4) or cadmium chloride (curves 1' and 4') to molten mixtures of potassium chloride and cadmium chloride. Curves 1 and 1' are the same as the like-numbered curves in Fig. 7 and refer to a temperature of 780°C. Curves 4 and 4' represent the data obtained at 600°C with cadmium chloride and potassium chloride.

Even without any mathematical analysis, the data show that the complex consists of equal moles of $CdCl_2$ and KCl. This follows from the approximately equal heat of reaction for an increment of KCl added to pure $CdCl_2$ and an increment of $CdCl_2$ added to pure KCl. Further evidence is that the curves cross at 55 mole % which is close to the stoichiometric 50 mole % point. No other complex appears to exist at the temperature of 780°C.

The mass action expression, in terms of the mole fraction, is

$$(x-\bar{a})(y-\bar{a}) = \bar{a}k(x+y-\bar{a}) \qquad [2]$$

where x and y are the initial number of moles of reactants, $\bar{a}$ is the moles of complex formed, and $(x + y - \bar{a})$ is the total number of moles present at equilibrium.

The instability constant may be calculated either from the fraction of reaction $\bar{a}'$, or from the slope of the curves at their intersection. The former method is less satisfactory than the latter if the instability constant is small, but in the present case it is equally satisfactory. The value of $\bar{a}'$ is obtained for the point of intersection of the two curves, where $\Delta\bar{H}$ = 3400 cal/mole. Hence, $\bar{a}'$ = 3400/12,600 = 0.27. (The value of 12,600 cal/mole is the heat of reaction derived from our experiment of adding an increment of molten cadmium chloride to molten potassium chloride, as shown in Fig. 7 for the abscissa: KCl, 100%.) This value is substituted into the following equation [see Eq. 33 of ref. (1)]

$$k = \frac{(1-2\bar{a}')^2}{4\bar{a}'(1-\bar{a}')} = \frac{(1-0.54)^2}{4(0.27)(0.73)} = 0.27 \qquad [3]$$

To use the second method, $\bar{a}''$ is found at the point of the intersection of the curves, from the slope of the curves. Since the intersection should have occurred at the stoichiometric point, consider $x = y = 1$ at the point of intersection.

$$\bar{a}'' = \frac{\partial \bar{a}'}{\partial x} = \frac{1}{\theta} \cdot \frac{\partial \Delta \bar{H}}{\partial x} \qquad [4]$$

Since the abscissa represent the mole per cent, $\frac{x}{x+y} \times 100$, of the components weighed out, that is the initial composition of the melt, the slope of the curve at the stoichiometric point is with respect to the mole per cent (or mole fraction) and must be converted to a function of x as follows

$$\frac{\partial \Delta \bar{H}}{\partial x} = \frac{y}{(x+y)^2} \cdot (\text{Slope}) \qquad [5]$$

$$\bar{a}'' = \frac{1}{\theta} \cdot \frac{y}{(x+y)^2} \cdot (\text{Slope})$$

$$= \frac{1}{12{,}600} \cdot \frac{1}{4} (-18{,}500) = -0.367 \qquad [6]$$

if $x = y = 1$

The instability constant is calculated from the following equation [see Eq. 37 and 38 in Ref. (1)]

$$k = \left[\frac{\bar{a}'}{2\bar{a}''y}\right]^2 \cdot \left[\frac{1-\bar{a}'}{\bar{a}'}\right]$$

$$= \left[\frac{0.27}{2(-0.367)}\right]^2 \cdot \frac{(1-0.27)}{0.27} = 0.137 \times 2.7 = 0.37 \qquad [7]$$

This result of 0.37 calculated from the slope of the curves agrees fairly well with value of 0.27 calculated from the ordinate of the curve. The average value of 0.32 will be used in following discussions.

Another possibility for the composition of the complex presents itself for consideration on the basis that the curves cross at 55 mole per cent potassium chloride. This composition represents a compound having the formula $6KCl \cdot 5CdCl_2$ which has a mole percentage of KCl of 6/11 x 100 = 54.5% or a mole ratio of cadmium chloride to potassium chloride of 0.83. This possibility seems to derive support from the differing values of the partial molal heat effects for the addition of $CdCl_2$ to pure KCl ($\Delta \bar{H}$ = 12,600 cal) and KCl to pure $CdCl_2$ ($\Delta \bar{H}$ = 10,300 cal) which give a ratio of 0.82, a result very close to the ratio obtained from the point of intersection of the curves. However, this possibility has been discounted because the calculation of the instability constants from the ordinate, $\bar{a}'$, of the curve [see formula 33 of reference (1)] gives a value of $k = 1.0 \times 10^{-3}$, whereas the calculation from the slope of the curve, via $\bar{a}''$, [see formula 37 of reference (1)] gives the greatly different value of $1.0 \times 10^{+3}$.

Returning now to a consideration of the simple complex, $KCl \cdot CdCl_2$, since it has a relatively large instability constant, this means that the complex is moderately dissociated. At the stoichiometric point the melt contains about 50% of the constituents in the form of complex. (This follows from the relation that the amount of complex formed by adding 1 mole of A and then 1 mole of B to an infinite amount of 1:1 mixture is $(1 \times \bar{a}'_x) + (1 \times \bar{a}'_y) = 0.27 + 0.27 = 0.54$.) It is rather surprising that the complex is dissociated even in the presence of a large excess of either one of its components. This follows from the mass action law which shows that on adding an increment of salt to an infinite amount of the other constituent, the whole increment is not converted into complex, that is to say, the fraction of reaction, $\bar{a}'$, is appreciably less than unity

$$a'_x = \frac{\bar{a}(1+k) - y}{(1+k)(2a - x - y)} \qquad [8]$$

As the content of y in the melt becomes infinite with respect to both the increment x and the complex $\bar{a}$, the value of $\bar{a}'_x$ approaches the limit

$$\bar{a}'_x = \frac{1}{1+k} = \frac{1}{1+0.32} = 0.76$$

On this basis the true heat of reaction of potassium chloride and cadmium chloride to form a mole of complex must be larger than the observed value of 12,600 cal and have the value of 12,600/0.76 = 16,600 cal. With this derived value for the heat of reaction and with the value of k = 0.32 two curves were drawn, 3 and 3′ (see Fig. 7) for comparison with the two experimentally determined curves. The agreement is fair. It will be noted, however, that the derived curves cross at a value of $\Delta \bar{H}$ = 4300 cal instead of the experimentally determined value of 3400 cal, because of the higher value of the heat of reaction used in the computation.

Probably the best fit of derived curves with the experimental data is obtained if the curves are chosen so as to intersect at 3400 cal and to have the value of 12,600 cal at the right and left sides of the graph. Calculation yielded the result that the value of k would be 2.7 and the value of the true heat of reaction would be 46,620 cal. These derived curves are shown in Fig. 7 as dotted lines 2 and 2′. These fit the experimental data better, but it is doubtful that such a large extrapolation is meaningful in view of the probable experimental error of the data, hence, we reject this interpretation. A value of k = 2.7 leads to the result that the reaction mixture contains only about 15% of complex at the stoichiometric point and that only about 27% of an increment is converted into complex when added to the pure salts.

The feature of the experimental data for which we have no explanation at present is the intersection of the curves at a mole fraction of about 55 mole per cent instead of the stoichiometric value of 50%. With a melt of stoichiometric composition, an increment of either salt should yield the same partial molal heat effect. A difference in activity coefficients is not an acceptable explanation, since the same reaction mixture (hence, the same activities) is used for both increments. Perhaps the discrepancy can be explained on the basis of the formation of another complex which is too dissociated to yield a definite inflection in the curves.

The heat of reaction (12,600 cal) resulting from the addition of $CdCl_2$ to KCl is larger than that (10,300 cal) obtained by adding KCl to molten $CdCl_2$, whereas on the basis of simple considerations they are expected to be equal. The difference might be due either to a lower activity of cadmium chloride in the mixture in comparison with potassium chloride, or to the formation of a small amount of a higher complex, for

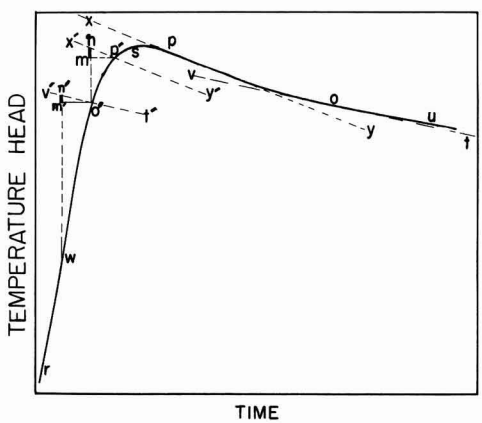

Fig. 9. Method of using the cooling curve, *sou*, for correcting the heat lost during the period of temperature rise, *rws*.

example, $2KCl \cdot CdCl_2$, when $CdCl_2$ is added to molten KCl.

The cadmium chloride-potassium chloride system was also investigated at a temperature of 600°C. At this temperature potassium chloride is solid, and consequently all the experiments with increments of KCl had to be corrected by the heat of fusion of KCl, for which purpose we took the round number of 6500 kcal. The melt becomes solid at about 75 mole % potassium chloride, hence, our data was extended only to a melt of 73 mole % KCl. In Fig. 8 the curves 4 and 4′ for the 600°C determination are compared with the curves 1 and 1′ obtained at 780°C. The data for the 600°C determinations yielded about the same instability constant as the data for 780°C. This follows because the curves 4 and 4′ cross at about the same point as curves 1 and 1′ and the slopes are not very different for these two pairs of curves at the points of intersection.

Discussion of the Literature

There are a number of publications in the literature dealing with the nature of the molten cadmium chloride-potassium chloride system. The constitutional diagram of the system, first investigated by Brandt (3) shows the existence of the congruently melting compound $KCl \cdot CdCl_2$ and the incongruently melting compound, $4KCl \cdot CdCl_2$. However, the existence of a solid compound does not prove its existence in a melt.

Attempts have been made to determine the composition of the complex in the molten system by means of various physical measurements. The rationale behind these studies is that the deviation of a physical property from an additive or ideal value based on the properties of the parent compounds would be greatest at the stoichiometric point. However, since both positive and negative deviations from ideal behavior occur for mixtures of fused salts that are known not to form complexes, these measurements do not generally lead to an unequivocal conclusion.

The physical property of the system that has been investigated most is electrical conductivity. This was first measured by Sandonnini (4) whose data on specific conductivity showed a slight minimum at 40 mole % potassium chloride. Mulcahy and Heymann (5) computed the equivalent conductivities from Sandonnini's data. Finding the greatest departure from additivity at 65 mole % potassium chloride, they suggested the formula, $2KCl \cdot CdCl_2$. Bloom and Heymann (6) found that the equivalent conductivity of the mixture was at a minimum between 55 and 60 mole % potassium chloride (their specific conductivities did not show a definite minimum) and that the temperature coefficient of the conductivity was a minimum at 50 mole %. The electrical conductivity of the system was also investigated by Sakai (7).

Several other physical properties of the system have been investigated. Harrap and Heymann (8) found that the viscosity of the system at 650°C was at a minimum between 50 and 60 mole % potassium chloride. Measurement of the densities and molar volumes of the system by Boardman, Dorman, and Heymann (9) showed that the system had large positive deviations from additivity. The measurement of surface tension by Boardman, Palmer, and Heymann (10) showed a negative deviation from ideal behavior, but no well defined minimum that would unambiguously define a compound. Barton and Bloom (11) measured the vapor pressure of the system and calculated activity coefficients for 900°C. Their discussions of the composition of the complex were speculative. Bloom, Davis, and James (12) investigated the surface tension and surface heat of the system and had this to say: "This method, in common with results of electrical conductivity, viscosity, molar volume, etc., do not lead unequivocally to the stoichiometric composition of such complex ions, although there is general acceptance of their presence in certain systems."

The Raman spectra of the system have also been investigated. Bues (13) favored the $CdCl_3^-$ complex ion on the basis of his measurements, but Bredig and Van Artsdalen (14) claim that Bues' data could better be interpreted to prove the existence of the $CdCl_4^{2-}$ complex. Bredig (15) backed up his assertion in a subsequent publication dealing with Raman spectra and electrical conductivity, and in a paper published the following year (16) claimed that the measurement of activity coefficients that had been published by Russian investigators supported his view.

Bockris and co-workers also entered the discussion. On the basis of the measurement of the self-diffusion of Cd^{++} ion in the molten mixture, Bockris and Angell (17) found the maximum rate to occur at the composition corresponding to $KCl \cdot CdCl_2$. Tanaka, Balasubramanyam, and Bockris (18) also measured the Raman spectra of the system and considered that the data indicated that the complex ion was $CdCl_3^{-1}$ and thus supported Bues instead of Bredig. However, they differed from the former in finding that the complex was pyramidal, whereas Bues had found it to be a planar triangle. The arguments of Tanaka, Balasubramanyam, and Bockris were somewhat tenuous as they were not based entirely on experimental findings, and some of the Raman lines were very weak.

Summary

The foregoing discussion indicates that measurements of the physical properties of the system did not lead to a decisive determination of the composition of the complex ion in the melt and none of the methods led to a value for the instability constant. The method of partial molal heat effect, in contrast, has led to an unambiguous determination of the composition of the complex, as well as to an approximate value of the instability constant. The fundamental reason that the calorimetric method has been more successful is that it involves measurements on the chemical reaction itself, and in this way it is unique. It leads to a determination of the "fraction of reaction." It requires no prior knowledge of the physical constants of the components or of the complex, whereas the other methods depend on deducing the existence or the concentration of a complex by comparing physical properties of static systems.

Acknowledgment

The authors wish to thank the Division of Research, Chemistry Branch, Atomic Energy Commission, for the continuing support of our projects on calorimetry.

Manuscript received June 13, 1966; revised manuscript received Sept. 6, 1966.

Any discussion of this paper will appear in a Discussion Section to be published in the December 1967 JOURNAL.

REFERENCES

1. A. Brenner, *This Journal*, **112**, 611 (1965).
2. Thomas B. Douglas, National Bureau of Standards, Private communication.
3. H. Brand, *Neues Jahrb. Mineral., Geol.*, **32**, (B1), 627 (1911). Data reproduced in "International Critical Tables," Vol. IV, p. 55, McGraw-Hill Publishing Co., New York (1928).
4. C. Sandonnini, *Gazz. chim. ital.*, **50**, 289 (1920).
5. M. F. R. Mulcahy and E. Heymann, *J. Phys. Chem.*, **47**, 485 (1943).
6. H. Bloom and E. Heymann, *Proc. Roy. Soc.*, **A188**, 392 (1947).
7. Kaoru Sakai, *J. Chem. Soc. Japan* (Pure Chem Sect.) **75**, 182 (1954); *Nippon Kagaku Zasshi*, **77**, 1172 (1956); *ibid.*, **78**, 1257 (1957).
8. B. S. Harrap and E. Heymann, *Trans. Faraday Soc.*, **51**, 268 (1955).
9. N. K. Boardman, F. H. Dorman, and E. Heymann, *J. Phys. Chem.*, **53**, 375 (1949).
10. N. K. Boardman, A. R. Palmer, and E. Heymann, *Trans. Faraday Soc.*, **51**, 277 (1955).
11. J. L. Barton and H. Bloom, *ibid.*, **55**, 1792 (1959).
12. H. Bloom, F. G. Davis, and D. W. James, *ibid.*, **56**, 1179 (1960).

13. W. Bues, *Z. anorg. Chem.*, **279**, 104 (1955).
14. M. A. Bredig and E. R. Van Artsdalen, *J. Chem. Phys.*, **24**, 478 (1956).
15. M. A. Bredig, *Electrochim. Acta*, **5**, 299 (1961).
16. M. A. Bredig, *J. Chem. Phys.*, **37**, 451 (1962).
17. J. O'M. Bockris and C. A. Angell, *Electrochim. Acta*, **1**, 308 (1959).
18. M. Tanaka, K. Balasubramanyam, and J. O'M. Bockris, *ibid.*, **8**, 621 (1963).

APPENDIX

Graphical Method of Correcting for Heat Leakage in Calorimetry

In Fig. 9, rws is the temperature-time curve resulting from the reaction and st is the cooling curve.—The graphical correction involves no assumption other than that the rate of heat leakage is a function of temperature head. Thus, for any given temperature head while the temperature of the reaction vessel is rising (point p', for example) the rate of loss of heat is the same as that noted at the same temperature (point p, for example) while the reaction vessel is cooling. Thus p and p' (and O and O') are characterized by the same temperature head and, therefore, by the same rate of heat loss. The heating effect of stirring is neglected.

Divide the curve rs into a number of segments, such as wo' and o'p'. The correction is applied to each segment, then summed. The segments need not be of the same length.

Example of graphical method: Draw tangent xy at p and with triangle and straight edge reproduce same slope x'y' at p'. Draw line nmo'. The length of mn is the correction. Repeat performance for each segment, such as wo'. The correction is the sum of the lines such as mn and m'n'. These can be summed up by marking off the lengths on the edge of a sheet of paper.

The reason that mn is the temperature correction, ΔT, for the segment between o' and p' is that the slope of xy gives the rate of temperature change, dT/dt for that temperature head. mp' represents the time, dt, that the system was at that approximate temperature head during the heating period.

$mn = dT/dt \times dt = \Delta T$.

Phenomena at an Electrode Covered with an Electrolyte Film

F. G. Will

General Electric Research and Development Center, Schenectady, New York

ABSTRACT

The anodic oxidation of hydrogen is studied on a large horizontal electrode covered with an electrolyte film of millimeter thickness. Polarization curves and the potential distribution in the film are obtained for various film thicknesses and electrolyte concentrations. Concentration gradients in the film electrolyte are measured and found to be very small. Convection in the film and water transport above the film are shown to exist. Both phenomena appear to be significant factors in keeping the concentration gradients small. Theoretical considerations suggest that the convection is induced by surface tension gradients. The convection is formally taken into account in an analysis of the rate-controlling transport of the reacting gas through the film. This involves the introduction of a diffusion layer thickness as parameter. Excellent agreement is found between experimental and calculated polarization curves and potential distribution. The phenomena occurring at the model electrode are believed to represent similar phenomena occurring at actual gas diffusion electrodes. Certain ramifications also exist with regard to wet corrosion.

The transport of reacting gases through thin films of electrolyte covering a metal surface plays an important role in many fuel cell and battery electrodes and in metal corrosion. In the case of fuel cell electrodes operating on gases like hydrogen, hydrocarbons, and oxygen, it is very likely (1-9) that the reacting gas passes through a thin electrolyte film covering the pore walls or the catalyst particles prior to reacting at the electrode surface. Likewise, in hermetically sealed batteries, oxygen and hydrogen that are evolved especially during overcharge are expected to diffuse through thin electrolyte films before reacting on one of the battery plates or an auxiliary electrode (10-12). "Wet" metal corrosion often involves the simultaneous anodic dissolution of the metal and cathodic reduction of oxygen from the air. The rate at which oxygen diffuses through the liquid layer covering the metal surface (13) often controls the rate of corrosion.

A previous experimental study (2) of the oxidation of hydrogen on a platinum electrode partially immersed in sulfuric acid had strongly suggested gas transport through a thin electrolyte film as rate-controlling reaction step. This mechanism was further supported by the good agreement between experimental polarization curves and curves resulting from a mathematical analysis (3). The analysis was made under the assumptions of diffusion control without convection in the film and of constant electrolyte concentration throughout the length of the film. Furthermore, the analysis contained the film thickness as an adjustable parameter.

However, we might expect a substantial increase of the electrolyte concentration in the film due to the formation of hydrogen ions and the migration of anions in the film (14, 15). If, on the other hand, concentration gradients exist, we expect convection in the film electrolyte, caused either by evaporation and condensation of water vapor, or by gradients in surface tension (13, 16-19).

It is the aim of this paper to test the assumptions of the previous analysis experimentally and to verify the predicted potential and current distribution in the film. This information cannot be obtained by direct measurements on porous electrodes or partially immersed electrodes, owing to the small thickness of the electrolyte film (20) and the short length of the reaction zone. Hence, measurements were carried out on a scale-up model of an electrode covered with a thin film of electrolyte.

The results obtained on such an experimental model have important ramifications regarding a better understanding of the gas transport phenomena occurring in many porous electrodes and in corrosion. To which extent information obtained on the model can be transferred to actual systems depends on the extent of hydrodynamic similarity (19) between model and system and has to be decided from case to case.

Experimental

The scale-up model used in the following study consists of a horizontal platinum foil, 40 cm long, 2.42 cm wide, and 50μ thick that has been cemented to a plane-

parallel glass bar of equal length and width. Acid-resistant, high-temperature cure epoxy resin was used for cementing. The cemented foil proved to be flat within $\pm 10\mu$. The glass bar with foil is tightly fitted on three sides into the rectangular depression of a Teflon bar. A small rectangular reservoir for the electrolyte borders on the fourth side of the glass bar. The top edges of the Teflon vessel rise 1 mm above the top of the platinum foil. The Teflon vessel with glass bar and foil is contained in a glass cell. A platinum foil counter electrode and a platinum screen reference electrode are introduced into the reservoir through a glass joint. This part also has provisions for introducing gas and electrolyte. The gas leaves the cell through a water trap. Platinum wire probes of 0.5 mm diameter are introduced through glass joints in the top of the glass cell. The probes are located in the center line of the foil and spaced 2 cm apart from each other. Their flat ends are spaced at an accurate height of 0.25 mm above the foil. Counter electrode, reference electrode, and the tips of all probes are platinized. The electrolyte, contained in the reservoir, spreads over the platinum foil, forming a film of uniform thickness. A steady stream of hydrogen was blown over the electrolyte film at a rate of about 10 cm^3/min. To minimize evaporation of the film, the hydrogen, before entering the cell, was blown through two gas wash bottles containing sulfuric acid of the same concentration as used in the experiment. These concentrations were 8*N*, 1*N*, 0.4*N*, 0.1*N*, and 0.02*N*. All experiments were carried out at a controlled room temperature of 25° ± 1°C.

Electrolyte films of thicknesses 2, 1, and 0.5 mm were applied. The film thicknesses were measured mechanically to a precision of $\pm 25\mu$. A platinum tube with a flat end, rigidly mounted on a precision cathetometer, was lowered through a glass joint after removing the respective probe. An ohm-meter was connected between the platinum tube and the platinum foil. The moments that the platinum rod first touched the electrolyte surface and then the platinum foil could be precisely determined by the changes in the deflection on the ohm-meter.[1]

A block diagram of the electrical setup is shown in Fig. 1. The lower part of the diagram contains a schematic of the electrolytic cell with the grounded test electrode (platinum foil) T, counter electrode C, reference electrode R, and probes P1 to P20. Potentials E_a' between 0 and 0.8v are applied between R and T by means of a potentiostat, and the cell current I through C and T is measured as a function of E_a'. In all plots and equations, the corrected applied potential E_a occurs instead of E_a'. E_a is identical to the potential measured between probe 1 and test electrode T and is related to E_a' by

$$E_a = E_a' - E_{1R} \qquad [1]$$

where E_{1R} is the ohmic voltage drop between probe 1 and reference electrode R. The local electrode potentials $E(x)$, *i.e.*, the potential distribution, are measured as the potentials between the various probes P1 to P20 and T. The impedances between the various probes and T were measured at frequencies of 1 and 10 kHz using an impedance bridge. A 1 μF capacitor effectively prevented the bridge circuit from interfering with the d-c measurements. Thus, the impedances could be measured while different d-c potentials E_a' were being applied. At 10 kHz, the ohmic component of the measured impedance is essentially identical to the electrolyte resistance between the particular probe and the test electrode. After calibration with known electrolyte concentrations, the magnitude of this resistance is an accurate measure for the concentration of the electrolyte in the vicinity of that particular probe.

[1] The suggestion of this simple and precise method by J. D. Livingston of our laboratory is gratefully acknowledged.

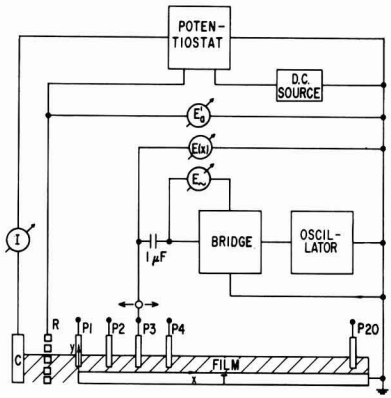

Fig. 1. Block diagram of the electrical setup and electrolytic cell: T, test electrode; C, counter electrode; R, reference electrode; P1 to P20, probes.

Results

Current-potential curves.—Polarization curves for different concentrations of sulfuric acid and different film thicknesses are shown in Fig. 2. The cell current per centimeter width of the electrode, I/W, is plotted against a square root expression containing the applied potential E_a and an exponential of E_a. The reasons for plotting the polarization curves in this particular way will become apparent in the Discussion section.

The following features of the polarization curves are noted: (*i*) The effect of the film thickness on the slope of the polarization curves is relatively small. (*ii*) Decreasing the concentration of the sulfuric acid decreases the slope of the curves drastically, *i.e.*, increases the polarization for fixed current drastically. (*iii*) A limiting current is obtained for 8*N* H_2SO_4. The limiting current is considerably larger for 1 mm than for 2 mm film thickness.

Potential distribution.—Figure 3 shows a linear plot of the local electrode potentials against the distance

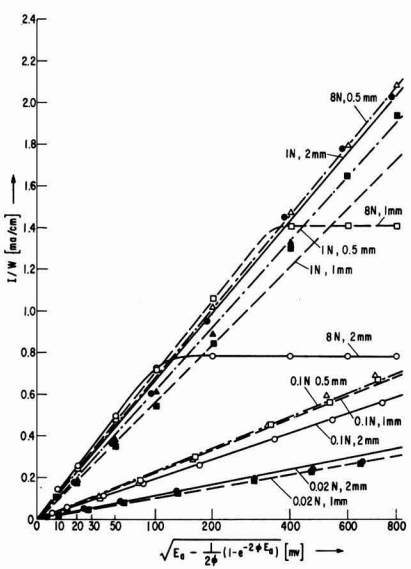

Fig. 2. Polarization curves for various acid concentrations and film thicknesses: I/W, cell current per unit width of electrode; E_a, applied potential; Ψ, F/RT.

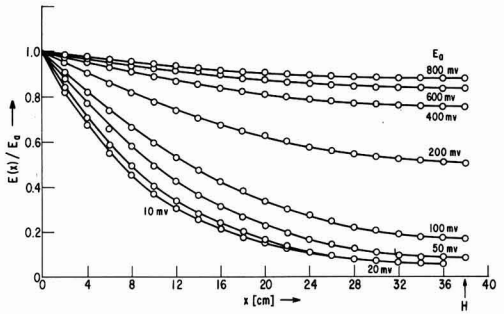

Fig. 3. Potential decay for 8N H_2SO_4 and 2 mm film thickness with applied potential E_a as parameter.

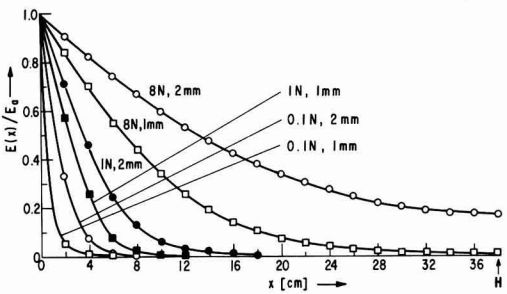

Fig. 4. Potential decay for fixed applied potential $E_a = 100$ mv with the concentration and film thickness as parameters.

x for $8N$ H_2SO_4 and 2 mm film thickness with the applied potential E_a as a parameter. $E(x)$ is plotted in dimensionless units as ratio $E(x)/E_a$. The distance x along the film is counted from the beginning of the film at probe 1. We find that the potential decay is quite small for the larger applied potential and that the rate of decay is substantially increased as the applied potential is decreased. This finding applies to all acid concentrations and film thicknesses.

The effect of the acid concentration and the film thickness on the potential decay for a fixed applied potential of 0.1v is shown in Fig. 4. As expected, the potential decays much more rapidly as the acid concentration or the film thickness are decreased. In $0.02N$ H_2SO_4, and for $\delta = 2$ mm the potential decays to 2% of the applied value between probe 1 and 2 and to less than 1% for $\delta = 1$ mm.

Concentration changes.—The impedances between the various probes and the test electrode were measured in $0.4N$ H_2SO_4 at a film thickness of 1 mm. The flow rate of hydrogen was decreased to about 1 cm^3/min to minimize evaporation of the film. For a fixed applied potential of 100 ± 0.5 mv, the current, the potential distribution, and the impedances were measured as a function of time over a period of 240 hr.

During this period, the film thickness decreased from 1.0 to 0.9 mm and the current from 0.84 to 0.82 ma. Concurrently, the potential decay became slightly larger, as shown in Fig. 5. The maximum change amounted to less than 5%.

The electrolyte resistances at $t = 0$ between the various probes and the test electrode fell in the range 18.7-24.4 ohms. The spread in resistance values is caused by the nonuniformity of the vertical spacing of the probes above the test electrode. After 240 hr, the resistances varied from 18.4 to 25.4 ohms. The changes of the resistances, ΔR, at the various probes, in per cent deviation from their original values, are plotted in Fig. 5. We note that the resistances have become slightly larger near the reservoir, at probe 1 and 2, and near the film end. Between probes 3 and 13, on the other hand, the resistances have become

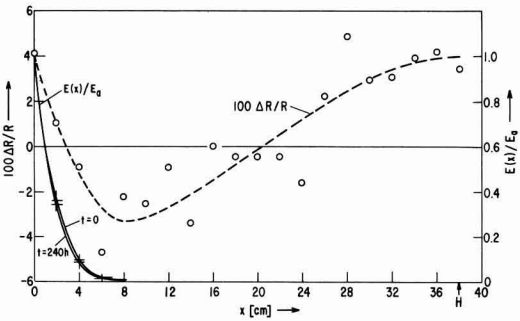

Fig. 5. Resistance changes in per cent deviation from original values after 240-hr polarization at 100 mv in 0.4N H_2SO_4. Also potential distribution at $t = 0$ and $t = 240$ hr.

slightly smaller. This reflects a tendency of the acid concentration to become slightly smaller in the reservoir and near the film end and slightly larger in the regions of the film where the oxidation of the hydrogen occurs. However, the effect is quite small, the changes of the acid concentration amounting to less than ±5% along the whole length of the film.

Water vapor transport.—Water vapor may be transported above the film from areas of the film with low electrolyte concentration to those with higher concentration. The rate of vapor transport would then be expected to have an effect on the magnitude of the concentration changes and, hence, the electrolyte resistance.

The possible effect of vapor transport was studied by decreasing the rate of vapor transport perpendicular to the film relative to the rate of hydrogen transport. This was effectively done by floating a Teflon membrane of 3μ thickness on the 1 mm thick film of $0.4N$ H_2SO_4. Hydrogen permeates through Teflon membranes roughly 30 times faster than water vapor.[2] The probes were inserted through small holes in the Teflon membrane. The current for $E_a = 100$ mv was 15% smaller (0.71 ma) than without the Teflon membrane (0.84 ma) due to the limited rate of permeation of hydrogen through the membrane. The electrolyte resistances between $x = 0$ and 20 cm changed in a manner similar to that shown in Fig. 5 which applies to the case without membrane. However, the relative changes were approximately double as large as without the membrane. Hence, the concentration gradients between $x = 2$ and 20 cm were about double as large as without membrane. For $x > 20$ cm, the concentration changes amounted to less than 1%.

Convection of film electrolyte.—Possible convection of the film electrolyte was tested for by adding a small amount of red pigment to the electrolyte. The electrode was covered with a 1 mm film of $1N$ H_2SO_4. A potential of 800 mv was applied. The current of 4.6 ma did not change on addition of the pigment through the glass joints in the top of the cell. The pigment quickly conglomerated to form particles of a few tenths of a millimeter diameter which floated in the film electrolyte. Within a few minutes, these particles moved from near the center of the film to the vicinity of the film edges. This motion proved to be independent of any applied potential. The cell was then left standing for 12 hr without a potential applied. The particles remained essentially motionless during this time. A potential of 800 mv was now applied and the motion of several particles monitored with markers. The particles in the film between probe No. 1 ($x = 0$) and probe No. 6 ($x = 10$ cm) showed a distinct motion in the direction of the reservoir while the particles closer to the film end ($x > 20$ cm)

[2] Private communication by W. L. Robb of the General Electric Research and Development Center.

remained essentially motionless. As soon as the applied potential was turned off ($E_a = 0$), the particles stopped moving. With a potential applied again, the particles started moving again. The velocity of the particles near probe No. 4 ($x = 6$ cm) was determined in repeated runs as $1.3 \cdot 10^{-3}$ cm/sec $\mp$ 10%.

Discussion

Concentration changes and convection.—If there were no convection in the film electrolyte, we would expect an exponential increase of the electrolyte concentration in the film over that in the reservoir (14, 15). In this case, the steady-state current would be due to migration and diffusion of hydrogen ions.

The finding that the electrolyte concentration changes very little indicates the presence of convection in the film electrolyte. Indeed, convection was proved to exist by observing the motion of particles added to the film electrolyte.

We suggest two effects that are likely to cause the observed convection: (*i*) motion induced by gradients of the surface tension in the electrolyte and (*ii*) motion induced by water vapor transport above the electrolyte.

Motion induced by surface tension.—The formation of hydrogen ions at the electrode surface is expected to give rise to concentration gradients in the film parallel to the surface and also perpendicular to the surface. The concentration gradients, in turn, cause gradients of the surface tension in the electrolyte which are known to set the liquid in motion if certain instability criteria are fulfilled.

A number of papers have dealt with convection cells or Bénard cells (21) driven by surface tension gradients (18) and established the criteria for convective instability in liquid films (22-26). Pearson (22) derived a characteristic dimensionless constant B, whose value determines the onset of convective instability. If the driving forces are concentration gradients in the film rather than temperature gradients, one obtains

$$B = (\delta^2/\mu D_+)\ (\partial\sigma/\partial c_+)\ (\partial c_+/\partial y) \qquad [2]$$

δ = film thickness, μ = viscosity, c_+ = concentration, D_+ = diffusivity of electrolyte, σ = surface tension, y = coordinate perpendicular to the film. For the case of constant flux at the bottom of the film ($y = 0$), Pearson calculates a critical value $B_{crit} = 48$. $B > B_{crit}$ characterizes the onset of convective instability. Using Eq. [2] we find that for a 1 mm thick film of 1*N* H_2SO_4 a concentration gradient of only 10^{-3} mole/l/cm is required to cause convective instability.

It is important to note that convective instability caused by density gradients is governed by a dimensionless constant, called Rayleigh number (27), which is proportional to δ^4 and that the critical Rayleigh number is more than an order of magnitude larger than B_{crit}. Thus, in films of 1 mm thickness and thinner, convective instability can confidently be attributed to the surface tension rather than the buoyancy mechanism (22).

In contrast to cellular motion, Levich (19) treated gross motion of the film electrolyte parallel to the surface induced by surface tension gradients which are caused by temperature or concentration gradients in the x-direction. He derived a parabolic velocity distribution

$$v_x = (3/4\delta\mu)\ [(y-\delta/3)^2 - (\delta/3)^2]\ \partial\sigma/\partial x \qquad [3]$$

where v_x = x-component of the velocity of the liquid. Equation [3] predicts a motion of the electrolyte in the direction of the surface tension gradient near the electrode surface (lower 2/3 of film thickness) and in the opposite direction near the film surface (upper 1/3 of film thickness). The surface tension of sulfuric acid increases with increasing concentration in the range of 0-50% by weight (28). The change amounts to about 1 dyn/cm/mole/l. The observed change of the electrolyte resistance in 0.2*M* H_2SO_4 for $0 < x < 8$ cm (see Fig. 5) corresponds to a concentration gradient of $2.5 \cdot 10^{-3}$ mole/l/cm. Using this value, we calculate from Eq. [3] an average velocity in the lower 2/3 of the film of $0.7 \cdot 10^{-3}$ cm/sec. This is about one half the observed velocity of the suspended particles ($1.3 \cdot 10^{-3}$ cm/sec) and suggests that surface tension gradients are likely to be a significant factor in causing convection in the film electrolyte and thereby reducing concentration gradients.

Water vapor transport.—A rough calculation of convective transport of water vapor above the film shows that a flow velocity of only $2 \cdot 10^{-2}$ cm/sec is sufficient to keep the concentration gradient of the electrolyte near the film surface at the low observed value. The fact that the concentration gradient is roughly doubled when a Teflon membrane is used also suggests that water vapor transport is significant in reducing concentration gradients. The evaporation and condensation of water vapor are expected to cause convection in the film electrolyte due to capillary and gravity forces.[3]

Diffusion layer thickness.—Since the film electrolyte is in motion, the reacting gas (hydrogen) is carried to the electrode surface by convective diffusion. The gas flux and, hence, the current density is larger than for pure diffusion through the electrolyte film. Mathematically, the treatment of this problem is very complicated because it involves the introduction of the velocity of the electrolyte as a function of x and y into the convective diffusion equation. A specific case of this general problem was treated by Levich (19), but is not applicable to the present problem. In general, the flux in a convective diffusion regime can be expressed in terms of Fick's law of diffusion by introducing a diffusion layer which is a function of the coordinate x and contains various material constants (19).

Lacking a theory that would allow us to express the diffusion layer thickness in this way, we introduce a diffusion layer thickness δ' formally as an adjustable parameter.

The previous analysis (3) of electrochemical reactions involving the slow diffusion of a reacting gas through the electrolyte film was made under the assumption of no convection and constant concentration in the film electrolyte. The analysis will now be modified in terms of a diffusion layer thickness δ', which, due to convection, is only some fraction of the actual film thickness δ.

Current-potential curves.—For penetrations of the electric field small compared to the length of the film, *i.e.*, if the potential at the film end, E_H, is essentially zero, the expression

$$I/W = 2\sqrt{\delta/\delta'}\ \sqrt{FDc_o\kappa}\ \sqrt{E_a - (1-e^{-2\Phi E_a})/2\Phi} \qquad [4]$$

results for the current-potential curve. W is the width of the electrolyte film, D and c_o the diffusion coefficient and the solubility of hydrogen in sulfuric acid, respectively; κ is the conductivity of the electrolyte, and $\Phi = F/RT$. It is interesting to note that the current in the original expression (3) is independent of δ.

For $E_a >> RT/F$ and penetrations of the electric field large compared to the length of the film, *i.e.*, for $E_H \lessapprox 50$ mv, the concentration of molecular hydrogen at the surface of the test electrode approaches zero along the whole length of the film. Under these conditions, a maximum diffusion current

$$I_m/W = 2\ (\delta/\delta')\ FDc_o/\delta \qquad [5]$$

should be obtained.

The value of the applied potential, E_m, for which the maximum diffusion current at any given value of $(H/\delta)_m$ is obtained, can be calculated from

[3] The possible significance of vapor transport was also suggested by Bennion and Tobias (29).

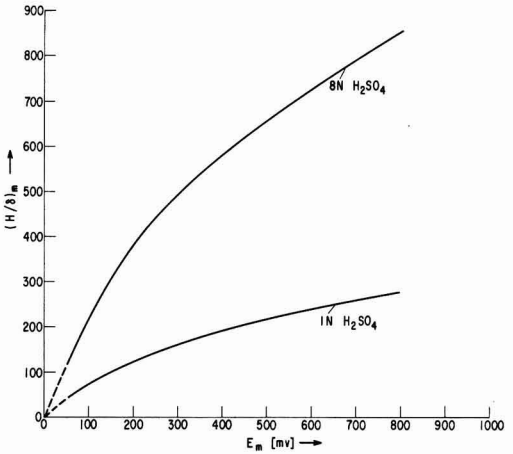

Fig. 6. Values of the ratio film length H to film thickness δ for which the applied potentials E_m produce the maximum diffusion current in 8N and 1N H_2SO_4.

$$E_m - E_H = (FDc_o\,\delta/\delta'\kappa)\ (H/\delta)^2_m \qquad [6]$$

where $E_H = 0.05$v. An increase of H/δ beyond $(H/\delta)_m$ produces essentially no increase of the current. Figure 6 correlates values of $(H/\delta)_m$ and E_m over a wide range of potentials for 8*N* and 1*N* H_2SO_4.

According to Eq. [4], straight lines should result in a plot of I/W against $\sqrt{E_a - [1 - \exp(-2\Phi E_a)]/2\Phi}$. Equation [5] predicts a maximum diffusion current for 8*N* H_2SO_4 whose magnitude is inversely proportional to δ. According to Eq. [6] and Fig. 6, the maximum diffusion current should start at lower potentials for the larger film thicknesses. It is seen from Fig. 2 that the experimental curves follow the predicted behavior. A good quantitative fit between experimental and theoretical curves is obtained for the values of δ/δ' shown in Table I. Also tabulated are the experimental values for the slopes of the curves in Fig. 2, the maximum diffusion currents and the values for E_m. For all acid concentrations, the values of δ/δ' lie between 1.8 and 2.9, *i.e.*, the diffusion layer thickness is only about 1/2 to 1/3 of the film thickness.

Potential distribution.—For small values of the applied potential, *i.e.*, $E_a << RT/F$, the local electrode potential can be written as

$$E(x)/E_a = \exp\left(-2\sqrt{F^2Dc_o/\kappa RT}\sqrt{\delta/\delta'}\,x/\delta\right) \qquad [7]$$

Figure 7 shows a plot of the logarithm of $E(x)/E_a$ against x/δ for $E_a = 10$ mv and different acid concentrations and film thicknesses. As predicted by Eq. [7], the experimental points lie on straight lines. Their slopes can be matched with the theoretical slopes

$$2\sqrt{F^2Dc_o/\kappa RT}\sqrt{\delta/\delta'}$$

for the values of δ/δ' given in Table II. While two of these values (2.30 and 1.90) agree well with the values given in Table I, the other three values are by some 25 to 35% smaller than those in Table I.

Table II. Values of δ/δ'

	8*N*		1*N*		0.1*N*
	2 mm	1 mm	2 mm	1 mm	2 mm
δ/δ'	2.30	1.50	2.20	1.40	1.90

For large values of the applied potential, *i.e.*, $E_a >> RT/F$, and large penetrations of the electric field, *i.e.*, $E_H \gtrapprox 50$ mv, one obtains

$$\psi(x) = E_a - E(x) = (FDc_o\,\delta/\delta'\kappa)\ \{(H/\delta)^2 - [(H-x)/\delta]^2\} \qquad [8]$$

The potential decays less rapidly than the exponential decay given by Eq. [7]. We expect straight lines in a plot of the ohmic potential drop $\psi(x)$ in the electrolyte film against $(H/\delta)^2 - [(H-x)/\delta]^2$. Their slopes are given by $FDc_o\,\delta/\delta'\kappa$ and should depend on the film thickness δ only insofar as δ enters through the correction factor δ/δ' with values between 2 and 3. Figure 8 shows that these predictions are fulfilled very well for 8*N* H_2SO_4 and $\delta = 2$ and 1 mm. The four top curves, shown in Fig. 3 for $E_a = 200$, 400, 600, and 800 mv, all fall on one straight line when plotted as in Fig. 8. The same is true for all potentials between $E_a = 400$ and 800 mv in the case of $\delta = 1$ mm. For the other concentrations and film thicknesses, the condition $E_H \gtrapprox 50$ mv is not fulfilled. Hence, Eq. [8] cannot be applied. A quantitative fit between the

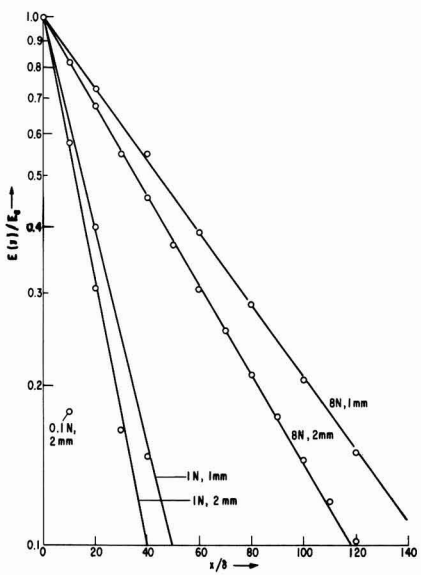

Fig. 7. Semi-logarithmic plot of the potential decay for E_a = 10 mv at various normalities, and δ = 1 and 2 mm.

Table I. Values of δ/δ'

	8*N*			1*N*			0.1*N*			0.02*N*	
	2 mm	1 mm	0.5 mm	2 mm	1 mm	0.5 mm	2 mm	1 mm	0.5 mm	2 mm	1 mm
S_{exp}, ma/cm $\sqrt{V}$	2.56	2.44	2.36	2.30	1.96	2.14	0.67	0.77	0.79	0.39	0.34
S_{th}, ma/cm $\sqrt{V}$	1.71	1.71	1.71	1.34	1.34	1.34	0.50	0.50	0.50	0.25	0.25
$\delta/\delta' = (S_{exp}/S_{th})^2$	2.24	2.04	1.91	2.94	2.14	2.55	1.80	2.37	2.50	2.50	1.92
$I_{m\ exp}/W$, ma/cm	0.79	1.41									
$I_{m\ th}/W$, ma/cm	0.35	0.69									
δ/δ'	2.26	2.04									
$E_{m\ exp}$, mv	130	350									
$E_{m\ th}$, mv	85	200									
δ/δ'	2.28	2.00									

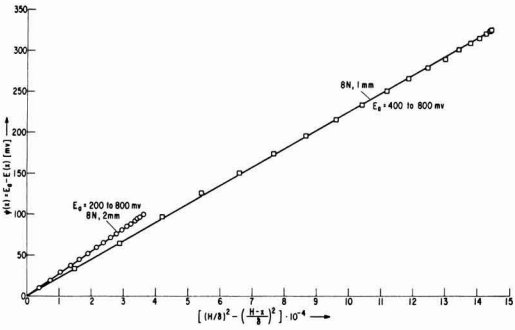

Fig. 8. Ohmic potential drop in the electrolyte as a function of the distance in a square plot for large E_a in 8N H_2SO_4 for $\delta = 1$ and 2 mm.

slopes of the straight lines in Fig. 8 and the slopes calculated from Eq. [8] is obtained with $\delta/\delta' = 2.63$ for $\delta = 2$ mm and $\delta/\delta' = 2.18$ for $\delta = 1$ mm. These values agree moderately well with those given in Table I.

Hydrodynamic similarity between model and gas electrodes.—The degree of hydrodynamic similarity between the model electrode and actual gas electrodes can strictly be obtained only by a rigorous analysis with dimensionless quantities. Such an analysis leads to a system of second order partial differential equations. These can be solved only in special cases and with approximations which are often so stringent that the case treated no longer represents the original problem. Levich (19) treated a special case of convective diffusion of a gas through a liquid film with surface tension-induced motion. However, he did not concern himself with concentration gradients in the liquid and ionic motion due to migration, diffusion and convection. He derived a Reynolds number for the film which is

$$Re = (\delta^2\rho/4\mu^2)\ (\partial\sigma/\partial c_+)\ (\partial c_+/\partial x) \qquad [9]$$

when written in terms of a concentration gradient as driving force. The dependence of Re on δ^2 and on the concentration gradient is the same as that of Pearson's dimensionless constant B in Eq. [2]. Own unpublished calculations show that $\partial c_+/\partial x$ is, to a first approximation, inversely proportional to δ^2. This means that the film Reynolds number and Pearson's constant B are independent of the film thickness and would indicate hydrodynamic similarity between model and actual gas electrode. We stress that this conclusion is based on an approximate solution of the problem and not the result of a rigorous analysis.

Before we can establish similar arguments with regard to the significance of water vapor transport in gas electrodes we have to obtain knowledge about the thickness of films as a function of the pore radius. A rough calculation shows, however, that vapor transport in pores of 4μ diameter with 0.1μ thick films is a feasible mechanism.

Experimental results show that good hydrodynamic similarity must exist between the millimeter thick films on the model electrode and the micron thick films (2, 3, 20) on partially immersed electrodes under diffusion control. The current-potential curves in both cases are essentially identical and follow the behavior predicted for electrodes under diffusion control in the absence of concentration gradients in the film electrolyte. For the case of the large concentration gradients expected (14, 15) in the absence of convection and vapor transport, the predicted current-potential curves are quite different (30) from the experimental curves.

Several experimental facts also suggest that fair hydrodynamic similarity exists between the model electrode and actual gas electrodes under diffusion control. Polarization curves obtained on actual hydrogen (4) and oxygen diffusion electrodes (4, 5), the latter at higher current densities, show the same typical behavior as those obtained on the model electrode and as predicted by Eq. [4].

Conclusions

Polarization curves obtained on the model electrode, which is completely covered with an electrolyte film of precisely known thickness, display a dependence of the current on the square root of the potential and an exponential of the potential. This dependence is predicted by an analysis of rate-controlling diffusion of the reacting gas through the film under the assumption of constant concentration of the film electrolyte. Experimental evidence for convection in the film and transport of water vapor above the film is presented, and both phenomena are made responsible for the observed lack of substantial concentration gradients in the film electrolyte. Theoretical considerations suggest that the motion of the film electrolyte is induced by surface tension gradients. A diffusion layer thickness δ' is formally introduced in the analysis which, due to the convection, is only a fraction of the film thickness δ. For values of δ'/δ between 1/3 and 1/2 a quantitative fit between observed and calculated polarization curves is obtained. The measured potential distribution also follows closely the predicted behavior, namely, the potential decays exponentially for small polarizations and less steeply, as the square of the distance x, for large polarizations.

Polarization curves obtained on partially immersed electrodes and on actual gas electrodes often display the same typical behavior as the curves obtained on the model electrode. We conclude from this fact that a good degree of hydrodynamic similarity exists between these different systems. This conclusion is also borne out by theoretical considerations. Hence, we expect the phenomena observed on the model electrode to be fairly representative for similar phenomena occurring on actual gas electrodes.

Acknowledgments

The author gratefully acknowledges the active help of Mr. F. R. Landsberger in the experimental part and valuable discussions with Dr. D. J. BenDaniel.

Manuscript received Dec. 20, 1965; revised manuscript received Sept. 23, 1966. This paper was presented at the Buffalo Meeting, Oct. 10-14, 1965.

Any discussion of this paper will appear in a Discussion Section to be published in the December 1967 JOURNAL.

REFERENCES

1. H. C. Weber, H. P. Meissner, and D. A. Sama, *This Journal*, **109**, 884 (1962).
2. F. G. Will, *ibid.*, **110**, 145 (1963).
3. F. G. Will, *ibid.*, **110**, 152 (1963).
4. F. G. Will, Paper presented at the Pittsburgh Meeting of the Society, April 1963, Abstract No. 181.
5. P. Ruetschi and J. B. Ockerman, Private communication.
6. R. P. Iczkowski, *This Journal*, **111**, 605, 1079 (1964).
7. Yu. V. Alekseev and Yu. A. Popov, *Soviet Electrochem.*, **1**, 363 (1965).
8. A. G. Pshenichnikov, G. I. Shnaider, and R. Kh. Burshtein, *ibid.*, **1**, 367 (1965).
9. T. Katan and S. Szpak, *This Journal*, **112**, 1166 (1965).
10. A. Dassler, U. S. Pat. No. 2104973, Jan. 1938; A. E. Lange, E. Langguth, E. Breuning, and A. Dassler, U.S. Pat. No. 2131592, September 1938.
11. G. Neumann and U. Gottesmann, U. S. Pat. No. 2571927, Oct. 1951.
12. K. Dehmelt and H. von Dohren, *Proc. 13th Ann. Power Sources Conf.*, **13**, 85 (1959).
13. I. L. Rosenfeld and K. A. Zhigalova, *Dokl. Akad. Nauk SSSR*, **104**, 876 (1955).
14. K. J. Vetter, "Elektrochem. Kinetik," p. 151, Springer, Berlin (1961).

15. J. A. Rockett and R. Brown, *This Journal*, **113**, 207 (1966).
16. J. Thomson, *Phil. Mag.*, Ser. 4, **10**, 330 (1855).
17. A. V. Hershey, *Phys. Rev.*, **56**, 204 (1939).
18. M. J. Block, *Nature*, **178**, 650 (1956).
19. V. G. Levich, "Physicochemical Hydrodynamics," (translated from Russian), p. 384, Prentice Hall, Englewood Cliffs (1962).
20. R. H. Muller, Paper presented at the Washington Meeting of the Society, Oct. 1964, Abstract No. 4.
21. H. Bénard, *Am. Chim. Phys.*, **23**, 62 (1901).
22. J. R. A. Pearson, *J. Fluid Mech.*, **4**, 489 (1958).
23. E. Palm, *ibid.*, **8**, 183 (1960).
24. L. E. Scriven and C. V. Sternling, *ibid.*, **19**, 321 (1964).
25. J. C. Berg and A. Acrivos, *Chem. Eng. Sci.*, **20**, 737 (1965).
26. L. E. Scriven and C. V. Sternling, *Nature*, **187**, 186 (1960).
27. Lord Rayleigh, *Phil. Mag.*, **32**, 529 (1916).
28. Gmelins Handbuch der anorganischen Chemie, "Schwefel," p. 661, 8. edition B2, Verlag Chemie, Weinheim (1960).
29. D. N. Bennion and C. W. Tobias, Paper presented at the Washington Meeting of the Society, October 1964, Abstract No. 5.
30. F. G. Will, Unpublished calculations.

Technical Notes

Fuel Cell Performance as a Function of Catalyst Surface Area

Harold I. Zeliger[1]

Union College, Schenectady, New York

In order to study the relationship between specific platinum surface area and fuel cell performance, it is necessary to have electrodes which are prepared similarly and which contain catalysts that are similar but with varying platinum content and specific platinum surface area. In the work described below the dependence of fuel cell performance on the surface area of the catalyst was demonstrated.

Platinized asbestos samples with varying platinum content were prepared by repeated (6 cycle) platinization (1) of a single starting batch of asbestos as follows.

Asbestos (5g) was impregnated with a 3% solution of chloroplatinic acid and the excess solution was filtered off. The moist impregnated asbestos was dried and reduction was carried out with hydrogen at 100°C. The platinization was repeated 5 more times, with samples taken at the end of each cycle. Platinized asbestos samples with 1, 2, 3, 4, 5, and 6% platinum were prepared in this manner from a single starting batch of asbestos. A 3% solution was used because it was found empirically that this added 1% of platinum per cycle.

The electrodes used in this study were modified Neidrach-Alford (2) electrodes. They consisted of a mixture of catalyst, Teflon binder, and conducting graphite diluent (which was required in these electrodes because of the small quantities of platinum present) pressed into a supporting platinum screen which also served as a current collector. A porous Teflon film on the gas side of the electrode provided for proper electrode wetting so that both the electrolyte and reacting gas had satisfactory access to the catalyst incorporated into the structure. This electrode structure provided for high electronic conductivity and rapid input and removal of reactants and products.

All the electrodes prepared were evaluated as oxygen cathodes in standard test fuel cells. The test cells contained the test electrode, a Teflon-bonded (2) hydrogen counter electrode with 34 mg platinum per cm^2, and 5*N* sulfuric acid electrolyte.

Fuel cell performance data were obtained under the condition of steady d-c drain. The cells tested were discharged through a resistive load. IR free potentials were obtained by interrupting the flow of current (sweep speeds of 100 μsec/division were adequate) and monitoring the voltage change on an oscilloscope.

Specific platinum surface areas were determined by measuring the dissociative chemisorption of hydrogen on platinum (3), using the apparatus of McKee (4).

Platinum contents and specific platinum surface areas of the six samples of platinized asbestos prepared are given in Table I.

Table I. Properties of catalysts prepared through stepwise platinization

Catalyst	% Pt	Specific Pt surface area in m^2/g
A	1.0	46
B	2.0	42
C	3.0	37
D	4.0	32
E	5.0	28
F	6.0	23

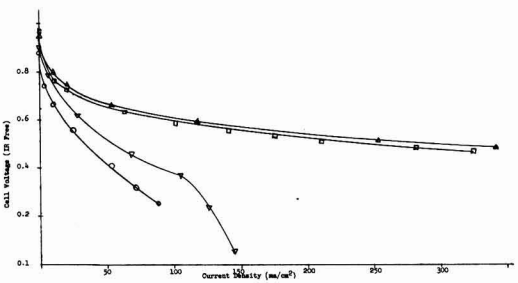

Fig. 1. IR free performance curves for electrodes 1, 2, 3, and 4 on oxygen at ambient temperature, obtained via direct d-c discharge method. Anodes, standard electrodes with 34 mg Pt/cm^2; cathodes, test electrodes with varying Pt content; electrolyte, —5N H_2SO_4, ⅜ in. electrolyte gap. ○, Electrode 1 (0.17 mg Pt/cm^2); ▽, electrode 2 (0.33 mg Pt/cm^2); □, electrode 3 (0.66 mg Pt/cm^2); △, electrode 4 (1.0 mg Pt/cm^2).

[1] Present address: Avco Space Systems Division, Lowell, Massachusetts.

Table II. Data for comparison of current density obtained per unit area of platinum

Electrode No. and catalyst	Mg Pt per electrode	Specific Pt surface area in m^2 per g	Total Pt area in m^2	Current density at 0.7v IR free in ma/cm^2	Current density per unit area at 0.7v IR free, in $ma/cm^2/m^2$
1-A	3.0	46	0.139	7.9	57.0
2-B	6.0	42	0.252	14.9	59.0
3-D	12.0	32	0.392	22.8	58.0
4-F	18.0	23	0.414	25.0	61.0

Electrodes 1, 2, 3, and 4 were prepared incorporating catalysts A, B, D, and F, respectively, and containing 0.17, 0.33, 0.66, and 1.0 mg Pt/cm^2. The electrodes were evaluated as cathodes in fuel cells. Oxygen rather than hydrogen was used for the evaluation, because hydrogen is such a good fuel that it gives excellent performance with very small amounts of platinum catalyst. IR-free polarization curves for the four electrodes are given in Fig. 1.

Comparison of fuel cell performance with specific platinum surface area was made by measuring the current density produced per unit area of platinum at a 0.7v potential for each of the test electrodes. Table II summarizes the data. As can be seen from the data in Table II, there is an excellent correlation between surface area and performance. All four electrodes, each with a different platinum content, gave between 0.057 and 0.061 $ma/cm^2/m^2$ of platinum area at 0.7v.

It is believed that the interior of a metal catalyst does not contribute to the catalytic process. The above described work supports the conclusion that this is indeed the case for the electrocatalytic reduction of oxygen in fuel cells.

Acknowledgments

The author is indebted to Professor K. V. Nahabedian of Union College and L. W. Niedrach of the General Electric Research and Development Center for their guidance and assistance in this work. The author also wishes to gratefully acknowledge the assistance of D. W. McKee of the G. E. R&D Center for his assistance in determining surface areas. H. A. Liebhafsky, Manager Electrochemistry Branch of General Electric R&D Center, is sincerely thanked for making available the facilities with which the experimental work was carried out.

Manuscript received Sept. 1, 1966; revised manuscript received Oct. 12, 1966. The information reported in this paper is part of an M.S. thesis submitted to Union College.

Any discussion of this paper will appear in a Discussion Section to be published in the December 1967 JOURNAL.

REFERENCES

1. D. A. Richards, *Phil. Mag.*, **16**, 778 (1933).
2. L. W. Niedrach and H. R. Alford, *This Journal*, **112**, 117 (1965).
3. G. C. Bond, "Catalysis by Metals," Chap. 8, Academic Press, London and New York (1962).
4. D. W. McKee, Unpublished results.

The Anodic Oxidation of Alloys

G. C. Wood, C. Pearson, A. J. Brock, and S. W. Khoo

Corrosion Science Division, Department of Chemical Engineering,

The University of Manchester Institute of Science and Technology, Manchester, England

Surprisingly little previous work on anodic film growth on alloys, either of a fundamental or practical nature, has appeared in the open literature. This is true even for dilute alloys but is particularly so for compositions far removed from those of the pure "valve" metals. Investigations are in progress to elaborate the theory of film growth on binary alloys between valve metals, and between valve metals and metals which do not themselves form this type of film, and to pursue possible applications of such films in the fields of corrosion-resistant materials, capacitors, and catalysts. The present communication presents results and theories principally for niobium-base alloys, but certain concepts introduced are considered of much more general significance.

Experimental

Specimens cut from sheet or spark-machined as slices from rod were prepared from zone-refined niobium, electron-beam-melted niobium, and from binary alloys of niobium containing, respectively, nominally 5, 20 and 50 a/o (atomic per cent) zirconium, titanium, tungsten, vanadium, or molybdenum. Additional experiments were conducted on Nb-V, Ti-V, Nb-Mo, and Ti-Mo alloys containing 70, 85, or 95 a/o of vanadium or molybdenum. The alloys were generally made from electron-beam-melted or comparable purity metals. After chemical polishing, followed by a 10-sec etch in 40% HF, the samples containing up to 50 a/o alloying element were anodized at 10 ma/cm^2 or at 100 $\mu a/cm^2$ to an appropriate cell voltage, followed by current decay, in 3% W/V ammonium tartrate solution (*p*H adjusted to 7) at 25°C. The alloys richer in vanadium or molybdenum were prepared only at 10 ma/cm^2 with current decay in this electrolyte or alternatively in the nonaqueous electrolyte of 20% W/V ammonium pentaborate in ethylene glycol.

After visual examination for adhesion, compactness, and color, the frequency dispersions of balancing series capacitance and dissipation factor of films were measured in 1M sodium chromate solution (*p*H adjusted to 7.2) at 25°C using a General Radio capacitance measuring assembly type 1610-B with a 50-mv p-p signal. These data also permitted the calculation of average a-c resistivities, on the assumption of the validity of a simple electrical analogue for the film of a resistor in parallel with a capacitor at any one frequency. It was also assumed that the A/V ratio of 23 and dielectric constant of 41.4, which refer to Nb_2O_5 films on pure niobium, held. Although this is not strictly true, any errors involved in the assumption do not greatly affect the subsequent argument. It should be noted that resistivities measured in chromate solution cannot be compared directly with those measured for films on pure metals in tartrate solution (1). This is because of the influence of the double layer impedance on the measured film impedance, for reasons (2) that will be explained elsewhere.

Results

Thick, relatively good quality films were readily produced on niobium and the alloys containing up to 50 a/o additions, with approximate current efficiencies of 100% at 10 ma/cm^2 and 64-72% at 100 $\mu a/cm^2$. Current decay performed at the end of the main anodizing run had little effect on the film properties, but enabled reproducible film thicknesses to be obtained. These were 230, 1150, and 2300A, respectively, for pure niobium, but films on the alloys were ap-

parently a little thicker except for tungsten alloys where they were a little thinner. Deviations from the above thicknesses for 50 a/o alloys were never greater than 20-30% from capacitance measurements and were generally less than this when compared with an optical step gauge constructed with Nb_2O_5 films on niobium, and from considerations of the charge required to form films to a given cell voltage. Thus, although there was undoubtedly some error in defining the film thicknesses and consequently in calculating resistivities, this was not sufficient to invalidate the comparisons of alloy behavior seriously. It is very important to note that all these films appeared of comparable quality, although it is likely that there were minor differences in compactness, solubility, etc. This contrasts strongly with experiments on pure metals in tartrate electrolyte where it was found (1, 2) that only niobium and zirconium gave good films. Film formation on titanium was limited by extensive oxygen evolution and on tungsten by film solubility, and it was impossible to anodize vanadium or molybdenum. It is the authors' experience that even films formed on vanadium or molybdenum in nonaqueous electrolytes are nonadherent and of poor quality. All the present films were insoluble in tartrate or chromate solutions, even after several days. Clearly their solubilities in more severe electrolytes will vary and further work is progressing to pursue this aspect.

Figures 1a and 1b, giving the frequency dispersions of dissipation factor for films formed to 10 and 100v, respectively, on niobium and its alloys, show that in general alloying increased the dielectric loss of the films. Additionally, it tended to increase the slopes of plots of series capacitance against frequency (which have been omitted in the interests of brevity).

Figures 2a and 2b illustrate the frequency dispersions of average a-c resistivity for films approximately 230 and 2300Å thick on niobium and the 50 a/o alloys, derived from Fig. 1a and 1b as mentioned earlier. The values were largely independent of whether the initial current density of formation was 10 ma/cm² or 100 μa/cm². The results were identical, within experimental error, for films on the two purities of niobium. The average resistivities and frequency dispersions of resistivity were greater for the oxide on niobium than on any of the alloys. The various curves

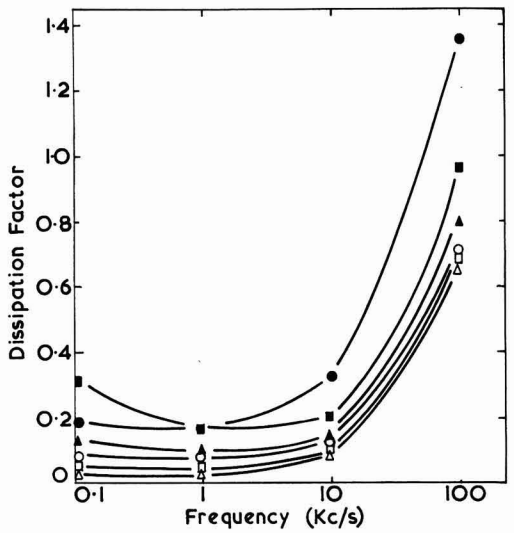

Fig. 1a. Cell voltage of 10v. Dissipation factor vs. frequency (kc/s) for films formed on niobium and Nb-50 a/o alloys. △, Niobium; □, Nb-Zr; ○, Nb-Ti; ▲, Nb-Mo; ■, Nb-V; ●, Nb-W. The symbols are the same for Fig. 1 and 2.

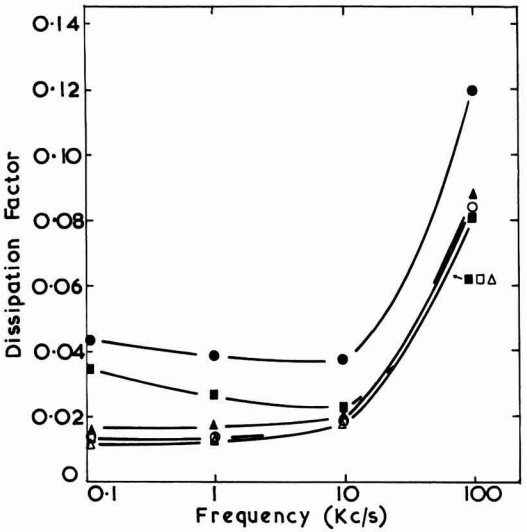

Fig. 1b. Cell voltage of 100v.

almost converge at 100 kc/s with the exception of those for Nb-50 a/o W, probably because the latter were somewhat thinner. At lower frequencies the resistivity was always lower with alloy addition, the effect generally increasing in the order zirconium, titanium, molybdenum, vanadium, and tungsten. This

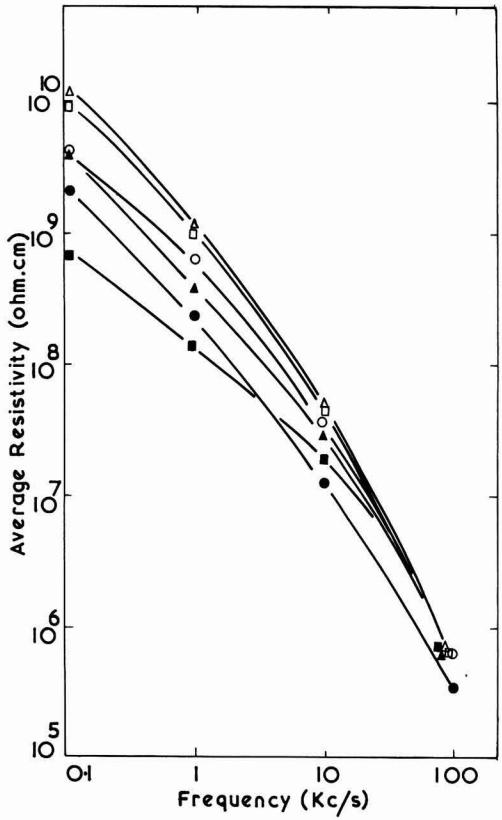

Fig. 2a. Approximately 230Å films; average resistivity (ohm cm) vs. frequency (kc/s) for films on niobium and Nb-50 a/o alloys.

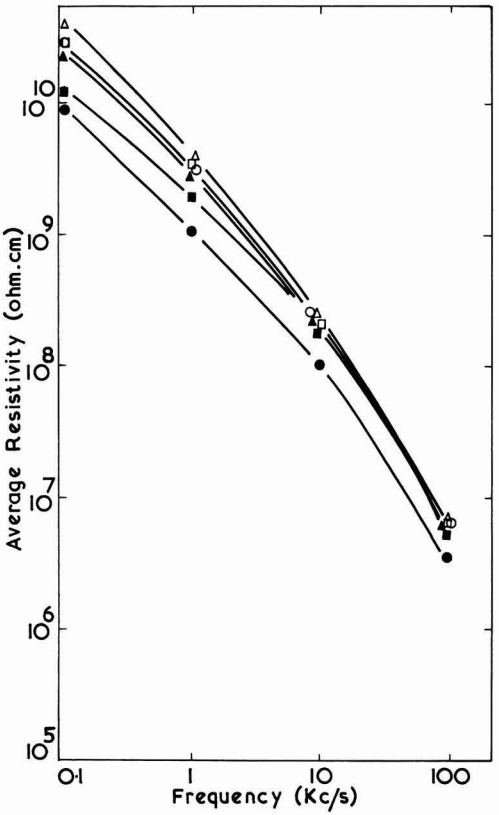

Fig. 2b. Approximately 2300Å films

result appears to be a general one with all the alloy systems that the authors have studied. Curves for films on the more dilute alloys lay in the anticipated order between those for the pure metal and the 50 a/o alloys.

Thus, with the apparent exception of tungsten, the addition of a valve metal to niobium led to higher resistance films than did the addition of vanadium or molybdenum, which do not themselves normally develop typical thick anodic films. An important observation was that the effect of the alloying additions studied in reducing the resistivity of films on niobium was most pronounced for the thinner films. The film capacitances were also relatively larger and showed a greater frequency dispersion. Particularly with Nb-50 a/o V and Nb-50 a/o Mo the thicker films appeared of much better quality; indeed for 2300Å films it is remarkable to observe that the curve for the film on Nb-50 a/o Mo alloy is little lower than that for the film on pure niobium. The reason for this consistent result will be evident later. By analogy with previous results for films on the niobium and zirconium (1), it might have been expected that the curve for Nb-50 a/o Zr would lie above that for pure niobium. Presumably this is not so because the alloy is two-phase and oxide above the niobium-rich regions, which predominates, will produce the dominant dielectric loss. It should also be noted that for all alloys the trend of the thicker the film the higher its average resistivity held at all frequencies. The spaces between curves increased as alloying element was added in the order zirconium, titanium, molybdenum, and vanadium because the improvement of film quality with increased thickness increased in this order.

Electron probe microanalysis at low kilovoltages of stripped and attached films examined in plan proved that tungsten and titanium were incorporated into 2300Å films on 50 a/o alloys in their alloy proportions, and the slight apparent enrichment of vanadium and depletion of molybdenum in the appropriate films were probably insignificant. Similar conclusions were recently reached for copper and zinc entry into films on aluminum alloys (3).

With progressive alloying additions greater than 50 a/o vanadium or molybdenum to niobium or titanium there was a gradual transition from films with good properties to insignificant film formation. On Nb-70 a/o V and Nb-70 a/o Mo films were formed, at rather lower current efficiencies than those given earlier, to voltages of 10, 50, or 100v (corresponding to 230, 1150, and 2300Å films, respectively, on pure niobium). They may in fact have been somewhat thicker than these figures indicate, with a porous outer layer and most of the voltage concentrated across an inner barrier layer, but this remains to be determined. The films were of the usual visual appearance, displaying interference colors and were insoluble or dissolved only very slowly in tartrate, chromate, or distilled water. Films of 10v (nominally 230Å) gave very high capacitances, close to values expected for the double layer capacitance, probably indicating a high degree of microporosity. As the film thickness was increased the impedance characteristics progressively improved until at 100v (nominally 2300Å) the capacitances were relatively low and the frequency dispersion of capacitance was only slightly greater than that expected for a top quality anodic film. The resistivities of these films were sufficiently high to suggest that they may be useful practically, but were several times lower than for the 50 a/o alloys or pure niobium. On Nb-85 a/o V and Nb-85 a/o Mo films could also be formed to high voltages at an even lower current efficiency, but viscous dissolution products could be seen streaming away from the anode, reminiscent of electropolishing. These films, especially when only formed at 10 or 50v, continued to dissolve in the forming electrolyte, in chromate solution, or in distilled water. Films formed at 100v tended to persist in an adherent form for long periods, but showed low impedances which fell with time, indicative of continued dissolution. Nb-95 a/o V and Nb-95 a/o Mo could not be anodized in the aqueous tartrate but films could be formed on the former alloy in the almost "nonaqueous" borate electrolyte (as indeed they could on the other alloys). However, these were soluble in water or in aqueous solutions. The same general pattern was true of Ti-V and Ti-Mo alloys except there was a greater tendency to poorer and more soluble films, as would be expected from the poorer film-forming properties of titanium itself.

Discussion

In attempting to explain the above results it is worthwhile initially demonstrating briefly that analogous concepts developed for the thermal oxidation of alloys appear inapplicable.

1. There is little, if any, preferential oxidation effect, as in thermal film growth, during which one alloying constituent is preferentially incorporated into the film. Thus, a mixed oxide must be considered, although it is not yet known how alloying elements are distributed through the film. From the ability to form films on alloys containing only small concentrations of niobium, it might have been postulated that this element would be expected toward the exterior of the film. Work on the analogous case of InSb, using a sensitive chemical analysis method (4) however, indicated that this is perhaps unlikely because the film contained a uniform distribution of both elements through its thickness, except for the outer 100Å where the concentration of the soluble component, antimony, fell almost to zero.

2. Since all the added ions, whether of higher or lower valency than five, reduce the a-c resistivity of the film, it is apparent that Hauffe's valency rules are of little application to anodic films, whether the a-c

conduction process occurring during impedance measurements be related to d-c electronic conductivity, electronic relaxation processes due to anion vacancies and their associated electrons, or to ionic relaxation processes associated with anion vacancies or interstitial cations. It is possible that all additions to the cation lattice make a more disordered structure, promote ionic relaxation effects, and thus reduce the low frequency resistivity.

3. Consideration of the effect of the addition element on the Pilling-Bedworth ratio in altering the degree of compactness of the oxide has proved useful in thermal oxidation, but the criterion does not apply here, if ionic sizes are considered.

The most useful approach is to compare the properties of these mixed anodic alloy oxide films, such as their solubilities, with those of metallic alloys interacting with electrolytes. Thus the "theory of parting limits" indicates that a noble metal will tend to prevent the selective dissolution of a base metal with which it is alloyed, even when present in only relatively low concentrations. The precise parting limit, often in the range 50-70 a/o of the soluble element, may be sharp or diffuse depending on the alloy and the solution. In certain alloys the base metal is leached out leaving a skeleton rich in the more noble metal. This concept is of course much related to electrochemical processes and does not specifically refer to oxides. In the analogous situation with anodic films, ions of the valve metal, such as Nb^{5+}, effectively play the part of the noble metal and tend to suppress the dissolution of V^{5+}, W^{6+}, or Mo^{6+} ions and their associated oxygen ions from the film.

The experiments described earlier suggest that there is a diffuse transition between solubility and insolubility of anodic films. The "useful" parting limit will depend on the alloy, the electrolyte, and the application. Thus, for the V-Nb system it would be in the range 70-80 a/o V for exposure to certain neutral electrolytes, but less vanadium in the alloy would be permissible in certain severe environments and more if forming were conducted in a nonaqueous electrolyte and the film kept dry subsequently. Similar considerations apply to the other alloy systems.

A film model may be envisaged in which there is an outer porous layer and an inner more compact layer. The precise nature of the "pores" cannot yet be stated, although preliminary electron microscopial examination confirms their existence; they will probably be extremely fine for the more dilute alloys and coarser in alloys rich in soluble component. The degree of this porosity will fall progressively from the oxide/electrolyte interface to the alloy/oxide interface. In certain cases, *e.g.*, in the 50 a/o alloy, it appears that it terminates after only a short distance into the film (perhaps about 100Å), when there is no longer a feasible continuous path of soluble material connecting with the electrolyte. This penetration would be approximately constant for all greater film thicknesses. In other alloys, such as the Nb-85 a/o V and Nb-85 a/o Mo alloys it is more extensive, as witnessed by the continuous stream of soluble material leaving the anode. Such a model is in agreement with the observation that thicker films have generally better properties and superior impedance characteristics. This would be expected because the thicker films would possess much thicker compact regions adjacent to the alloy protected from dissolution.

In view of the above considerations, it is tempting to suggest that the dielectric properties, particularly at low frequencies, of even good quality films on certain valve metals may be modified by hydrated or electrolyte anion-rich regions between the film crystallites. There are instances where impedances of films, *e.g.*, on aluminum, are modified by the anion type and *p*H of the electrolyte, and the authors will return to these matters elsewhere.

The general conclusion is therefore that metals such as molybdenum and vanadium, which cannot themselves normally be anodized, can be made to produce films by alloying with relatively low proportions of valve metals such as niobium and titanium. Zirconium, aluminum, and possibly tungsten would probably afford similar protection. Also the properties of films on metals such as titanium and tungsten, which are relatively poor, can be improved by alloying with metals giving superior films.

Acknowledgments

The authors thank Professor T. K. Ross for providing facilities and for his interest and the Science Research Council and the Commonwealth Scholarship Fund to two of the authors (C. P. and S. W. K. respectively). They are indebted to Dr. A. G. Knapton and Dr. T. Raine of Associated Electrical Industries Ltd., Power Division, for making the alloys.

Manuscript received Aug. 22, 1966; revised manuscript received Oct. 21, 1966.

Any discussion of this paper will appear in a Discussion Section to be published in the December 1967 JOURNAL.

REFERENCES

1. G. C. Wood and C. Pearson, *Nature*, **208**, 547 (1965).
2. C. Pearson, Ph.D. Thesis, Univeristy of Manchester, 1966.
3. G. C. Wood and A. J. Brock, *Nature*, **209**, 773 (1966).
4. J. F. Dewald, *This Journal*, **104**, 244 (1957).

SOLID STATE SCIENCE

Analysis of N-Type GaAs with Electron-Beam-Excited Radiative Recombination

H. C. Casey, Jr., and R. H. Kaiser

Bell Telephone Laboratories, Incorporated, Murray Hill, New Jersey

ABSTRACT

The study of spontaneous emission for n-type GaAs has shown that the spectral shape and peak position may be utilized to determine the free electron concentration within ±15% near concentrations of 5 x 10^{17} cm^{-3} and ±7% at 5 x 10^{18} cm^{-3}. Excitation of the sample with a 1μ diameter electron beam gives such sensitivity with a 3-6μ spatial resolution. This sensitivity and spatial resolution are sufficient for investigating sample inhomogeneities that are related to the spatial variations in the quantum efficiency.

Several investigations (1, 2) of radiative recombination in heavily doped GaAs have shown that the photoluminescent peak shifts to higher energy as the donor concentration is increased above 5 x 10^{17} cm^{-3}. Cusano (3) has reported data demonstrating the dependence of the cathodoluminescent (electron-beam excitation) peak energy and the spectral half-width on the donor concentration. For n-type GaAs, the average distance between impurity atoms is close to the diameter of the Bohr orbit of a donor electron in the crystal for concentrations in excess of 5 x 10^{17} cm^{-3}, and the density of states becomes a function of the substitutional impurity concentration (4). Since the spontaneous emission is given by an integral containing the conduction and valence band density of states and their corresponding occupation probabilities (5), the spectral shape will depend on the impurity concentration. Therefore, the observed dependence of the spectral shape on free electron concentration is also suggested by fundamental theoretical arguments. This paper explains how the dependence of the spectral shape on the free electron concentration may be used to determine the donor concentration in micron-sized regions. No attempt will be made to calculate the density of states and then the spectral shape to demonstrate explicitly the dependence of spectral shape on impurity concentration. However, the spectral shapes presented here may permit comparison of the various models for the density of states and indicate which approach best describes n-type GaAs in the 0.5 to 5 x 10^{18} cm^{-3} impurity range.

There are many nondestructive techniques for determining the electrically active impurity concentration; however, only electron-beam excitation offers micron-sized resolution. Hall measurements are the most sensitive and accurate, but give an average value for the entire sample and cannot be used on layered structures of the same conductivity type. Optical methods [photoluminescence or Reststrahlen-band minimum (6)] normally require excitation of a thin layer of a large cross section, and therefore spatial variations will not be resolved. Schottky barrier diodes (7) can be used for thin layers with 50-100μ diameter spots, but at donor concentrations in excess of 5 x 10^{17} cm^{-3} the high conductance makes the capacitance measurements difficult. Most applications for electroluminescent GaAs devices require free electron concentrations in the decade of 5 x 10^{17} to 5 x 10^{18} cm^{-3}, and it is in this concentration range where the spectral shape may be utilized to determine the substitutional donor concentration. This concentration determination is confined to a hemispherical volume whose radius can be approximated by the sum of the electron-beam radius, the depth of electron penetration, and the diffusion length for holes. A total radius on the order of 4-6μ would be expected for a 40-kev beam voltage in n-type GaAs. At lower beam energies, features as small as 3μ have been resolved in the cathodoluminescence.

The quantum efficiency η_q of n-type GaAs for electron-beam excitation has a strong dependence on free electron concentration n_o (3, 8). The quantum efficiency initially increases as n_o increases, and then η_q decreases rapidly when n_o exceeds about 5 x 10^{18} cm^{-3}. Also, the quantum efficiency for a given wafer can vary greatly over a distance of only a few microns (9, 10). Therefore, it is extremely useful to have an analytical tool with a spatial resolution of the same order of magnitude as the macroscopic crystal variations. By procedures discussed in this paper, it is possible to investigate the variations in quantum efficiency and consider the possibility that these variations correspond to free electron variations or compensation.

Experimental Procedure

The samples used in this study were single-crystal, <100> oriented, Te-doped, floating-zone wafers prepared at Bell Telephone Laboratories. The electron concentrations, 0.2 to 8 x 10^{18} cm^{-3}, were measured on each wafer investigated. The wafers were polished to provide a damage-free surface with a bromine-methanol etch described by Sullivan and Kolb (11). In fact, the usual preparation of a wafer for device fabrication, one which gives a planar damage-free surface, satisfies all the requirements of sample preparation for cathodoluminescence.

The electron-beam-excitation system is an electron probe microanalyzer, the Cambridge Microscan, in which a light pipe has been inserted to transmit the recombination radiation through the specimen chamber exit port. This excitation system is shown schematically in Fig. 1. The finely focused electron beam at A is deflected synchronously with the display cathode-ray tube. The electron beam strikes the GaAs wafer at B and creates one hole-electron pair for each 4.5 ev of beam energy (12). A small fraction of these generated carriers produces infrared radiation by recombining radiatively. This radiation is

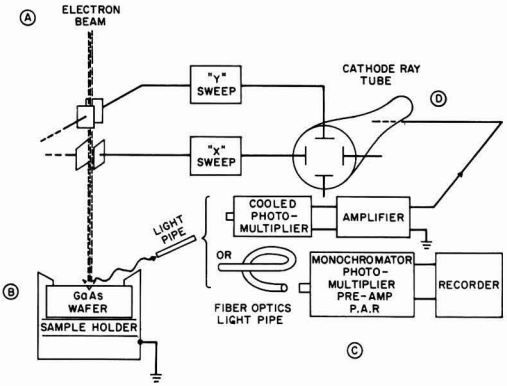

Fig. 1. Schematic representation of the electron-beam excitation system and the infrared detection systems.

transmitted outside the specimen chamber by the light pipe that views the sample at 70° from the surface normal with a solid angle of approximately 3 x 10^{-2} steradians. For display of spatial variations in the radiative-recombination intensity, a dry-ice cooled Amperex 150 CVP (S-1 response) photomultiplier detects the radiation transmitted through the light pipe as shown at C; after amplification this photomultiplier signal serves to intensity-modulate the cathode-ray tube D. In this manner recombination radiation intensity variations over approximately 300 x 300μ areas may be observed at magnifications of several hundred times in the television-type picture that appears on the cathode-ray tube. Wittry and Kyser (9, 10) have described some features of the spatial variations; further elaboration on the features in the scanning-infrared images, especially precipitation and dislocations, is given in the next paper (13).

In the place of the photomultiplier, a fiber optics light pipe may be used to transmit the radiation to a Leiss double-prism monochromator (resolution = 4 mev) in order to resolve the spectral shape. The infrared radiation, chopped at 37.5 Hz, is detected at the exit of the monochromator by the cooled photomultiplier, and the resulting signal amplified by a Princeton Applied Research lock-in amplifier which drives a recorder. The electron-beam accelerating voltage was generally 40 kev, and the beam current could be varied from 2.0 to as low as 0.07 μa with a beam diameter of 2μ or less and obtain resolvable spectra. During measurements of spectral shape the beam current was held constant at 0.5 μa or less, and the beam was generally stationary rather than scanning a line or area. The temperature of the excited region (14) was approximately (30 + 80I_B) °C where I_B is the beam current in microamperes.

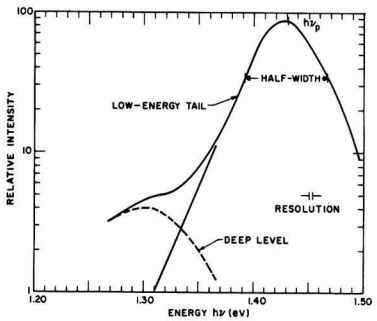

Fig. 2. Typical cathodoluminescent spectrum for n-type GaAs containing 1.75×10^{18} electrons/cm³. The electron beam voltage was 40 kv and the beam current was 0.3 μa.

Experimental Spectra

A typical cathodoluminescent spectrum is shown in Fig. 2 for a sample containing 1.75 x 10^{18} electrons/cm³. The electron-beam voltage was 40 kev and the beam current was 0.3 μa. The low-energy side of the spectrum appears exponential and can be represented by $I = I_o \exp(\beta h\nu)$, where I is the intensity, β the low-energy tail slope, and $h\nu$ the emission energy. At lower intensities the emission is dominated by a deep level as shown. In more lightly doped material and at temperatures below room temperature, this deep level becomes more dominant and can prevent an accurate determination of the low-energy tail slope. The width of the spectrum at one-half the maximum intensity and the energy of the maximum intensity $h\nu_p$ are also shown.

The spectral shapes for a series of samples containing 0.2 to 5 x 10^{18} electrons/cm³ have been summarized in Fig. 3, 4, and 5 by plotting the low-energy tail slope, the energy of the maximum intensity $h\nu_p$, and the half-width as a function of the free electron concentration. (The technique described here still applies above 5 x 10^{18} cm^{-3}, but the drastic decrease in quantum efficiency made it difficult to resolve the spectral shape.) The thermal equilibrium free electron concentration is used rather than the donor concentration because n_o is the quantity determined by

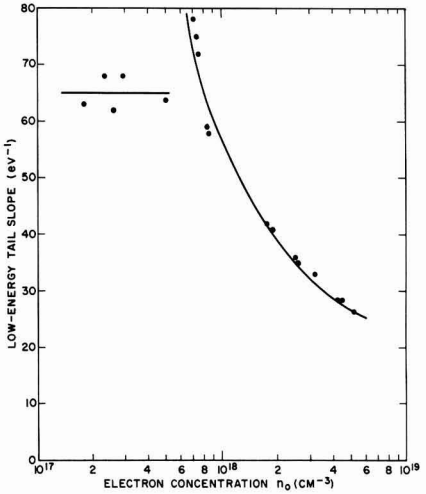

Fig. 3. Low-energy tail slope as a function of the free electron concentration.

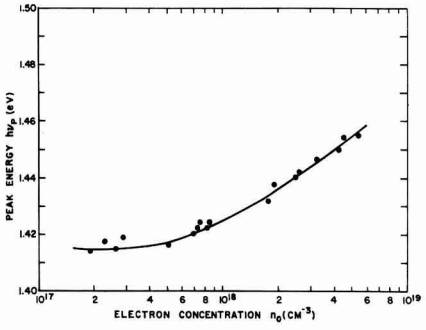

Fig. 4. Peak energy as a function of the free electron concentration.

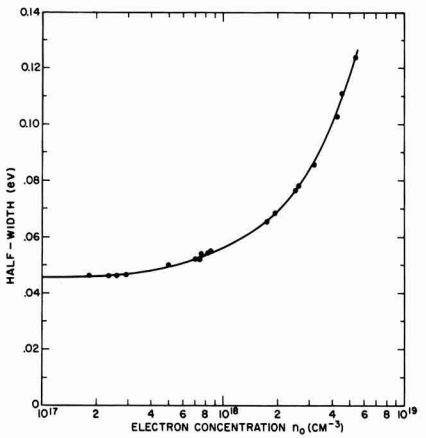

Fig. 5. Half-width as a function of the free electron concentration.

Hall measurements [see Discussion, ref. (13)]. In Fig. 3 the slope of the low-energy tail appears to be constant until a concentration of about 5 x 10^{17} cm^{-3} is reached, then a discontinuity occurs which is followed by a smooth decrease in slope as the electron concentration becomes larger. The slopes at the lower concentrations are influenced by emission from the deep level and are subject to increasing uncertainties. Therefore, without additional study no significance should be placed in the discontinuity shown near a concentration of 5 x 10^{17} cm^{-3}. The peak energy is shown by Fig. 4 to shift to higher energies as the electron concentration exceeds 5 x 10^{17} cm^{-3}. The half-widths summarized in Fig. 5 show a change of 2.5 times over the decade of concentration from 5 x 10^{17} to 5 x 10^{18} cm^{-3}, and the experimental data show very little scatter. From these three figures it should now be obvious that from the spontaneous emission spectral shape it is possible to determine if a sample contains more or less than 5 x 10^{17} electrons/cm^3, and if more, the concentration value.

Since the emission intensity was observed to vary across the sample (9, 10), it was necessary to resolve the spectra in regions that differ in total emission intensity. No variations in spectral shape between regions of differing quantum efficiency were observed for any floating-zone sample. This lack of variation in spectral shape between regions of varying emission intensity suggests two possibilities: either the free electron concentration does not vary between regions, or the sensitivity of spectral shape to variations in n_o is insufficient to resolve possible differences in n_o. To separate these possibilities it is necessary to determine the sensitivity of this technique, the dependence of quantum efficiency on n_o, and the variations in Te concentration between regions differing in emission intensity. The sensitivity of this technique is considered in the next section, while the dependence of quantum efficiency on n_o and the magnitude of the Te concentration variations that could lead to variations in n_o are considered in the following paper (13) on inhomogeneities in GaAs.

Discussion

Figures 3, 4, and 5 show that the spectral shape depends on n_o only above about 5 x 10^{17} cm^{-3}. Of the three spectral shape properties, the low-energy tail slope is the least reliable. This difficulty results from the distortion of the low-energy tail that can occur because of the deep level shown in Fig. 2, as previously discussed. Also, for the lightly doped samples the slopes are quite steep, and any slow responses in the detection and recording system can introduce sizable errors. The build-up of a carbon contamination spot[1] on the sample due to the electron beam was found to reduce the emission intensity. This effect was minimized by using only as large a beam current as necessary to detect the spectral shape and by using a cold finger cooled by liquid nitrogen. At heavier doping levels the emission peak tends to flatten out, and the exact value of $h\nu_p$ can be difficult to determine. Even though the exact energy of the peak intensity is difficult to measure, the value of the peak intensity is rather obvious. Therefore, the spectral width at half the maximum intensity is an accurate and easy quantity to determine. The lack of data scatter in Fig. 5 as compared with Fig. 3 and 4 demonstrates the greater inherent ease in determining the half-width. For these reasons, the half-width will be used as the primary means of determining n_o, and the low-energy tail slope and peak energy will be considered as supplementary data. Taking ±0.005 ev as the resolvable difference in half-width results in a sensitivity of ±0.3 x 10^{18} cm^{-3} for the concentration range covered in Fig. 5.

The sensitivity of ±0.005 ev is a very conservative quantity. For example, the ±0.3 x 10^{18} cm^{-3} sensitivity would suggest that at 7 x 10^{17} cm^{-3} it would not be possible to tell the difference between 5 and 7 x 10^{17} cm^{-3}, while Fig. 5 shows that this distinction is readily made. Therefore, a sensitivity of ±15% at the lower concentrations and ±7% at the higher concentrations might be more reasonable. As mentioned in the introduction, the spatial resolution for this sensitivity depends on the beam voltage and is typically 3-6μ.

Several experimental factors can influence the spectral shape. If the steady-state minority carrier density becomes large enough, a superlinear peak will emerge on the low-energy side of the peak (15). For excitation densities below this level, the spontaneous emission at these impurity concentrations has a linear dependence on the beam current. Also, the effect of self-absorption on the spectral shape must be considered. A detailed analytical treatment of self-absorption cannot be made for the case of a finely focused beam for two basic reasons: (*a*) presently available models for the energy loss of energetic electrons are not adequate for properly describing the carrier generation rate in two independent spatial coordinates, and (*b*) the experimental absorption coefficients for heavily doped GaAs have not been measured for absorption coefficients above 10^3 cm^{-1}, the range where self-absorption might be significant. By making certain reasonable approximations it is possible to consider qualitatively what quantities contribute to self-absorption and their effect on spectral shape.

For description of the variation of electron penetration with beam voltage, the carrier generation rate may be approximated by neglecting the lateral scattering and representing the energy loss by Lenard's law (16)

$$I/I_o = \exp(-\alpha_e x) \qquad [1]$$

where I/I_o is the fraction of the electron flux transmitted, α_e the electron linear absorption coefficient, and x the distance measured from the sample surface. The advantage of using Lenard's law is that it is simple mathematically and analogous to the more familiar expression for optical absorption. The disadvantage is that it does not completely fit the experimental results. The absorption coefficient in Lenard's law depends on beam voltage and can be represented by (17)

$$\alpha_e = 1.9 \times 10^{11} \rho Z^{1/2} E_o^{-2} \qquad [2]$$

where ρ is the sample density, Z the atomic number, and E_o the beam voltage. For a density of 5.32 g-cm^{-3}

[1] A representative presentation of carbon contamination which also occurs in electron microscopes: Hans Gunther Heide, "*Electron Microscopy*," Vol. 1, p. A-4, Sydney S. Breese, Jr., Editor, Academic Press, New York (1962).

and Z of 32, α_e decreases from 1.4 x 10^4 cm^{-1} at 20 kv to 3.6 x 10^3 cm^{-1} at 40 kv. Therefore, the carrier generation rate will vary exponentially in depth as given in Eq. [1], and generation of carriers deeper in the sample will occur as the beam voltage increases.

The distribution in depth of the steady-state minority carrier density depends not only on the generation rate, but also on the diffusion length for holes L_p. This dependence is shown by solution of the continuity equation (neglecting lateral scattering) with suitable boundary conditions. For surface recombination velocities equal to the thermal velocity, an approximate expression for the minority carrier density may be written as

$$p(x) = KE_o[\alpha_e\tau_{nr}/(\alpha_e^2L_p^2 - 1)] [\exp(-x/L_p) - \exp(-\alpha_e x)] \quad [3]$$

where K is a spatially independent factor and τ_{nr} the over-all lifetime which is dominated by the nonradiative lifetime. The generated spectral shape will be uniform in depth and have an intensity proportional to $p(x)$. [Wittry recently presented a more complex analysis for the steady-state minority carrier density. The distribution in depth depends on L_p and the penetration of the beam into the sample, but not as simple exponentials (18)]. At 40 kv and for an L_p of 1.25μ, about 50% of the emission occurs within 3μ of the surface and 95% within 10μ. Emission from a given depth x will be observed after being attenuated by a factor of exp $[-\alpha(h\nu)x_1]$ where $\alpha(h\nu)$ is the optical absorption coefficient at the energy $h\nu$, and x_1 the distance traversed in the solid ($x_1 = x/\cos 70°$). When the $\alpha(h\nu)x_1$ product is the order of unity or larger, significant self-absorption will occur.

The effect of self-absorption on spectral shape really becomes the question of what effect changes in L_p for samples of the same free electron concentration will have on the spectral shape. Reference to the available absorption coefficient data reveals that significant self-absorption is to be expected only above the peak energy. Studies of absorption and photoluminescence by Lucovsky *et al.* (19) have shown that the spontaneous emission peak occurs where the logarithmic slope of the absorption coefficient is $(kT)^{-1}$, where k is Boltzmann's constant and T the temperature. From Fig. 4 and Hill's absorption data (2) the emission peak is found to occur at an absorption coefficient of approximately 10^3 cm^{-1}. Above the peak energy the absorption coefficient will approach a value slightly greater than 10^4 cm^{-1}. For the nominal values of α_e and L_p previously considered in Eq. [3], the emission will occur within less than 10μ of the surface so that the self-absorption, as represented by the $\alpha(h\nu)x_1$ product approaching or exceeding unity, will occur only for emission on the high-energy side of the peak. It is certainly not readily possible to demonstrate experimentally at a given n_o the variation of spectral shape with L_p, but a change in electron penetration can have a similar effect to variations in L_p. Therefore, the dependence of spectral shape on the steady-state hole distribution in depth may be illustrated by varying the beam voltage.

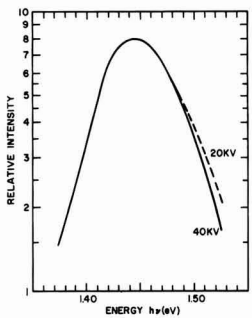

Fig. 6. Demonstration of the effects of self-absorption in a sample of $n_o = 3.2\times10^{18}$ electrons/cm³. The deeper penetration of electrons at 40 kv may be seen to result in greater self-absorption only at energies above the peak energy.

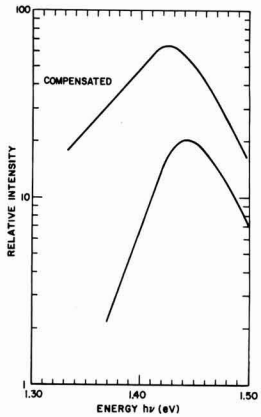

Fig. 7. Comparison of the spectrum for compensated (upper curve) and uncompensated (lower curve) samples with the same n_o of 2.6×10^{18} electrons/cm³. The relative quantum efficiencies of the uncompensated and compensated samples do not significantly differ. They are displaced in intensity only to clearly illustrate their spectral shapes.

Figure 6 shows the spectra at 40 and 20 kv for a sample containing 3.2 x 10^{18} electrons/cm³. The spectrum at 20 kv was normalized to the 40 kv spectrum by setting the intensities equal at 1.400 ev. The two spectral shapes diverge only well above the peak intensity. The difference in penetration, as represented by a change in α_e by a factor of 4, leads to no change of the low-energy tail slope or peak position, but changes the half-width by 0.005 ev. Because changes in the electron penetration and L_p have a similar effect on the steady-state minority carrier density, Fig. 6 suggests that variations in L_p by a factor of 2 or more at a given n_o would be necessary to change the half-width an observable amount. Fortunately, significant optical absorption coefficients occur at emission energies greater than the peak energy, and the effect of self-absorption is minimized.

By use of the calibration curves, it is possible to identify compensated samples. The spectrum for a compensated sample with a net free electron concentration of 2.6 x 10^{18} cm^{-3} is shown in Fig. 7 along with the spectrum of an uncompensated sample of the same n_o (see figure caption). Reference to Fig. 3, 4, and 5 shows that the half-width of the compensated sample corresponds to an n_o larger than 2.6 x 10^{18} cm^{-3}, while the peak position corresponds to a smaller concentration. In addition, the low-energy tail slope corresponds to a larger n_o by an order of magnitude. Thus, a compensated sample is characterized by a peak position that is too low for the n_o indicated by the half-width, and also a low-energy tail slope much less than expected for its half-width. By considering the effect of compensation on the edge absorption coefficient and the resulting spontaneous emission in the manner described by Lucovsky *et al.* (19), it can be seen that the decreased slope and peak energy are consistent with compensation effects. Comparison of Fig. 6 and 7 illustrates the manner in which self-absorption and compensation influence the spectral shape and shows the variation in L_p at a given n_o cannot lead to spectra representative of compensation.

Conclusions

The spontaneous emission spectral shape, characterized by half-width, peak energy, and logarithmic slope of the low-energy tail, depends uniquely on the

free electron concentration above concentrations of about 5 x 10^{17} cm^{-3}. A sensitivity of ±15% may be expected near 5 x 10^{17} cm^{-3} and ±7% at 5 x 10^{18} cm^{-3} with a spatial resolution of 3-6μ. The spectral shape also readily identifies compensated samples. This technique of measuring the free electron concentration from the spectral shape may also be applied to photoluminescence which is generally simpler experimentally; however, most bulk or layered samples are often inhomogeneous, and the small spatial resolution of electron-beam excitation is necessary for investigation of these features. The technique presented here should be applicable to p-type GaAs, but the concentration at which the spectral shape begins to depend on the acceptor concentration will probably be about a factor of 10 higher because of the larger effective mass of holes.

Acknowledgments

The authors are indebted to R. G. Sobers and K. L. Lawley for growing the floating-zone crystals and to F. Ermanis for making the many Hall measurements.

Manuscript received July 18, 1966. This paper was presented at the Cleveland Meeting, May 1-6, 1966.

Any discussion of this paper will appear in a Discussion Section to be published in the December 1967 JOURNAL.

REFERENCES

1. M. I. Nathan, Gerald Burns, S. E. Blum, and J. C. Marinace, *Phys. Rev.*, **132**, 1482 (1963).
2. D. E. Hill, *Phys. Rev.*, **133**, A866 (1964).
3. D. A. Cusano, *Solid State Comm.*, **2**, 353 (1964).
4. B. I. Halperin and Melvin Lax, *Phys. Rev.*, **148**, 722 (1966).
5. Gordon Lasher and Frank Stern, *ibid.*, **133**, A553 (1964).
6. W. G. Spitzer and J. M. Whelan, *ibid.*, **114**, 59 (1959).
7. H. K. Henisch, "Rectifying Semiconductor Contacts," p. 214, Oxford University Press, New York (1957).
8. H. C. Casey, Jr., *Bull. Am. Phys. Soc.*, **10**, 1199 (1965).
9. D. B. Wittry and D. F. Kyser, *J. Appl. Phys.*, **35**, 2439 (1964).
10. D. F. Kyser and D. B. Wittry, "The Electron Microprobe," T. D. McKinley, K. F. J. Heinrich, and D. B. Wittry, Editors, p. 691, John Wiley & Sons, Inc., New York (1966).
11. M. V. Sullivan and G. A. Kolb, *This Journal*, **110**, 585 (1963).
12. W. Czaja, *Helv. Phys. Acta*, **34**, 760 (1961).
13. H. C. Casey, Jr., *This Journal*, **114**, 153 (1967).
14. J. Vine and P. A. Einstein, *Proc. IEE*, **111**, 921 (1964).
15. H. C. Casey, Jr., and R. H. Kaiser, *Appl. Phys. Letters*, **8**, 113 (1966).
16. P. Lenard, *Ann. Phys. Chem.*, **56**, 255 (1895).
17. V. E. Cosslett and R. N. Thomas, *Brit. J. Appl. Phys.*, **15**, 883 (1964).
18. D. B. Wittry, The Electron Probe Microanalysis Conference, May 6, 1966, College Park, Md.
19. G. Lucovsky, A. J. Varga, and R. F. Schwarz, *Solid State Comm.*, **3**, 9 (1965).

Investigation of Inhomogeneities in GaAs by Electron-Beam Excitation

H. C. Casey, Jr.

Bell Telephone Laboratories, Incorporated, Murray Hill, New Jersey

ABSTRACT

Striations concentric with the growth axis, which are usually considered as impurity fluctuations, represent the inhomogeneity most frequently encountered in GaAs. Images of such striations were obtained by scanning-electron-beam-excited recombination radiation (SEBERR) and displayed on a cathode-ray tube. The samples investigated were Te-doped, floating-zone GaAs containing 2 x 10^{17} to 8 x 10^{18} free electrons-cm^{-3}. The spectral shape of recombination radiation demonstrated that any variation in free electron concentration within a cross section normal to the growth axis must be less than about 10%. In addition, the spectral shape showed that compensation is not the reason for the difference in the Te concentration and the free electron concentration. Precipitation of a Te-rich ternary solid solution with a crystal structure other than GaAs may be the most consistent explanation for the striation inhomogeneity and also may account for the cathodoluminescent features associated with dislocations.

In GaAs many techniques have shown the presence of concentric striations normal to the crystal growth axis. These striations represent fluctuations or inhomogeneities in several properties of the semiconductor crystal. Since the striations are readily revealed by etching (1), they obviously affect the rate of many etches. They also have been reported to cause variations in the infrared transmission (2). Schlieren imaging (3, 4) shows that the striations give fluctuations in the index of refraction and that no significant strains are associated with the striations (4). In the images produced by scanning-electron-beam-excited recombination radiation (SEBERR) and displayed on a cathode-ray tube, bands of decreased intensity were observed (5, 6); these bands will be shown to be the striations which can be revealed by etching. This variation in emission intensity indicates that the striations affect the radiative recombination. Striations have been observed also by x-ray diffraction microscopy in silicon (7) and by resistivity probing in germanium (8). Light emission from reverse-biased GaP p-n junctions clearly reveals striations and their effect on reverse breakdown (9). Because of striations, it is necessary, when preparing wafers for epitaxial growth, to use etching techniques that are not sensitive to these inhomogeneities (10); it is also necessary to consider the effect of these inhomogeneities on diffusion and p-n junction lasers (2, 3, 11,12).

Such an effect which causes variations in so many semiconductor properties has stimulated numerous investigations of both the origin and the nature of striations. Recent studies of InSb single crystals have shown that the formation of striations is the result of temperature fluctuations at the solid-liquid interface due to sharp temperature gradients in the growing crystal near the interface (13). For Te in GaAs, striations were shown by autoradiograms (14) and

electron probe microanalysis (15) to be Te concentration variations. These measurements of Te concentration also revealed that the average Te concentration exceeds the free carrier concentration as determined by Hall measurements. A transmission electron microscope study showed the striations in the particular crystals studied to contain bands of very fine precipitates (16). The result of using the Schlieren technique suggests the striations are variations in the index of refraction due to free electron concentration variations or band-gap changes (4). A number of reasons for the variations in the crystal properties and the difference in the total Te and free electron concentration have been proposed: (*a*) un-ionized Te, (*b*) fluctuations in free electron concentration, (*c*) compensation, (*d*) band-gap changes, and (*e*) precipitation.

Of the many techniques just described for observing the striations, none discriminates entirely between the proposed reasons for the variations. For example, the transmission electron microscope shows precipitation, but does not rule out other possibilities such as variations in free electron concentration. This paper explains how electron-beam excitation may be utilized to observe and investigate the striations and also to discriminate between the proposed reasons for the variations. Another benefit of SEBERR is that the range of magnification and resolution permits observation of such interesting features as dislocations and the discrete nature of some striations. The other techniques, although very useful, are generally limited to low magnifications where the fine features are not resolved or to such extremely high magnifications that the large-scale variations are lost and do not directly demonstrate the effect of the inhomogeneities on radiative recombination.

As previously reported (17), the spontaneous emission spectral shape and peak position may be used to determine the free electron concentration within $\pm 15\%$ near concentrations of 5×10^{17} cm^{-3} and $\pm 7\%$ at 5×10^{18} cm^{-3}, or to determine if a sample is compensated. These concentrations cover the range where the striations are most pronounced and also the range most useful for electroluminescent devices. In addition, the characteristic x-rays generated by the electron beam permit quantitative measurement of the impurity concentration if the spectrometer system has sufficient sensitivity. A Cambridge Microscan can detect Te concentrations only above about 10^{20} cm^{-3}, but by using a fully focusing spectrometer Wittry (15) was able to achieve a sensitivity in the low 10^{18} cm^{-3} concentration range. The spatial resolution for cathodoluminescence (CL) is 3-6μ and 2-3μ for x-rays. This paper is concerned only with CL, but Wittry's x-ray results (15) for Te variations will be discussed in order to describe the striations properly.

Relationship between Cathodoluminescent and Etching Features

It is beneficial first to consider the factors that contribute to the observed contrast in SEBERR images. For a sample scanned by a constant-current beam at a fixed-beam voltage, the measured intensity of the recombination radiation is proportional to the quantum efficiency η_q in a material of uniform generation rate times a factor which accounts for nonradiative surface recombination. This factor F_s will depend on surface-recombination velocity, minority carrier diffusion length, and beam voltage. At a fixed-beam voltage and a constant surface-recombination velocity, the principal effect of F_s on the observed intensity will be due to the diffusion length L_p or the over-all lifetime τ, since $L_p = \sqrt{D\tau}$ where D is the diffusion constant for holes. Wittry's results (18) indicate that τ becomes smaller at the higher impurity concentrations, and thus the factor due to nonradiative surface recombination F_s has a functional dependence on the free electron concentration n_o, $F_s \propto f(n_o)$. The quantum efficiency is simply the ratio of the hole-electron pairs that recombine radiatively to the total that recombine. This relationship is expressed as (19)

$$\eta_q = \frac{C}{{n_i}^2} \tau_{nr} n_o \int_0^\infty \alpha(h\nu) \exp(-h\nu/kT)\, d(h\nu) \quad [1]$$

where C is a collective constant, ${n_i}^2$ the thermal equilibrium electron-hole density product, τ_{nr} the over-all lifetime which is dominated by the nonradiative lifetime, and $\alpha(h\nu)$ the absorption coefficient at the energy $h\nu$. The absorption coefficient has a strong dependence on n_o at the concentrations being considered (20) and will cause the integral in Eq. [1] to decrease above concentrations of 10^{18} cm^{-3}. No data are now available to describe the concentration dependence of ${n_i}^2$, but some preliminary calculations based on a model by Halperin and Lax (21) suggest that the dependence will be small. The dependence of τ_{nr} on n_o has not been established, but τ_{nr} can depend on both the concentration of other impurities serving as traps and also on the lattice imperfections. For the present argument, the surface recombination factor F_s will be neglected and the observed intensity taken as η_q. Therefore, contrast in CL shows variations in the minority carrier generation rate, or for a uniform generation rate it measures variations in free electron concentration, unknown impurities, and/or lattice defects.

For comparison of the CL and the preferentially etched surface features over a reasonable portion of a wafer, an area was defined on a <111> oriented wafer containing 2.2×10^{18} cm^{-3} electrically active Te atoms. A smooth surface was obtained by chemically polishing by a procedure using a bromine-methanol etch and intensive stirring (22). Then a "home-plate" shaped mesa with a 0.060 in. base was produced by masking and etching the surrounding material to a depth of 10μ. Areas on this mesa of approximately $300 \times 300\mu$ were scanned by a 40-kv, 0.05-μa electron beam, and the SEBERR pictures were obtained from the cathode-ray tube as previously reported (17). The only optically observable surface irregularities were scratches that occurred during processing. The cathodoluminescent picture of the mesa, made by joining the many pictures of the scanned areas, is shown in the left half of Fig. 1. The sample was then etched with a solution known to reveal dislocations (23); the resulting optical photomicrograph is shown in the right half of Fig. 1. The cathodoluminescent and optical pictures are shown as mirror images so that features found at a certain distance to the right of the center line may be compared with the features at the same distance to the left.

There are a number of features with a unique correspondence between the etched and cathodoluminescent pictures. The irregular, roadlike lines are surface scratches obtained in processing the sample and are actually necessary to align and join the many pictures properly in the composite picture. The dark spots in the cathodoluminescence surrounded by bright regions about 100μ in size correspond uniquely to pits surrounded by smooth regions in the etch portion of the figure. Increased magnification readily identifies the pits as dislocation etch pits. The slightly curved vertical bands of decreased infrared emission spots appear as striations or bands of irregular, overlapping pits. A careful comparison of the left and rights sides of Fig. 1 conclusively demonstrates that the features of dislocations and striations seen by etching are completely reproduced in cathodoluminescence.

General Cathodoluminescent Characteristics of Striations and Dislocations

Examination of SEBERR pictures of samples taken from several Te-doped, floating-zone GaAs ingots reveals typical properties of striations and dislocations which are described in this section. This information

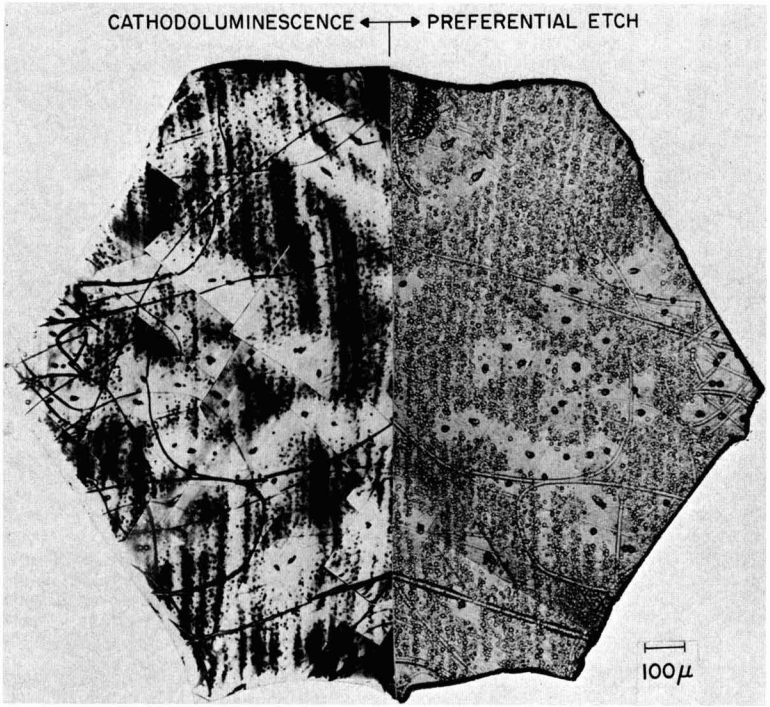

Fig. 1. Comparison of the cathodoluminescent and preferential etch features in GaAs. The free electron concentration is 2.2×10^{18} cm^{-3}.

will be utilized in the next section to infer the nature of the inhomogeneities.

The wafers in Fig. 2 cover a decade in free electron concentration, and for this figure as well as Fig. 3 the wafers were cut normal to the growth axis resulting in <100> orientation. In parts (a) and (b) of Fig. 2, the concentric, circular nature of the striations may be seen. The sample in Fig. 2(c) has a very large dislocation density, and the concentric nature of the striations is not recognizable in a picture of an area this small. The free electron concentrations of the samples in Fig. 1 and Fig. 2(c) are about the same; however, the striation regions of decreased recombination radiation in Fig. 1 are discrete, small, overlapping spots, while in the other wafer these regions appear continuous. Three samples from the same ingot are shown in Fig. 3 to further illustrate this property. Figure 2(b) is representative of most samples up to free electron concentrations of 6×10^{18} cm^{-3}. At higher concentrations the quantum efficiency rapidly decreases, and variations, if present, would be lost in the detector and amplifier system noise.

The dark spots at dislocations have the unique feature of usually being surrounded by a radially symmetrical region of increased emission intensity even in the dark band of the striations. In Fig. 1, 2, and 3 these regions have a radius of approximately 10-50μ. Often, as in Fig. 1, this high-intensity region surrounding a dislocation has the same quantum efficiency as the bright bands between the dark striations. The size of the dark spot at the dislocation is usually at least twice as large as the resolution of this technique (about 3-6μ), and therefore the contrast must be caused by more than just the line associated with the extra plane of atoms.

The three pictures in Fig. 3 show that an interesting and consistent relationship exists between the occurrence and size of discrete spots in striations, and the size of the dislocation spot and its surrounding bright region. Samples shown in Fig. 3 are from the same ingot and have free electron concentrations of 1.7, 2.5, and 3.2×10^{18} cm^{-3}, respectively. The approximate diameters of a dislocation and a bright region, and the size of the striation spot in Fig. 3 are summarized in Table I. This table shows that the larger striation spots occur with the larger dislocation spots and bright regions.

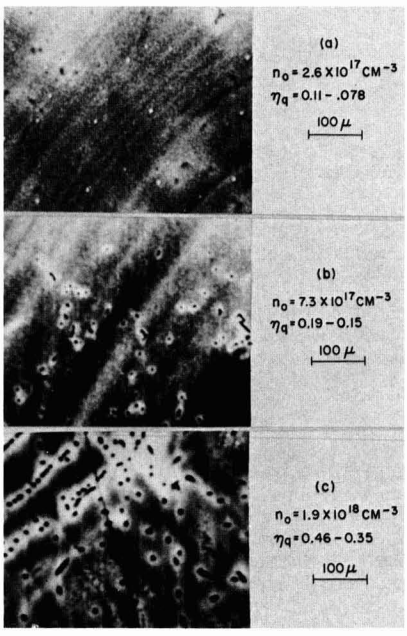

Fig. 2. Typical properties of the inhomogeneities in GaAs as illustrated by SEBERR pictures. The relative quantum efficiency η_q is given for the bright region surrounding the dislocation (dark spots) and the dark bands in the striations.

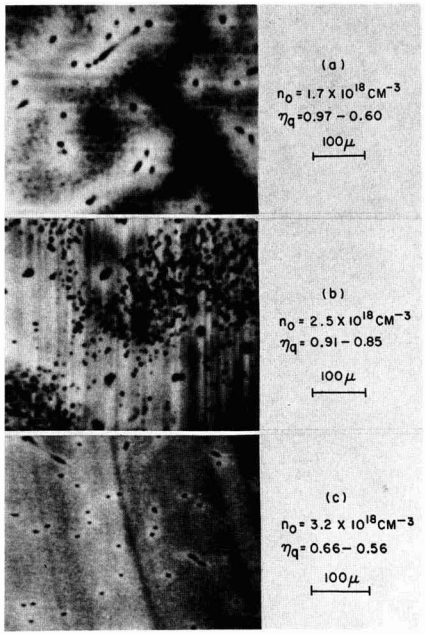

Fig. 3. SEBERR pictures demonstrating the size relationships of the dark spots at the dislocation, the radially symmetric bright region surrounding the dislocation, and the discrete nature of striations.

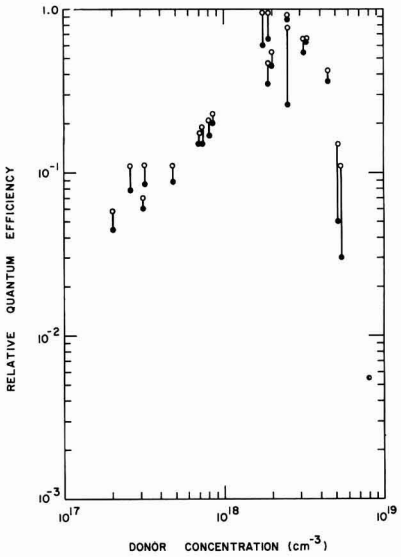

Fig. 4. Relative quantum efficiency as a function of free electron concentration. The open circles represent the efficiency in the bright regions near dislocations and the solid circles represent the efficiency in the dark bands of the striations.

Since the contrast displayed on a cathode-ray tube can be deceptive, it is necessary to obtain the magnitude of the relative quantum efficiency variations by measuring the relative output voltage of the photomultiplier. The resulting efficiencies for bright regions near dislocations and the dark striation bands are plotted as open and closed circles respectively in Fig. 4. The efficiency limits for these wafers show the same general dependence on free electron concentration as the average values given by Cusano (24) and Kyser and Wittry (6). The rapid decrease in quantum efficiency above about 5 x 10^{18} electrons-cm^{-3} may be attributed partly to movement of the absorption edge to higher energies as described by the Burstein (25) shift which reduces the integral in Eq. [1] (19).

The spontaneous emission spectral shapes were resolved for the samples summarized in Fig. 4. Both the bright areas near dislocations and the dark striations were considered, but no differences in spectral shape were found on any wafer. This result means that the free electron concentration fluctuations must be less than ±15% near 5 x 10^{17} cm^{-3} and ±7% near 5 x 10^{18} cm^{-3} (17). These limits of uncertainty are rather conservative, and with extreme care the uncertainty will be half the above values. Also, spectral shapes which are characteristic of compensation (17) were not observed in the striations.

Discussion of Results

Initially, it is necessary to examine the relationship between the free electron concentration and the donor concentration. At Te concentrations above 10^{17} cm^{-3}, the average distance between impurity atoms is close to the diameter of the Bohr orbit of a donor electron in a crystal, and Hall measurements reveal conduction by carriers in impurity bands or band tails (26). Under these conditions the free electron concentration no longer has any temperature dependence. This result indicates that for concentrations above 10^{17} cm^{-3} each donor atom located substitutionally in an As site contributes one free electron, and substitutional donors do not exist in a neutral or un-ionized state which would demand a temperature dependence of the free electron concentration. The possibility of the compensation as an explanation for the differences between n_o and the Te concentration or for the CL contrast can readily be eliminated since none of the spectral properties related to compensation (17) was observed.

Table I. Size relationships of cathodoluminescent features

Figure	Diameter of dislocation spot, μ	Diameter of bright region, μ	Striation spot size, μ
3(a)	12	60	4-6
3(b)	20	100	10-12
3(c)	6	25	Continuous

The striations have been shown to be Te fluctuations by Wittry's (15) electron probe microanalysis and autoradiograms by Cronin *et al.* (14). Bands of increased Te concentration showed a decrease in CL intensity (15), which means the dark bands (and presumably the dark spots at the dislocations) in Fig. 1, 2, and 3 are the regions of greater Te concentration. Not only are Te fluctuations present, but the average Te concentration was significantly greater than n_o (14, 15). For example, in a sample containing 5.2 x 10^{18} electrons-cm^{-3}, the average Te concentration was approximately 7 x 10^{18} cm^{-3} (15), and chemical analysis of one of our samples with n_o = 8 x 10^{18} cm^{-3} showed it contained 1.5 x 10^{19} Te atoms-cm^{-3}. This discrepancy between the impurity concentration and the free electron concentration was also observed for Se (27) (results of numerous other papers suggest this is a general effect), but the differences are larger at a given Se concentration than observed for Te. Clearly, Te must be present in a form other than as a substitutional donor on an As site.

A variation of the free electron concentration would be expected because the striations are Te concentration fluctuations. However, the lack of any observable variations in spectral shape between bright and dark bands in the striations limits the possible range of variation to approximately 10%. With 30% Te fluctuations, Wittry (15) was also unable to find any spectral shape variations. In general, at high concentrations n_o does not follow the Te concentration;

in fact, Vieland and Kudman (27) found that n_o varied as $(Se)^{1/3}$ above concentrations of 4×10^{18} cm^{-3}. This dependence of n_o on the Te concentration suggests that the bands of greater Te concentration would not be accompanied by a comparable n_o change. The spectral shape technique does limit the possible variation in n_o, but cannot demonstrate a complete absence of n_o variation.

Equation [1] can be used for showing that differences in quantum efficiency between the bright regions and the dark bands of the striations, if attributed to differences in free electron concentration alone, will lead to an inconsistent result. Since the SEBERR pictures show dislocations as dark spots surrounded by bright regions of the same intensity as the bright striation bands throughout the n_o concentration range studied, it will be assumed that the dark bands in low concentration samples are bands of greater Te concentration as found for the more heavily doped samples. Below concentrations of 10^{18} cm^{-3}, the absorption coefficient is constant at a given $h\nu$, and with a constant τ_{nr} and n_i^2 Eq. [1] becomes

$$\eta_q = C_1 n_o \qquad [2]$$

where C_1 is a constant containing the various constant factors. From the data in Fig. 4, the dark striations would be predicted to contain a smaller concentration than the bright regions: $n_o(\text{dark}) < n_o(\text{bright})$. At higher concentrations, α at a given $h\nu$ decreases rapidly, and small changes in n_o cause a larger change in the integral in Eq. [1] than the linear dependence on n_o. In this case Eq. [1] becomes

$$\eta_q = C_2 \int_0^\infty \alpha(h\nu) \exp(-h\nu/kT)\, d(h\nu) \qquad [3]$$

with the various constants represented by C_2. At concentrations above 10^{18} cm^{-3} the dark regions in Fig. 4 would be due to a smaller α at a given energy, and hence $n_o(\text{dark}) > n_o(\text{bright})$, which is inconsistent with the previous inequality. Inclusion of the nonradiative surface recombination will lead to more complex expressions than Eq. [2] and [3], but will not change the above inequalities between concentrations in the bright and dark regions. Thus, any possible variation in the free electron concentration, which has been limited to about 10%, will not be the principal source of contrast or inhomogeneity seen in cathodoluminescence.

From the above discussion, the most probable source of contrast seen in the SEBERR pictures is the nonuniform distribution of the precipitated Te-rich phase or complex associated with the difference between Te concentration and n_o. Whether the inhomogeneities are band-gap variations will depend entirely on the nature of the precipitation. The contrast would be interpreted in terms of Eq. [1] as τ_{nr} variations. The spatial characteristics are more fully described in Table I by comparing the diameter of the dark spots at dislocations and the surrounding bright regions along with the size of the spots in the striations for the samples shown in Fig. 3. In general, this difference in Te concentration and n_o can be described as a Te-rich ternary solid solution with a crystal structure other than GaAs, but a more explicit description would only be speculation. For example, a solid solution of GaAs-Ga_2Te_3 can form as the crystal cools below 827°C (28). However, to explain the size of the bright regions around the dislocations requires diffusion of Te (at 827°C or lower) from the dark bands to the "dislocation" at very much larger diffusion rates than observed for donors in GaAs (29). Therefore, the Te-rich phase or complex must either be grown into the crystal or be formed by a species which is capable of extremely rapid diffusion.

Vacancies diffuse rapidly, and Vieland and Kudman (27) have suggested a complex involving a Ga vacancy and three Se atoms to describe the cube root dependence of n_o on the Se concentration. Mass action relations were written to describe the cube root dependence; however, mass action relations only mathematically describe equilibrium reactions and do not necessarily prove the existence of the assumed reactants. Acceptors also diffuse rapidly, but there is no evidence of any significant amount of compensation in these highly doped crystals.

The experimental observation that the free electron concentration is consistently less than the chemical donor concentration seems to be a general relationship for GaP (30) as well as GaAs. A fundamental understanding of this phenomenon is lacking at the present time.[1] Electron-beam excitation may be useful as a quantitative measurement technique in experiments intended to study this effect. This technique of studying inhomogeneities in bulk crystals should be applicable to many other compounds, especially the III-V mixed crystals. The only requirements are that the energy of the radiative recombination must exceed about 1.2 ev to permit detection with photomultipliers, and the quantum efficiency be not less than about 10^{-5}.

Conclusions

The features in SEBERR pictures were found to have a complete correspondence to those seen in photomicrographs of preferentially etched surfaces. These features included both dislocations and striations. Dislocations are characterized by 6-12μ dark spots that are usually surrounded by 25-100μ bright regions. The striations appear as either continuous bands or bands of discrete spots of decreased radiative recombination. In previously published results, the striations were found to contain Te concentrations in excess of the free electron concentration. Hall measurements and theoretical considerations show that Te atoms located substitutionally in the lattice cannot exist at these concentrations in an un-ionized form. Other techniques readily demonstrate the presence of inhomogeneities, but do not discriminate between the various reasons suggested for the variations in crystal properties. The infrared emission spectral shape demonstrates that compensation is not present in the striations, nor can very large free carrier variations be present. The contrast in cathodoluminescence and the difference between the total Te concentration and the free electron concentration are therefore accounted for by precipitation of a Te-rich solid solution or complex.

Acknowledgments

The author is indebted to several people for contributions to this paper. The floating-zone crystals were grown by R. G. Sobers, and the Hall measurements were made by F. Ermanis. R. H. Kaiser assisted in the spectral shape measurements, K. L. Lawley aided in the etching studies, and M. B. Panish provided information on the Ga-As-Te phase diagram.

Manuscript received July 18, 1966. This paper was presented at the Cleveland Meeting, May 1-6, 1966.

Any discussion of this paper will appear in a Discussion Section to be published in the December 1967 JOURNAL.

REFERENCES

1. T. S. Plaskett and A. H. Parsons, *This Journal*, **112**, 954 (1965).
2. G. Ziegler and H.-J. Henkel, *Z. Angew. Phys.*, **19**, 401 (1965).
3. H. Salow and K.-W. Benz, *ibid.*, **19**, 157 (1965).
4. M. E. Drougard, *J. Appl. Phys.*, **37**, 1858 (1966).
5. D. B. Wittry and D. F. Kyser, *ibid.*, **35**, 2439 (1964).
6. D. F. Kyser and D. B. Wittry, "The Electron Microprobe," p. 691, T. D. McKinley, K. F. J. Heinrich, and D. B. Wittry, Editors, John Wiley & Sons, Inc., New York (1966).
7. G. H. Schwuttke, *J. Appl. Phys.*, **34**, 1662 (1963).
8. J. A. M. Dikhoff, *Solid-State Elec.*, **1**, 202 (1960).
9. M. Gershenzon and A. Ashkin, *J. Appl. Phys.*, **37**, 246 (1966).
10. R. R. Moest, *This Journal*, **113**, 141 (1966).

[1] Note added in proof: A recent paper, G. Schottky, *J. Phys. Chem. Solids*, **27**, 1721 (1966), considers the Ga vacancy-donor atom complex in considerable detail.

11. J. C. Marinace, *ibid.*, **110**, 1153 (1963).
12. M. H. Pilkuhn and H. Rupprecht, *Trans. Met. Soc.*, **230**, 296 (1964).
13. K. Morizane, A. F. Witt, and H. C. Gatos, *This Journal*, **113**, 51 (1966).
14. G. R. Cronin, G. B. Larrabee, and J. F. Osborne, *ibid.*, **113**, 292 (1966).
15. D. B. Wittry, *Appl. Phys. Letters*, **8**, 142 (1966).
16. E. S. Meieran, *J. Appl. Phys.*, **36**, 2544 (1965).
17. H. C. Casey, Jr., and R. H. Kaiser, *This Journal*, **114**, 149 (1967).
18. D. B. Wittry, Electron Probe Microanalysis Conference, May 6, 1966, College Park, Md.
19. H. C. Casey, Jr., *Bull. Am. Phys. Soc.*, **10**, 1199 (1965).
20. D. E. Hill, *Phys. Rev.*, **133**, A866 (1964).
21. B. I. Halperin and Melvin Lax, *ibid.*, **148**, 722 (1966).
22. M. V. Sullivan and G. A. Kolb, *This Journal*, **110**, 585 (1963).
23. M. S. Abrahams and C. J. Buiocchi, *J. Appl. Phys.*, **36**, 2855 (1965).
24. D. A. Cusano, *Solid State Comm.*, **2**, 353 (1964).
25. E. Burstein, *Phys. Rev.*, **93**, 632 (1954); see also T. S. Moss, *Proc. Phys., Soc. (London)*, **B67**, 775 (1954).
26. D. N. Nasledov, *J. Appl. Phys.*, **32**, 2140 (1961).
27. L. J. Vieland and I. Kudman, *J. Phys. Chem. Solids*, **24**, 437 (1963).
28. M. B. Panish, *This Journal*, **114**, 91 (1967).
29. R. W. Fane and A. J. Goss, *Solid-State Elec.*, **6**, 383 (1963).
30. F. A. Trumbore, H. G. White, M. Kowalchik, R. A. Logan, and C. L. Luke, *This Journal*, **112**, 782 (1965).

Textural and Electrical Properties of Vacuum-Deposited Germanium Films

J. D. Williams and L. E. Terry[1]

Solid State and Thin Film Devices Division, Sandia Corporation, Albuquerque, New Mexico

ABSTRACT

An investigation has been conducted to determine the effect of condensation rate and substrate temperature on the textural and electrical properties of germanium films vacuum-deposited on amorphous substrates. All films deposited were either amorphous or polycrystalline. Regions in the condensation rate-substrate temperature plane exist which exhibit very high degrees of preferred orientation of the polycrystalline films. It was confirmed that substrate temperature influences the textural properties of the films. Also, for large variations in condensation rate, different preferred orientations were obtained for a constant substrate temperature. This demonstrates that film structure is a function of both the substrate temperature and the deposition rate.

Thin-film semiconductor research activity has been greatly stimulated by the need for improvement in one or more of the aspects of lower cost, smaller size, greater reliability and radiation resistance in electronic components and circuits. The electrical properties of semiconducting films are intimately related to their textural properties; therefore, this investigation of germanium films has been conducted to determine the effect of condensation rate and substrate temperature on the textural and electrical properties of the films. Two papers reporting textural properties of vacuum-deposited germanium films on heated amorphous substrates produced seemingly contradictory results. Davey (1) working with condensation rates on the order of 1 Å/sec, reported [110] texture for substrate temperatures in the 175°-350°C range. He found that a competition for growth occurs in the 350°-575°C range and that the texture varies principally between being powder, [110] and [111]. Above 575°C he found that the [111] texture became dominant. Via and Thun (2), working at 80 Å/sec, reported practically amorphous films at substrate temperatures up to 400°C. In the 400°-500°C range, they found mixed orientation of [110] and [100]. At approximately 500°C, the [100] orientation disappears and a mixture of [110] and [111] is found. At temperatures above 600°C, they found that the preferred [110] is by far predominant.

Sloope and Tiller (3), investigating vacuum-deposited germanium films on heated single-crystal substrates, found that the tendency of a film to exhibit epitaxy increases with increasing substrate temperature. Krikorian and Sneed (4) reported a similar observation in their investigation of sputtered germanium films deposited on heated single-crystal substrates. These observations, plus our own preliminary findings, led us to expect that a given preferred orientation obtained on heated amorphous substrates at low condensation rates and low temperatures could also be obtained at higher substrate temperatures and condensation rates.

During the course of our work, Davey *et al.* (5), published another paper which stated that, for thicknesses of germanium films greater than 500Å, the [110] texture was independent of all the other deposition parameters. A careful examination of Davey's data revealed that, for a constant substrate temperature, 240°C, the deposition rate was varied between 1 and 100 Å/sec. Likewise, for a constant deposition rate of 8.25 Å/sec, the substrate temperature was varied between 225° and 600°C. Therefore, we have chosen to investigate the textural properties of germanium films formed in an extended portion of the rate-temperature range.

Experimental Procedure and Equipment

Two hundred germanium films were vacuum-evaporated onto glazed alumina ceramic and Corning No. 7059 glass substrates with the following range of deposition parameters: (*a*) substrate temperature 25° to 700°C, (*b*) condensation rate 0.5 to 380 Å/sec, (*c*) deposition pressure 10^{-8} to 5 x 10^{-6} Torr, and (*d*) thickness 800 to 50,000Å. The vacuum evaporations were performed with the fixtures and bakeable ion-pumped system shown in Fig. 1. The molybdenum and 304 stainless steel fixture permitted seven samples to be prepared in one pumpdown cycle. Magnetic rotary motion feedthroughs allowed a selection of groups of 2-3-2 substrates for a choice of temperature and condensation rates. The 0.1-ohm centimeter n-type germanium source material was heated to evaporation temperatures with a Varian electron gun. Open cylindrical alumina and quartz crucibles, resistance-

[1] Present address: Motorola Inc., Phoenix, Arizona.

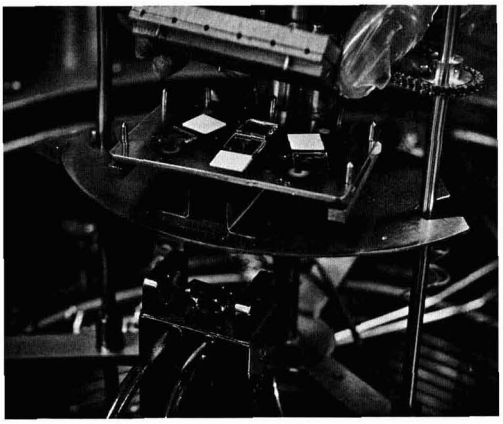

Fig. 1. Substrate holder and heater

heated by helical tungsten baskets and heavy tungsten coils with no inserts, were used as evaporation sources to obtain condensation rates above 100 Å/sec. Substrate heating was accomplished by two methods: (*i*) A molybdenum or stainless steel block, with heater wire imbedded in it, was placed in intimate contact with the substrate; (*ii*) The substrates were placed in a cylindrical oven. The contact heater was capable of raising the substrate temperature to approximately 600°C, and the oven was capable of producing substrate temperatures up to at least 800°C. Construction details of the contact heater are shown in Fig. 2.[2] Substrate temperatures were monitored by chromel-alumel thermocouples in contact with the back of the substrates. A considerable temperature differential is created between the front and back surfaces of the substrates when they were heated by the contact heater. In some cases this temperature difference is as much as 250°C. These differences were carefully correlated with the back surface temperatures by attaching thermocouples to both front and back surfaces and simulating the evaporating conditions. All temperatures in this report refer to the front surface of the substrate.

[2] The imbedded heater wire was Thermocoax manufactured by the Amperex Corporation, Hicksville, New York.

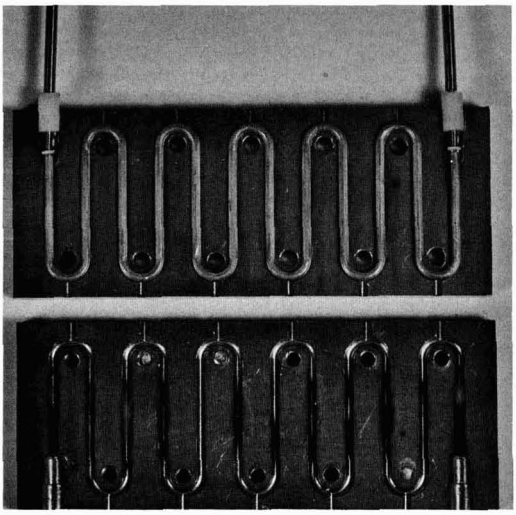

Fig. 2. Contact heater

The substrates were cleaned by the following procedure[3]: (*i*) 15-min ultrasonic bath in Alconox (3 g/liter distilled H_2O), (*ii*) 15-min ultrasonic rinse in room temperature distilled water, (*iii*) 10-min immersion in a boiling 10% solution of H_2O_2, (*iv*) boiling in ultrasonic rinse in distilled water, (*v*) drying in ethanol vapor, and (*vi*) storing in jars with ground glass seals.

The deposition parameters were varied by controlling the electron-gun beam current, the power delivered to the tungsten coil, and/or the deposition time. The source dimple of the electron gun was always filled with approximately 2g of germanium. The source material was slowly outgassed and the evaporation conditions allowed to reach equilibrium before the shutter was opened. Since the source material was never depleted by more than a few per cent during any evaporation, the effective source area and volume remained nearly constant, resulting in uniform condensation rates. Films were measured for thickness on a Zeiss interference microscope with the exception of a few of the very high substrate temperature films which exhibited rather rough surfaces. A beta-ray backscattering instrument was used to measure the average thickness of these films.

All samples were analyzed by x-ray diffraction on a General Electric XRD-6 diffractometer unit. The Bragg reflection peaks from the (111), (220), (311), and (400) planes were scanned at 4° and 0.4°/min. The method of determining the degree of preferred orientation of the films and a description of the crystallographic notation is given in Appendix A.

Results and Discussion

Crystallite orientation.—All films deposited on amorphous substrates were either amorphous or polycrystalline. Films deposited in the 1-100 Å/sec condensation rate and 25°-150°C substrate temperature range were all amorphous. Polycrystallinity was observed between 150° to 200°C but consistent, repeatable results were not obtained until the substrates were heated to above 200°C. A composite plot showing regions of preferred orientation in the substrate temperature-condensation rate plane is given in Fig. 3. Additional information pertinent to the data pre-

[3] This is cleaning procedure No. 1 reported in "A Comparison of Substrate Cleaning Procedures," J. D. Williams and J. N. Shafer, presented at the San Francisco Meeting of the Electrochemical Society, May 1965, Abstract No. 115.

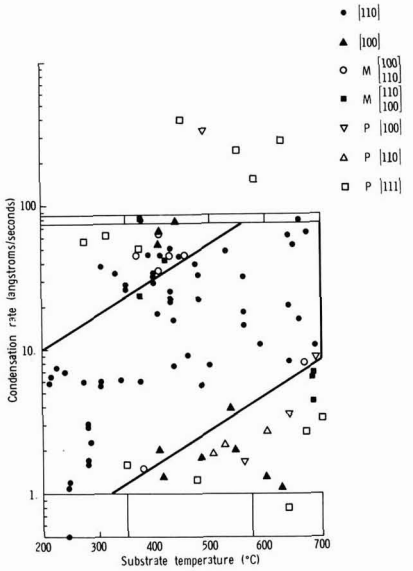

Fig. 3. A composite plot of crystallographic orientation, substrate temperature and condensation rate.

Table I. Additional data relative to Figure 3

Film number	Thickness (Angstroms)	Rate (Å/sec)	Substrate temp (°C)	Orientation	R_{220} (R_{111} always = 1)	R_{311}	R_{100}
2-3-2	800	1.65	350	P[111]	0.505	0.1	0.02
2-12-1	900	1.25	475	P[111]	0.58	0.8	0.94
3-4-1	1,100	0.8	640	P[100]	0.74	0.71	1.36
2-12-3	900	1.25	410	[100]	1.25	0.01	2.7
4-11-2b	1,400	0.5	245	[110]	97	0.1	0.7
2-13-2	2,200	1.83	485	[100]	0.95	0.1	3.2
2-24-1	2,430	2.7	600	P[110]	1.32	0.47	1.2
3-2-1	2,160	3.6	640	P[100]	0.88	0.9	1.76
3-4-2	1,620	1.08	620	[100]	0.8	0.5	3.1
3-4-3	1,900	1.25	600	[100]	1.02	0.76	3.9
3-14-2c	2,160	36	410	M[100/110]	2.0	0.1	2.8
4-9-3	2,430	8.1	670	M[100/110]	0.4	0.01	1.64
2-10-1	2,700	5.6	485	[110]	5.6	0.13	0.01
2-13-1	2,700	2.2	525	P[110]	1.69	0.94	1.5
2-18-1	2,530	1.7	560	P[100]	1.13	0.65	1.3
2-26-1	2,600	1.73	560	P[100]	1.22	1.18	1.28
2-26-2	2,600	2.06	545	[100]	1.3	0.92	2.4
2-26-3	2,600	1.88	505	P[110]	1.24	0.425	0.465
3-14-1a	2,700	45	430	M[100/110]	4.28	0.7	4.6
3-14-2a	2,700	45	410	[110]	3.99	0.35	2.52
3-14-3a	2,700	45	370	M[100/110]	2.33	0.26	3.18
3-14-3b	2,700	45	390	[110]	3.58	1.51	2.13
3-16-2c	3,240	54	410	[100]	1.98	0.3	3.44
3-7-2	2,700	1.5	380	M[100/110]	1.9	0.5	2.1
3-7-1	3,590	2	410	[100]	1.5	0.2	3.6
2-24-2	3,510	3.9	535	[100]	2.1	0.47	3.12
3-11-1b	5,400	22.5	430	[110]	7.62	0.69	3.4
3-16-1a	4,600	76.8	440	[100]	2.1	0.6	3.97
3-16-1b	4,730	79	440	[100]	1.4	0.65	4.1
3-16-2a	3,920	65	410	[100]	3.1	0.72	5.9
3-16-2b	3,780	63	410	M[100/110]	3.2	0.6	3.77
3-16-3a	5,000	83.5	375	M[110/100]	3.74	0.5	3.17
3-16-3b	5,000	83.5	375	[110]	5.0	0.6	3.97
3-17-1a	5,570	44	445	[110]	5.1	1	2.3
3-17-2b	5,130	42.8	420	M[110/100]	5.03	0.64	4.78
3-17-3a	4,590	38	305	[110]	6.5	0.3	4.55
3-17-3b	4,050	33.7	330	[110]	13.7	0.8	4
3-20-2a	5,120	21.3	430	[110]	6.49	0.7	2.3
3-23-2a	5,400	18	560	[110]	5	0.78	1.78
3-23-2b	4,860	16.2	660	[110]	2.7	0.43	1.1
3-23-2c	4,460	14.7	560	[110]	4.3	0.45	0.7
3-23-3a	5,400	22.5	480	[110]	7	0.4	3.5
3-25-1a	5,400	9	460	[110]	5.2	0.42	1.91
4-1-2	4,600	6.4	685	M[110/100]	2.02	0.615	1.45
4-9-1	4,050	3.4	700	P[111]	0.8	0.43	0.7
4-11-1a	3,920	1.2	245	[110]	25	0.7	1.84
4-11-1b	3,650	1.1	245	[110]	55	0.8	1.95
4-10-3a	4,580	1.7	280	[110]	40	0.6	2.1
4-10-3b	4,330	1.6	280	[110]	45	0.7	1.9
Ge-x-13	4,100	65	675	[110]	2.9	0.3	0.45
3-20-3a	5,670	23.6	375	M[110/100]	3.6	0.43	3.4
3-25-3b	5,800	16	435	[110]	10.2	0.4	0.48
4-13-3a	5,800	6.5	215	[110]	117	1.4	2.5
4-13-3b	5,800	6.5	215	[110]	146	1.14	1.7
3-11-1a	6,075	25.3	430	[110]	7.31	0.69	3.4
3-25-3a	6,350	17.6	405	[110]	9.3	0.46	0.55
3-25-2c	6,900	7.7	435	[110]	2.1	0.43	0.71
3-11-2c	7,020	29.2	400	[110]	5	0.576	3.15
3-25-2b	7,030	7.8	500	[110]	3.78	0.38	0.2
3-11-2b	7,840	32.6	400	[110]	14	0.78	5.2
3-11-2a	8,100	33.8	400	[110]	15	0.574	3.27
3-13-1a	8,640	48	530	[110]	6.1	0.52	1.76
3-13-2c	9,450	39	475	[110]	7	0.265	2.2
3-20-1a	8,900	33	480	[110]	7	0.24	2.1
3-20-1b	8,630	32	560	[110]	3.4	0.42	2.1
3-23-1a	7,830	10.8	590	[110]	5.5	0.425	2.0
3-23-1b	7,830	10.8	690	[110]	2.7	0.52	1.5
4-2-1	8,100	9	690	P[100]	1.1	0.87	1.5
4-10-1a	8,240	2.3	285	[110]	146	0.94	0.16
4-10-1b	8,100	2.25	285	[110]	53	0.37	0.35
4-10-2a	8,240	3.05	280	[110]	146	0.93	0.01
4-10-2b	8,100	3.0	280	[110]	135	1.2	0.17
4-10-2c	7,840	2.9	280	[110]	250	1	0.38
3-6-2	74,900	20	640	[110]	2.9	0.74	1.74
3-11-3a	10,120	28.2	350	[110]	10.2	0.915	5.3
3-11-3b	9,720	27	350	[110]	11.1	0.8	5.5
3-13-2a	10,800	45	455	M[100/110]	7.62	0.35	5.08
3-13-3a	12,150	50	430	[110]	3.7	0.3	2.1
3-13-3b	12,150	50	430	[110]	3.67	0.27	2.2
3-26-1a	11,080	6.15	340	[110]	250	0.7	4.2
3-26-1b	10,800	6	375	[110]	241	0.7	5.6
3-26-2a	11,200	6.2	275	[110]	53	0.8	0.4
3-26-2b	10,800	6	305	[110]	40	0.82	0.3
3-36-2c	10,100	5.6	305	[110]	23.8	0.85	0.2
3-26-3a	13,500	7.5	225	[110]	159	0.9	0.3
3-26-3b	12,550	7.0	240	[110]	121	0.33	0.35
3-31-1	16,000	53	650	[110]	6.5	0.55	3.56
3-31-2	11,000	61	640	[110]	7.31	0.44	4.2
3-31-3	12,500	8.3	640	[110]	6.7	0.58	1.01
4-2-2	12,150	6.75	685	M[110/100]	2.4	0.52	1.82
4-2-3	10,800	4.5	685	M[110/100]	1.75	0.535	1.48
Ge-x-3	19,000	61	315	P[111]	0.45	0.4	0.31

Table I (Continued)

Film number	Thickness (Angstroms)	Rate (Å/sec)	Substrate temp (°C)	Orientation	R_{220} (R_{111} always = 1)	R_{311}	R_{100}
Ge-x-2	17,000	58	275	P[111]	0.05	0.6	1
Ge-x-4	22,000	46	395	P[111]	0.5	0.2	0.22
Ge-x-6	43,000	240	550	P[111]	0.8	0.66	0.68
Ge-x-7	23,000	147	580	P[110]	1.04	0.723	0.832
Ge-x-8	39,000	390	450	P[111]	0.94	0.6	0.511
Ge-x-9	40,000	330	490	P[100]	0.11	0.66	1.92
Ge-x-11	50,000	280	630	P[111]	0.9	0.74	0.945

sented there is given in Table I. In Fig. 4 the three regions of the substrate temperature condensation rate plane previously investigated by Davey and Via and Thun are outlined. Three broader regions designated A, B, and C are also labeled to aid in the discussion of the figure.

Davey's first results are shown in the lower portion of Fig. 4. He found [110] texture[4] for low substrate temperatures (175°-350°C) and [111] texture for high substrate temperatures (525°-650°C) with the indicated mixed orientations in between. Via and Thun's results are shown near the top of the figure. Their films were all deposited at a condensation rate of 80 Å/sec. Polycrystallinity was first observed at 350°C. Mixed orientation was found up to 600°C, and the [110] texture was by far predominant above 600°C. The results of the present work extend into both regions and clearly indicate that a continuous range exists which connects the two regions of [110] texture. This is shown as region B in Fig. 4. In these polycrystalline films, a certain crystallographic plane of each crystallite is arranged parallel to the substrate surface, but we expect that the orientation is random in the other two directions. Two possible factors which influence the texture are: (*i*) that a larger binding energy exists between the condensing atoms than between the film atoms and the substrate surface, and (*ii*) the surface mobility of the atoms is an increasing function of the substrate temperature. According to a generalization of Bravais, the bounding planes which develop in growth are likely to be those which are parallel to the crystallographic planes of densest packing. There are many exceptions to this, but in the diamond structure the [110] is the most dense plane. In order to maintain similar conditions on the sub-

[4] The word texture is used to denote preferred orientation of crystallite faces parallel to the plane designated by the smallest integer Miller indices. For germanium the x-ray peaks are actually from the (111), (220), (311), and (400) reflections.

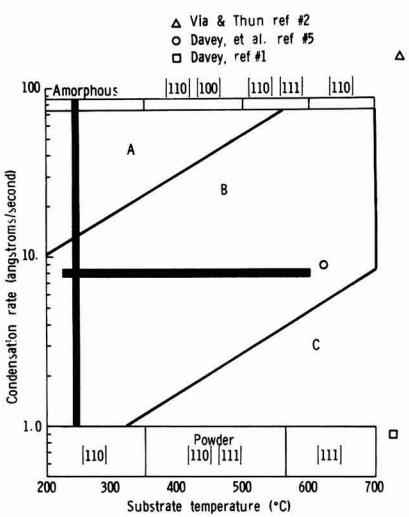

Fig. 4. Regions of special interest of the composite plot

strate surface, the surface mobility of atoms must be increased as the deposition rates increase, to keep successively arriving atoms from burying the preceding atoms which have not had time to form an appropriate lattice.

In general, the textures other than [110] reported by Davey, Via, and Thun are also confirmed by our investigation. The differences found probably result from different definitions of preferred orientation. For example, we actually classed as [100] the region designated by Davey as [111]. But if only the first three reflection planes were used for comparison, then we also would have obtained the [111] texture there. All condensation rates in the range 100-380 Å/sec in the substrate temperature range 250°-600°C caused the random powder orientation which probably results from the burying effect mentioned earlier. For substrate temperatures greater than 650°C and condensation rates of 10 Å/sec or less, the films are very granular. All of these films exhibit either the random powder orientation or a mixed orientation, probably because the evaporant atoms are not arriving fast enough to permit any orderly bonding arrangement.

Table I also contains values of R_{111}, R_{220}, R_{311}, and R_{400} calculated by the method outlined in Appendix A. In the left center portion of region B, values of R_{220} as high as 250 were obtained, indicating very strong [110] texture. For some specially selected rates and temperatures outside region B, [110] texture can also be obtained; but, in general, in regions near the indicated borders, the competition for growth results in a mixed texture.

The theory of nucleation on amorphous substrates is not well understood. Many and widely different theories and models have been proposed even when the experiments performed have been conducted on cleaved or ultraclean single-crystal substrates. For example, lattice constants of the parent crystal and the growth film were once expected to be within 15% for epitaxy to occur (6). A new concept, pseudomorphism, has been developed to explain the fact that oriented overgrowth has been observed for even greater differences in lattice constants. Such variables as substrate temperature and condensation rate are often of greater significance than the amount of lattice misfit (7, 8). The glass substrates used in our experiments, even though ultraclean, do not exhibit the ordered surface of a single-crystal substrate. Therefore, they do not lend themselves readily to conventional epitaxial theories.

The diamond structures of germanium can be considered as two interpenetrating face-centered cubic lattices. Because of the complicated covalent bonding of the diamond-type semiconductor structure, a rigorous treatment of the dependence of crystallographic formation on the substrate temperature is not given. However, a heuristic argument, following a development of Rhodin and Walton (9), is presented to offer a qualitative understanding of the changes in orientation with temperature and rate.

Rhodin and Walton considered the formation of a deposit of a face-centered cubic metal as a function of substrate temperature at a constant incident rate. At the low-temperature limit, the critical nucleus is a single atom, and the nucleation rate, I, can be expressed as

$$I_1 = R\left(\frac{R}{\nu N_0}\right)\exp\left[\frac{(2Q_{ad}-Q_D)}{kT}\right] \quad [1]$$

which is obtained from a general expression

$$I_n = R\left(\frac{R}{\nu N_0}\right)^n \exp\left[\frac{(n+1)Q_{ad}+E_n-Q_D}{kT}\right] \quad [2]$$

where n = number of atoms in the critical nucleus, E_n = dissociation energy of the critical nucleus ($E_1 = 0$), R = rate of incidence of vapor atoms, N_0 = density of adsorption sites, ν = a frequency term of the order of 10^{12}/sec, Q_{ad} = heat of adsorption of adsorbed atom, Q_D = activation energy for surface diffusion, k = Boltzmann constant, and T = absolute temperature.

At the low-temperature limit, the critical nucleus should be a single atom. Therefore, each time that a pair is formed it will usually grow, rather than decay into two single atoms. As the supersaturation is decreased, either by increasing substrate temperature or by decreasing incidence rate, a supersaturation point is reached where the probability of a pair decaying is equal to the probability of its growing. Below this point of supersaturation, a pair will be a critical nucleus until supersaturation is reached where the stable configuration formed by adding a single atom to the pair becomes unstable. Then the three-atom cluster becomes the stable nucleus.

As the substrate temperature is increased, a temperature is reached at which the pair is no longer stable (Eq. [2]). The next smallest cluster (three-atom) is one that has a minimum of two bonds per atom. One way of achieving a minimum of two bonds per atom is to have three atoms arranged in a triangle. The critical nucleus is the pair and the nucleation rate is

$$I_2 = R\left(\frac{R}{\nu N_0}\right)^2 \exp\left[\frac{(3Q_{ad}+E_2-Q_D)}{kT}\right] \quad [3]$$

where E_2 is the dissociation energy of the pair.

Another way of achieving a minimum of two bonds per atom is to have four atoms arranged in a square. The critical nucleus for this arrangement can be taken as three atoms in a capital L arrangement, and the nucleation rate is

$$I_3 = R\left(\frac{R}{\nu N_0}\right)^3 \exp\left[\frac{(4Q_{ad}+E_3-Q_D)}{kT}\right] \quad [4]$$

where E_3 is the dissociation energy of the three atoms in the critical nucleus.

The three-atom smallest stable cluster leads to an orientation in which the [111] plane is parallel to the substrate. The four-atom configuration leads to the [100] orientation. Therefore, Eq. [4] applies where the [100] is the first orientation to be observed, and Eq. [3] when the [111] orientation is first observed. Similarly, other orientations can also be observed. To obtain the temperature, T_1, at which the smallest stable cluster of one bond per atom changes to the two bond per atom (a triangular arrangement), one need only to equate Eq. [1] and [3] to obtain

$$T_1 = \frac{-(Q_{ad}+E_2)}{k\ln\left(\frac{R}{\nu N_0}\right)} \quad [5]$$

Likewise, the temperature, T_2, at which the smallest stable cluster of one bond per atom changes to the two bond per atom (a square arrangement), is obtained by equating Eq. [1] and [4]. This yields the following expression for T_2

$$T_2 = \frac{-(Q_{ad}+E_3/2)}{k\ln\left(\frac{R}{\nu N_0}\right)} \quad [6]$$

The preceding discussion, for the simple faced-center cubic metal, illustrates, at least for the initial stages of growth, that the type of orientation obtained for a given deposit is a function of substrate temperature. Since the nucleation rate is also dependent on the incidence rate of vapor atoms, the number of atoms in a critical nucleus is dependent on the condensation rate as well as the substrate temperature.

The preceding development would be more plausible if the complete films were formed as successive complete monolayers. The experimentally observed orientation rate and temperature dependence could then be

described by heterogeneous nucleation rate theory. However, monolayer formation does not seem to be the normal mode of growth for alkali halides and various metals previously studied (10). Since it is more likely that the germanium nuclei are experiencing three-dimensional growth, it therefore appears that a combination of heterogeneous and homogeneous nucleation is occurring.

Crystallite sizes.—When the size of the individual crystal is approximately 2000Å or less, one may use information obtained from diffractometer line broadening in estimating crystallite sizes. The extent of line broadening is given by the Scherrer formula

$$t = \frac{K\lambda}{(B_M^2 - B_S^2)^{1/2} \cos\theta} \qquad [10]$$

where B_M = width of diffraction line measured at half its maximum intensity, B_S = width from standard of crystallite size larger than about 2000Å, t = diameter of the crystal particle, K is a constant taken to be equal to 0.9, θ the Bragg angle, and λ is the wavelength of characteristic x-ray target material. All diffraction lines have a measurable breadth because of divergence of the incident beam and width of the x-ray source in diffractometers. The expression $B_M^2 - B_S^2$ assumes a Gaussian distribution of the counts and is essentially zero whenever the particle size exceeds approximately 2000Å. A standard half-width B_S was obtained for the XRD-6 unit by scanning the peaks from 40μ germanium powder samples. Six calibration samples of 40μ powder yielded an 8.8-min resolution width for the (111) peak and 11.6-min for the (220) peak.

Half widths for the (111) and (220) peaks were measured and are presented in Fig. 5 as a function of the substrate temperature. The data represented here covers deposition rates from 0.2 to 80 Å/sec and thicknesses from 2500 to 15,000Å. The data were grouped in temperature increments of 25°C, and the peak widths averaged within this temperature increment. Thus, each point represents approximately eight samples whose peak widths normally varied less than 2 min. The (111) and (220) crystallite size increases with temperature and, in agreement with Davey (5), the (220) crystallite sizes are larger than the (111) crystallites over the whole temperature range. Crystallite sizes calculated from the peak half-width data are also presented in Fig. 5. Some individual films from region B over the complete temperature range were also checked for crystallite size. It was found that the crystallite sizes of individual films followed the average data of Fig. 5 very closely. Thus, even though R_{220} peaks in the 250°-350°C range, the crystallite sizes are increasing functions of temperature. The [110] crystallite films in the 275°-280°C temperature range were also investigated for changes in crystallite size as a function of deposition rate. It was found that at a substrate temperature of 280°C when the condensation rate was increased from 1-8 Å/sec the [110] crystallites increased from 800 to 1200Å in average size.

Electrical properties.—In single-crystal semiconductor technology the most important parameters are resistivity, conductivity type, carrier mobility, carrier concentration, and lifetime of injected carriers. Because most single-crystal devices are minority carrier devices, the quantities mentioned above are those most pertinent to minority carrier devices. Vacuum-deposited semiconductor films presently produced on amorphous substrates are no more than polycrystalline films with large (>1000Å) diameter crystallites which may or may not exhibit a preferred crystallographic orientation. The most successful use of these semiconductor films has been in majority carrier devices. In polycrystalline films, the parameters mentioned are not always as meaningful as they are in single-crystal materials; however, they do form a basis of comparison and are widely used in thin-film research. The electrical parameters measured for these films are the conductivity type, the resistivity, and the Hall coefficient. All measurements were made at room temperature.

Lattice defects, grain boundaries, and other film imperfections found in polycrystalline films exhibit acceptor-type characteristics. Therefore, in these films the apparent doping level is shifted, in general, from source to film in the direction of higher p-values. All of the films deposited exhibited p-type conductivity, although the source material was n-type.[5]

Figure 6 shows the resistivity of the films *vs.* substrate temperature as measured with a four-point probe.[6] The data was also grouped in temperature increments and averaged. A few values of mobility are shown at key points in Fig. 6. Although the resistivity again increases slightly at temperatures above 400°C, the mobility of crystallite sizes continue to increase. Rectifying grain boundaries in polycrystalline material will cause fluctuation in the electric field intensity. Therefore, the resistivity will register higher values than in similarly doped single-crystal material.

[5] The film conductivity type was checked by a thermoelectric probe and by observing the sign of the Hall voltage. The film conductivity type was checked immediately after the films were removed from the vacuum chamber.

[6] For films less than 10^5Å thick $\rho = 4.532 \times 10^{-8}\ V/I\ W$, where V is in volts, I in amperes, and W in angstroms.

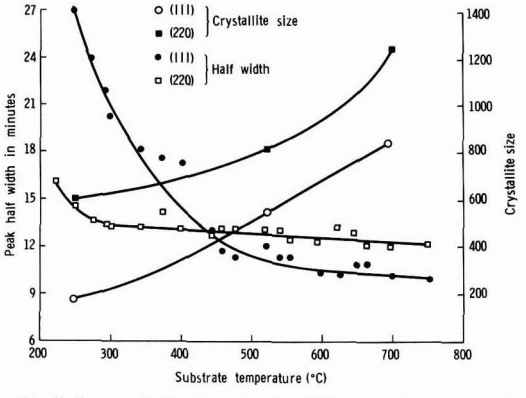

Fig. 5. Average half widths for the (111) and (220) peaks and crystallite size *vs.* substrate temperature.

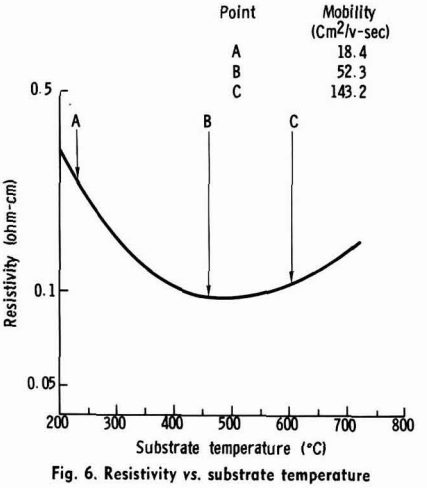

Fig. 6. Resistivity *vs.* substrate temperature

Conclusions

For large variations in condensation rate, different preferred orientations can be obtained for a constant substrate temperature. This fact, combined with the well-known variations in textural properties with changes of substrate temperature, suggests that film structure is a function of both the substrate temperature and the deposition rate. The [110] textural characteristics produced at low-substrate temperatures and low-condensation rates can be extended through higher substrate temperatures if the condensation rate is increased. Thus, since the results of Davey and Via and Thun fall at opposite ends of a continuous substrate temperature condensation rate region they are basically in agreement rather than contradictory.

From x-ray diffraction line broadening, the crystallite sizes increase with substrate temperature. The crystallites of [110] texture are always larger than the [111] oriented crystallites. The ratio R_{220}, which gives a quantitative measure of the degree of preferred orientation, peaks in the 250°-350°C, 2-7 Å/sec portion of region B. Crystallite sizes were also observed to increase with condensation rate. A 50% increase in crystallite size could be observed by increasing the temperature or by increasing the condensation rate across the ranges of region B.

The resistivity and Hall mobility of the films are dependent on the substrate temperature during deposition. The resistivity varies down to a minimum of approximately 0.1 ohm-cm near a substrate temperature of 500°C. The Hall mobility increases with substrate temperature. Values from 1 to 150 cm^2/sec were obtained. The resistivity values seem to depend on the number of crystallites oriented, since they pass through a minimum soon after the degree of preferred orientation peaks. The mobility continues to increase and therefore must depend on the average crystallite size.

Manuscript received May 10, 1965; revised manuscript received Aug. 29, 1966. This paper was presented at the Toronto Meeting, May 3-7, 1964. This work was supported by the United States Atomic Energy Commission.

Any discussion of this paper will appear in a Discussion Section to be published in the December 1967 JOURNAL.

REFERENCES

1. John E. Davey, *J. Appl. Phys.*, **32**, 877 (1961).
2. G. C. Via and R. E. Thun, *8th Nat. Vacuum Symp. Trans.*, October 1961, p. 950.
3. B. W. Sloope and C. O. Tiller, *10th Nat. Vacuum Symp. Trans.*, October 1963, p. 339.
4. E. Krikorian and R. J. Sneed, *10th Nat. Vacuum Symp. Trans.*, October 1963, p. 368.
5. J. E. Davey, R. J. Tiernan, T. Pankey, and M. D. Montgomery, *Solid-State Electron*, **6**, 205 (May-June 1963).
6. F. L. Frank and J. H. van der Merwe, *Proc. Roy. Soc.*, **A198**, 205 (1949).
7. S. A. Semiletov, *Kristallograiya*, **I**, No. 5, 542 (1956).
8. G. A. Bassett, J. W. Menter, and D. W. Pashley, in "Structure and Properties of Thin Films," Neugebauer, Editor, p. 11, John Wiley and Sons, New York (1959).
9. T. N. Rhodin and Derek Walton, "Metal Surfaces," Proc. ASM Meeting, October 27, 28, 1962, pp. 259-286.
10. D. W. Pashley, "Thin Films," p. 62, Amer. Soc. for Metals, Metals Park, Ohio (1964).

APPENDIX A

Determination of Preferred Orientation

A standard definition of what is meant by "preferred orientation" of polycrystalline films does not exist. The following definition was developed and used in this paper. A ratio that provides a quantitative measure of the relative amount of preferred orientation is defined as follows

$$R_{ijk} = \frac{h_{ijk}{}^{s}}{h_{111}{}^{s}} \frac{h_{111}{}^{Ps}}{h_{ijk}{}^{Ps}}$$

where $h_{ijk}{}^{s}$ = height of (ijk) plane reflection peak, above noise, for sample being measured; $h_{ijk}{}^{Ps}$ = height of (ijk) plane reflection peak, above noise, for powder standard (for germanium $h_{111}{}^{Ps} = 1$, $h_{220}{}^{Ps} = 0.57$, $h_{311}{}^{Ps} = 0.39$, $h_{400}{}^{Ps} = 0.07$); $h_{111}{}^{s}$ = height of (111) plane reflection peak, above noise, for sample being measured; and $h_{111}{}^{Ps}$ = height of (111) plane reflection peak, above noise, for powder standard.

Thus, for example, we have

$$R_{220} = \frac{h_{220}{}^{s}}{h_{111}{}^{s}} \cdot \frac{h_{111}{}^{Ps}}{h_{220}{}^{Ps}}$$

and

$$R_{400} = \frac{h_{400}{}^{s}}{h_{111}{}^{s}} \cdot \frac{h_{111}{}^{Ps}}{h_{400}{}^{Ps}}$$

It is apparent then that if

$$R_{220} = 1$$

then the height of the (220) plane reflection peak in the sample and the height of the (111) reflection peak in the sample are in the same ratio as these two peaks in the powder standard. However, if

$$R_{220} > 1$$

then the ratio of the height of the (220) plane reflection peak to that of the (111) plane reflection peak for the sample is larger than the corresponding ratio for the powder standard. Thus we have preferred orientation of (220) over the (111) in the sample.

Similarly, if

$$R_{220} < 1$$

then the (111) is preferred over the (220).

It is apparent that all the ratios are normalized to the (111) plane. Therefore, if we have $R_{400} > R_{220}$ then the (400) plane is preferred over the (220) plane.

If a particular plane exhibited a relative ratio of at least one greater than the next highest ratio, the sample was considered to exhibit preferred orientation in that direction. If no more than three of the peaks exhibited ratios within one of each other, the preferred orientation of the sample was considered mixed between the two highest ratios; and if all four ratios were within one of each other, the sample was considered to exhibit the random powder orientation. The above criterion can be used for all evaluations except those in which the (111) reflections are predominant. In these cases, all ratios are one or less; therefore the criterion becomes one-half below rather than one above: *i.e.*, the (111) direction is preferred if $R_{111} = 1$ and all other R_{ijk}'s are below one-half; mixed orientation between the two highest reflections is obtained if no more than three of the peaks exhibit ratios within one-half of each other; and if all four ratios were within one-half of each other, the sample was considered to exhibit the random powder orientation. If no peaks were observed, the sample was considered to be amorphous. The notation used throughout this paper is as follows: [111] =preferred orientation or texture; $M\begin{pmatrix}111\\110\end{pmatrix}$ = mixed orientation with $R_{111} > R_{220}$; and P[111] = powder orientation with $R_{111} >$ the other R_{ijk}.

Preparation of Epitaxial $Ga_xIn_{1-x}As$

R. W. Conrad, P. L. Hoyt, and D. D. Martin

Texas Instruments Incorporated, Dallas, Texas

ABSTRACT

Single-crystal, epitaxial $Ga_xIn_{1-x}As$ alloys have been prepared on (100), semi-insulating GaAs substrates, using an open-tube, vapor phase deposition system. High-purity elemental gallium, indium, and arsenic were used as source materials. Severe distortion of substrate and deposit was observed when thin substrates (less than *ca.* 11 mils) were used. This was attributed to the large lattice mismatch between deposit and substrate. The electron Hall mobility showed a pronounced minimum for alloys in the middle of the composition range, in agreement with earlier results.

In contrast to the $GaAs_xP_{1-x}$ alloy system, relatively few studies of the preparation and properties of $Ga_xIn_{1-x}As$ alloys have been reported. Abrahams *et al.* (1) prepared polycrystalline $Ga_xIn_{1-x}As$ alloys by gradient freeze and zone-leveling techniques. The variations of lattice thermal conductivity, electron mobility, and band gap were determined as a function of alloy composition. Woolley *et al.* (2) apparently prepared more homogeneous polycrystalline alloys by directional freezing. The variation of energy gap with composition was found to be linear up to about 80 mole % GaAs. At higher GaAs contents, a more rapid increase in energy gap was observed. Hall measurements of these alloys gave mobilities lower than obtained by Abrahams *et al.* when single-carrier treatment of the data was used. This was attributed to mixed conduction. Homogeneous polycrystalline alloys were recently prepared by Hockings *et al.* (3) by zone-leveling. Thermal conductivity, Seebeck coefficient, and electrical resistivity were measured as functions of temperature, impurity concentration, and alloy composition. Electron mobilities were reported for several samples with $x = 0.3$ and 0.7. However, these samples were very highly doped with selenium (from 7×10^{17} to $4 \times 10^{18}/cm^3$). Sirrine (4) briefly described the nonseeded growth of several single crystals of $Ga_xIn_{1-x}As$ using halogen vapor transport in a closed system. Minden (5) reported on the preparation of single-crystal $Ga_xIn_{1-x}As$ alloys, both unseeded by a closed tube method, and epitaxial on GaAs substrates using an open-tube system. Minden's open-tube system employed sources of elemental arsenic and gallium-indium solutions. Considerable fractionation of the gallium-indium source occurred, making control of composition difficult. Electrical properties were not reported.

The present investigation further deals with the open-tube preparation and properties of epitaxial $Ga_xIn_{1-x}As$ alloys on GaAs substrates. Instead of mixed gallium-indium solutions as a source material, separate reservoirs of gallium and indium are used.

Experimental

Materials preparation.—Initially, a deposition system employing separate reservoirs of crushed GaAs and InAs was tried. Transport of the gallium- and indium-halides and introduction of arsenic were accomplished by passing $AsCl_3/H_2$ mixtures over the heated source materials. Control of alloy composition in this system however was not straightforward in that InAs and alloys with greater than about 50 mole % InAs were difficult to prepare. For this reason and for reasons of economy, flexibility, and purity, a different type of system was devised.

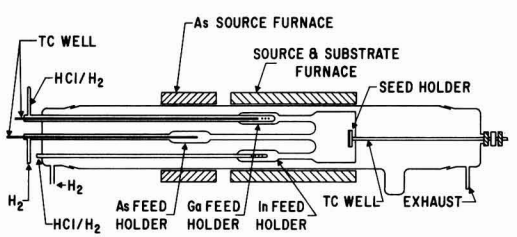

Fig. 1. Open-tube vapor deposition system for epitaxial $Ga_xIn_{1-x}As$ alloy preparation.

The open-tube deposition system used in this work is shown schematically in Fig. 1, and is constructed of fused quartz. Purified H_2 was passed over heated elemental arsenic[1] to transport arsenic vapor to the deposition zone. Mixtures of purified H_2 and HCl (prepared by H_2 reduction of $AsCl_3$) were passed through the heated gallium[1] and indium[1] reservoirs to transport the volatile gallium and indium chlorides to the deposition zone. (The concentration of HCl in the gas mixture is fixed at about 6 v/o by the vapor pressure of $AsCl_3$, which is maintained at 25°C.) The compositions of the deposited alloys were primarily controlled by the relative flow rates of the gas mixture through the gallium and indium reservoirs. These could be varied continuously from 0 to about 70 cc/min. An additional flow of H_2 of about 30 cc/min was introduced into the outer reactor tube to prevent back-diffusion and to aid in sweeping out the reaction products.

A two-zone resistance furnace was used to provide temperature control of the arsenic, gallium, indium, and substrate. One zone controlled the arsenic temperature (typically 440°C). The second zone controlled the gallium and indium reservoirs simultaneously (at 865°-870°C) since they are side-by-side. Control of the substrate temperature (745°-750°C) was accomplished by placing the substrate on a movable holder and positioning it at the proper location in the temperature gradient at the end of the gallium-indium source zone. The substrate had to be held in a vertical position because of the steepness of the temperature gradient. With care, all temperatures were maintained at ± 2°C.

Substrates used in this investigation were (100)-oriented wafers cut (30 mils thick) from chromium-doped GaAs pulled crystals. Room temperature resistivities of such crystals were about 10^8 ohm-cm. The wafers were chemically polished using the method of Reisman and Rohr (6), and etched in 5:1:1 $H_2SO_4:H_2O_2:H_2O$ immediately prior to use.

Materials evaluation.—The alloy layers were shown to be epitaxial by x-ray diffraction. Epitaxial layer thicknesses were determined by bevel-lap and stain techniques. A good stain for delineating the junction in GaAs and GaAs-rich alloys was the Fe-HNO_3-H_2O stain (7). For InAs and InAs-rich alloys, a brief treatment with 1.5% NaOCl in H_2O provided sharp contrast between substrate and layer (8).

Compositions were determined by x-ray diffraction techniques, assuming a linear variation of lattice

[1] 99.9999% pure.

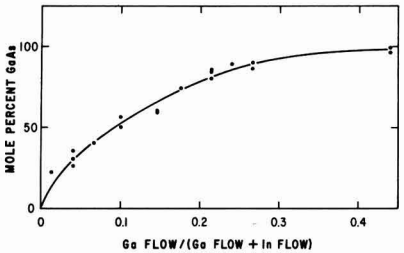

Fig. 2. Variation of composition of epitaxial $Ga_xIn_{1-x}As$ alloys with change in fractional $HCl-H_2$ mixture flow through gallium reservoir.

constant with alloy composition. The sharpness of the alloy diffraction peaks also provided a qualitative measure of deposit homogeneity.

Hall and resistivity measurements were made on ultrasonically cut six-armed specimens with indium solder contacts, using either a-c or d-c techniques, depending on whether the sample resistance was low or high.

Results and Discussion

Physical properties.—Deposition rates obtained with this system ranged from 20 to 35 μ/hr, essentially independent of substrate temperature over the range 720°-760°C, and also independent of alloy composition. These results are in contrast with the observation (5) that InAs deposition occurs efficiently only at temperatures below 700°C.

Alloy composition could be varied in a straightforward fashion by changing flow rates over the gallium and indium sources. This relation is shown in Fig. 2. The abscissa is the ratio of the flow rate of the $HCl-H_2$ mixture over the gallium source to the total flow rate of the $HCl-H_2$ mixture over both gallium and indium sources. This is similar to the variation of alloy composition with source composition found by Minden (5). In contrast, however, we have experienced no difficulty in fabricating alloys with less than 10 mole % InAs. The relationship shown in Fig. 2 is unusual in view of the fact that deposition rate is essentially independent of alloy composition even though GaAs appears to deposit preferentially. We have no explanation for this at present.

The homogeneity of alloys produced in the deposition system using compound source materials has been described previously (9). Material produced in the present system was similarly examined using reflectivity and absorption methods and found to be homogeneous within the limits of resolution of the analytical methods (about ± 3% absolute).

Often the alloy layers had macroscopically smooth, shiny surfaces and sharp substrate-deposit interfaces. Occasionally, for reasons not yet clear, physical defects of the "hillock" type were obtained in the more GaAs-rich alloys. These generally were protrusions with apparently (100) facets. For InAs-rich alloys, defects took the form of short line imperfections oriented along <110> directions. These line imperfections appear to be (100) analogs of the (111) stacking faults in epitaxial GaAs described by Gabor (10).

The hillock imperfections appeared to be connected with substrate quality, since some substrate crystals yielded higher hillock densities than others. The line imperfections, however, did not appear to be closely connected with the substrates. Since such line imperfections were only observed in InAs-rich alloys, they may be related to the large lattice mismatch (InAs, 6.06Å; GaAs, 5.65Å).

When alloys were deposited on very thin GaAs substrates (less than about 11 mils thick), the samples were severely plastically distorted. Figure 3 shows a

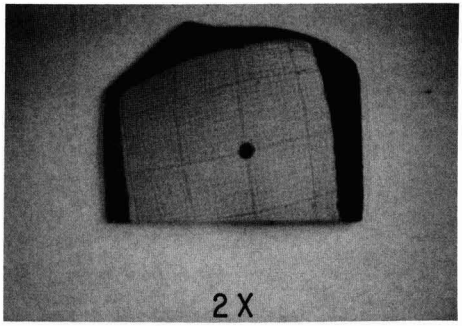

Fig. 3. Distorted epitaxial $Ga_{0.75}In_{0.25}As$ sample obtained by deposition on a 10 mil thick (100) GaAs substrate.

39μ thick layer of $Ga_{0.75}In_{0.25}As$ on a substrate 10 mils thick. (The sample was photographed through a hole in a piece of graph paper to illustrate the curvature.) Surface contour measurements showed this sample to be symmetrically curved about its center point with a radius of curvature of 12 cm. A detailed study of this phenomenon was not performed. However, we did ascertain that (*i*) the effect was caused by alloy deposition since heat-treatment of a thin substrate under conditions similar to those used during a deposition did not produce bending, and (*ii*) qualitatively the effect appears to become more severe as the InAs content of the alloy is increased. Since the thermal expansion coefficients of InAs and GaAs are not very different over the temperature range 50°-700°C (11), the distortion is attributed to the considerable mismatch of lattice constants.

Electrical properties.—The initial investigations of the electrical properties of the $Ga_xIn_{1-x}As$ system were at the end points of the alloy range, *i.e.*, GaAs and InAs. Table I shows the electrical properties of the better deposits. Next, alloys of various compositions were prepared and evaluated. Generally, deposits were n-type with excess carrier concentrations in the 10^{15}-10^{16} cm^{-3} range. However, we observed that use of low arsenic reservoir temperatures (<*ca.*400°C) invariably produced p-type, high-resistivity layers (10^4-10^5 ohm-cm at 300°K) for GaAs and alloys with less than about 70 mole % InAs. The resistivities of such deposits were essentially independent of alloy composition. The nature of the impurity or defect causing such behavior is not known; however, the invariance of resistivity with composition implies an acceptor level which stays approximately a fixed distance from the valence band through the alloy range. This has been partially confirmed by conductivity measurements as a function of temperature for several such samples. The activation energy of con-

Table I. Hall and resistivity data on InAs and GaAs layers on (100) GaAs substrates

Sample No.	Layer thickness, μ	300°K Mobility, cm^2/v-sec	300°K Excess carrier conc, cm^{-3}	77°K Mobility, cm^2/v-sec	77°K Excess carrier conc, cm^{-3}
		InAs			
−128	24	2.1×10^4	1.1×10^{16}	5.9×10^4	7.6×10^{15}
−124	16	2.0×10^4	1.7×10^{16}	4.8×10^4	1.2×10^{16}
−52	14	1.9×10^4	1.5×10^{16}	5.3×10^4	9.8×10^{15}
−50	20	2.3×10^4	8.7×10^{15}	7.0×10^4	6.1×10^{15}
66-280	28	1.7×10^4	4.2×10^{15}	5.9×10^4	2.5×10^{15}
		GaAs			
15	12	6.6×10^3	5.5×10^{15}	2.6×10^4	4.4×10^{15}
114	9	6.4×10^3	1.2×10^{16}	2.3×10^4	8.9×10^{15}
94	12	6.6×10^3	2.5×10^{15}	3.2×10^4	1.8×10^{15}
129	19	7.0×10^3	1.4×10^{15}	2.6×10^4	1.2×10^{15}
133	16	8.0×10^3	8.3×10^{14}	3.5×10^4	7.5×10^{14}

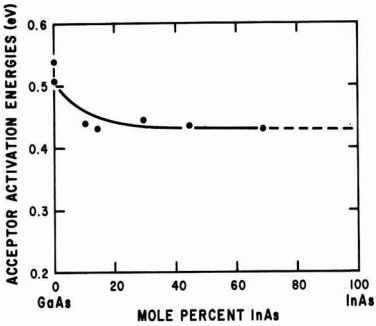

Fig. 4. Activation energy in electron volts for conduction of unknown acceptor impurity or defect as a function of $Ga_xIn_{1-x}As$ alloy composition.

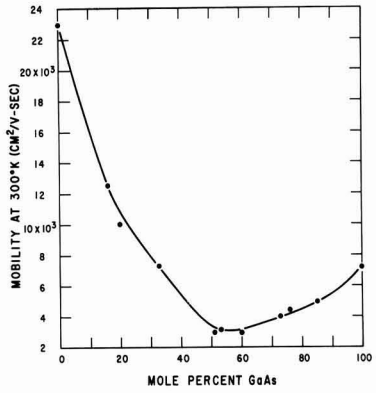

Fig. 5. Electron Hall mobilities at 300°K for epitaxial $Ga_xIn_{1-x}As$ alloys on (100) GaAs substrates.

duction (ΔE) as a function of alloy composition is shown in Fig. 4. The ΔE values shown are uncorrected for variations of mobility and densities of states with temperature. However, in all cases the variation of the logarithm of conductivity with reciprocal absolute temperature was linear over a large temperature range (from 100° to 300°K). The energy level of the unknown acceptor appears to become deeper than $E_g/2$ at about 70 mole % InAs. This is consistent with our observation that p-type high resistivity alloys with more than 70 mole % InAs could not be obtained. The electrical properties (at 300°K) of alloys with more than 70 mole % InAs prepared at excessively low arsenic temperatures (less than about 400°C) were typically $<$ about 10^{15} electrons/cm^3 with very low mobilities ($<$ about 2000 cm^2/volt-sec). This is consistent with an acceptor deeper than $E_g/2$.

The reason for the change from p-type high resistivity to n-type, low resistivity with increasing arsenic temperature is not clear. Three likely explanations of such behavior however are (*i*) a strong dependence of an impurity vapor-solid segregation coefficient on arsenic pressure, (*ii*) increased shallow donor impurity contamination from the arsenic at the higher temperatures, (*iii*) a physical defect whose concentration is dependent on the arsenic pressure. Unfortunately very little is known about the influences of items (*i*) and (*iii*) on epitaxial film growth, and we cannot definitely eliminate the possibility of (*ii*).

The variation of electron Hall mobility (at 300°K) of our best samples with alloy composition is shown in Fig. 5. (The excess electron concentrations of these samples, determined from Hall measurements, are all in the range 1-8 $\times$ 10^{15}/cm^3, except for the GaAs sample, which was 8 $\times$ 10^{14}/cm^3.) These mobilities are similar to those observed by Abrahams *et al.* (1) for polycrystalline alloys with higher excess electron concentrations. Invariably, the mobilities of the alloys decreased with decreasing temperature, in contrast to the temperature variation of mobility of GaAs and InAs. This implies scattering from a charged center of some type. Since the mobilities of the GaAs and InAs samples prepared in this system compare favorably with published values, we suspect that alloy formation *per se* may be responsible in part for the low mobilities. However, alloy scattering of the kind described by Brooks (12) does not appear to be applicable in this case, since a negative temperature dependence of mobility is predicted.

Conclusion

An open-tube system employing separate reservoirs of gallium, indium, and arsenic is a satisfactory method for fabricating epitaxial layers of $Ga_xIn_{1-x}As$ alloys on GaAs substrates with good physical properties. There appears to be considerable strain associated with lattice mismatch. However, InAs, for which lattice mismatch is greatest, can be prepared with electrical properties comparable to bulk material.

The electrical properties (primarily electron mobility) of the alloys prepared in such a system are not improved over polycrystalline alloys prepared by gradient freeze and zone-leveling techniques. However, the versatility of the open-tube system permits fabrication of material suitable for device fabrication and investigation.

Acknowledgments

The authors wish to thank L. G. Bailey for his informative discussions and W. Neff and M. Jeffcoat for assistance in materials synthesis.

This work was supported by the Electronics Technology Division of the Air Force Avionics Laboratory under Contract AF 33(615)-1272.

Manuscript received July 15, 1966; revised manuscript received Sept. 20, 1966.

Any discussion of this paper will appear in a Discussion Section to be published in the December 1967 JOURNAL.

REFERENCES

1. M. S. Abrahams, R. Braunstein, and F. D. Rosi, *J. Phys. Chem. Solids*, **10**, 204 (1959).
2. J. C. Woolley, C. M. Gillett, and J. A. Evans, *Proc. Phys. Soc. London*, **77**, 700 (1961).
3. E. F. Hockings, I. Kudman, T. E. Seidel, C. M. Schmelz, and E. F. Steigmeier, *J. Appl. Phys.*, **37**, 2879 (1966).
4. R. Sirrine, *This Journal*, **111**, 750 (1964).
5. H. T. Minden, *ibid.*, **112**, 300 (1965).
6. A. Reisman and R. Rohr, *ibid.*, **113**, 296 (1966).
7. P. L. Hoyt and R. W. Haisty, *ibid.*, **113**, 296 (1966).
8. G. R. Cronin, R. W. Conrad, and S. R. Borrello, *This Journal*, **113**, 1336 (1966).
9. R. W. Conrad, C. E. Jones, and E. W. Williams, *ibid.*, **113**, 287 (1966).
10. T. Gabor, *ibid.*, **111**, 817 (1964).
11. L. Bernstein and R. J. Beals, *J. Appl. Phys.*, **32**, 122 (1961).
12. H. Brooks, Unpublished work.

Transport Processes in the Thermal Growth of Metal and Semiconductor Oxide Films

F. C. Collins and T. Nakayama

Polytechnic Institute of Brooklyn, Brooklyn, New York

ABSTRACT

The transport problems involved in the thermal growth of thick oxide films are reexamined on the basis of a semiconductor model of the oxide film, in which the electron and hole concentrations are assumed to be in local thermodynamic equilibrium. The coupled transports of ions and of electrons or holes required in the Wagner electrochemical model of film growth are related separately to the electrostatic and Fermi potential gradients in the oxide film. The electrostatic potential difference across the oxide film is shown to be fixed by the free energy of formation of the oxide and by the transport coefficients of the several migrating species. The effect of externally applied fields on the thermal growth process is discussed. Anomalies pointed out by Raleigh are shown not to be inconsistent with the electrochemical model of film growth. The question of local electroneutrality in the film relative to the parabolic growth law is also examined.

Interest in the theoretical aspects of the thermal growth of oxide films has been greatly stimulated by recent experimental studies particularly by the intensive investigations of the growth of amorphous silicon dioxide films on single crystals of silicon (1). The work of Jorgensen (2) in this connection is of special interest particularly his finding that the thermal growth rate can be altered by the application of an external electric potential. This indicates that film growth involves ionic migration in agreement with the electrochemical model of film growth of Wagner (3), Mott (4), and Cabrera and Mott (5).

The electrochemical model assumes the transport of charged species, rather than neutral molecules, across the growing oxide film with counterflow of electrons and holes to maintain electrical neutrality. Whether the growth of a particular oxide film is supported by the transport of a metal cation or an oxygen anion may be established by a marker experiment. In the case of most metal oxides, the metal cation is the dominant species transported. However several investigators (6) have found that an oxygen anion is the species transported in the case of the growth of silicon dioxide films.

In the interests of an explicit presentation, the electrochemical model will be discussed within the framework of the case of the silicon dioxide thermal growth, which is selected because of the relatively large amount of published experimental data for this system. The general concepts outlined may be extended to other thermal oxides without difficulty. The possible species transported and the corresponding electrode reactions at the opposite interfaces of the silicon dioxide film are shown in Fig. 1. The nonelectrochemical case of the diffusion of neutral oxygen molecules which react at the silicon-silicon dioxide surface is also illustrated. It will be treated later in the discussion of alternatives to the electrochemical model.

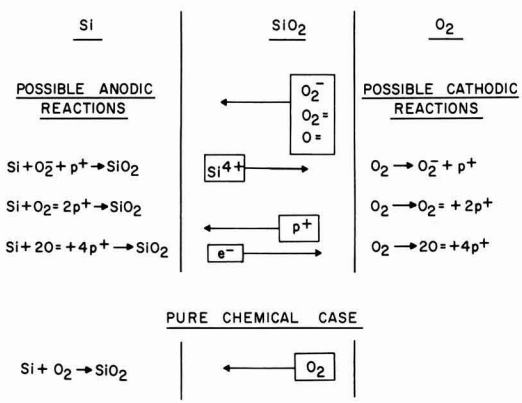

Fig. 1. Electrochemical model of the thermal growth of silicon dioxide films in a pure oxygen ambient.

It is clear that the transport of an ionic species must be balanced by the transport of an equivalent number of electrons or holes in order to prevent build-up of charge on the opposite sides of the film. However the counterflows of ions and of electrons and holes do not necessarily bring about local electroneutrality in the oxide film.

In most ionic crystals, first-order electroneutrality is provided for in that the current-carrying ionic defects are generally present as oppositely charged pairs. Thus in SiO_2, anionic conduction could occur by anti-Frenkel defects (equal concentrations of oxygen interstitials and vacancies) or by oxygen anionic defects compensated by cations of some impurity. Electroneutrality then requires that the electronic carrier concentration compensate the difference in the concentration of the two kinds of ionic defects at every point in the oxide film. This condition will not necessarily be established by balance of the ionic and electronic currents.

Fromhold (7) has shown that the generally observed parabolic law of growth requires local neutrality throughout the bulk of the film. Thus the transport processes must be subject to some additional constraint in order to provide local electroneutrality.

Raleigh (8) has recently cast some doubt on the interpretation of the Jorgensen experiments in terms of the simple variation of the drift rate of diffusing ions under the externally applied potential. He points out that the application of an external field in the direction which accelerates growth will retard the flux of holes and electrons while promoting the migration of ions. He explains the Jorgensen results on the basis of an electrolysis superposed on the normal diffusion-controlled oxide film growth.

The present paper attempts the resolution of these questions on the basis of the electrochemical model of film growth.

Semiconductor Model of Oxide Films

The substrate in oxide film thermal growth problems may be generally treated as metallic. This is true even in the case of semiconductor substrates such as

silicon, which will be degenerate at the temperatures encountered in thermal growth. On the other hand, even those oxide films which have wide band gaps and are insulators at room temperature will behave as semiconductors at the temperatures at which thermal growth occurs. For example, amorphous intrinsic silicon dioxide with an optical absorption edge of about 1900Å has a carrier density at 1000°C at least equal to that of an intrinsic semiconductor with a band gap of 1.5 ev at room temperature.

It is to be expected that the electron and hole densities in oxide films undergoing thermal growth will correspond to conditions of thermal equilibrium except for some slight perturbation due to the small flux of holes and electrons involved in the growth process. The presence of ionic species and structural disorders may cause the oxide film to behave as an extrinsic semiconductor, apart from the question of the effect of the space charge of ionized impurities on local electron and hole densities. However in any case the electron and hole densities are fixed by thermodynamic considerations other than satisfaction of an electroneutrality condition. The semiconductor model of the oxide film requires that the Fermi or electrochemical potential for holes and electrons be explicitly distinguished from the electrostatic field acting on all charged species. This distinction appears not to have been brought out in previous treatments. The transport of holes and electrons is most conveniently formulated in terms of the gradient of the Fermi potential, but the latter is largely irrelevant to the transport of ions which drift under the gradient of the electrostatic potential. In the next section of this paper, it will be shown that the requirement of conservation of charge in the transport process leads to a formulation of the Fermi potential difference across the film in terms of the free energy change involved in the oxidation reaction and of the transport coefficients. In the present section, the principles of transport of holes and electrons will be reviewed for later reference.

The equilibrium concentrations of holes p and that of electrons n in a semiconductor are given by the well-known equations

$$p = n_i e^{q(\phi - V)/kT} \quad [1]$$

$$n = n_i e^{q(V - \phi)/kT} \quad [2]$$

where n_i is the concentration of electrons in the intrinsic material, ϕ is the Fermi potential, V is the electrostatic potential, and the other symbols have their usual significance. The fluxes of holes J_P and that of electrons J_n are given by the generalized Fick's first laws

$$J_p = -\frac{kT}{q}\mu_p \frac{dp}{dx} - \mu_p p \frac{dV}{dx} \quad [3]$$

$$J_n = -\frac{kT}{q}\mu_n \frac{dn}{dx} + \mu_n n \frac{dV}{dx} \quad [4]$$

where μ_p and μ_n are the respective mobilities, x is the position coordinate in the film, and Einstein's relation $D = \mu q/kT$ has been used. On differentiating Eq. [1] and [2] and inserting the results into Eq. [3] and [4] we obtain

$$J_p = -\mu_p p \frac{d\phi}{dx} \quad [5]$$

$$J_n = \mu_n n \frac{d\phi}{dx} \quad [6]$$

where the fluxes are formally proportional to the gradient of the Fermi potential. The total electronic current is given as usual by

$$I = q(J_p - J_n) = -q(\mu_p p + \mu_n n)\frac{d\phi}{dx} \quad [7]$$

$$= -\sigma_e \frac{d\phi}{dx}$$

where σ_e is the electronic conductivity as ordinarily defined.

The flux J_i of the i_{th} ionic species across the growing oxide film is given by

$$J_i = -D_i \frac{dc_i}{dx} - D_i \frac{\alpha_i q}{kT} c_i \frac{dV}{dx} \quad [8]$$

where D_i is the diffusion coefficient of the i^{th} species, c_i its concentration, and α_i the number of electronic charges on it, taken with due regard to sign. A steady value of electrostatic potential across the film requires that

$$I + \sum_i \alpha_i q J_i = 0 \quad [9]$$

The growth rate of the film is proportional to the sum of the flux terms where all migrating species are assumed to contribute to growth and may be represented as

$$\frac{dX}{dt} = S \sum_i |\alpha_i| J_i \quad [10]$$

Here, if J_i is given in terms of number flux

$$S = \frac{M/\beta}{\rho N_o} \quad [11]$$

where M is the molecular weight of the oxide, β is twice the number of oxide ions in the molecular formula of the oxide, ρ is the density, and N_o is Avogadro's number.

The growth rate is then related to the electronic current by

$$\frac{dX}{dt} = -\frac{SI}{q} \quad [12]$$

The Fermi Potential Profile

The further development of the problem requires the calculation of the Fermi potential as a function of position within the oxide film. The standard cell potential E^o corresponding to the oxidation process is given by the thermodynamic equation

$$E^o = -\Delta G^o/\alpha q \quad [13]$$

where ΔG^o is the free energy change of the redox reaction expressed in electron-volts and α is the number of electrons involved in the oxidation. The Fermi potential difference $\Delta\phi$ across the film at infinite electronic impedance is given by

$$\Delta\phi = \phi(X) - \phi(O) = E^o \quad [14]$$

where the metal-oxide interface has been selected as the origin of the coordinate system, and X is the outer surface of the film. Under the condition of infinite electronic impedance, there is no electrostatic potential difference across the film, the charges balancing separately in each of the electrical double layers at the surfaces of the oxide film.

If electric current is transported across the film by electron and hole conduction at a finite rate, the Fermi potential is lowered accordingly and is given by

$$\Delta\phi = E^o + \Delta V \quad [15]$$

In the limit of very small electronic impedance, $\Delta\phi$ approaches zero[1] and

$$\Delta V = -E^o \quad [16]$$

This is analogous to the well-known situation in a semiconductor p-n junction.

In the further development of this discussion, the mathematical handling of the general case of several

[1] Cabrera and Mott (5) present a detailed discussion of the background of Eq. [14] and [16].

ionic diffusing species with arbitrary charges and the transport of both holes and electrons becomes unwieldy. We shall therefore restrict the present treatment to that of the migration of a univalent anion in a p-type oxide. The treatment may be extended to other specific situations by analogy.

We shall also simplify matters by assuming electroneutrality throughout the oxide film. This could be brought about by complete compensation of the anions by immobile cationic defects. The maximum deviations from electroneutrality consistent with a parabolic law of growth will be presented in a subsequent section of this paper, together with an exploration of the considerations tending to produce electroneutrality.

Let us first examine the situation with respect to electronic transport. By combining Eq. [1] and [5] and making use of $V(x) = x\ \Delta V/X$, where the latter is a consequence of electroneutrality, we obtain

$$J_p e^{qx\Delta V/kTX} dx = \mu_p n_i\, e^{q\phi/kT} d\phi \qquad [17]$$

which may be integrated between the points $x = 0$ and $x = x$ to yield

$$J_p = \frac{\Delta V}{X}\,\mu_p n_i \frac{(e^{q\phi_o/kT} - e^{q\phi/kT})}{(e^{qx\Delta V/kTX} - 1)} \qquad [18]$$

where ϕ_o is the Fermi potential at the point $x = 0$. Because of the large excess of electrons in the metal compared to the semiconductor oxide film and its adsorbed oxygen layer it may be presumed that the Fermi level in the semiconductor is pinned to that of the metal at the metal interface. Equation [18] then gives the profile of the Fermi potential $\phi(x)$ in terms of the electrostatic potential difference across the oxide film and the hole concentration

$$p(O) = n_i e^{q\phi_o/kT} \qquad [19]$$

in the semiconductor at its interface with the metal.

Equation [8] for the flux J of univalent anions may be put into the form

$$J e^{-qx\Delta V/kTX} = -D\frac{d}{dx}\,(ce^{-qx\Delta V/kTX}) \qquad [20]$$

which may be integrated to yield[2]

$$J = \frac{Dq\Delta V}{kTX}\,\frac{[c(O)\ e^{q\Delta V/kT} - c(X)]}{(e^{q\Delta V/kT} - 1)} \qquad [21]$$

For the special case of holes and univalent anions, Eq. [9] simplifies to

$$J_p = J \qquad [22]$$

If now Eq. [18] is evaluated at the point $x = X$ and combined with Eq. [19], [21], and [22], we obtain

$$\frac{Dq}{kT}\,[c(O)\ e^{q\Delta V/kT} - c(X)] = \mu_p p\ (O)\ (1 - e^{q\Delta\phi/kT}) \qquad [23]$$

The Fermi level difference $\Delta\phi$ may be obtained explicitly by introducing Eq. [15]

$$e^{q\Delta\phi/kT} = \frac{\mu_p p\ (O) + \dfrac{Dc}{kT}\,c(X)}{\mu_p p\ (O) + \dfrac{Dq}{kT}\,c(O)\,e^{-qE^o/kT}} \qquad [24]$$

The unknowns in Eq. [23] and [24] may be taken as the electrostatic potential difference ΔV and the boundary concentrations $c(O)$ and $c(X)$, if we assume that the transport coefficients $\sigma_p = q\mu_p p_o$ and D are available in principle. It may be readily confirmed that the boundary concentrations in the growing oxide film are not those corresponding to the equilibrium concentrations of the Nernst equation

$$\Delta\phi = E^o - \frac{kT}{q}\ln\frac{c(O)}{c(X)} \qquad [25]$$

as in this case Eq. [21] yields a value of $J = 0$. Possible experiments would be the measurement of the Fermi level difference $\Delta\phi$ by an electrometer. With this information, Eq. [23] and [24] may be solved for the ratio of the unknown boundary concentrations $c(O)$ and $c(X)$. Measurement of the growth rate enables the two boundary concentrations to be determined separately by use of Eq. [10] and [21].

Deviations of the Oxide Film from Electroneutrality

Here we shall investigate quantitatively the magnitude of the maximum space charge in the oxide film which is consistent with a parabolic growth law within the ordinary experimental errors encountered in this type of measurement. Let us commence with some arbitrary distribution of space charges $C(x)$ which will be taken to be positive and univalent for the sake of convenience. The potential distribution is then obtained from Poisson's equation

$$\frac{d^2V}{dx^2} = -\frac{qC(x)}{\epsilon} \qquad [26]$$

where ϵ is the permittivity of the oxide.

A single integration with the boundary condition $(dV/dx)_o = -\mathcal{E}_o$ yields

$$\frac{dV}{dx} = -\mathcal{E}_o - \frac{q}{\epsilon}\int_o^x C(x')\,dx' \qquad [27]$$

A second integration with the boundary condition, $V(O) = 0$, leads to

$$V = -\mathcal{E}_o\,x - \frac{q}{\epsilon}\int_o^x\int_o^{x'} C(x'')\,dx''dx' \qquad [28]$$

The ionic flux is then obtained in terms of a differential equation by rearranging Eq. [8]

$$J e^{qV(x)/kT} = -D\frac{d}{dx}\,[c(x)\,e^{qV(x)/kT}] \qquad [29]$$

Particular note is to be taken that the concentration of the diffusing species c is not necessarily equal to the net concentration C of the defects responsible for space charge in Eq. [26]. Integration using the boundary conditions $V(O) = 0$ and $V(x) = \Delta V$ yields

$$J = -\frac{D\,[c(X)\,e^{q\Delta V/kT} - c(O)]}{\displaystyle\int_o^x e^{-[E_o x + w(x)]q/kT}\,dx} \qquad [30]$$

where

$$w(x) = \frac{q}{\epsilon}\int_o^x\int_o^{x'} C(x'')\,dx''dx' \qquad [31]$$

Further progress cannot be made without introducing assumptions concerning the magnitude and nature of the distribution $C(x)$. Let us determine the effect of a small arbitrary space charge on the ionic flux J. Expanding the exponential in the denominator of Eq. [30] we obtain

$$\int_o^x e^{-qE_o x/kT}\left[1 - \frac{qw(x)}{kT}\right]dx = \frac{kT}{q\mathcal{E}_o}\,[1 - e^{-qE_o X/kT}] - W(X) \qquad [32]$$

where

$$W(X) = \frac{q}{kT}\int_o^X w(x)\,e^{-qE_o x/kT}\,dx \qquad [33]$$

Introducing Eq. [32] into [30], we obtain

$$J = -\frac{D[c(X)\,e^{q\Delta V/kT} - c(O)]}{\dfrac{kT}{q\mathcal{E}_o}\,[1 - e^{-qE_o X/kT}] - W(X)} \qquad [34]$$

[2] Equation [18] is equivalent to one previously derived by Fromhold (9).

It may be expected that the term $W(X)$ will cause the growth behavior to deviate from the parabolic law.

Under the condition of a uniform charge density so that $C(x) = C$, Eq. [32] is readily integrated and yields

$$w(x) = \frac{qC}{2\epsilon} x^2 \qquad [35]$$

Equation [33] may likewise be now integrated

$$W(X) = \frac{-q^2C}{2kT_\epsilon}\left\{ e^{-qE_o X/kT}\left[\frac{kT}{q\mathcal{E}_o} X^2 + 2\left(\frac{kT}{q\mathcal{E}_o}\right)^2 X + 2\left(\frac{kT}{q\mathcal{E}_o}\right)^3\right] - 2\left(\frac{kT}{q\mathcal{E}_o}\right)^3 \right\} \qquad [36]$$

The boundary field $\mathcal{E}_o$ may be evaluated from Eq. [28] and is

$$-\mathcal{E}_o = \frac{\Delta V}{X} + \frac{qCX}{2\epsilon} = \frac{\Delta V}{X}\left(1 + \frac{qCX^2}{2\epsilon\Delta V}\right) \qquad [37]$$

In the field migration case, $(q\Delta V/kT) >> 1$, enabling considerable simplification of the problem. The ratio $q\Delta V/kT$ will ordinarily be of the order of 10. The expansion of the denomination of Eq. [30] places an upper limit on $w(x)$ of the order of 0.01V. Further for the case of relatively small space charge density C, we may approximate

$$-\frac{1}{\mathcal{E}_o} = \frac{X}{\Delta V}\left(1 - \frac{qCX^2}{2\epsilon\Delta V}\right) \qquad [38]$$

With the use of the above, together with Eq. [36], Eq. [34] takes the following limiting form with neglect of terms higher than first order in $qCX^2/2\epsilon\Delta V$ and $kT/q\Delta V$

$$J\left\{\frac{kTX}{q\Delta V} - \frac{qCX^3}{2\epsilon\Delta V}\right\} = Dc(X) \qquad [39]$$

Upon making use of Eq. [10] formulated for a single univalent anionic diffusing species and rearranging, we have

$$\frac{dX}{dt}\left(X - \frac{q^2CX^3}{2kT\epsilon}\right) = SD\frac{q}{kT\epsilon}c(X) \qquad [40]$$

Integration yields

$$\frac{X^2}{2} - \frac{q^2CX^4}{8kT\epsilon} = k_2 t \qquad [41]$$

The coefficient $q^2C/8kT\epsilon$ could be determined experimentally from a plot of t/X^2 *vs.* X^2. Alternatively, the space charge density C corresponding to a stated deviation δ, say 2%, from the parabolic growth law may be evaluated. For the interesting case of a silicon dioxide film of 5000Å thickness, and dielectric constant of 4, thermally grown at 1000°C, we obtain

$$C = \frac{4kT\epsilon\delta}{q^2X^2} = 1.25 \times 10^{13}\ \text{cm}^{-3} \qquad [42]$$

with

$$\sum = \int_o^x C\,dx = 1.25 \times 10^8\ \text{cm}^{-2}$$

This order-of-magnitude value of the space charge density indicates that charge compensation of the diffusing ions in the case of the silicon dioxide film need not be fully complete in order to yield an apparent parabolic growth law from the experimental point of view.

Partial or complete compensation of diffusing anions may be brought about by holes, if the oxide is p-type, or by immobile cations. Let us examine the situation of complete compensation via the first of these cases. This corresponds to the introduction of the additional condition that

$$p(x) = c(x) \qquad o \leq x \leq X \qquad [43]$$

in addition to the balance of the hole and anionic fluxes previously considered, Eq. [9].

The boundary concentrations are then immediately given by

$$c(X) = c(O)\, e^{qE_o/kT}$$

with the aid of Eq. [1] and [15]. The electrostatic potential difference ΔV following rearrangement of Eq. [23] is given by

$$e^{q\Delta V/kT} = \frac{R + e^{qE_o/kT}}{Re^{qE_o/kT} + 1} \qquad [44]$$

where

$$R = \frac{\mu_p}{Dq/kT}$$

The transport coefficients may be individually evaluated from experiment by the use of Eq. [21], [43], and [44]. The validity of the assumed condition of Eq. [43] may then be tested by comparing the transport coefficients above calculated with those obtained by independent measurement.

Compensation of the diffusing anions by immobile cations implies the condition that

$$c_-(x) = c_+(x) \qquad [45]$$

where c_- and c_+ are the concentrations of anions and cations, respectively. From Eq. [20] and [21] we obtain

$$c_-(x) = c_-(O)\, e^{qx\Delta V/kTX} - J\frac{kTX}{Dq\Delta V}\left(e^{qx\Delta V/kTX} - 1\right) \qquad [46]$$

where the final term represents the perturbation of the Boltzmann distribution by the transport process. It is now easily established that the cation distribution corresponding to Eq. [46] is such that if the cations were mobile, the free diffusion term of Eq. [8] would be of a direction to oppose the growth of the oxide film while the field term will contribute to the growth. Thus it would appear that complete compensation of diffusing anions by diffusing cations is generally inconsistent, with the following exception: where $q\Delta V/kT >> 1$, then Eq. [21] assumes the limiting form

$$J_- = \frac{Dq}{kT}c(x)\frac{\Delta V}{X} \qquad [47]$$

with the concentrations of anions and cations uniform throughout the film.

Raleigh Electrolysis Theory

Raleigh (8) has suggested that in consequence of the conservation Eq. [9] an externally applied electric field of itself should have no effect upon the growth rate because, if the field promotes the migration of the ions supporting the growth of the film, it must hinder the migration of the electrons or holes, the transport of which is required to maintain over-all electrical neutrality. He proposes that the effect of the applied potential in the Jorgensen experiments in accelerating or retarding the thermal growth of the silicon dioxide film is due to an electrolytic cell process superposed on the normal thermal growth. It is the purpose of this section to formulate this proposal in more detailed terms and to show that it is consistent with the Wagner electrochemical model of film growth.

In terms of the diffusion of neutral molecules, the oxidation of silicon may be represented as in Fig. 1 with the chemical reaction $Si + O_2 \rightarrow SiO_2$ occurring at the silicon-silicon dioxide interface. If no ionization of the oxygen occurs, its transport in the film occurs solely by free diffusion, thus

$$J = -D\frac{dc}{dx} \qquad [47]$$

where c here refers to the effective concentration of the species O_2 in the film. In the steady state J is constant implying that

$$\frac{dc}{dx} = \frac{c(X) - c(O)}{X} \quad [48]$$

which leads to the parabolic growth law as earlier noted.

As pointed out by Raleigh, the neutral species O_2 may be in thermodynamic equilibrium with ionized forms. Examples of possible equilibria for the case of silicon dioxide growing in a perfectly dry oxygen ambient are shown in Fig. 1. For the sake of simplicity, let us consider just the first of these equilibria which may be formulated in terms of the equilibrium constant

$$K = \frac{[O_2^-]p}{[O_2]} \quad [49]$$

on introducing Eq. [49] into Eq. [47], we obtain

$$J = -D\frac{p}{K}\frac{d[O_2^-]}{dx} + \frac{Dq}{kT}\frac{p}{K}[O_2^-]\frac{\Delta V}{X} - \frac{Dq}{kT}\frac{[O_2^-]}{K}p\frac{d\phi}{dx} \quad [50]$$

where Eq. [1] had been specialized to the case of electroneutrality. The last term of Eq. [50] represents the contribution of hole flux to the net transport of the oxygen molecules. Upon again making use of Eq. [49], Eq. [50] takes the form

$$J = -D\frac{[O_2]}{[O_2^-]}\frac{d[O_2^-]}{dx} - \frac{Dq}{kT}[O_2]\left[\frac{d\phi}{dx} - \frac{\Delta V}{X}\right] \quad [51]$$

Let us now consider the case that an external field E is applied across the oxide film by insulated electrodes so that no transport of holes takes place externally. The electrostatic potential gradient and the Fermi potential gradient are each increased by the amount E. It is clear from Eq. [51] that no increase of the flux J will occur, in complete agreement with the discussion of Raleigh.

The situation is completely altered if the field is applied by means of electrodes which are in ohmic contact with the oxide film. Here hole transport through the external circuit takes place, and the Fermi potential differences across the film is fixed by the potential ΔU applied by the external source. The treatment developed in this paper remains applicable with $\Delta\phi$ replaced by $\Delta\phi + \Delta U$ throughout. The application of an anodic potential is then tantamount to the situation which would exist in an oxidation reaction with a higher free energy change but with all other physical variables remaining the same.

Acknowledgment

The authors are indebted to Dr. Raleigh for kindly furnishing them with a preprint of his paper and for helpful discussion. They are also grateful to Dr. R. N. Hall for useful discussion of the problem.

Manuscript received Feb. 21, 1966; revised manuscript received Sept. 9, 1966.

Any discussion of this paper will appear in a Discussion Section to be published in the December 1967 JOURNAL.

REFERENCES

1. T. Nakayama and F. C. Collins, *This Journal*, **113**, 706 (1966). (This paper contains a list of 24 references to the prior work on the thermal growth of silicon dioxide films.)
2. P. J. Jorgensen, *J. Chem. Phys.*, **37**, 874 (1962).
3. C. Wagner, *Z. Phys. Chem.*, **B21**, 25 (1933); **B32**, 447 (1956); *Trans. Faraday Soc.*, **34**, 851 (1938); C. Wagner and K. Grunewald, *Z. Phys. Chem.*, **B40**, 455 (1938).
4. N. F. Mott, *Trans. Faraday Soc.*, **36**, 472 (1940); **43**, 429 (1947).
5. N. Cabrera and N. F. Mott, *Rept. Progr. Phys.*, **12**, 163 (1948).
6. W. G. Spitzer and J. R. Ligenza, *J. Phys. Chem. Solids*, **17**, 196 (1961); N. Karube, K. Yamamoto, and M. Kamiyama, *Japan J. Appl. Phys.*, **2**, 11 (1963); W. A. Pliskin and R. P. Gnall, *This Journal*, **111**, 872 (1964); P. Balk, C. Aliotta, and L. V. Gregor, *Trans. Metall. Soc. AIME*, **233**, 563 (1965).
7. A. T. Fromhold, Jr., *J. Chem. Phys.*, **40**, 335 (1964); *J. Phys. Chem. Solids*, **25**, 1129 (1964).
8. D. O. Raleigh, *This Journal*, **113**, 782 (1966).
9. A. T. Fromhold, Jr., *J. Phys. Chem. Solids*, **24**, 1081 (1963).

Studies of the Defect Structure of Nonstoichiometric Rutile, TiO_{2-x}

R. N. Blumenthal, J. Baukus, and W. M. Hirthe

Metallurgy and Materials Science, Department of Mechanical Engineering, College of Engineering, Marquette University, Milwaukee, Wisconsin

ABSTRACT

The electrical conductivity of single crystals of rutile was measured in the "c" and "a" directions over the temperature range 1000°-1500°C and from 1 to 10^{-15} atm of oxygen. Based on the excellent fit observed between the theoretically derived relation

$$\sigma^5 = (A\sigma + B)P_{O_2}{}^{-1} + I'\sigma^3$$

and the experimental conductivity data, the nonstoichiometric defect structure of rutile was rationalized in terms of quasi-free electrons and both triply and quadruply ionized titanium interstitials. In addition, this equation satisfies a contribution due to impurity conduction where I' is proportional to a temperature dependent concentration of ionized impurities or a contribution due to intrinsic conduction where I' is proportional to a temperature dependent concentration of holes in the valance band.

The standard enthalpy of formation for the following defect reactions in rutile

$Ti + 2O = O_2(g) + Ti_i{}^{+3} + 3e;$	$\Delta H_a{}^o = 9.6 \pm 0.2$ ev	(a)
$Ti + 2O = O_2(g) + Ti_i{}^{+4} + 4e;$	$\Delta H_b{}^o = 10.8 \pm 0.2$ ev	(b)
$Ti_i{}^{+3} = Ti_i{}^{+4} + e;$	$\Delta H_c{}^o = 1.2 \pm 0.4$ ev	(c)
$I = I^+ + e;$	$\Delta H_d{}^o = 3.7 \pm 0.2$ ev	(d)

were determined from the temperature dependence of A, B, and I' obtained from the above relation and from the experimental expression for the temperature dependence of electron mobility. The values of $\Delta H_a{}^o$, $\Delta H_b{}^o$, and $\Delta H_c{}^o$ are in agreement, within experimental error, with those obtained in an earlier investigation based on conductivity measurements in the c direction only. If impurity conduction is involved, $\Delta H_d{}^o$ is equal to the standard enthalpy of formation for the ionization of an impurity. If intrinsic conduction is involved, $\Delta H_d{}^o$ is equal to the band gap energy which is thought to be between 3 and 4 ev for rutile. The ratio of electrical conductivities for the c and a direction is essentially independent of oxygen pressure above 1100°C; but at the lower temperatures, 1000° and 1100°C, the ratio is dependent on pressure in contradiction to the initial assumption that mobility is a function of temperature only.

Nonstoichiometric rutile may be classified as a metal-excess, n-type semiconductor on the basis of experimental observations (1, 2). Recent investigations (3-5) have favored a defect model consisting of quasi-free electrons and titanium interstitials in one or more states of ionization. In an earlier investigation in this laboratory (5) the nonstoichiometric defect structure of rutile was rationalized in terms of a defect model involving quasi-free electrons and both triply and quadruply ionized titanium interstitials.

The investigation reported here was initiated to obtain additional conductivity data for the c direction, particularly in the oxygen pressure range 10^{-2} to 10^{-9} atm, in order to account for the marked temperature dependence of the term in the electroneutrality equation attributed to the concentration of ionized impurities revealed in subsequent analyses of the experimental data and to refine calculations of the parameters in the theoretically derived relation. In addition, the conductivity was measured in the a direction over the same range of temperature and oxygen partial pressure in order to determine the validity of this type of relation and the dependence of conductivity on crystallographic direction.

Experimental Procedure

Single crystal specimens of dimensions 0.15 x 0.25 x 1 in. with the longitudinal axis parallel to the c or a direction were cut from a boule obtained from the National Lead Company. The apparatus and techniques employed were essentially the same as those described in the earlier investigation (5). The electrical conductivity was measured over the range 1000°-1500°C and from 1 to 10^{-15} atm of oxygen. This range of oxygen pressure effectively covers the stability limit of rutile (6, 7), TiO_{2-x}, at 1500°C, and includes the major portion of the phase field at 1000°C where the pressure corresponding to the stability limit is about 7×10^{-19} atm.

Results and Discussion

Isobaric plots of the logarithm of electrical conductivity *vs.* the reciprocal of absolute temperature for oxygen partial pressures from 1 to 10^{-3} atm are shown in Fig. 1 and 2 for the c and a direction, respectively. The experimental technique utilized in this investigation was substantiated by the excellent agreement between the conductivity measured in both c and a directions from 1000° to 1500°C in 1 atm of air and the data of Cronemeyer (8).

In order to analyze the data, experimental plots of $\log \sigma$ *vs.* $\log P_{O_2}$ were obtained in the following manner. Values of the conductivity were selected at 100°C intervals between 1000° and 1500°C from the plots of $\log \sigma$ *vs.* $1/T$. For the isobaric plots, Fig. 1 and 2, the values of conductivity at 1000° and 1100°C were taken from the straight line extrapolated from higher temperatures rather than the measured conductivity data for a few of the points. Justification for this treatment lies in the fact that the previous investigation (5) revealed that the appearance of a two-slope behavior in this range of temperature is the result of contamination of the specimens *in situ* during the period of time the measurements are being taken. The partial pressure of oxygen corresponding to the above values of conductivity for various atmospheres was

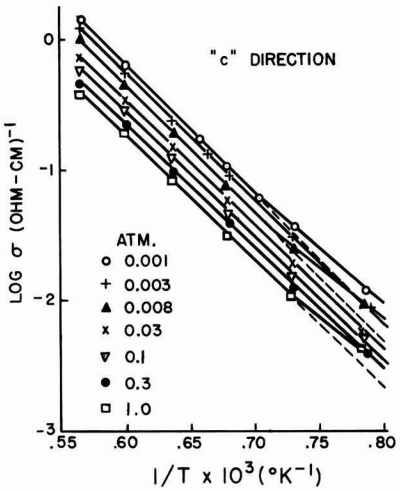

Fig. 1. Logarithm of electrical conductivity of rutile single crystal in the c direction vs. the reciprocal of absolute temperature for oxygen partial pressures from 1 to 10^{-3} atm.

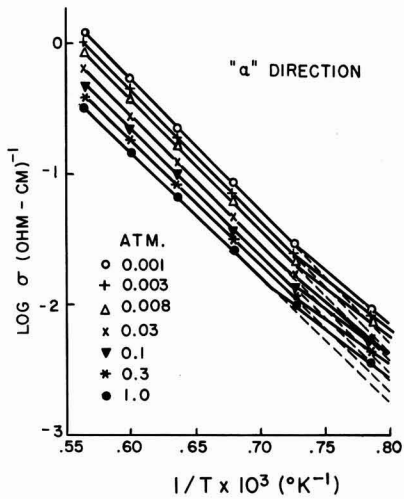

Fig. 2. Logarithm of electrical conductivity of rutile single crystal in the a direction vs. the reciprocal of absolute temperature for oxygen partial pressures from 1 to 10^{-3} atm.

calculated and combined with the respective conductivity to obtain the isothermal plots at 100°C intervals between 1000° and 1500°C of log σ *vs.* log P_{O_2} shown in Fig. 3 and 4 for the c and a directions, respectively. The curvature of the 1000°C isotherms at the low pressure end of the plots was verified experimentally by subjecting the specimen to partial pressure less than 10^{-15} atm followed by a return to 10^{-15} atm. The conductivity values before the further reduction and after the increase to 10^{-15} atm were the same indicating that the curvature is representative of the equilibrium situation.

The objection to the analysis presented in the earlier investigation lies in the fact that it does not account for the temperature dependence of the third term in the electroneutrality equation revealed in subsequent analyses of the experimental conductivity data. Therefore, an electroneutrality expression of the following type

$$n = 3(\mathrm{Ti_i}^{+3}) + 4(\mathrm{Ti_i}^{+4}) + I^+ \qquad [1]$$

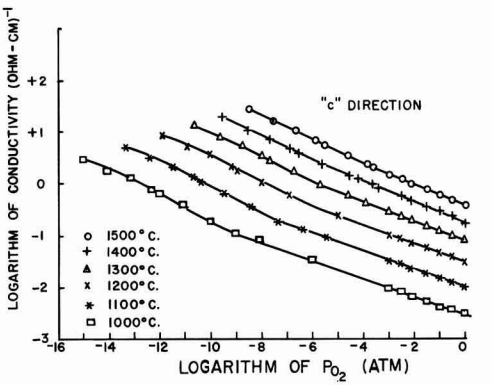

Fig. 3. Isothermal relation between the logarithm of electrical conductivity in the c direction and the logarithm of partial pressure of oxygen in the range 1000°-1500°C.

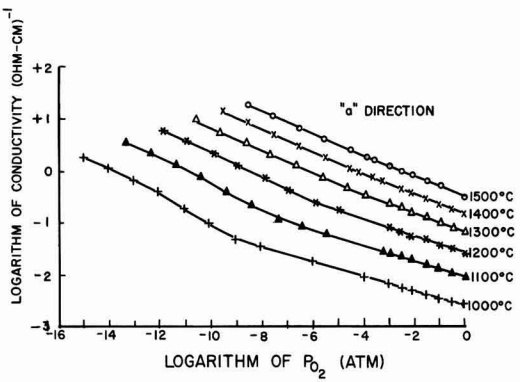

Fig. 4. Isothermal relation between the logarithm of electrical conductivity in the a direction and the logarithm of partial pressure of oxygen in the range 1000°-1500°C.

where $(\mathrm{Ti_i}^{+3})$ is the concentration of triply ionized titanium interstitials, $(\mathrm{Ti_i}^{+4})$ is the concentration of quadruply ionized titanium interstitials, and I^+ is the temperature dependent concentration of ionized impurities which act as donors, was employed to obtain a quantitative relation between σ and P_{O_2}. The relation for the ionization of the impurity is

$$I = I^+ + e \qquad [2]$$

and from the law of mass action the equilibrium constant can be written as

$$K_6 = \frac{I^+ n}{I} \qquad [3]$$

If the assumption is made that $I >> I^+$, the expression for the conductivity as a function of oxygen partial pressure may be obtained by combining Eq. [1], the mass action equations for defect equilibrium, and the equation for extrinsic electron conduction

$$\sigma^5 = (A\sigma + B)P_{O_2}{}^{-1} + I'\sigma^3 \qquad [4]$$

where

$$A = 3K_4'C^4; \qquad B = 4K_5'C^5; \qquad I' = IK_6C^2 \qquad [5]$$

It should be pointed out at this time that Eq. [4] will also apply for the case of intrinsic conduction where I^+ is the temperature dependent concentration of holes in the valence band. The corresponding equation for conduction involving holes and electrons is

Table I. Calculated values of the parameters A, B, and I' in the expression $\sigma^5 = (A\sigma + B)\, P_{O_2}{}^{-1} + I'\,\sigma^3$ and the standard error (95% confidence limit) in the calculation of these parameters at 100°C intervals from 1000° to 1500°C:

Temperature, °C	A	Standard error of A (±)	B	Standard error of B (±)	I'	Standard error of I' (±)
			c Direction			
1000	8.64×10^{-14}	7.68×10^{-15}	4.82×10^{-14}	6.53×10^{-15}	9.41×10^{-6}	1.27×10^{-6}
1100	4.20×10^{-11}	3.54×10^{-12}	3.22×10^{-11}	5.64×10^{-12}	1.22×10^{-4}	2.04×10^{-5}
1200	7.59×10^{-9}	4.92×10^{-10}	1.12×10^{-8}	1.38×10^{-9}	8.03×10^{-4}	1.84×10^{-4}
1300	8.32×10^{-7}	4.16×10^{-8}	1.63×10^{-6}	1.95×10^{-7}	4.76×10^{-3}	1.35×10^{-3}
1400	3.47×10^{-5}	8.40×10^{-7}	1.67×10^{-4}	6.21×10^{-6}	8.61×10^{-3}	3.22×10^{-3}
1500	1.33×10^{-3}	3.42×10^{-5}	7.94×10^{-3}	3.78×10^{-4}	6.66×10^{-4}	1.89×10^{-2}
			a Direction			
1000	8.23×10^{-15}	1.99×10^{-15}	4.85×10^{-15}	9.93×10^{-16}	7.14×10^{-6}	3.61×10^{-7}
1100	5.17×10^{-13}	7.63×10^{-13}	5.17×10^{-12}	7.70×10^{-13}	8.82×10^{-5}	5.38×10^{-6}
1200	1.13×10^{-9}	1.17×10^{-10}	2.40×10^{-9}	2.28×10^{-10}	6.53×10^{-4}	5.81×10^{-5}
1300	1.15×10^{-7}	8.05×10^{-9}	4.79×10^{-7}	2.85×10^{-8}	3.68×10^{-3}	3.67×10^{-4}
1400	6.17×10^{-6}	3.03×10^{-7}	4.63×10^{-5}	1.55×10^{-6}	1.64×10^{-2}	1.36×10^{-3}
1500	2.87×10^{-4}	8.38×10^{-6}	2.23×10^{-3}	6.90×10^{-5}	3.48×10^{-2}	6.67×10^{-3}

$$\sigma = nq\mu + pq\mu' \qquad [6]$$

where p is the concentration of holes and μ' is the hole mobility. However, previous investigations (2, 9, 10) of the thermoelectric power of rutile have suggested that

$$\mu >> \mu' \qquad [7]$$

Consequently, Eq. [6] reduces to the relation for extrinsic electron conduction, and Eq. [4] also represents the conductivity as a function of the partial pressure of oxygen for a defect model based on both triply and quadruply ionized titanium interstitials and intrinsic conduction.

A computer program was written for Eq. [4], and the calculated values of the parameters in this equation and their standard errors are tabulated in Table I. It is apparent from the values of the standard error as the parameter shown in Table I that Eq. [4] represents an acceptable fit of the experimental data for both the c and a directions. Thus the excellent agreement between Eq. [4] and the experimental data for the electrical conductivity in both the c and a direction provides a quantitative confirmation of a defect model involving both triply and quadruply ionized titanium interstitials and a third term in the electroneutrality equation which is dependent on temperature.

Plots of the logarithm of the parameters A, B, and I' *vs.* the reciprocal of absolute temperature yield straight lines for both c and a directions. The standard enthalpies of formation for the reactions

$$\mathrm{Ti} + 2\,\mathrm{O} = \mathrm{O_2(g)} + \mathrm{Ti_i}^{+3} + 3e; \quad \Delta H_a^\circ \qquad [8]$$

$$\mathrm{Ti} + 2\,\mathrm{O} = \mathrm{O_2(g)} + \mathrm{Ti_i}^{+4} + 4e; \quad \Delta H_b^\circ \qquad [9]$$

$$I = I^+ + e; \quad \Delta H_d^\circ \qquad [2]$$

can be calculated from the slopes of these lines by assuming (2) that the electron mobility is proportional to the exp (0.1 (ev)/kT). In addition, the standard enthalpy of formation for the ionization reaction

$$\mathrm{Ti_i}^{+3} = \mathrm{Ti_i}^{+4} + e; \quad \Delta H_c^\circ \qquad [10]$$

can be calculated from the equation

$$\Delta H_c^\circ = \Delta H_b^\circ - \Delta H_a^\circ \qquad [11]$$

Table II. Standard enthalpies of formation calculated for both c and a direction data

	ΔH_a° c	ev a	ΔH_b° c	ev a	ΔH_c° c	ev a	ΔH_d° c	ev a
Previous investigation (5)	9.3	—	10.7	—	1.4	—	—	—
This investigation	9.5	9.8	10.7	11.0	1.2	1.2	3.7	3.7
Error*	±0.2	±0.2	±0.2	±0.2	±0.4	±0.4	±0.2	±0.2

* Estimate of error includes experimental error as well as the error in the assumed value of the temperature dependence of electron mobility.

The results of these calculations for both c and a direction data are shown in Table II and compared with data of the previous investigation. The good agreement in ΔH_a°, ΔH_b°, and ΔH_c° between these investigations based on c direction data indicates that the interpretation of the nonstoichiometric defect structure is independent of the physical significance given to the third term on the right-hand side of the electroneutrality equations. The agreement in these values of enthalpies based on c and a direction conductivity further substantiates the validity of the proposed nonstoichiometric defect structure since these thermodynamic quantities should be independent of crystallographic direction. The values of ΔH_d° based on c and a direction data are independent of direction, and this is consistent with the concept of an impurity ionization energy or intrinsic conduction. However, the magnitude of ΔH_d°, 3.7 ev, suggests intrinsic conduction because the intrinsic band gap energy is thought to be between 3 and 4 ev as the result of numerous optical and thermal measurements (1).

In order to substantiate further the validity of Eq. [4], the parameters A, B, and I' were extrapolated to 600°C, and the conductivity was calculated as a function of temperature in the range 1500° to 600°C for 1 atm of air. A comparison of the temperature dependence of the conductivity as calculated from Eq. [4] with the data of Cronemeyer over the same range of temperature in air is shown in Fig. 5 and 6 for the c and a directions, respectively. It is significant to note that Eq. [4] yields the well-known two-slope behavior for a plot of log σ *vs.* $1/T$. The agreement in the magnitude of the conductivity is good in the high-temperature regions, but there is some discrepancy in the low-temperature regions. This discrepancy can be accounted for in Eq. [4] if I' is assumed to be proportional to the number of impurities which act as donors when ionized. For this case, the magnitude of the conductivity and the experimental activation energy will depend on the nature and concentration of impurities present in the crystal employed in the particular investigation.

Since only conductivity data was taken in this investigation, the electron mobility could not be determined. However, the ratio of electron mobility in the c to the mobility in the a direction was determined by

Table III. Comparison of the ratios of the experimental conductivity with the calculated parameters of Eq. [4] raised to the appropriate power

Temperature, °C	σ_c/σ_a	$(A_c/A_a)^{1/4}$	σ_c/σ_a	$(B_c/B_a)^{1/5}$	σ_c/σ_a	$(I_c'/I_a')^{1/2}$
1000	1.64	1.80	2.03	1.58	1.20	1.15
1100	1.51	1.69	1.64	1.44	1.23	1.18
1200	1.53	1.61	1.44	1.36	1.23	1.11
1300	1.50	1.64	1.30	1.28	1.22	1.14
1400	1.46	1.54	1.20	1.29	—	—
1500	1.41	1.47	1.25	1.29	—	—

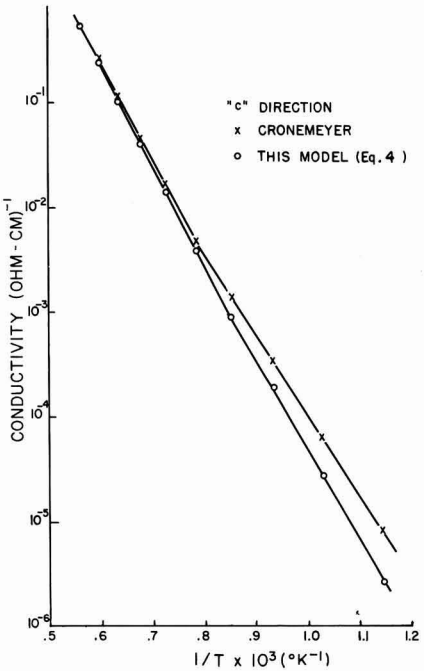

Fig. 5. Comparison of the temperature dependence of electrical conductivity in the c direction as calculated from Eq. [4] with the data of Cronemeyer over the same range of temperature in air.

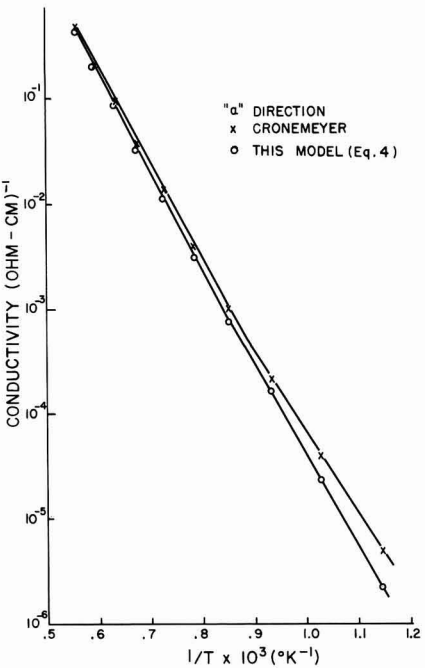

Fig. 6. Comparison of the temperature dependence of electrical conductivity in the a direction as calculated from Eq. [4] with the data of Cronemeyer over the same range of temperature in air.

plotting the ratio of the conductivities as a function of the logarithm of partial pressure of oxygen at 100° intervals between 1000° and 1500°C as shown in Fig. 7. From Fig. 7 it can be seen that the mobility is essentially independent of pressure at the higher temperatures within the limits of experimental error. At the lower temperatures, 1000° and 1100°C, the ratio of the mobilities is dependent on pressures in contradiction to the initial assumption that the mobility was dependent on temperature only. In general, the ratio of the mobilities decreases with increasing temperature in the range of this investigation. This plot clearly indicates the limitation of the technique employed in this investigation and the need for electron mobility data in order to understand the nature of the transport mechanisms in rutile below 1000°C.

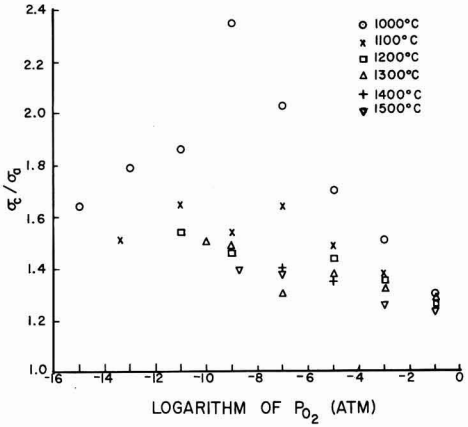

Fig. 7. Isothermal relation between the ratio of electrical conductivity and the logarithm of partial pressure of oxygen in the range 1000°-1500°C.

As a check on the internal consistency of the data, the ratios of the experimental conductivities are compared with the ratios of the calculated parameters of Eq. [4] raised to the appropriate power in Table III. The corresponding values of conductivity ratio and parameter were selected in the oxygen pressure range where the particular defect was the major contributor to the concentration of conduction electrons, n, in the electroneutrality equation. The variation in these values with temperature can be explained in terms of the temperature dependence of the mobilities in the c and a direction. If these dependencies are not the same, some variation with temperature is reasonable.

Conclusions

The nonstoichiometric defect structure of rutile is rationalized in terms of quasi-free electrons and both triply and quadruply ionized titanium interstitials. In addition, there is a contribution to the electrical conductivity due to impurity conduction or intrinsic conduction. The experimental confirmation of this model is based on the excellent agreement between the theoretical relation

$$\sigma^5 = (A\sigma + B)\, P_{O_2}{}^{-1} + I'\sigma^3$$

and the c and a direction conductivity data measured over the temperature range 1000° to 1500°C over the oxygen partial pressure range 1 to 10^{-15} atm.

The standard enthalpy of formation for the following defect reactions in rutile

$$\mathrm{Ti} + 2\,\mathrm{O} = \mathrm{O_2(g)} + \mathrm{Ti_i^{+3}} + 3e; \quad \Delta H_a^\circ = 9.6 \pm 0.2\text{ev (a)}$$

$$\mathrm{Ti} + 2\,\mathrm{O} = \mathrm{O_2(g)} + \mathrm{Ti_i^{+4}} + 4e; \quad \Delta H_b^\circ = 10.8 \pm 0.2\text{ev (b)}$$

$$\mathrm{Ti_i^{+3}} = \mathrm{Ti_i^{+4}} + e; \quad \Delta H_c^\circ = 1.2 \pm 0.4\text{ev (c)}$$

$$I = I^+ + e; \quad \Delta H_d^\circ = 3.7 \pm 0.2\text{ev (d)}$$

where determined from the temperature dependence

of A, B, and I' obtained from the above relation and from the experimental expression for the temperature dependence of electron mobility. The values of ΔH_a^o, ΔH_b^o, and ΔH_c^o are in agreement, within experimental error, with those obtained in the previous investigation based on conductivity measurements in the c direction only. If impurity conduction is involved, ΔH_d^o is equal to the standard enthalpy of formation for the ionization of an impurity. If intrinsic conduction is involved, ΔH_d^o is equal to the band gap energy which is thought to be between 3 and 4ev for rutile.

Values of the electrical conductivity calculated from the above equation yield the well-known two slope behavior on a plot of logarithm of electrical conductivity vs. reciprocal of absolute temperature. The calculated values agree in magnitude with the data of Cronemeyer for the same range of temperature, 600°-1500°C, and a pressure of 1 atm of air. The ratio of electrical conductivities in the c and a direction is essentially independent of oxygen partial pressure above 1100°C; but at the lower temperatures, 1000° and 1100°C, the ratio is dependent on pressure in contradiction to the initial assumption that mobility is a function of temperature only. In general, the ratio of conductivities, *i.e.*, mobilities, decreases with increasing temperature in the range of this investigation.

Acknowledgments

The authors gratefully acknowledge the assistance of Mr. Joseph Zuercher and the support of Aerospace Research Laboratories, Office of Aerospace Research, United States Air Force, Contract No. AF 33(615)-1244.

Manuscript received June 16, 1966; revised manuscript received Sept. 19, 1966.

Any discussion of this paper will appear in a Discussion Section to be published in the December 1967 JOURNAL.

REFERENCES

1. F. A. Grant, *Rev. Mod. Phys.*, **31**, 646 (1959).
2. H. P. R. Frederikse, *J. Appl. Phys.*, **32**, 2211 (1961).
3. T. Hurlen, *Acta Chem. Scand.*, **13**, 365 (1959).
4. D. S. Tannhauser, *Solid St. Commun.*, **1**, 223 (1963).
5. R. N. Blumenthal, J. Coburn, J. Baukus, and W. M. Hirthe, *J. Phys. Chem. Solids*, **27**, 643 (1966).
6. R. N. Blumenthal and D. H. Whitmore, *This Journal*, **110**, 92 (1963).
7. L. Porter, Private communication.
8. D. C. Cronemeyer, *Phys. Rev.*, **87**, 876 (1952).
9. H. P. R. Frederiske and W. R. Hosler, "Properties of Rutile, I. Electrical Conductivity and Thermoelectric Power," NBS Rpt. No. 6585, Nov. 1, 1959.
10. J. Rudolph, *Z. Naturforschg.*, **14a**, 727 (1959).

Germanium Oxidation in Nitric Acid

Ernest W. Valyocsik

Research Laboratories, General Motors Corporation, Warren, Michigan

ABSTRACT

The oxidation in nitric acid of single crystal Ge (100) surfaces and of polycrystalline Ge (111) surfaces has been studied at 27.5°C over the concentration range 7.0-15.6N HNO_3. The surface oxide growth rate decreases smoothly with time and is not described by simple film growth laws. The average oxide nuclei size at saturation thickness decreases with increasing acid concentration, and more rapid surface saturation occurs with increasing acid concentration. No induction period for surface oxide growth was observed over the range of concentrations studied. The oxide films which grew on the Ge surfaces had saturation thicknesses inversely dependent on acid concentration, and the saturation thickness was also observed to be dependent on the crystallographic orientation of the Ge surface. Structural studies of the oxide layers by infrared, x-ray, and electron diffraction techniques indicate that the surface oxide grown under these conditions is crystalline hexagonal germanium dioxide.

Etching solutions in practice contain strong oxidizing agents which attack a semiconductor surface with subsequent dissolution of the products in the bulk solution. One such commonly employed oxidizing agent is nitric acid. Even after etching in dilute solutions, Ge surfaces still retain a thin oxide layer. At higher concentrations the removal of the reaction products from the solid-liquid interface into the bulk liquid is restricted to such an extent that the growth of thick oxide films is promoted on the semiconductor surface (1-4).

The object of the present work was to study the kinetics of oxide growth and the nature and structure of the oxide layers grown on Ge surfaces over an extended range of nitric acid concentrations. Measurements were made on the oxide films by several techniques in an effort to determine the crystallographic structure of the films grown under these conditions. It is the purpose of this paper to report the results of a study of Ge surface oxidation in concentrated nitric acid solutions.

Experimental Method

Materials.—Samples of Ge for oxidation were in the form of rectangular slabs. The Ge was obtained from two sources: (*A*) Polycrystalline samples (n-type, resistivity 2.5 ohm-cm) of size 1.4 x 9.0 x 15.8 mm were cut from Ge crystals grown in our laboratory by the Czochrolski method. Many of the samples possessed low-angle grain boundaries. The principal orientation of the largest faces of the rectangular slabs was parallel to the (111) planes to within 10° as determined by x-ray techniques. (*B*) Single crystal samples (n-type, arsenic doped; resistivity range 13-24 ohm-cm) of size 0.43 x 4.9 x 15.0 mm were cut from a boule of zone-refined Ge. The orientation of the largest faces was parallel to the (100) planes.

All chemicals used in this study were of reagent grade quality. Normalities of the nitric acid solutions were determined by standard titrimetric methods and ranged from 7.0 to 15.6N. It has been shown by Cretella and Gatos (1) that the dissolution rate of Ge in HNO_3 reaches a maximum at 6N. Ge oxidation was not studied in solutions of concentration less than 7.0N.

Surface treatment.—The rectangular Ge slabs were attached to the faces of glass plates with low-melting wax and lapped with a water slurry of 800 mesh silicon carbide. This was followed by lapping the surfaces to a shiny finish with $\sim 1\mu$ alumina. The samples were then removed from the glass plates and washed free of wax with boiling methanol.

Prior to reaction the Ge slabs were etched for 2 min at room temperature in 30% H_2O_2 (one part by volume) 49% HF (one part by volume) and de-ionized water (one part by volume). After etching, the

surfaces were visibly bright and shiny although they are known not to be "oxide free."

Apparatus.—Reactions were carried out in a thermostat controlled at 27.50° ± 0.05°C. All weighings were made to an accuracy of ± 4 μg.

Procedure.—Before reaction the samples were weighed, and all exposed areas of the rectangular Ge slabs were measured.

Nitrogen gas was bubbled through the solution for about 1 hr prior to placing the Ge into the solution in order to sweep the solution free of dissolved oxygen gas. The solutions were covered but not stirred during reaction. Samples were removed at given time intervals, placed in methanol, and boiled for 15 min. After removal from the methanol, the samples were rinsed several times with fresh methanol and dried before reweighing. The weight change of each sample was the net difference between the weight lost by Ge dissolution and the weight gained by surface oxide growth during the reaction time interval.

In the first few experiments the oxide thickness was determined by dissolution of the oxide in 49% HF at room temperature. There was no additional detectable weight loss of the sample after 5 min in 49% HF at room temperature. Ge is not soluble in HF at these conditions. Thus, it is assumed that the HF treatment removed the oxide only.

Following oxide removal, the samples were reweighed, and the oxide thickness was calculated. Since this method of thickness determination destroyed the sample for further studies, a technique was developed (5) whereby infrared absorption (6) was used to measure oxide film thickness *in situ.*

Lippincott and co-workers (6) have observed a strong fundamental absorption at 11.5μ (attributed to the Ge-O stretching mode) and a somewhat weaker set of fundamental absorption bands at about 17, 18, and 19μ. Combination or overtone bands due to the lattice vibration at about 7.50, 6.90, and 6.55μ, which are much weaker in strength relative to Lippincott's set at 17-19μ, have also been observed in our laboratory (5). Depending on the oxide thickness range, one or other of these bands can be used to measure the oxide thickness. The weaker bands are more appropriate for the thicker oxide layers. Film thickness measurements were made on a Perkin-Elmer Model 21 Infrared Spectrometer equipped with a scale expansion accessory. A weighed, oxidized sample was placed in one beam of the spectrometer with an unoxidized Ge sample in the reference beam and the spectrum scanned. The oxidized sample was then placed in water and part of the surface oxide dissolved. The sample was dried, then carefully reweighed, and the infrared absorption measurement repeated. This procedure was continued until all detectable oxide was removed. The integrated intensities corresponded to the peak heights so that after calibration the peak heights were measured to determine the oxide thickness of the samples. A calibration curve for oxide thickness *vs.* infrared absorption of the 18μ band is reproduced in Fig. 1.

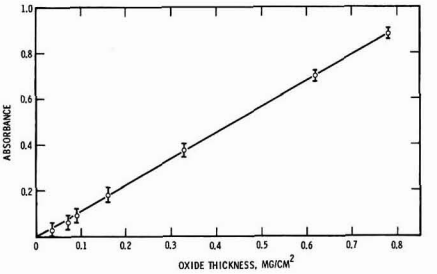

Fig. 1. Infrared absorption measurement of oxide film thickness

Results and Discussion

Nucleation of surface oxides.—On immersion of a Ge sample in nitric acid the surface is rapidly oxidized with some dissolution of the oxidized Ge. Dissolution decreases with continuing reaction presumably because of local saturation at the solid-liquid interface. Cretella and Gatos (1) had observed that in stirred concentrated HNO_3 solutions the behavior of Ge is similar to that in nonstirred solutions except that higher concentrations or longer times were required to achieve saturation of the surface by the oxide. Due to the rapid decrease in solubility of germanium oxide (7) with increasing nitric acid concentration, supersaturation of the interface takes place more rapidly at the higher acid concentrations. As the solubility limit is approached, the oxide can nucleate to produce crystalline particles on the Ge surface. The effect of an oxide-saturated interface on Ge dissolution was tested by preparing HNO_3 solutions containing dissolved hexagonal GeO_2 powder. These solutions were prepared by vigorously stirring the HNO_3 with excess GeO_2 powder over night at the temperature of the bath. After stirring was terminated, the excess GeO_2 powder settled to the bottom of the beaker. The solutions were ready for reaction after bubbling N_2 through them. A comparison run was conducted for Ge reaction in pure 7.5*N* HNO_3 and in 7.5*N* HNO_3 saturated with GeO_2. Referring to Fig. 4, one sees that the maximum Ge weight loss in 7.5*N* HNO_3 occurs at approximately 1.5 hr after reaction starts. Single crystal Ge (100) samples were removed from solution after 1.7 hr of reaction time. This was done to check the effect of solution saturation at the maximum weight loss point. The results showed that the Ge sample in pure 7.5*N* HNO_3 lost 3.18 mg/cm² while the sample in 7.5*N* HNO_3 saturated with GeO_2 lost 2.69 mg/cm² of weight. The oxide thicknesses at these times were 1.78 mg/cm² for reaction in pure acid as compared to 2.61 mg/cm² for the oxide saturated acid. These values are the averages for three Ge samples in each solution. There was a definite decrease in the dissolution of the Ge sample and an increase in the surface oxide thickness with the GeO_2 present in solution prior to reaction. The magnitude of the dissolution did not approach that characteristic of 10.2*N* HNO_3 (Fig. 4). Two alternatives can be considered: (*a*) the solution was not equilibrated with the GeO_2 prior to reaction, or (b) saturation of the interface may not be the controlling factor in Ge dissolution or surface oxide growth. In their work Brauer and Müller (7) found that solutions of 2-5*N* HNO_3 had equilibrated with GeO_2 within 10 hr at 25°C. Solutions far from equilibrium could not easily account for the magnitude of the effect on the dissolution of the Ge sample. The oxide layers grown in the 7.5*N* HNO_3 containing GeO_2 did appear more uniform than those grown in the pure acid. The fact that dissolution of the Ge in the oxide saturated acid was not entirely eliminated may be related to factors other than interface saturation which are important in controlling the sample dissolution and oxide nucleation rate. Reactions of single crystal Ge (100) surfaces with pure 15.6*N* HNO_3 and GeO_2 saturated 15.6*N* HNO_3 after 1.7 hr showed sample weight gains of 0.204 mg/cm² and 0.221 mg/cm² for the pure and oxide saturated acid, respectively.

Figure 2 shows photomicrographs of Ge (111) surfaces oxidized in 7.0*N* HNO_3 for 1 and 3 hr. The oxide nuclei are seen to have a definite crystalline structure and appear to have a random surface orientation. Konorov and Romanov (4) have also observed the growth of definite hexahedral crystals of ~10μ dimensions on the Ge surface in 7*N* HNO_3. The growth of these oxide nuclei on Ge surfaces is similar to the growth of As_2O_3 nuclei that takes place on GaAs surfaces oxidized in concentrated nitric acid solutions (8, 9). In the early stages of oxidation at the lower

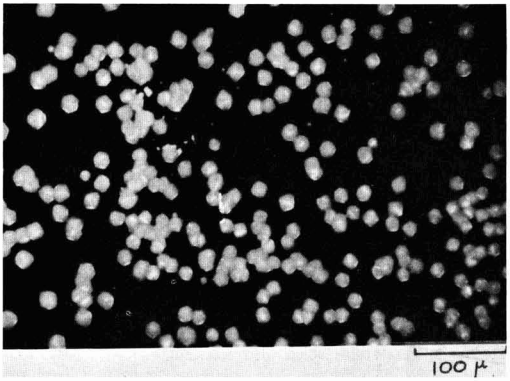

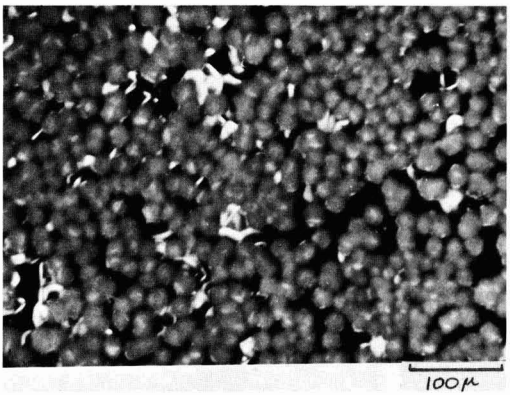

Fig. 2. Ge (111) surfaces oxidized in 7.0N HNO_3 for (a) (top) 1 hr and (b) (bottom) 3 hr.

acid concentrations the oxide nucleates and grows in patches on the surface, accompanied by severe surface etching. With continued oxidation the nuclei grow, with additional nucleation occurring, presumably at points of high local saturation, until the surface is completely covered. Thus, a protective oxide layer forms; that is, the oxide layer grows to a limiting thickness and then stops, with no further reaction taking place. These oxide nuclei adhere strongly to the surface, but for Ge samples left for long times in the less concentrated solutions the chemical attack may be so severe that, on occasion, spalling of the oxide film takes place.

At the higher acid concentrations (greater than 11*N*) nucleation occurs very rapidly at many random sites, and the surface density of nuclei is very large. This observation is in agreement with the results of Faust (3). The nucleation rate of the oxide particles on the surface is so high and the surface density so great that the nuclei do not grow to large sizes. The protective effect of the oxide layer was also noted by Cretella and Gatos (1) and Miuller and co-workers (2).

Figure 3 is a photomicrograph of a Ge (111) surface oxidized for 30.2 hr in 11.9*N* HNO_3 at 27.5°C. This surface can be compared with those oxidized in 7.0*N* HNO_3 as shown in Fig. 2. The oxide nuclei sizes are noticeably smaller than those grown at lower acid concentrations.

Oxide film growth.—In Fig. 4 are plotted the data at 27.5°C for the weight change, in mg/cm², of polycrystalline Ge samples (each point a separate sample) as a function of time in solution with no stirring. For solutions with concentration 10.2*N* and less we observed an initial net sample weight loss since the weight lost by Ge dissolution exceeds the weight gained by surface oxide growth. After a time interval, the sample weight gain from oxide film growth overtakes the weight lost by dissolution. For concentrations greater than 10.2*N*, a net sample weight gain is noted from the beginning. All of the weight change curves approach limiting values.

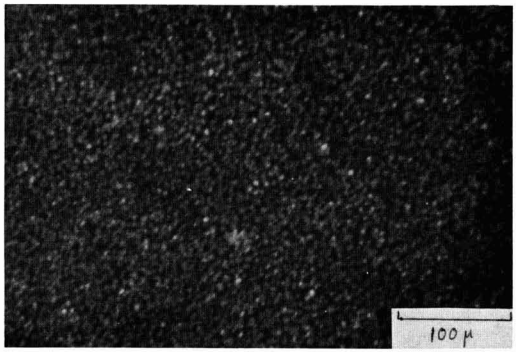

Fig. 3. Ge (100) surface oxidized for 30.2 hr in 11.9N HNO_3 at 27.5°C. Oxide nuclei sizes are notably smaller than those grown in 7.0N HNO_3.

The data for oxide film growth on Ge (111) surfaces at 27.5°C in varying HNO_3 concentration are given in Fig. 5. No induction period for oxide growth was observed at any acid concentration in the range studied although Cretella and Gatos (1) report an induction period to oxide growth at 7.5*N* HNO_3. This is probably due to differences in the preparation of the samples. The initial growth rate of the film is high, but, as the protective oxide film builds up on the Ge surfaces, the growth rate decreases, and the film thickness approaches a maximum value. This saturation value for films grown in 7.0*N* HNO_3 (Fig. 5) is seen to be on the order of five times the value for films grown in 15.6*N* HNO_3 solutions. As was discussed above, the high nucleation rate of surface oxides at the high acid concentration produces rapid saturation of the Ge surface with a protective layer. A similar trend was noted by Cretella and Gatos (1). The average oxide thickness, in microns, was calculated by assuming that the density of the surface oxide was that of the bulk hexagonal GeO_2, 4.228 g/cm³ (10). The basis for this assumption is discussed in the next section.

The surface oxide layer was observed to improve in uniformity with increasing acid concentration. Figure 6 is a comparison of single crystal Ge (100) surfaces oxidized for 12 hr in 7.5, 10.2, 11.9, and 15.6*N* HNO_3. At 7.5*N* HNO_3 the oxide layer is "patchy" while the

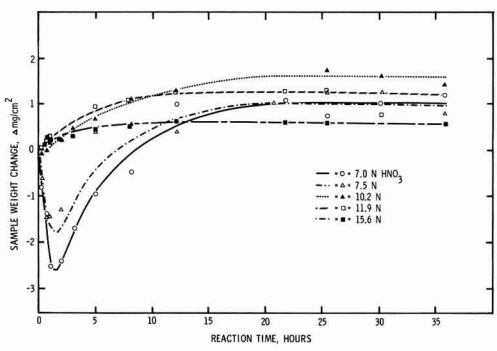

Fig. 4. Weight change of polycrystalline Ge samples with time at 27.5°C. At lower HNO_3 concentrations a net sample weight loss occurs initially.

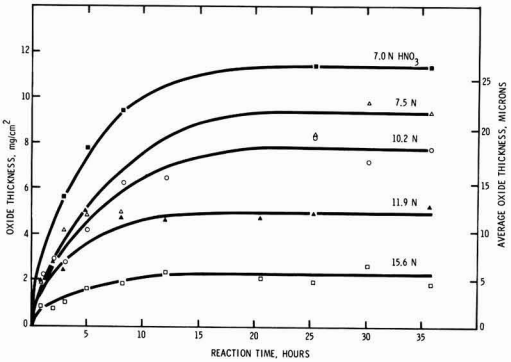

Fig. 5. Oxide growth on polycrystalline Ge (111) surfaces at 27.5°C. Film thicknesses approach saturation values.

most uniform layers are grown in 15.6*N* HNO_3. The variation in the appearance of the samples from dark to white results from the variation in visible light reflection from the surfaces with change in oxide thickness. An electronmicrograph of a Ge (100) surface oxidized for 2 hr in 15.6*N* HNO_3 at 27.5°C is reproduced in Fig. 7. The oxide nuclei density for layers grown in 15.6*N* HNO_3 is seen to be much greater than that for layers grown in 7.0*N* HNO_3 (Fig. 2).

Temperature dependence studies were not pursued to any extent since the contiguity of the oxide layers showed no marked improvements in a preliminary study. Hot nitric acid produced a layer with a higher density of fine-grained oxide nuclei than the layers grown at room temperature (9a). Faust (3) also had noted this. For long reaction times at high temperatures the acid concentration became less certain as a result of loss of nitrogen oxides. A fine-grained oxide layer was observed to grow at lower temperatures when the Ge surface was oxidized in contact with an inert surface such as polyethylene (9a).

Surface oxide characterization.—Germanium dioxide is known to exist in at least three polymorphic forms (10, 11): (*a*) hexagonal crystalline, (*b*) tetragonal crystalline, and (*c*) amorphous GeO_2. At ordinary temperatures tetragonal GeO_2 is the thermodynamically stable modification (12), but, when Ge is oxidized, the normally occurring forms are the hexagonal or amorphous GeO_2, depending on conditions. Tetragonal GeO_2 can be formed by conversion from hexagonal GeO_2 by using a fluxing agent (13). The phase diagram of the Ge-GeO_2 system has been determined (14, 15), and the transition temperature for the tetragonal to hexagonal crystalline modification has been measured to be 1033°C (12).

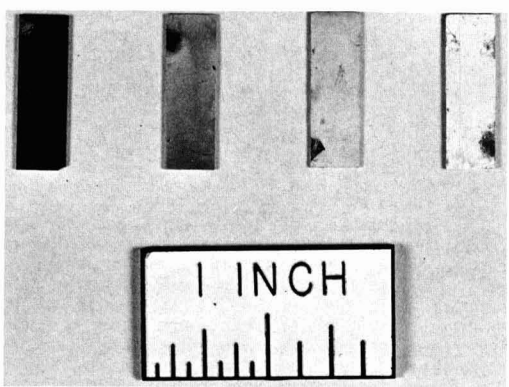

Fig. 6. Comparison of single crystal Ge (100) surfaces oxidized for 12 hr in (l. to r.) 15.6N, 11.9N, 10.2N, and 7.5N HNO_3. Film uniformity improves with increasing acid concentration.

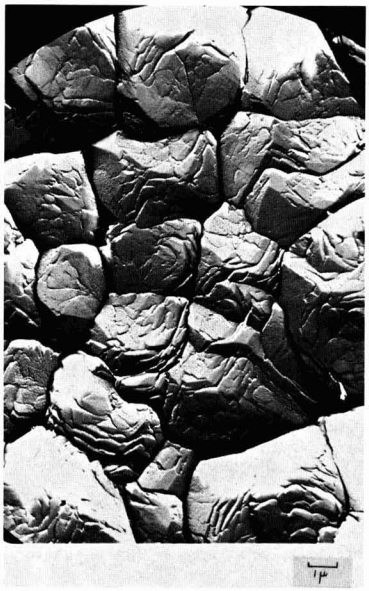

Fig. 7. Electronmicrograph of a Ge (100) surface oxidized for 2 hr in 15.6N HNO_3 at 27.5°C. The oxide layer is seen to be composed of densely packed crystalline oxide nuclei.

In order to determine the form assumed by the oxide in the nitric acid oxidation studies, structural studies were performed on the surface oxide layers by three techniques: (*a*) infrared absorption, (*b*) x-ray diffraction, and (*c*) electron diffraction. The method used for infrared absorption measurements has already been described. The spectra were compared to those published (6) on the polymorphs of GeO_2. The results indicated that the oxide layers grown in 7.0-15.6*N* HNO_3 on Ge surfaces are composed of hexagonal GeO_2. Infrared spectra characteristic of amorphous (16) and tetragonal GeO_2 were not detected.

X-ray diffraction studies were undertaken to characterize the surface oxide further. Oxidized samples were mounted in a General Electric XRD-5 unit, and diffraction patterns of the surface oxide were obtained using chromium Kα radiation. Measured d-values for the surface GeO_2 were compared to published values (17, 18). Only hexagonal GeO_2 lines were identified. No lines characteristic of tetragonal GeO_2 were detected.

Thin layers of surface oxide, grown for short periods in HNO_3, were prepared for electron diffraction studies in a Siemens Elmiskop I in an effort to determine the nature of the oxide at the Ge-GeO_2 interface. 100 kev electrons were diffracted from the thin oxide layers at low angles (1°-2°) of incidence, and measured patterns were compared with published results for GeO_2 (19). Hexagonal GeO_2 was identified, but, again, no tetragonal GeO_2 was detected in the surface oxide layers. The results of these structural studies indicate that the surface oxide layers grown on Ge surfaces in concentrated HNO_3 are crystalline hexagonal GeO_2..

Orientation effect.—The growth of oxide layers on Ge surfaces in concentrated HNO_3 appears to be affected by the crystallographic orientation of the Ge surface. Figure 8 is a photomicrograph of a grain boundary on a polycrystalline Ge (111) surface oxidized for 30.2 hr in 11.9*N* HNO_3. Faust (3) also noted a dependence of oxide film growth on the Ge surface

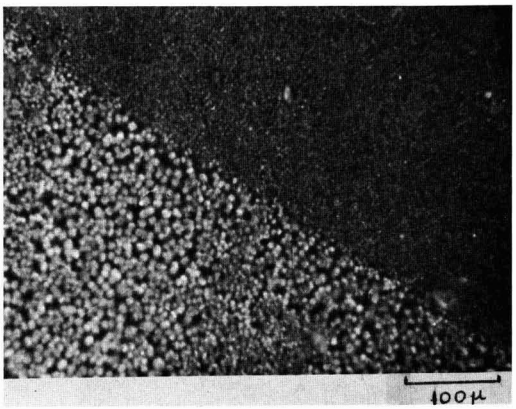

Fig. 8. Oxidation of a grain boundary on a polycrystalline Ge (111) surface after 30.2 hr in 11.9N HNO_3 at 27.5°C. An orientation effect on oxide film growth is visible.

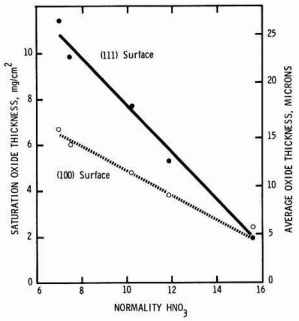

Fig. 9. Dependence of saturation oxide film thickness on HNO_3 concentration at 27.5°C. The surface orientation becomes less important with increasing acid concentration.

orientation, but quantitative data were lacking. Our study considered film growth on Ge (111) and Ge (100) surfaces. Saturation oxide layer thickness, measured by infrared absorption, is compared in Fig. 9. Two interesting features are readily apparent from the data of Fig. 9: (*a*) saturation oxide film thickness is inversely dependent on HNO_3 concentration, and (*b*) oxide film thickness is orientation dependent. The difference in film thickness with Ge surface orientation is seen to decrease with increasing acid concentration. It is interesting to note that the etching rate decreases with increasing acid concentration (1, 2), while the oxide nucleation rate increases with increasing acid concentration. An orientation effect on the etching rate of Ge in solution has been detected by others (20-22). Harvey and Gatos (21) observed that the dissolution rates were (100) > (110) > (111) for the three principal crystallographic orientations at 30°C while Camp (20) found that the order of (100) and (111) was reversed below 25°C. Schwartz and Robbins (22) studied the etching rates of Ge in HNO_3 solutions containing low concentrations of HF. Their results show that the rate dependence on orientation is (110) > (111) > (100). Miuller and co-workers (2) also noted a reduced etching rate for (100) and (110) compared to (111) surfaces. These data indicate that at the lower HNO_3 concentration the etching rate of the Ge surface may be the rate-controlling factor, while at the higher acid concentrations the nucleation rate may be the dominant factor so that the orientation of the surface becomes less important (Fig. 9). As a result, it is difficult to apply a simple diffusion model, proposed for silicon (23), to the oxidation behavior of Ge in solution.

The dissolution of Ge is evidently a complex heterogeneous reaction with simultaneous oxidation of Ge surface atoms and hydration of oxidation products followed by their transfer into solution. Nitric acid as the oxidizing agent complicates the interpretation because of the complex kinetic relationship of nitric acid with its various reaction products (24, 25). Briner and co-workers (26, 27) have shown that the oxidizing power of HNO_3 in concentrated solutions depends on the undissociated species. Cretella and Gatos find that the rate of oxidation of Ge is proportional to the product of HNO_2 and undissociated HNO_3. Their reasoning is based on the mechanism proposed by Vetter (24)

$$HNO_2 + HNO_3 = N_2O_4 + H_2O \quad \text{slow} \quad [1]$$

$$N_2O_4 = 2NO_2 \quad \text{fast} \quad [2]$$

$$NO_2 + e^- = NO_2^- \quad \text{fast} \quad [3]$$

Miuller and co-workers (2) also consider the active species to be NO_2. The apparent over-all rate of oxidation, as deduced from the observed weight changes, is related to the exposed Ge surface area. As this area decreases with the build up of a protective oxide layer, the apparent growth rate of the surface oxide decreases, and the oxide thickness approaches a saturation value. A lack of detailed knowledge of the oxidizing agent and of the exact nature of the possible oxidation products (H_2GeO_3, $HGeO_3^-$, GeO_2, . . .) that are diffusing through the surface-liquid interface, precludes a quantitative model of the oxide growth process at the present time.

Some qualitative remarks can be made however. The rate limiting process cannot be purely a diffusion process as evidenced by the orientation dependence and the way the dissolution kinetics are affected by saturating the HNO_3 with GeO_2 prior to sample oxidation. Miuller and co-workers (2) propose a chemical oxidizing-hydrating mechanism of Ge atom transfer into solution where the rate of the process is limited by the chemical heterogeneous reaction and the accompanying diffusion into solution. Their proposed mechanism follows several steps: (*i*) the exposed Ge surface atom, with an individual pair of electrons, bonds with the oxygen atom from NO_2; (*ii*) a surface dipole is formed; (*iii*) coordination bonds can be formed between protons and the oxygen atom in acid solution, Ge retains a positive charge; (*iv*) the molecule $GeO(OH)_2$ is separated from the surface as a result of hydrolysis and can react with a second NO_2 molecule; (*v*) a new surface of Ge atoms with unshared electron pairs is exposed after the oxide has gone into solution, and the cycle starts anew. The relative importance of each of these steps (plus others, perhaps) in limiting the oxide growth rate is, for the moment, speculative. Additional work on the kinetics of oxide growth will be necessary in order to establish, with any certainty, the chemical mechanism which dominates the oxidation process. Presumably, the temperature dependence studies, under consideration in our laboratory, may provide a more complete view of the reaction mechanism involved. The higher acid concentrations used in our study did not reveal any gross differences from the results published for Ge oxidation at lower acid concentrations (1, 2, 4).

Summary and Conclusions

The study of Ge oxidation in HNO_3 has been extended to high acid concentrations. Thick oxide layers can be grown on Ge surfaces in the concentration range 7.0-15.6*N* HNO_3. Film uniformity improves with increasing acid concentration. No induction period for oxide growth was observed over the acid concentration range studied. The oxide growth rate decreases smoothly with time and is not described by simple film growth laws. Saturation film thickness was observed to be inversely dependent on acid concentration. The oxide nuclei sizes at saturation film thickness decrease markedly with increasing acid concen-

tration. The saturation film thickness was found to be dependent on the crystallographic orientation of the Ge surface. This result indicates that the rate limiting step in oxide growth is probably not purely diffusion controlled. Structural studies, by infrared, x-ray and electron diffraction techniques, of the oxide layers grown on Ge surfaces in concentrated HNO_3 solutions indicate, unambiguously, that the surface oxide is crystalline hexagonal GeO_2.

Acknowledgments

The author would like to express his gratitude to D. E. Swets for the polycrystalline Ge crystals and P. A. Gudaitis for technical assistance. T. R. McKinney performed electron diffraction analyses, and Miss A. Forster performed x-ray analyses on oxidized samples. Discussions with W. A. Albers, Jr., C. E. Bleil, R. N. Hollyer, Jr., and P. V. Mohan were of much benefit to the author.

Manuscript received June 17, 1966; revised manuscript received Sept. 1, 1966.

Any discussion of this paper will appear in a Discussion Section to be published in the December 1967 JOURNAL.

REFERENCES

1. M. C. Cretella and H. C. Gatos, *This Journal*, **105**, 487 (1958).
2. R. L. Miuller, T. P. Markova, and S. M. Repinskii, *Leningr. Univers., Vestnik* (16): 106 (1959).
3. J. W. Faust, Jr., *Acta. Met.*, **11**, 1077 (1963).
4. P. P. Konorov and O. V. Romanov, *Sov. Phys.—Solid State*, **5** [10], 2225 (1964).
5. P. V. Mohan and W. A. Albers, Jr., Private communication.
6. E. R. Lippincott, A. Van Valkenburg, C. E. Weir, and E. N. Bunting, *J. Research Nat. Bur. Stand.*, **61**, 61 (1958).
7. G. Brauer and H. Müller, *Z. anorg. u. allgem. Chem.*, **287** [1-2], 71 (1956).
8. D. F. Kyser and M. F. Millea, *This Journal* **111**, 1102 (1964).
9. M. E. Straumanis and C. D. Kim, *ibid.*, **111**, 1186 (1964).
9a. W. A. Albers, Jr., and P. V. Mohan, Unpublished data.
10. A. W. Laubengayer and D. S. Morton, *J. Am. Chem. Soc.*, **54**, 2303 (1932).
11. J. H. Müller and H. R. Blank, *ibid.*, **46**, 2358 (1924).
12. J. I. Carasso and M. M. Faktor, "The Electrochemistry of Semiconductors," pp. 216-219, P. J. Holmes, Editor, Academic Press, New York (1962).
13. W. A. Albers, Jr., E. W. Valyocsik, and P. V. Mohan, *This Journal*, **113**, 196 (1966).
14. V. O. Candidus and D. Tuomi, *J. Chem. Phys.*, **23**, 588 (1955).
15. F. A. Trumbore, C. D. Thurmond, and M. Kowalchik, *J. Chem. Phys.*, **24**, 1112 (1956).
16. P. V. Mohan, Private communication.
17. W. Zachariasen, *Z. Krist*, **67**, 226 (1928).
18. V. M. Goldschmidt, *Z. physik Chem.*, **17B**, 172 (1932).
19. ASTM Powder Diffraction File; Data Cards 9-379, 4-0497, 4-0498.
20. P. R. Camp, *This Journal*, **102**, 586 (1955).
21. W. W. Harvey and H. C. Gatos, *ibid.*, **105**, 654 (1958).
22. B. Schwartz and H. Robbins, *ibid.*, **111**, 196 (1964).
23. H. Robbins and B. Schwartz, *ibid.*, **107**, 108 (1960).
24. K. Vetter, *Z. phys. Chem.*, **194**, 199 (1950); *Z. anorg. Chem.*, **260**, 242 (1949).
25. E. Abel, *Monatshefte fur Chem.*, **89**, 74 (1958).
26. E. Briner, *Helv. Chim. Acta.*, **18**, 363 (1935).
27. E. Briner and P. Bolle, *ibid.*, **18**, 368 (1935).

Precipitates Induced in GaAs by the In-Diffusion of Zinc

J. F. Black and E. D. Jungbluth

The Bayside Laboratory, research center of

General Telephone & Electronics Laboratories Incorporated, Bayside, New York

ABSTRACT

Imperfections in GaAs due to the in-diffusion of zinc at temperatures in the range of 700°-1100°C have been investigated by means of x-ray diffraction topography, optical microscopy, and infrared transmission microscopy. The imperfections, which were generated in the diffused layer, were identified as submicroscopic precipitates. Precipitation was almost unavoidable when metallic zinc was used as the diffusant source. Although precipitation could be prevented when $ZnAs_2$ was used as a source, prolonged diffusion always resulted in precipitation. It was concluded that diffusion-induced dislocations plus precipitation, or diffusion-induced precipitation alone, was occurring in our samples.

The study of defects generated in semiconductors by the in-diffusion of p- or n-type impurities has achieved considerable impetus in recent years. In particular, the generation of dislocations due to the diffusion of phosphorus or boron into silicon has been extensively investigated (1). The documentation of diffusion-induced defects in silicon is in contrast to the small amount of published information on these effects in the compound semiconductor GaAs. Recent work (2-4) has shown that surface layers with a high content of structural defects can be produced in GaAs by the vapor phase in-diffusion of zinc. Zinc is widely employed as a p-diffusant in GaAs; therefore it is imperative to define the conditions that give rise to these defects so that their occurrence may be controlled.

This paper presents some results of an investigation of zinc-diffusion-induced imperfections in GaAs. Diffused samples were examined by x-ray anomalous transmission, by infrared transmission microscopy, and by optical microscopy of etch structures. Previous indications (2) of severe lattice damage by diffusion of zinc into GaAs were confirmed, and it was established that this damage was largely due to submicroscopic precipitation in the diffused layer. It was further established that precipitation and its consequent lattice damage in the diffused GaAs could be avoided by proper control of diffusion conditions.

Experimental Techniques

Sample preparation.—The starting material was commercially available single crystal GaAs, boat-grown by the gradient freeze technique. The single crystals displayed dislocation densities ranging from about $10^2/cm^2$ to $10^5/cm^2$, as determined by etch pit counts. Wafers 0.5-1.5 mm thick were cut from these crystals and were then chemically etched or chemically polished to remove all traces of damage resulting from cutting and grinding operations. All diffusions were made by a standard technique; the GaAs samples were contained along with 1g of GaAs powder

and 10 mg of pure zinc (or in some cases with only 10 mg $ZnAs_2$) in evacuated quartz ampoules of 50 cm^3 volume. Each diffusion was carried out with one or more low dislocation density samples in the capsule in addition to other samples of high dislocation density and of differing n-doping level. The low-dislocation-density samples were required for x-ray anomalous transmission topographs, while the high-dislocation-density samples allowed evaluation of the effects of initial crystal perfection. The samples of differing n-doping level made it possible to estimate the zinc penetration profile (p-n junction depth *vs.* n-doping level) for each diffusion run. Diffusion was carried out at temperatures ranging from 700° to 1100°C for a period of 2 hr with GaAs powder and pure zinc in the capsule, unless otherwise noted. All diffusions were carried out so that the end of the capsule containing the diffusant source was maintained at a temperature 10°C below the diffusion temperature. After diffusion the ampoule was cooled by gradually withdrawing it from the furnace over a period of 2 min and then immersing it in water. In this way the contents of the capsule were cooled to room temperature within 3 min. A few diffusion runs were terminated by rapid quenching and a few by slow cooling in the furnace. Rapid quenching was accomplished by withdrawing the capsule from the furnace, plunging it into a bucket of water and crushing with a long-handled pliers. It is estimated that in this way samples were cooled to room temperature within 5 sec.

Examination of samples.—Large-area x-ray diffraction topographs of starting material with low dislocation densities were recorded by the anomalous transmission method (5). This method is highly sensitive to the perfection of the material. Highly imperfect crystals strongly attenuate the x-ray transmission, especially in the immediate vicinity of imperfections. Thus crystal imperfections are revealed as areas of reduced x-ray intensity within the x-ray topographs.

GaAs wafers studied with this x-ray method were oriented in <111> directions. The diffused junctions on the As face were always removed by chemical etching prior to recording x-ray topographs. Since defects confined to shallow surface layers, such as occur in diffused junctions, appear sharpest where the x-ray beam leaves the crystal, the wafers were always positioned so that the Ga face corresponded to the exit surface of the beam on the crystal (6). This allowed etch pit studies, which were carried out on the Ga face, to be correlated with defects shown in x-ray topographs. In many of the samples studied, the diffusions resulted in very strong x-ray absorption by the crystal, and crystal wafers were defined as being opaque to x-rays when no diffracted image could be obtained. Pictures of the diffraction topographs are photographic negatives; consequently, highly imperfect regions appear dark.

In addition to anomalous transmission studies, etch structures were also examined to reveal the presence of crystalline defects. The etch structures were developed on a Ga (111) surface by swabbing the surface with a freshly prepared mixture of one part 30% H_2O_2 and five parts 2% NaOH for 2 to 5 min. This etchant was selective to surface orientations near a (111) Ga surface and developed small pits with a well-defined triangular shape. The pits could be developed over a range of orientations, although with distortion in symmetry, as much as 10° from <111> Ga direction, thus obviating preparation of accurately oriented samples. At sample orientations more than a few degrees from <111>, however, the number of pits produced in a given sample was reduced, so all etching was carried out on surfaces within 2° of an (111) Ga surface. Etch pit counts obtained on a well-oriented wafer were in substantial agreement with etch pit counts obtained with a known GaAs dislocation etch (1 conc. $NHO_3 - 2H_2O$ solution).

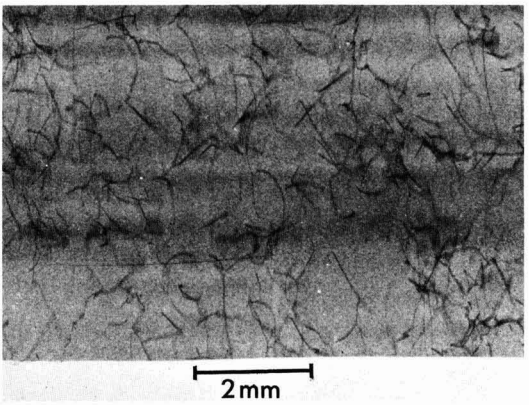

Fig. 1. X-ray topograph of low dislocation density GaAs

Infrared transmission microscopy was accomplished by means of a commercially available image converter adapted to the ocular of an inverted stage microscope. Infrared photomicrographs were recorded on Eastman Kodak Type I-M 4 x 5-in. spectrographic plates.

Results

Description of the defect structure.—The dislocation density of the samples used for most of the x-ray anomalous transmission studies was no more than 200/cm^2 (by etch pit count). Figure 1 shows an x-ray topograph typical of this material. After standard diffusions at 700° and 725°C such material showed a slight reduction in the anomalous transmission intensity, but no change in the appearance or in the number of the dislocations occurred. Furthermore, no additional defects, such as misfit dislocation networks, could be detected in the x-ray topographs. At 750°C the intensity due to anomalous transmission was reduced about 20% by the in-diffusion of zinc, and there was still no change in the dislocation structure. Standard diffusions at temperatures higher than 750°C resulted in complete x-ray absorption by the sample, indicating that a high degree of crystal lattice imperfection had been produced. The fact that the transmitted x-ray intensity was reduced (resulting in ultimately opaque samples), while the original dislocation structure was preserved indicates that the diffusion process has produced a substantially uniform microscopic strain in the crystals. Patel and Batterman (7) have reported a similar kind of reduction in anomalous x-ray transmission through silicon, caused by annealing single crystals contaminated with oxygen. These authors established the presence of microscopic strains resulting from the formation of Si-O clusters in the early stages of the precipitation of silicon oxides. This connection of microscopic strain with precipitation is significant because in the present work other evidence of precipitation, *i.e.* high densities of etch pits, appeared in the diffused layer, concomitant with the reduction in anomalous x-ray transmission.

Figure 2 shows three photomicrographs of etched cross sections of diffused samples mounted and polished to produce a (111) Ga plane of section. In an investigation of the precipitation of Cu_2O in copper single crystals Young (8) has described etch structures strikingly similar to those of Fig. 2a. Young observed triangular pit etch structures in oxygen-doped copper single crystals annealed to cause small Cu_2O particles to form. Each particle, even when submicroscopic in size, gave rise to a surrounding cluster of densely packed etch pits, which was interpreted to be due to dislocations produced by plastic deformation which accompanied the formation and growth of the precipitate particles. The dense pitting that is observed throughout the surface layer of the

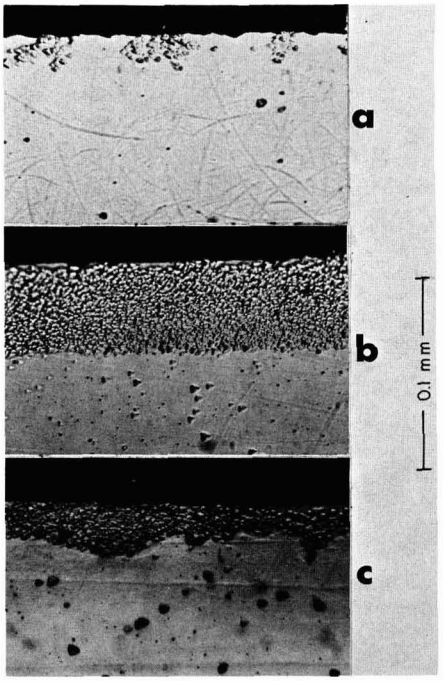

Fig. 2. Etched cross sections of GaAs wafers diffused from a pure zinc source: a, 2 hr at 750°C; b, 2 hr at 800°C; c, 24 hr at 700°C.

sample diffused at 800°C is therefore consistent with the complete x-ray opacity of the GaAs slices that were subjected to standard diffusions at temperatures greater than 750°C. Additional data and pertinent comments for diffusions performed with pure zinc as a source are contained in Table I.

The etched cross sections of samples diffused at a temperature of 700°C showed no evidence of imperfections in the diffused layer even though there had been appreciable diffusion of zinc into these samples (attested by the development of a p-n junction 8μ deep in samples of $n = 5.9 \times 10^{18}/cm^3$). There was, nevertheless, a defect structure layer present that was so thin (1 or 2μ) that it was difficult to develop a clearly defined etch structure in cross section. This layer was detected by carefully etching the diffused surface of the samples. The fact that such a layer, however thin, was detected is again consistent with the reduction in transmitted x-ray intensity noted for these samples. These results suggest a pre-precipitation

Table I. Data on diffusions for 2 hr from a pure zinc-powdered GaAs source

Temp, °C	Depth of p⁺p junction, μ	Comments
700	7	Slight reduction in x-ray transmission, no change in etch structure
725	10	Slight reduction in x-ray transmission, no change in etch structure
750	20	20% reduction in x-ray transmission, scattered etch pit clusters in p⁺ layer, sample still transparent to IR
775	35	Completely opaque to x-rays, high etch pit density in p⁺ layer
800	50	Completely opaque to x-rays, nearly opaque to IR, high etch pit density in p⁺ layer
900	110	Completely opaque to x-rays, completely opaque to IR, high etch pit density in p⁺ layer
1000	125	Completely opaque to x-rays, completely opaque to IR-high etch pit density in p⁺ layer
1100	125	Completely opaque to x-rays, completely opaque to IR, high etch pit density in p⁺ layer

incubation period of about 2-hr duration in 700°C standard diffusions. At diffusion times longer than two hours at low temperatures, *e.g.*, 24 hr at 700°C, deep zinc penetration was achieved, and the diffused layers were again so highly defective as to be opaque to x-rays. Such a layer is shown in cross section in Fig. 2c.

The infrared absorption increased along with the x-ray absorption, but was not nearly as sensitive a measure of diffusion-induced damage. For instance, the sample of Fig. 2c, though completely opaque to x-rays was still somewhat transparent to IR radiation; the sample of Fig. 2b was opaque to x-rays and very nearly opaque to IR; while a sample with structure like that of Fig. 2b but diffused at 900°C was opaque to both x-rays and IR. In no instances were structures such as decorated dislocations revealed by IR transmission microscopy. Note that the starting dislocation density (etch pit density) is preserved in the region below the diffused layer of Fig. 2c. The only difference apparent between damaged layers produced at low diffusion temperatures (700°C) and those produced at higher temperatures (800°C) was that the boundaries of the layers produced at the lower temperatures were more irregular. This probably is related to the fact that the diffusion-induced damage begins in isolated regions of these samples (see Fig. 2a). These regions, indicated by the etch pit clusters, spread out and penetrate more deeply with time. Until the diffusion depth is large compared with the mean distance between clusters, however, we continue to see evidence of the heterogeneous beginnings of the diffusion-induced damage in the uneven boundary of the defect structure layer.

The samples shown in Fig. 2 had initial dislocation densities of $10^3/cm^2$ to $10^4/cm^2$ by etch pit count. The starting dislocation density did not have a strong effect on the occurrence of highly defective layer structures; the defect structure could be equally well developed in samples with starting dislocation densities of $200/cm^2$ and $100{,}000/cm^2$. This indicates that the diffusion-induced damage was not critically dependent on the presence of existing dislocations, as would have been the case, for example, if the damage were due to decoration of existing dislocations. Clustering of etch pits such as is seen in the sample diffused at 750°C in Fig. 2a was specially prevalent in the early stages of diffusion at temperatures in the range 700°-750°C. Again, if the production of diffusion induced damage was heterogeneous, it would be most apparent in the early stages of its occurrence.

When $ZnAs_2$ was used as the source of zinc, it was possible to preserve the crystal perfection in the diffused layers if the diffusions were not too deep and were not made at too high a temperature. For example, samples diffused for ½ hr at 800°C from a pure zinc-powdered GaAs source developed 25μ deep layers that were opaque to x-rays, while samples diffused for eight hours at 800°C from a $ZnAs_2$ source developed 25μ deep layers with no measurable reduction in anomalous transmission. This was most interesting because of the experience that some workers have reported in fabricating efficient light-emitting diodes (9). Diffusions from a $ZnAs_2$ source were found to yield better GaAs electroluminescent and laser diodes than diffusion from a pure zinc source. It would appear that these results can partly be explained by the differences in defect structure between p-layers prepared from pure zinc source and p-layers produced from $ZnAs_2$.

At diffusion temperatures higher than 800°C or for long diffusion times at 800°C (24 hr), diffusion from a $ZnAs_2$ source ultimately developed highly imperfect layers. One of the effects of using $ZnAs_2$ as a diffusant source is a lengthening of the incubation period before the onset of diffusion damage. The distribution of etch pits in the defect layer was found to be quite different from that observed for pure zinc diffusions. A good example of the structure produced by a $ZnAs_2$ diffu-

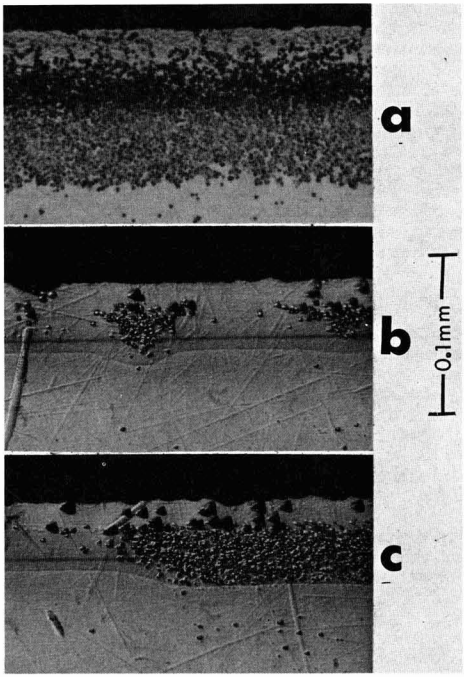

Fig. 3. Etched cross sections of GaAs diffused from $ZnAs_2$ source: a, 8 hr at 900°C; b and c, 24 hr at 800°C.

sion is shown in Fig. 3a. Although a detailed explanation of why the etch pit distribution is so different for $ZnAs_2$ cannot be given at this time, it is probably a result of the much less steep penetration profile produced by diffusion from $ZnAs_2$ (9).

A particularly good example of clustering of defects was observed in a sample diffused from $ZnAs_2$ and is shown in Fig. 3b and 3c. This sample has been etched with a p-n junction etch as well as with the hydroxide-peroxide defect structure etch. It can be clearly seen in Fig. 3b that clustering of etch pits is closely associated with a deeper penetration of the p-n junction. The heavy dark line just above the p-n junction was seen in p-type samples as well as in n-type samples and was identified as a p^+-p boundary by previous studies (10). By comparison with companion samples doped with tellurium to various levels of free electron concentration, the zinc concentration at the p^+-p boundary in the samples of Fig. 3b and 3c was estimated to be $6 \times 10^{18}/cm^3$, and at the p-n junction $3.0 \times 10^{17}/cm^3$. The deeper penetration of the p-n junction in regions of etch pit clusters suggest that the diffusion process induces defects to appear first in regions where there is already some kind of lattice disturbance in the crystal. This is also in line with our observation that clustering was more prevalent in samples of initial high imperfection. However, the kind of defect assumed to be inherent in the host matrix was not evident by x-ray contrast methods before the diffusion cycle. It would be expected that regions of imperfect lattice structures would show enhanced mobility of a diffusant (deeper penetration of p-n junction). Pilkuhn and Rupprecht (9) have shown similar evidence of enhancement in p-n junction depth in regions of crystal defects in GaAs. Evidence that these diffusion-induced defects can seriously affect device properties is shown in Fig. 3c, where the defects extend all the way to the p-n junction.

Optical micrographs of etch structures of a diffused sample are correlated with x-ray topographs in Fig. 4. Dense clustering of defects which occurred in this

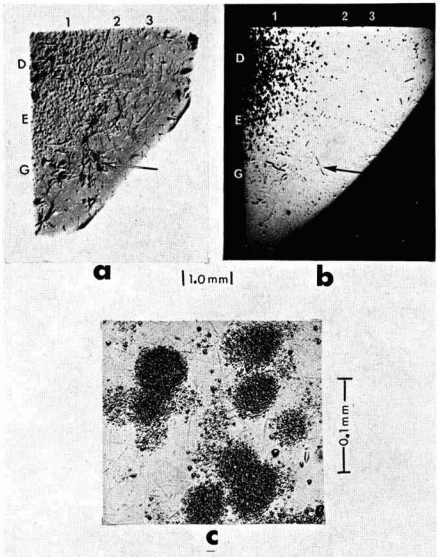

Fig. 4. a, X-ray topograph of clustered defect structure; b, corresponding etch structure; c, details of etch pit clusters.

sample, diffused at 750°C, is evident in Fig. 4a and b within region D1. More clustered defects are seen in the x-ray topograph than the etched surface, which is the plane of diffusion, because only the clusters that intersect the surface are seen by etching, while all of the clusters are seen by x-ray transmission. The clusters were also areas of reduced IR transmission, but the optical contrast was so slight that it could not be clearly registered on our IR sensitive plates. An enlarged view (Fig. 4c) shows that the defect clusters are composed of triangular type pits. These clusters of etch pits have the same structure as those shown in cross-section in Fig. 2a. The dark broad images in the diffraction topograph, such as are indicated by the arrows, are scratches introduced after the diffusion.

Figure 5 shows x-ray topographs of a sample before and after an 800°C diffusion. The sample was initially 1.0 mm thick and was diffused to a depth of 50μ. Because the diffused layers were opaque to x-rays, it was necessary to remove the diffused layer from the B side (the As side) and then angle lap and etch away nearly the entire layer on the A side to obtain the topograph shown in Fig. 5b. Notice that where the diffused layer has been completely removed, Fig. 5c, and region C in Fig. 5b, the original dislocation structure has been preserved. The original structure is still reflection dependent; hence no precipitation along dislocations has occurred in the bulk of the wafer. A clear line of demarcation separates what remains of the defective diffused layer on the A side from the underlying undisturbed material. The diffraction contrast at this boundary resembles the contrast seen in the clusters of Fig. 4. By means of control runs, *i.e.*, runs in which the treatment of samples was identical except that there was no zinc (or $ZnAs_2$) present in the capsule, it was established that only when zinc was indiffused did defect structures appear. This confirmed that these effects were due to zinc and not to thermal stresses, or the precipitation of impurities independent of the presence of zinc.

There was good reason to believe that these defects were due to precipitation, presumably a zinc-complex. A detailed argument and analysis of the data to justify this belief will be presented in the Discussion section, but we mention it at this point because the experiments to be described in the next three paragraphs were performed to confirm whether pre-

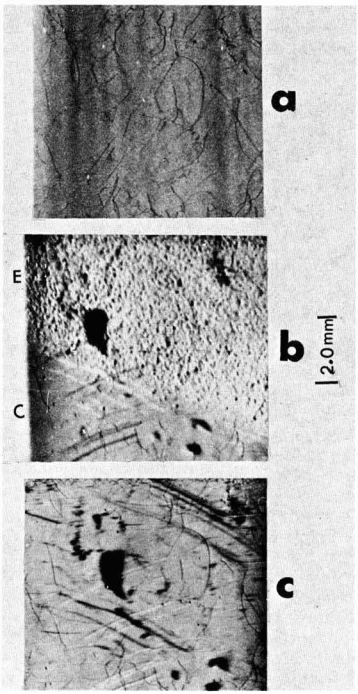

Fig. 5. X-ray topographs of zinc diffused GaAs: a, original sample; b, sample after diffusion at 800°C with B layer removed and A layer partially removed, region E indicates the A layer remaining and region C is the original bulk material; c, sample after removal of additional 30μ from A side. The dark spots are due to deep damage.

cipitation was responsible for the defect structures we had observed.

Experiments with zinc (melt) doped GaAs.—Electron probe analysis of several standard diffused samples established that the concentration of zinc at the boundary of the layer of high etch pit density was about 5 x 10^{18}/cm^3. This agreed with the observation that the boundary of this layer usually coincided with the p^+-p junction (Zn = 6 x 10^{18}/cm^3) in standard samples.

On samples melt-doped with zinc up to 3.7 x 10^{19} atoms/cm^3 (free hole concentration equal to zinc concentration within 10%) no trace of defects besides grown in dislocation tangles (about 5 x 10^3/cm^2) could be observed either by etching or by x-ray analysis. Even when the melt-doped samples were additionally annealed (in the presence of their own powder) under conditions of time and temperature where defects consistently occurred by diffusion into undoped GaAs, the zinc-melt-doped samples remained unaffected. However, when the zinc-melt-doped samples were subjected to a standard zinc diffusion at 1000°C the samples developed a defect layer structure and became opaque to x-rays and IR radiation.

The attenuation of optical transmissions was far stronger in diffused samples than in melt-doped samples for material of equal thickness, even though the concentration of zinc in the diffused samples was less than that in the melt-doped samples. For example, for a 100μ thick diffused layer with a zinc concentration ranging from 4 x 10^{19} atoms/cm^3 to 5 x 10^{18} atoms/cm^3(p^+-p boundary), optical transmissions over the range of wavelengths from 0.9 to 1.2μ (s-1 image convertor) were nil, while a 100μ thick wafer of the zinc-melt-doped GaAs was transparent in the same spectral region. If the diffusion-induced damage were largely a result of precipitation, this result might be expected except that the intensity of the IR attenuation implies a rather large amount of precipitate ($>>$ 10^{18} atoms/cm^3).

To ascertain whether the defects were due to some impurity unknowingly introduced during the preparation and diffusion processes, samples were analyzed by emission spectroscopy both before and after diffusion. Only three impurities were detected Cu 3-6 ppm, Mg 5-15 ppm, and Si 10-50 ppm, and their concentrations were unchanged by the diffusion process. It is possible that the residual impurities or that undetected impurities, such as oxygen, are responsible for the diffusion damage, but whatever the nature of the defect structures, they occurred only when zinc was indiffused.

Quenching experiments.—We found that the defect structure that appeared in zinc-diffused GaAs was identical whether samples were quenched from the diffusion temperature to room temperature in a matter of seconds or whether they were slowly cooled in the diffusion furnace over a period of many hours. The character of the defect structure was inspected by etching within 15 min of quenching, and by x-ray anomalous transmission within 30 min after quenching. In both instances the defect structure was fully developed. It was therefore concluded that the defects were occurring during the in-diffusion of zinc or were occurring extremely rapidly during cooling.

In a study of zinc diffused GaP, Gershenzon and Mikulyak (16) observed precipitate structures which they tentatively identified as zinc-rich. They likewise were not able to quench their samples fast enough to prevent the occurrence of these precipitates. It was concluded that the precipitation was occurring during the diffusion period and, furthermore, thermodynamic considerations then implied that the precipitate phase could not be pure zinc. These considerations apply in the present circumstances as well.

Free carrier concentration vs. zinc concentration.—The reduction in the free carrier concentration is a frequently used measure of the progress of precipitation in semiconductors (11). Thus the free carrier concentration was compared with the zinc concentration (average zinc concentration $\geq$ 5 x 10^{18} atoms/cm^3) in diffused samples known to contain well-developed defect (precipitate) structures. These samples were opaque to IR radiations as well as to x-rays. We did find samples which exhibited a free carrier (hole) concentration less than the zinc concentration, but we also found samples which showed agreement (within $\pm$30% spectroscopic analysis accuracy) between the free hole concentration and the zinc concentration. The ratio of free charge carriers to zinc depended in a systematic way on the exact diffusion conditions for each sample. These results are, however, the subject of a separate investigation (12) and they will not be described further in this paper.

The occurrence of these defects did not depend critically on the purity of the GaAs or on the particular method of crystal growth. It was induced in many different crystals, p-doped to 4 x 10^{19}/cm^3, n-doped to 6 x 10^{18}/cm^3 and undoped n = 1.2 x 10^{16}/cm^3, μ = 5,000 cm^2/v-sec, grown by the gradient freeze method in quartz boats, in crystals taken from ingots zone refined in graphite boats, and in crystals pulled from graphite, alumina, or boron nitride crucibles.

Discussion

The introduction of an impurity atom into a crystal by vapor phase diffusion can have two distinct but not necessarily separate effects on the lattice perfection: (*i*) the diffusion can cause dislocations to be introduced to accommodate lattice deformation effects of the solute atom; (*ii*) the diffusion can cause precipitates to appear. Solute atom deformation of the host lattice usually results in highly regular networks of dislocation lines. Diffusion induced precipitation

can be of several kinds and can occur (*a*) during cooling, because of reduced solubility of the diffusant at low temperatures; (*b*) during diffusion because of formation of stable compounds between the diffusant and the constituents of the host lattice; (c) during diffusion because of exolution of residual impurities, similar to the "common ion effect" which is well known in solution chemistry. We believe that the clusters and layers of high etch pit density produced in our samples by the in-diffusion of zinc are areas in which submicroscopic precipitation has occurred. No individual precipitate particles could be observed at magnifications up to 1000X. Although it seemed very likely that the diffusion induced precipitate was zinc, or some substance containing zinc as a major constituent, the experimental data were not sufficient to permit us to describe the precipitate in any detail.

The appearance of diffusion-induced dislocations will not automatically cause the appearance of precipitate structures, but if there are species present which are liable to precipitate, diffusion-induced dislocations will hasten their appearance. If precipitation occurs during in-diffusion or during a slow cool, dislocations of a type other than solute deformation dislocations will occur. These dislocations will be due to differences in the specific volume of the precipitate phase and the matrix phase and will be more localized and more intense than diffusion-induced dislocations.

In the following sections our data will be analyzed to show that both diffusion-induced dislocations with precipitation or precipitation alone are occurring. None of our results indicate the production of diffusion-induced dislocations alone.

The case for precipitation alone.—In samples diffused from pure zinc at temperatures below 775°C ($ZnAs_2$ source at temperatures below 850°C) there was no evidence of the regular networks of dislocation traces that are so characteristic of solute-induced lattice deformation. The x-ray topographs do, however, show that for diffusions from pure zinc the crystal perfection is being uniformly degraded (x-ray absorption is being increased). Such behavior is characteristic of the early stages of precipitation in highly perfect crystals (7). The heterogeneous nature of the defect structures observed in the early stages of their formation is characteristic of precipitation but not necessarily of diffusion induced dislocations. Also the distinct incubation period that is observed before damage to the crystal structure appears and the fact that this period is inversely proportional to both the temperature and the partial pressure of zinc (concentration of zinc), is consistent with a precipitation reaction. Furthermore the strong IR absorption which was observed in the defect structures is to be expected if precipitation is occurring but not if dislocations alone are present.

For those samples subjected to standard diffusions from a pure zinc source at 800°C or above, it was not possible to quench the precipitation. If the precipitation were supposed to have occurred during the diffusion period, this result is understandable. If the precipitation were supposed to have occurred after the diffusion, *i.e.,* during the cooling period, it is difficult to argue for a pure precipitation reaction unless the samples had initial high dislocation densities. The fact is that these samples had initial dislocation densities as low as 100/cm². For the moment we shall defer the question of precipitation during diffusion to pursue the argument for diffusion-induced dislocations with precipitation.

The case for diffusion-induced dislocations with precipitation.— If dislocations were generated during standard diffusions from pure zinc at 800°C and higher we could, at least qualitatively, explain the failure to quench the precipitation by citing the strong effects that dislocations are known to have in accelerating solid-state precipitation reactions (13, 14). The important question of whether or not dislocations are actually generated in GaAs by the in-diffusion of zinc has been answered by the recent work of Schwuttke and Rupprecht (4). They showed that under certain conditions the diffusion of zinc into GaAs can cause the regular arrays of dislocations characteristic of lattice solute deformation. For prolonged diffusion, however, a layer of intense crystal damage was produced. Although this may have been a layer of submicroscopic precipitation similar to the layers we have observed, it would be necessary to verify this by other techniques. For those samples of the current investigation in which we could have observed dilatational dislocations, had they occurred, the diffusion conditions were sufficiently different from those of Schwuttke and Rupprecht to explain the absence of dislocations. In those samples in which solute dilation dislocations should have been observed we are prevented from confirming their occurrence because of the high density of microprecipitation.

It must be emphasized that at high defect concentrations it is not possible to distinguish between crystal imperfections due to lattice solute deformation, *i.e.,* misfit dislocations, and crystal damage due to precipitation. The rather dramatic onset of the defect structure between 725° and 775°C (see Table I) is, nevertheless, consistent with the introduction of dislocations during the diffusion process. It has long been known that, at a temperature close to 2/3 T_m (15), where T_m is the absolute melting temperature, many of the so-called intermetallic compounds, including the III-V zinc blend type semiconductors, undergo a change in mechanical properties from brittle to ductile behavior. For GaAs 2/3 T_m is equal to 738°C, which is within the temperature range where our experiments suggest that dislocations are introduced. Whether precipitation occurred during in-diffusion or during cooling, diffusion-induced dislocations would be expected to enhance the rate of precipitation.

There are cases known, especially involving high dislocation densities ($> 10^6$/cm²) (13) where precipitation reactions occur with time constants of a second or so, *i.e.,* fast enough to make quenching very difficult. However, the amount of precipitant exsolved within this second or so is only a few parts per million. There are no cases extant of nearly instantaneous precipitation of relatively large amounts of material ($>$ 100 ppm) in the solid state. Although precipitation of a few parts per million of an impurity is sufficient to explain the strong attenuation of x-rays (7) it does not seem to be nearly enough to account for the strong IR absorption and scattering in our samples.

For example, the precipitation in the zinc-diffused regions of the crystals was sufficient to render these regions (only several thousandths of an inch thick) quite opaque to optical transmission as viewed through an IR image convertor (0.9 to 1.2μ wavelength). The average absorption coefficient of such a diffused layer containing between 4 x 10^{19} and 5 x 10^{18} zinc atoms/cm³ (800-100 ppm, respectively) was greater than 500 cm^{-1}. The average free-carrier concentration p = 2.0 x 10^{19}/cm³ agreed with the average zinc concentration within 30% which means that no more than about 6 x 10^{18} zinc atoms/cm³ could have been precipitated. The average free-carrier absorption coefficient for p-type GaAs in the 0.9-1.2μ spectral interval for a carrier concentration range from 5 x 10^{18}/cm³ to 4 x 10^{19}/cm³ is only about 200 cm^{-1} (20). Thus we must account for an excess "absorption" amounting to more than 300 cm^{-1}, apparently with a precipitate structure involving no more than 6 x 10^{18} zinc atoms/cm³ (120 ppm). Gershenzon and Mikulyak (16) have published optical measurements of zinc diffused GaP which indicate an excess absorption of 20 cm^{-1} in a sample containing precipitates and in which $\bar{p}$ = 2 x 10^{18} holes/cm³. No information was provided on the actual zinc concentration present in these samples, but the conditions of diffusion indicates an average zinc content of at least 5 x 10^{18} atoms/cm³. Therefore the excess absorption of 20 cm^{-1} appears to be due

to more than 3 x 10^{18} atoms/cm^3 of precipitated zinc. These measurements of zinc diffused GaP suggest that we need considerably more than 6 x 10^{18} zinc atoms/cm^3 (precipitated) to explain an excess IR attenuation of 300 cm^{-1} in GaAs. Nevertheless, we cannot be certain that 6 x 10^{18}/cm^3 or even 1 x 10^{18} atoms/cm^3 of precipitated zinc is not enough to explain the observed effects. A firm description of the sizes, distribution, and composition of the precipitate particles necessary to explain a given degree of particulate attenuation is required to calculate the corresponding zinc concentration. The authors could find no experimental papers in the literature that could provide an unqualified answer to this problem. The pursuit of a solution to this problem can be conducted on theoretical grounds, but this is not within the scope of this paper.

Let us return, now, to discussion of the case for precipitation during the diffusion period with or without help from diffusion-induced dislocations. The results of several investigations (17) of zinc doped GaAs have shown that the solubility of zinc in solid GaAs is greater than 7 x 10^{19} atoms/cm^3 at temperatures in the range of 700°-1100°C. How, then, can we explain the occurrence of precipitates in GaAs diffused with much less than 7 x 10^{19} atoms/cm^3 of zinc at these temperatures. The exsolution of residual impurities or the undetected introduction of other impurities during the diffusion offers a ready explanation. The question of the exsolution of residual impurities is a difficult one to answer experimentally, but the question of the introduction of impurities during diffusion is one that can be answered by experiment. Because the quartz capsules that we used were not of the highest purity, it was possible that undetected impurities had been leached out of the quartz to contaminate our samples during the diffusion period. For example, impurities such as Li, Na, and Ca, which are difficult to detect by the usual emission spectroscopy techniques, are known to be present in the range of 5-10 ppm in ordinary quartz. To check the possibility that impurities were being leached from the quartz, several GaAs wafers were diffused in Spectrasil capsules. Spectrasil is a highly pure grade of quartz, but nevertheless the zinc diffused samples still developed the usual precipitate structures. The fact that the free-carrier concentration was substantially equal to the zinc concentration in many samples with well-developed precipitate structures supports the premise that the precipitates are composed of an element other than zinc. On the other hand the fact that some samples do show much less free carriers than zinc is evidence that zinc *does* precipitate. It must be remembered, too, that because of problems in attaining a better degree of accuracy in the zinc analysis, *i.e.*, better than 30% accuracy, those samples which showed agreement of zinc analysis and free carrier concentration, still could have had, at the very least, 1.5 x 10^{18} zinc atoms/cm^3 tied up in the precipitate structure.

Although, the occurrence of crystal damage due to precipitation does not depend critically on the identity of the precipitating species, the identification of the species is critical, if we wish to understand the precipitation processes.

Conclusions

None of the recent experimental-theoretical investigations (18, 19) of the diffusion of zinc into GaAs take account of the possibility of diffusion induced damage, especially precipitation. Clearly, the current investigation shows that one must qualify such investigations: (*i*) by establishing the absence of such precipitation; (*ii*) by demonstrating that precipitation is of no consequence to the diffusion processes; or (*iii*) by modifying the transport equations to take account of precipitation. In particular it would be interesting to determine if the isoconcentration diffusion studies of Chang and Pearson (19) were conducted in the presence of diffusion-induced defects since these investigators employed vapor phase in-diffusion of zinc to prepare zinc-doped GaAs wafers for subsequent isoconcentration diffusion with radioactive zinc.

Acknowledgments

The authors wish to express their thanks to R. J. Modena, J. Daly, and J. Hurley for their technical assistance in various phases of the experimental work. They also wish to acknowledge the support and encouragement of Dr. B. Smith and Mr. D. J. Bracco in carrying out this investigation.

Manuscript received March 24, 1966; revised manuscript received Aug. 5, 1966.

Any discussion of this paper will appear in a Discussion Section to be published in the December 1967 JOURNAL.

REFERENCES

1. S. Prussin, *J. Appl. Phys.*, **32**, 1876 (1961); G. H. Schwuttke and H. J. Queisser, *ibid.*, **33**, 1540 (1962); M. L. Joshi and F. Wilhelm, *This Journal*, **112**, 185 (1965).
2. J. Black and P. Lublin, *J. Appl. Phys.* **35**, 2462 (1964); E. D. Jungbluth and J. Black, *Bull. Am. Phys. Soc.*, **10**, 581 (1965).
3. E. D. Jungbluth, *This Journal*, **112**, 580 (1965).
4. G. H. Schwuttke and H. Rupprecht, *J. Appl. Phys.*, **37**, 167 (1966).
5. H. Barth and R. Hoseman, *Z. Naturforsch.*, **13a**, 792 (1958).
6. E. D. Jungbluth, *Appl. Phys. Letters*, **7**, 302 (Dec. 1, 1965); V. Gerold and F. Meier, *Z. Physik*, **155**, 387 (1959).
7. J. R. Patel and B. W. Batterman, *J. Appl. Phys.*, **34**, 2716 (1963).
8. F. W. Young, Jr., "On the Formation of Dislocations Around Precipitate Particles of Cu_2O in Cu," p. 103, "Direct Observation of Imperfections in Crystals," Newkirk and Wernick, Editors, Interscience Publishers, Inc., New York (1962).
9. H. Rupprecht and C. Z. LeMay, *J. Appl. Phys.*, **35**, 1970 (1964): M. H. Pilkuhn and H. Rupprecht, *Trans. AIME*, **230**, 296 (1964).
10. J. Black, *This Journal*, **111**, 924 (1964); J. Marinace, *ibid.*, **110**, 1153 (1963).
11. H. Reiss and C. S. Fuller, "Diffusion Processes in Germanium and Silicon," Chap. 6, "Semiconductors," N. B. Hannay, Editor, Reinhold Publishing Co., New York (1959).
12. J. Black, To be published.
13. A. G. Tweet, *J. Appl. Phys.*, **30**, 1244 (1959).
14. J. N. Hobstetter, "Effect of Imperfections on Germanium and Silicon," Chap. 12, "Semiconductors," N. B. Hannay, Editor, Reinhold Publishing Co., New York (1959).
15. "Mechanical Properties of Intermetallic Compounds," J. H. Westbrook, Editor, John Wiley & Sons, Inc., New York (1960).
16. M. Gershenzon and R. M. Mikulyak, *J. Appl. Phys.*, **35**, 2132 (1964).
17. M. S. Panish, *J. Phys. Chem. Solids*, **27**, 291 (1966); L. L. Chang and G. S. Pearson *ibid.*, **25**, 23 (1964).
18. D. L. Kendall, Doctoral Dissertation Stanford University, Department of Materials Science Report No. 65-29 (1965).
19. L. L. Chang and G. S. Pearson, *J. Appl. Phys.*, **35**, 1960 (1964).
20. D. E. Hill, *ibid.*, **36**, 3405 (1965).

Decorated Dislocations and Sub-Surface Defects Induced in GaAs by the In-Diffusion of Zinc

J. F. Black and E. D. Jungbluth

The Bayside Laboratory, Research Center of

General Telephone & Electronics Laboratories Incorporated, Bayside, New York

ABSTRACT

The diffusion of zinc into GaAs can, under certain conditions, cause defects to appear in the diffused crystal. These diffusion-induced crystal imperfections have been investigated by means of x-ray anomalous transmission topography, optical microscopy, and infrared transmission microscopy. There were three kinds of defects observed: submicroscopic precipitation in the diffused surface layer, decorated dislocations below the diffused surface, and an unidentified defect structure which extended throughout the undiffused region of the wafers. Diffusion-induced decoration of dislocations initially present in samples was observed in crystals previously melt doped with zinc, but not in undoped or in n-doped crystals. The unidentified deep-lying imperfections occurred only in wafers with very intense precipitation in the diffused surface layer.

In a recent publication (1) the authors showed that the diffusion of zinc into GaAs could induce submicroscopic precipitation in the diffused layer. This precipitation was always accompanied by severe crystal damage in the diffused layer and in many cases there was sufficient precipitation to cause strong attenuation of optical transmissions. This paper presents the results of further investigations of zinc-diffused GaAs in which visible precipitate structures and damage to the underlying crystal were observed in addition to submicroscopic precipitation in the diffused surface. The visible precipitates, which were composed of submicroscopic particles condensed onto curvilinear dislocations initially present in the crystals, caused high attenuation of x-ray anomalous transmission and high attenuation of infrared (IR) transmissions. Zinc-diffusion-induced damage to the underlying crystal caused high attenuation of x-rays, but had little effect on transmission of optical radiations.

Experimental Techniques

Sample preparation.—The starting material was single crystal GaAs grown in quartz boats by the gradient freeze technique. Dislocation densities, by etch pit count, ranged from 50/cm^2 to 50,000/cm^2. Wafers cut from the crystals were ground flat and parallel and were then chemically polished in a Br_2-methanol solution to remove the crystal damage resulting from cutting and grinding operations. The final thickness of the wafers ranged from 0.5 to 1.5 mm. Unless otherwise indicated, the diffusions were carried out according to the following conditions: 10 mg of pure zinc 1g of GaAs powder in evacuated quartz capsules of 50 cm^3 volume (ordinary grade quartz); the diffusion time was 2 hr at a fixed temperature ranging from 800° to 1000°C. These diffusions are referred to as standard diffusions. Each diffusion included several samples of differing n-doping level in addition to the samples used for study of diffusion-induced defects. The purpose of the n-doped samples was to allow an estimate of the zinc penetration profile for each diffusion run, by measurements of p-n junction depth *vs.* n-doping level. At no time during the diffusion cycle was the temperature of the end of the capsule initially containing the diffusant source allowed to rise above that of the region containing the GaAs powder and the samples. The samples, which were laid flat in the boat with the Ga face up, were separated from the powder by a quartz partition. All diffusions were terminated by gradually withdrawing the ampoule from the furnace over a period of 2 min and then immersing it in water. It is estimated that by this procedure the contents of the capsule were cooled to room temperature within 3 min.

Examination of samples.—X-ray diffraction topographs were recorded by the anomalous transmission method (2) using Cu radiation. Highly imperfect regions of crystals strongly attenuate the x-ray transmission, especially in the immediate vicinity of the imperfections. Such regions show up as dark areas in the topographs of Fig. 2, 4, and 6. The GaAs wafers studied by the x-ray anomalous transmission technique were oriented in <111> directions. The diffused layers on the As face were always removed by chemical etching prior to examination by x-rays, and the wafers were positioned so that the Ga face corresponded to the exit surface of the x-ray beam. Because defects in shallow surface layers, such as occur in diffused samples, appear sharpest where the x-ray beam leaves the crystal (3), this procedure allowed etch structures produced on the Ga face to be correlated with defects shown in x-ray topographs.

Etch structures were developed on the Ga (111) surface by swabbing the surface with a freshly prepared mixture of one part 30% H_2O_2 and five parts 2% NaOH solution for several minutes. This etchant was selective to surface orientations within 10° of a (111) Ga surface and developed small pits with a well-defined triangular shape. Etch pit counts on a <111> Ga oriented wafer were in agreement with counts of etch pits developed by 1 part concentrated HNO_3 — 2 parts H_2O, a well-known dislocation etchant for GaAs. All etching with the NaOH-H_2O_2 defect etch was carried out on surfaces within 2° of a (111) Ga surface.

Infrared transmission microscopy was accomplished by means of a commercially available image convertor adapted to the ocular of an inverted stage microscope. Infrared photomicrographs were recorded on Eastman Kodak Type I-M 4x5 in. Spectrographic Plates.

Experimental Results and Discussion

Unless the diffusion of zinc into GaAs is properly controlled, intense submicroscopic precipitation will occur in the diffused layer. This precipitation will cause the appearance of an etch structure like that shown in Fig. 1b. In addition, such precipitation causes strong attenuation of x-ray anomalous transmission wavelengths and strong absorption (in excess of that corresponding to the free carrier absorption) of near-infrared radiation. A detailed description and discussion of these structures can be found elsewhere (1).

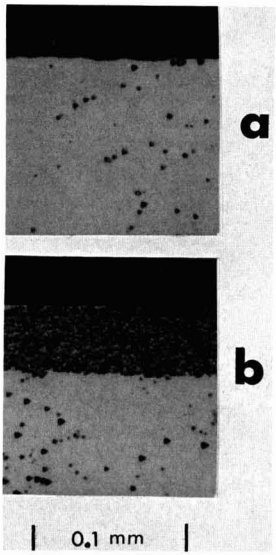

Fig. 1. Etch structure of GaAs sample: (a) initial etch structure, (b) after sample was subjected to a standard diffusion (see text) at 800°C. The plane of section is a (111) Ga plane normal to the surface of the sample. The layer of high etch pit density is a region containing submicroscopic precipitation.

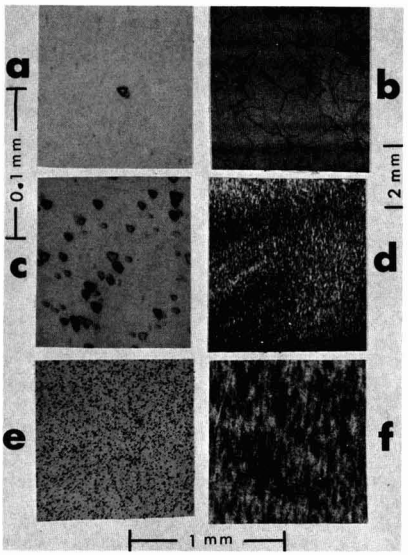

Fig. 2. Etch structures (on the left) and x-ray topographs (on the right) of a GaAs sample. Note the difference in scale between (a), (c) and (b), (d). (a) Initial etch structure, (b) initial x-ray structure, (c), (e) and (d), (f) etch structure and x-ray structure, respectively, of the crystal after it was subjected to a standard diffusion and after removing the damaged precipitate containing layer.

It is important to note here, however, that in samples in which submicroscopic precipitation had occurred it was found that the concentration of zinc along the sub-surface boundary of the precipitate containing layer was usually close to 1×10^{19} atom/cm^3. In crystals diffused under standard conditions at temperatures of 800°C or lower in which such precipitation had occurred, the careful removal of the damaged precipitate-containing layer was found to yield the underlying crystal essentially in its original state of crystal perfection (1). In standard diffusions performed at temperatures of 900°C or higher the crystal damage was not confined to the diffused layer but extended throughout the bulk of the wafer. The character of this subsurface damage was, however, different from the damage induced in the diffused surface layer.

An example of damage below the diffused layer is seen in the photographs of Fig. 2. A 1-mm thick wafer whose initial etch pattern is shown in Fig. 2a, and whose x-ray topograph is shown in Fig. 2b was diffused with zinc to a measured depth of 120μ. The initial etch pit count was 150/cm^2. After diffusion, 320μ were removed from each face, and the etch structure and x-ray topograph of the zinc-free substrate was recorded, Fig. 2c and 2d. The etch pit count after diffusion was $\sim$ 250,000/cm^2. Figure 2e and 2f compare the x-ray topograph and the etch structure of the zinc-free substrate on the same scale. As expected from the high etch pit count, the sample is nearly opaque to x-rays. A crystal which is opaque to x-rays is defined as a crystal whose anomalous transmission properties are so much reduced due to regions of imperfect lattice structure that no diffracted image can be obtained. Examination of the sample under IR transmission (0.9 to 1.2μ wavelength) showed little change in the IR transmissivity and no IR absorption structure like that suggested by the x-ray topograph. It is clear that diffusion has caused an increase of more than three orders of magnitude in the defect concentration of the crystal lattice below the diffused layer.

Because these defects occurred in a region that was essentially free of zinc ($<$ 5 ppm), and because the defects did not show up under IR microscopy, they cannot be submicroscopic precipitates of the type found in the diffused layer. This raises the question of the nature and the origin of these subsurface defects. One possibility is that we are observing precipitation, but in such an early stage of development that it is detectable by x-ray topography but not by IR transmission microscopy. The concentration of these subsurface defects was, however, too high to determine whether they were dislocations or precipitates by observation of the reflection dependence of individual defects in the x-ray topograph of Fig. 2d. If we suppose that these defects are due to precipitation, then we must explain how the presence of high concentrations of zinc and/or the presence of precipitates in the surface layer can cause precipitation deep in the interior of the crystal. For example, to what impurity can we attribute such precipitation? Spectroscopic analysis before and after diffusion showed no increase in residual impurities nor any (spectroscopically detectable) additional impurities. Though the nature of these deep-lying defects was not clearly established, the occurrence of dislocations in crystal material underlying a severely damaged surface layer is not inconsistent with the formation of such a layer. The existence of precipitation in the zinc-diffused layer is concomittant with the presence of high internal stresses in this layer. The more intense the precipitation the stronger the surface layer becomes and the higher the surface stresses become. Eventually these surface layer stresses exceed the yield strength of the interior GaAs crystal and dislocations are introduced. This would explain why interior defects were not produced by all diffusion runs; they only occur when the precipitation is sufficiently intense to cause stresses in the interior crystal lattice exceeding the yield strength. In this respect it is significant that in most of the crystals with interior crystal damage the precipitation in the surface layer was great enough to render this layer completely opaque to IR transmissions.

Further evidence that considerable stresses can be produced by the diffusion of zinc into GaAs is shown in Fig. 3. These are photomicrographs of diffused GaAs crystals that were cleaved normal to the diffused layer

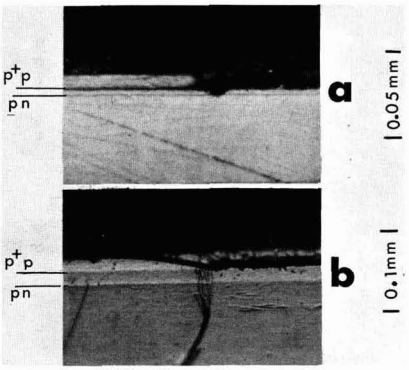

Fig. 3. Etched cross-sections of diffused and cleaved GaAs. (a) 800°C pure zinc source for 10 min, n(Te) = 3.1 x 10^{17}/cm^3, sample has been mounted and polished after cleaving, (b) $ZnAs_2$ source 800°C for 1 hr, n(Te) = 1.1 x 10^{18}/cm^3, curved lines are cleavage steps.

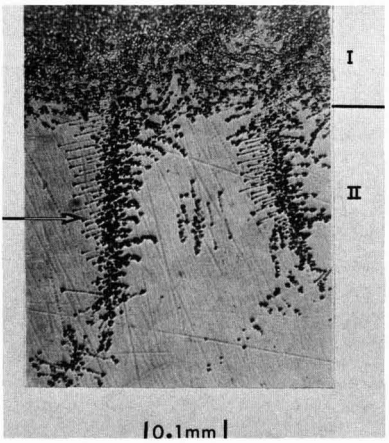

Fig. 5. Etched cross-section of zinc-(melt)-doped GaAs after standard zinc diffusion at 1000°C. I, region of general microprecipitation, opaque to x-rays; II, region of decorated dislocations (arrows).

in the process of fabricating injection electroluminescence devices. The material, which was <111> oriented, showed a tendency to fracture parallel to the plane of diffusion along the p^+-p boundary, indicating the presence of residual stress at this boundary. Such behavior would be expected of diffused zinc-blende-type crystals in which stresses were built up by the diffusion process. Diffusion-induced stresses become locked-in along the diffusion boundary when the sample is cooled from the diffusion temperature. This occurs because the yield strength of zinc-blende-type semiconductor crystals increases rapidly as the temperature is lowered and eventually exceeds the diffusion stresses. The diffusion stresses can then no longer be relieved by slip in the crystal and become locked-in. X-ray extinction contrast topographs of profile sections of zinc-diffused samples, published recently by Schwuttke and Rupprecht (4), also show regions of high residual stress immediately beneath a heavily damaged surface layer.

To determine whether precipitation could be made to occur in samples already doped with more than 5 x 10^{18}/cm^3 zinc, some melt-doped samples were subjected to annealing treatments. The samples were annealed in the presence of their own powder to prevent both out-diffusion of zinc and the decomposition of the sample. Figure 4 shows an x-ray topograph of a zinc-doped wafer before the annealing treatment. The dislocation density is about 5000/cm^2 by etch pit count and consists of individually resolved and tangled curvilinear dislocations. Although the zinc content of the melt doped samples was 3.7 x 10^{19} atoms/cm^3 (which was considerably more than the zinc concentration at which precipitation occurred in standard diffused samples), annealing of the samples for 2 hr at 1000°C had no effect on the crystal perfection. Contrary to expectations, there was no reduction in x-ray anomalous transmission nor in IR transmissivity; neither was there any change in the x-ray topograph (dislocation contrast), etch structure, or IR transmission structure. However, when a melt-doped sample was zinc diffused at 1000°C for 2 hr, it became opaque to x-rays and a precipitate structure was developed. This structure is shown in cross section in the photomicrograph of Fig. 5. In addition to the layer of submicroscopic precipitation and high etch pit density (region I), usually generated in GaAs by such a diffusion treatment, there was a region (II) about 200μ thick just ahead of this layer in which other more distinctive types of etch structures were seen. These etch structures were best correlated with x-ray anomalous transmission topographs and with infrared transmission microscopy in a sample sectioned parallel to the diffused layers. Thus the structures seen in Fig. 6a, 6b, and 6c were recorded after the diffused layers had been removed from both the A and B faces of a sample and after the sample had been further lapped and polished down to 100μ thickness in the region designated II in Fig. 5. To obtain good infrared transmission photomicrographs it was necessary to make the sample thin in order to minimize the optical absorption due to the high background zinc level. Notice that the dislocation structure in Fig. 6a is no longer visible as fine lines (compare with Fig. 4), but in place of the individual curvilinear dislocations and tangles, broad diffraction contrast images now appear. The very strong infrared absorption of these structures indicates that they too are precipitates of some kind. Examination of carefully polished samples as well as lightly etched samples at magnifications of 1000X failed to show any trace of sharp boundaries around these structures such as would have been present if a precipitate phase of microscopic dimensions had formed. This is the result expected if these structures have been formed by the decoration of dislocations, since this process leads to condensation of particles of submicroscopic size onto the dislocation line.

In Fig. 7 an area of the sample is shown at higher magnification to resolve details of the precipitates by

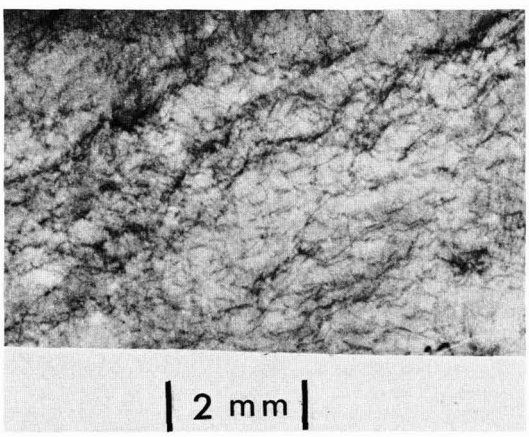

Fig. 4. X-ray topograph of zinc-(melt)-doped GaAs before diffusion.

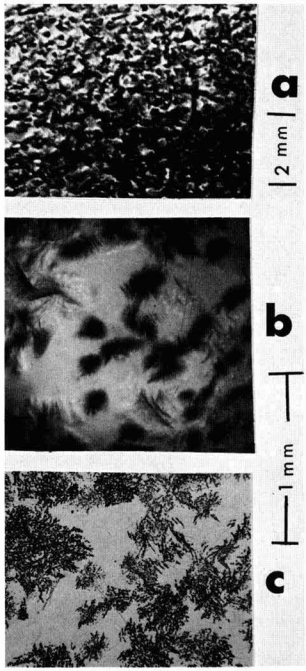

Fig. 6. Defects in region II, (see Fig. 5) sample preparation described in text. (a) X-ray topograph, (b) IR transmission photomicrograph, (c) etch structure of the area shown in (b).

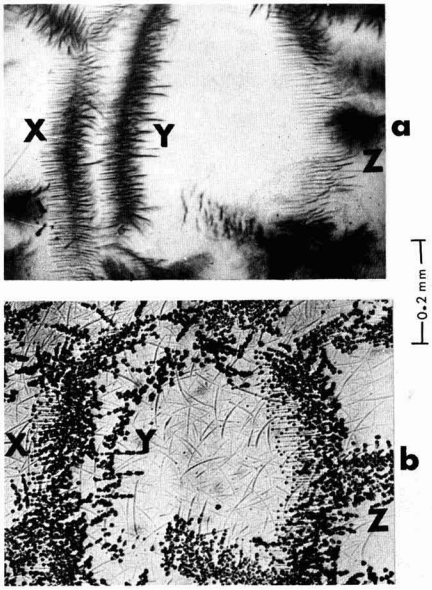

Fig. 7. Details of the precipitates and decorated dislocations in region II. (a) IR transmission structure, (b) etch structure of the area shown in (a).

infrared transmission and visible reflection microscopy. Figure 7a is the infrared transmission photomicrograph of the sample before etching, and Fig. 7b is the photomicrograph of the etch structure of the same region. The curved centipede-like configurations are the broad images seen at low magnification in Fig. 6a and are very similar to decorated dislocations that are revealed in silicon by the Dash method of Cu precipitation (5). The dislocation marked Y in the infrared photo is only partially visible in the etched sample because it is not as close to the plane of section, as for example, the dislocation at X. Infrared absorption not associated with decorated dislocation lines but associated with clusters of etch pits (microprecipitation) can be seen at locations such as Z in the figure. A very close correspondence exists between the infrared transmission structure and the etched structure.

There are several features of the defect structures in Fig. 6 and 7 that merit further discussion. The direction of the dislocations is more or less random, but the direction of the decorating spikes is quite regular and in fact lies almost normal to the direction of the dislocation. Most of the spikes lie along two of three directions the projections of which are 120° apart on the (111) plane, which is the plane of polish as well as the plane of diffusion. On a given dislocation practically all of the decorating spikes lie along the same direction. Also, in curvilinear dislocations long enough to show changes in direction greater than 10° or 15°, such as X and Y in Fig. 7a, the decoration becomes less intense as the direction of the dislocation line approaches the direction of the spikes. This is in agreement with observations of dislocations in GaP decorated by indiffusion of zinc (6). Very similar effects are observed in Cu decorated silicon (5, 7) where it has also been established that precipitate needles are oriented in <110> directions perpendicular to the Burgers vector of the particular dislocation or dislocation segment they decorate. This could also be the case in the present instance, though more detailed data are necessary to make definite conclusions. Abrahams and Buiocchi (8) have recently described etch structures in GaAs essentially the same as those associated with the precipitate spikes in Fig. 7. They identified their etch structures as decorated dislocations from etching behavior alone. Our observations, while confirming the conclusions of Abrahams and Buiocchi, provide more convincing evidence that these etch structures are due to decorated dislocations.

The appearance of a decorated dislocation structure, such as shown in Fig. 6 and 7, was unique to the diffused zinc-melt-doped GaAs samples. Despite diligent examination of many other zinc diffused samples, which were initially undoped or n-doped not a trace of similar structures was found. A comparison of spectroscopic analysis of the zinc-doped material before and after diffusion showed no new (spectroscopically detectable) impurities after the diffusion and no increase in the impurities initially present. There were only three impurities detected; Cu (4 ppm), Mg (5 ppm), and Si (30 ppm).

To determine if the regions containing precipitates were of significantly different composition than the surrounding crystal, electron probe microanalysis was conducted in region I and along the backbone of the centipede-like structures in region II. Since precipitation was observed only after the indiffusion of zinc, it was expected that more zinc would be found in the precipitates than elsewhere in the diffused crystal. However, zinc content in regions of precipitation was found to be no higher than in the surrounding precipitate-free material (where Zn = 4.0×10^{19} atoms/cm^3). Only near the surface of the diffused layer (about 50μ below the surface in region I) did the zinc concentration rise above that of the initial zinc doping level. This, in fact, was the only evidence that zinc had actually been diffused into the crystal.

Residual impurities were the next most likely precipitants. The Cu content was also determined to be no higher at the precipitates than in the surrounding regions. The limit of detection for Cu in GaAs was estimated to be the same as that for Zn in GaAs which is about 100 ppm. Electron probe microanalysis for Si and Mg, the other (known) residual impurities,

failed to show concentration of these elements at precipitates either. The Si and Mg analysis are not too meaningful though, since the limits of detection for these elements in GaAs were quite high (> 1000 ppm).

It has recently been shown (9) that submicroscopic precipitation in zinc-diffused GaAs is definitely zinc rich. Moreover, it has been established (1) that the critical concentration of diffused zinc necessary for the appearance of these precipitates is about 5×10^{18} atoms/cm^3. Thus the failure to observe a zinc concentration in excess of the background (initial) zinc concentration in the precipitates of regions I and II can be explained as follows. Since we need only 5×10^{18} zinc atoms/cm^3 (diffused) to form precipitates, the total zinc concentration at precipitates in the diffused melt-doped crystal need only be 4.5×10^{19} atoms/cm^3, not much different from the background zinc doping (4.0×10^{19} atoms/cm^3) in the crystal. Such a difference could not have been clearly distinguished by the electron probe since this was just about the limit of the analytical precision for zinc in this concentration range. If there had been much more than 5×10^{18} atoms/cm^3 excess zinc, say at least 1×10^{19} atoms/cm^3, it would have shown up in the probe analysis. It appears that only indiffused zinc is capable of decorating these dislocations initially present in the zinc-doped GaAs.

Acknowledgments

The authors wish to express their thanks to R. J. Modena, J. Daly, and J. Hurley for assistance in various phases of the experimental work. They also wish to acknowledge the support and encouragement of Dr. B. Smith and Mr. D. J. Bracco in carrying out this investigation.

Manuscript received Aug. 23, 1966.

Any discussion of this paper will appear in a Discussion Section to be published in the December 1967 JOURNAL.

REFERENCES

1. J. F. Black and E. D. Jungbluth, *This Journal*, **114**, 181 (1967).
2. H. Barth and R. Hoseman, *Z. Naturforsh.*, **13a**, 792 (1958).
3. E. D. Jungbluth, *App. Phys. Letters*, **7**, 302 (1965); V. Gerold and F. Meier, *Z. Physik*, **155**, 387 (1959).
4. G. H. Schwuttke and H. Rupprecht, *J. Appl. Phys.*, **37**, 167 (1966).
5. W. C. Dash, *ibid.*, **27**, 1193 (1956).
6. M. Gershenzon and R. M. Mikulyak, *ibid.*, **35**, 2132 (1964).
7. L. Fiermans and J. Vennik, *Phys. Stat. Sol.*, **12**, 277 (1965).
8. M. S. Abrahams and C. J. Buiocchi, *J. Appl. Phys.*, **37**, 1973 (1966).
9. J. Black, *This Journal*, **113**, 163C (1966).

Preparation and Properties of Epitaxial Gallium Phosphide

G. S. Kamath and D. Bowman

Xerox Corporation, Webster, New York

ABSTRACT

Gallium phosphide has been grown epitaxially by open tube vapor transport using Ga and PCl_3 as starting materials. The over-all reaction for the process can be represented by $5Ga + 2PCl_3 \rightarrow 2GaP + 3GaCl_2$. The undoped GaP obtained is p-type with carrier concentration $\sim 10^{14}$ cm^{-3} and mobilities up to 150 cm^2 v^{-1} sec^{-1} at 300°K. The transport properties as well as the mass spectroscopic analysis are presented and demonstrate the high purity of the GaP. The addition of water vapor to the hydrogen carrier gas progressively raises the resistivity of the p-type epitaxial layer. Semi-insulating GaP has been produced by this method with resistivities over 10^{10} ohm cm.

Gallium phosphide has been grown by many variations of the vapor transport process starting from the presynthesized polycrystalline form (1) as well as from the elements, Ga and P, themselves (2). In the present investigation Ga and PCl_3 were used as starting materials.

The two major objectives were to ascertain the over-all mechanism of the process and to study the influence of water vapor in the carrier gas on the nature of the epitaxial deposit.

Experimental Procedure

The apparatus used is shown schematically in Fig. 1 and is similar to the one reported by Oldham (3). Some innovations of special significance are the use of an Engelhard palladium diffusion purifier for the hydrogen carrier gas and the fully glass-enclosed solenoid-operated valves which eliminate all greased joints and valves for controlling gas flow. Low flow rates of hydrogen (30-80 cm^3 min^{-1}) plus the use of a bubbler in the gallium boat ensure thorough mixing of PCl_3 and Ga at the source temperature. The temperature profile was optimized to grow pure gallium phosphide. The source and substrate temperatures were comparatively low and gave GaP with minimum contamination from the GaAs substrate and the quartz reaction tube. The graded junction normally formed between GaAs and GaP was held to a minimum even though this resulted in some strain in the epitaxial layer. The minimum temperature for epitaxy at a practical growth rate ($\sim$10 μ/hr) was found to be about 780°C. The flow rates used were about 35 cm^3/min. H_2 through PCl_3 kept at 0°C. The ice point was chosen because the vapor pressure of PCl_3 is a rapidly varying function of the temperature and accurate control of this parameter is essential to maintain steady growth conditions at the substrate. The (111) A face of n-type GaAs was used for deposition as it proved to be the best suited for rapid growth of a

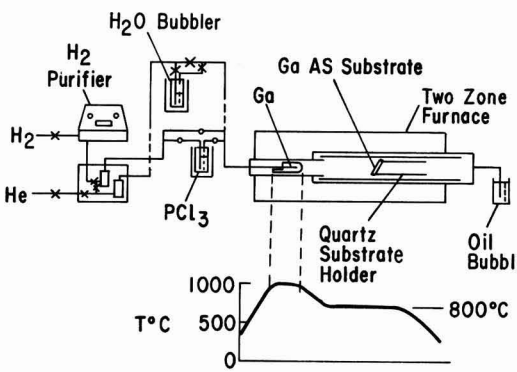

Fig. 1. Schematic of the GaP deposition train and the furnace temperature profile.

homogeneous epitaxial layer. The deposition rates were about 40 μ/hr and layers grown varied from 200μ to a few millimeters in thickness.

After deposition, the GaAs was removed with aqua regia and the side of the epitaxial layer adjacent to the GaAs lapped to remove any graded junction. This procedure yielded single crystals of GaP with arsenic contamination of only a few hundred ppm. Previous studies report an arsenic impurity in the per cent range (4, 9). Another important observation singular to the present work is that p-type GaP was invariably obtained in the normal undoped runs. Comparable experiments in the literature report low resistivity n-type deposits (3, 4), presumably due to sulfur or other impurities.

X-ray Laue patterns as well as etching and polishing studies confirm the epitaxy of the GaP, and optical absorption measurements from 0.4-10μ indicate the material to be pure with no detectable GaAs contamination. The purity of the samples is further confirmed by mass spectroscopic analysis, the results of which are given in Table III.

A slight modification of the apparatus was made to study the effect of water vapor on the deposit. Figure 1 shows the side arm with the water bubbler at a controlled temperature. It permits the addition of known amounts of water vapor into the carrier gas.

Electrical resistivity and the Hall coefficients were measured on several representative samples as a function of temperature. The contacts used were mainly pressure type to gallium dots ultrasonically applied to the clean GaP surface. When properly prepared, these contacts were found quite satisfactory for p-type material, i.e., ohmic and low resistance.

Results and Discussion

The over-all reaction.—The three possible reactions that should be considered are the following.

$$2Ga + PCl_3 \rightarrow GaP + GaCl_3 \quad [1]$$

$$5Ga + 2PCl_3 \rightarrow 2GaP + 3GaCl_2 \quad [2]$$

$$4Ga + PCl_3 \rightarrow GaP + 3GaCl \quad [3]$$

It must be emphasized that only the over-all reaction is being considered in its simplest form. The data now available does not warrant a discussion of the many complex intermediate steps.

Even the actual reaction probably involves more than one of these, but it was hoped one would be dominant. It has been assumed in the literature (5) that [1] is the most probable from analogy with the comparable GaAs reaction and because $GaCl_3$ is the most stable chloride. Preliminary results from the present investigation were inconsistent with this postulate, and this led to a systematic study of the over-all reaction mechanism. The pertinent data given in Table I covers over 50 deposition runs.

Column 3 shows the agreement between calculated and observed values for the amount of PCl_3 used to transport 50g of gallium. This quantity can be measured accurately by difference in volume before and after the run. On the contrary, the amount of gallium phosphide formed (column 4) is difficult to determine since it is in large part deposited on the quartz tube and cannot be removed completely. Both values are

Table I. Characteristics of the three principal reactions

Reaction No.	Efficiency,* %	PCl_3 used cm³/50g calc.	PCl_3 used cm³/50g obs.	GaP formed g/50g calc.	GaP formed g/50g obs.	End prod. Ga (cl)$_x$
1	50	31		36		$GaCl_3$
2	40	24.6	23-25	28	20-28	$GaCl_2$
3	25	15.4		17		GaCl

* Efficiency: Ga converted to GaP/Ga used up. All calculations made assuming 50g Ga source being used up in the reaction.

Table II. Influence of water vapor on the resistivity of the epitaxial GaP layer

No. of runs	p_{H_2O}, mm Hg	ρ, ohm cm	p_{O_2} calc., mm Hg
15	0	10^2-10^5	
5	0.1	10^2-10^5	10^{-14}
5	0.1-0.5	10^3-10^8	10^{-13}
10	1	10^8	10^{-13}
4	10	10^{10}	10^{-12}

seen to be in good agreement with those predicted by reaction [2]. Further, the grayish halide deposited at the cool exit side of the reaction tube can be shown to be $GaCl_2$, with properties (such as the melting point) described by Laubengayer and Schirmer (6). The dichloride invariably shows some dissociation into Ga + $GaCl_3$. These results suggest that [2] is the dominant over-all reaction under the conditions of transport.

Water vapor experiments.—The addition of small amounts of water vapor to the carrier gas affects the properties of the epitaxial layer drastically as can be seen from Table II.

The resistivity of the layer rises with increasing partial pressure of water vapor in the carrier gas. The role of oxygen in raising the resistivity of III-V compounds in general is well known (7). As the effect here is quite similar, it was assumed that the water vapor acts as a source of oxygen in the reaction zone. This led to the rough estimate of the oxygen present in the gas as follows. The concentration of water vapor in the carrier gas was determined from the flow rate of hydrogen through the water bubbler. Using the dissociation constant of water (18), the equivalent partial pressure of oxygen was calculated for the highest temperature in the reaction zone. This was used for making a qualitative comparative estimate of the amount of oxygen in the reaction zone. The complicated nature of the various reactions in the total process precludes any refined quantitative approach. The point of interest is that the use of water vapor allows the addition of oxygen to the hydrogen in concentrations less than 1 ppm. The values obtained appear in column 4, Table II.

Over thirty runs were made with controlled addition of water vapor into the hydrogen carrier gas. The results show that, with increasing water vapor concentration, the epitaxial layer stays p-type until extensive gallium oxide formation takes place. There is a systematic and reproducible variation in the resistivity of the GaP epitaxial layer as a function of the partial pressure of water vapor (p_{H_2O}). In electrical characteristics, the acceptor level changes from 0.4 to 0.9 ev with increased p_{H_2O}. The result is in agreement with the observations of D'Yakanov and coworkers (9).

The exact role of oxygen is not clear, and several possibilities suggest themselves. Oxygen may interact with the 0.4 ev level p-type impurity in two ways. (*i*) It may react with the impurity in the gas phase and prevent it from reaching the GaAs substrate or, (*ii*) it may be incorporated in the epitaxial layer and interact with the 0.4 ev level.

Mass spectroscopic analysis results show that if (*i*) is the mechanism, the variation in resistivity is not due to interaction of oxygen with Si as has been suggested for GaAs (10), since Table III shows that similar amounts of Si are present in both high and low resistivity samples. It can also be seen from the data that there is no systematic variation of any detectable impurity with the resistivity of the layer. The possibility remains that the impurity concerned may be one below detection limits.

The alternative (*ii*) is more complicated. As a donor, oxygen could act as a compensating n-type impurity. Gershenzon and co-workers (8) indicate a 0.47 ev donor level for oxygen. Such a level should give rise to n-type conductivity when the oxygen concen-

Table III. Results of mass spectroscopic analysis and electrical measurements on the epitaxial GaP

Sample No.	Si*	As*	B*	Al*	ρ, ohm cm	μ, cm v^{-1} sec^{-1}	n, cm^{-3}
A32	1.6	?	0.9	0.9	1.1×10^3	60	1×10^{14}
A38	8.2	400	0.07	1.5	4×10^3	140	1.2×10^{13}
A49		80	0.3	2.0	3×10^3	80	3×10^{13}
B9	6.0	2400	0.08	18.5	3×10^3	62	4×10^{13}
B10	0.3	2000		0.02	1×10^3	90	6×10^{13}
B11	6	2000	0.06	17	3×10^{10}	40	5×10^{6}
B60		80	0.2	6.0	5×10^{10}	40	3×10^{6}

* All values for impurity concentrations are in parts per million. Detection limits for most impurities 0.01-0.1 ppm.

tration is progressively increased. No such change has been observed which might indicate that the oxygen level, if present, is much deeper. If the oxygen level were deeper than the 0.9 ev acceptor level, it could compensate the 0.4 ev acceptor level, but never achieve high enough electron concentration to yield n-type samples. Alternatively the solubility of the oxygen may be governed by the concentration of the acceptor impurity at the 0.4 ev level. Identification of, and controlled doping experiments with, the acceptor and oxygen are necessary to determine which of these alternatives is the controlling factor in producing high resistivity GaP layers. Until such studies are available, the above models will have to be tentative suggestions only.

Several samples were analyzed by mass spectroscopic methods, and the results appear in Table III. The classic impurities in III-V compounds like groups II and VI and copper are below detection limits. The absence of several of these with shallow levels in the forbidden band, especially the group VI, is further confirmed by the transport properties given in the next section. The group III and V impurities present should be electrically neutral. The main impurity detected, silicon, does not seem to play the role generally allocated to it. Previous results (11, 12) report it to be a net shallow donor. At least at concentrations below $10^{17}/cm^3$ this is in disagreement with the present data. In this region silicon would have to be either self compensating or a net acceptor. Recent results on electroluminescence (13) in gallium phosphide infer the possibility of Si having a p-type level in GaP. Only a much more detailed study can lead to an unequivocal solution to this problem.

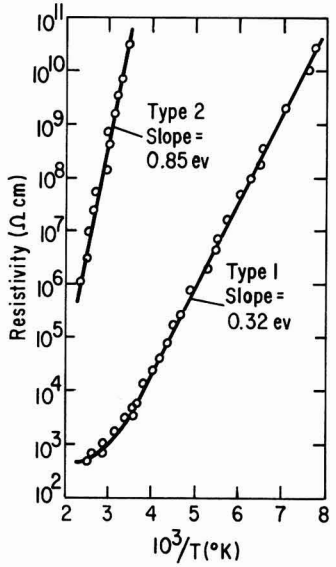

Fig. 2. Resistivity vs. 1/T for GaP. Type 1, low resistivity p-type (undoped); Type 2, high resistivity p-type (doped).

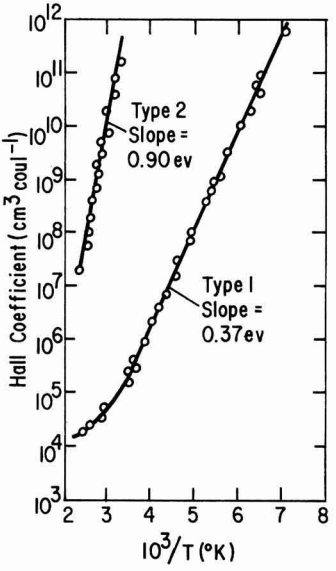

Fig. 3. Hall coefficient vs. 1/T for GaP, type 1* and type 2* (* see Fig. 2).

Transport properties.—Figure 2 shows the resistivity as a function of temperature for two types of samples; type 1, undoped low-resistivity p-type; and type 2, high-resistivity material grown at $P_{H_2O} > 0.1$ mm Hg (vide Table II). Type 1 ranged up to 10^6 ohm cm (300°K) in resistivity whereas type 2 exceeded 10^7 ohm (300°K).

Figure 3 gives the Hall coefficient as a function of temperature for the same samples. Since the Hall coefficient has a linear variation over six orders of magnitude a one-carrier system is assumed and the Hall mobility is then given by $R_H\sigma$.

Figure 4 represents the Hall mobility as a function of temperature for the two sets of samples. All type 1 samples show a similar variation in resistivity and Hall coefficient over a wide range of temperature. Type 2 samples could only be studied over a small

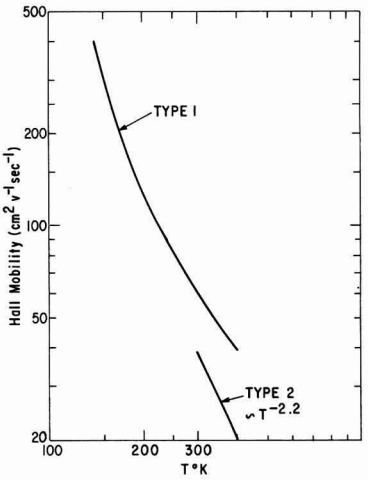

Fig. 4. Hall mobility vs. T for GaP, type 1* and type 2*

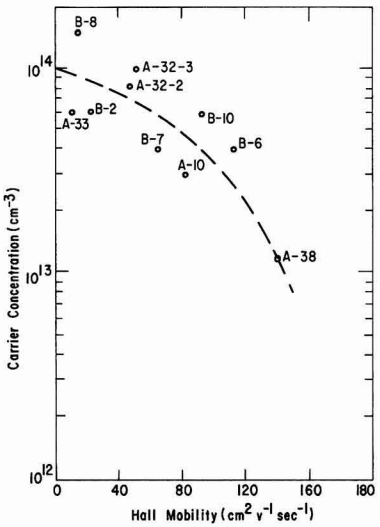

Fig. 5. Carrier concentration vs. Hall mobility at 300°K

range of temperature due to their high resistivity. The $T^{-2.2}$ dependence observed, consequently, has limited significance.

It is instructive to compare the results on type 1 samples with those in the literature. Alfrey and Wiggens (14) reported some results on p-type material with a carrier concentration $\sim 10^{17}$ cm^3 and mobility $\mu \sim 70$ cm^2 v^{-1} sec^{-1}. They found that μ varied as $T^{-3/2}$ above 100°K and attributed this to acoustic mode scattering. Below 100°K their data indicated a dominance of impurity scattering. Their acceptor impurity was a shallow one at 0.04 ev and was not identified. Essentially similar results were reported by Nasledov and Slobodchikov (15) and Allen and Cherry (16) for p-type material. Using a largely empirical and semi-qualitative approach Allen and Cherry also postulated a limiting mobility of ~ 250 cm^2 v^{-1} sec^{-1} and an effective mass ratio for holes ~ 0.5.

The present data for type 1 samples gives an exponential μ *vs.* T dependence below room temperature. Such a behavior indicates screened polar scattering following Ehrenreich's (17) calculations for III-V compounds, although the magnitude of the mobilities can be explained fully only by assuming some other form of scattering also to be present.

Figure 5 shows the carrier concentration as a function of Hall mobility at 300°K for a number of type 1 samples. Although the scatter is quite large, and only one high mobility, low carrier concentration point is shown, it is felt that the dashed line shows a general trend indicating a limiting Hall mobility of the order of 180 cm^2 v^{-1} sec^{-1}. Therefore, using arguments similar to those advanced by Allen and Cherry, a hole effective mass ratio somewhat less than their value of 0.5 is likely. This lower value would be in agreement with a greater predominance of optical polar scattering which has been observed.

In summary, the present study has helped establish the over-all reaction for the open tube transport process for the synthesis of GaP from Ga and PCl_3. It also provides a method for growing epitaxial layers of GaP with controllable resistivities in the range 10^2-10^{11} ohm cm by incorporating known levels of water vapor into the carrier gas. Results on the electrical and transport properties of single crystal epitaxial GaP obtained are reported.

Manuscript received April 5, 1966; revised manuscript received Aug. 17, 1966.

Any discussion of this paper will appear in a Discussion Section to be published in the December 1967 JOURNAL.

REFERENCES

1. C. J. Frosch and P. W. Foy, *This Journal*, **108**, 177C (1961).
2. W. F. Finch and E. W. Mehal, *ibid.*, **111**, 814 (1964).
3. W. G. Oldham, *J. Appl. Phys.*, **36**, 2887 (1965).
4. 3 above and H. Flicker, B. Goldstein, and P. A. Hoss, *ibid.*, **35**, 2959 (1964).
5. D. Effer and G. R. Antell, *This Journal*, **107**, 252 (1960).
6. A. W. Laubengayer and F. B. Schirmer, *J. Am. Chem. Soc.*, **62**, 1578 (1940).
7. Otfried Madelung, "Physics of III-V Compounds," p. 263ff, John Wiley & Sons Inc., New York (1964).
8. M. Gershenzon, F. A. Trumbore, R. M. Mikulyak, and M. Kowalchik, *J. Appl. Phys.* **36**, 1528 (1965).
9. L. I. D'yakonov, V. N. Maslov, and B. A. Sakharov, *Soviet Phys.—Doklady*, **10**, 650 (1966).
10. J. F. Woods and N. G. Ainslie, *J. Appl. Phys.*, **34**, 1469 (1963).
11. M. Rubenstein, *This Journal*, **112**, 1010 (1965).
12. F. A. Trumbore, H. G. White, M. Kowalchik, C. L. Luke, and D. L. Nash, *ibid.*, **112**, 1208 (1965).
13. M. R. Lorenz and M. Pilkuhn, *Bull. Am. Phys. Soc. Meeting*, New York, Jan. 1966, Abstract C.D. 12.
14. G. F. Alfrey and C. S. Wiggins, *Z. Naturforsch*, **15. a**, 267 (1960).
15. D. N. Nasledov and S. V. Slobodchikov, *Soviet Phys.—Solid State*, **4**, 2021 (1963).
16. J. W. Allen and R. J. Cherry, *J. Phys. Chem. Solids*, **23**, 163 (1962).
17. H. Ehrenreich, *ibid.*, **8**, 130 (1959).
18. F. D. Richardson and J. H. E. Jeffes, *J. Iron Steel Inst.*, **160**, 261 (1948).

Tracer Evaluation of Hydrogen in Steam-Grown SiO_2 Films

P. J. Burkhardt

Components Division, International Business Machines Corporation,

East Fishkill Facility, Hopewell Junction, New York

ABSTRACT

Silicon wafers were oxidized in capsules at 1000°C with 1 atm of tritium-tagged steam. The oxide films formed were investigated by conventional tritium counting techniques. The hydrogen profile suggested a complementary error function type in-diffusion of water, giving a C_o of 4 x 10^{19} molecules of H_2O per cm^3. The profile had a minimum value at around 600Å oxide thickness. The location of this value was independent of original oxide thickness. Following this minimum, the concentration again increased as the Si/SiO_2 interface was approached. The concentration of hydrogen near this interface was greater for the thinner oxide films. This observation led to the conclusion that either a hydrogen-containing intermediate is formed by the reaction between water and silicon and that the concentration of this intermediate is dependent on the oxidation rate or that a transition region exists in the oxide film which permits segregation of the diffusant near the Si/SiO_2 interface. Thermal biasing experiments followed by surface charge measurements and autoradiograms showed that mobile positive charge was present in the oxide near the Si/SiO_2 interface. However, this mobile charge was not hydrogen or a hydrogen-containing species. Out-diffusion experiments yielded an activation energy of 15.7 kcal/mole for the tritium species.

The rapid development of planar transistor and surface field effect transistor technology has brought with it an increasing demand for a better understanding of the insulator films that are used for diffusion masks and surface passivation, as well as for electrical insulators. In silicon technology, a film of thermally grown silicon dioxide has proven to be both effective and convenient. These films, originally suggested by Atalla *et al.* (1) are normally grown at temperatures of 1000°-1200°C in ambients of dry oxygen, pure steam, or oxygen-containing water vapor. Steam oxidation is the faster method and is therefore quite popular. The steam cycle is usually preceded by a period in either oxygen or inert gas to allow the silicon to come to temperature. Following the steam cycle, a final period in a dry ambient is sometimes used to "dry out" the oxide.

Kuper and Nicollian (2) have made a study of steam-grown oxides formed on ring-dot diodes and have noted that an n-channel is formed after steam oxidation. Treatment of these devices in a dry ambient at elevated temperatures tended to reduce the channel. Olmstead *et al.* (3) studied surface inversion under an oxide film by measuring channel resistance and found that annealing in forming gas produced an n-channel. Subsequent etching experiments showed that the region of oxide responsible for the channel was within 400Å of the Si/SiO_2 interface.

Balk (4) has found by electron spin resonance (ESR) studies of thermal oxides that an ESR peak occurs only when the final preparatory step does not include a hydrogen-containing species. Thus, steam oxides have no unpaired spins while steam oxides subjected to a period in dry oxygen do. Recently, Nishi (5) reported ESR studies which appeared to contradict Balk's findings. He reports resonance absorption centers produced by hydrogen annealing which can be removed by subsequent annealing in dry oxygen. Balk (6) also found that annealing of dry-oxygen-grown oxides in hydrogen increased the field effect mobility of electrons at the silicon surface. The field effect mobility of devices made using steam-grown oxides was higher than that for dry-oxygen-grown oxides. He further concluded that the primary effect of hydrogen was the annihilation of fast surface states. The fixed charge in the oxide played only a secondary role. The degree of reduction of the fast surface state density depended on the amount of hydrogen in the film, and, consequently, the field effect mobility of devices annealed in pure hydrogen was greater than that of devices annealed in forming gas or unannealed steam-grown oxides. These surface states are probably singly occupied nonbonding orbitals on silicon atoms which also give rise to the ESR peak and can be removed easily by the formation of highly covalent bonds with hydrogen atoms.

This study using oxides grown with tritium-tagged steam was undertaken to observe the disposition of hydrogen and perhaps to shed more light on the mechanism of steam oxidation.

Experimental

Sample preparation.—The oxidations were carried out in fused silica capsules. Each capsule contained several vapor-polished 2-10 ohm-cm p-type silicon wafers that were spaced apart by small indentations in the capsule wall. Each capsule also contained an amount of T_2O-enriched water which would produce 1 atm of vapor when the capsule was placed into a 1000°C furnace. The capsules, of course, were large enough so that the consumption of water vapor by the wafers and walls did not significantly reduce the partial pressure of water vapor in the ambient.

The loading of the capsules with a controlled amount of water was done with the apparatus shown in Fig. 1. The source water, obtained from the New England Nuclear Corporation, contained a T_2O enrichment of 0.5 Curie/g. The ampoule in which it was received was placed in liquid nitrogen to freeze the water, and then scored, opened, and dropped into the

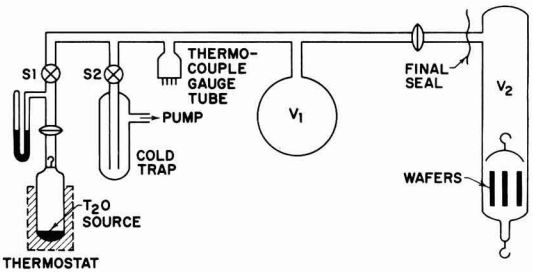

Fig. 1. Apparatus for loading fused silica capsules with tritium-tagged water.

source flask which was immediately connected to the rest of the apparatus. The water was again frozen in the source flask with liquid nitrogen, and the entire system was evacuated with an oil pump to a pressure of about 10μ. Next the source flask was thermostated slightly below room temperature (to avoid condensation in the rest of the system) and the source water vapor expanded into the entire apparatus until the equilibrium vapor pressure, determined by the thermostat temperature, was reached. Volume V_1 was chosen so that the amount of water in the entire system at the vapor pressure was the correct amount for subsequent condensation into the oxidation capsule.

The oxide thicknesses obtained by these capsule oxidations were within 5% of those obtained in a conventional flow system using 1 atm of steam.

Each capsule contained some 10 microcuries and had to be handled with care. The individual wafers however had less than 0.01 microcuries and could be handled conveniently. For the profiling and diffusion experiments, square sections having areas of about 0.6 cm^2 were cut. The oxide on the unpolished side was etched off with HF. Counting was done with a Nuclear-Chicago Model 6810 scintillation counter using a napthalene-dioxane base scintillant. Two counting methods were used in this investigation. The first involved counting the oxide directly on the wafer. For this method, a small aluminum pedestal was fastened to the base of the scintillant vial. The wafer section was placed on this pedestal, which located it near the middle of the vial. A guide edge was provided on the pedestal top so that the wafer section could be located precisely with respect to the counting phototubes. Finally, the vial was filled with scintillant and counted. Next, the wafer section was removed, rinsed in methanol, and placed in an etchant known as p-etch (7). This etchant, prepared by adding 15 ml of 49% hydrofluoric acid and 10 ml of 70% nitric acid to 300 ml of distilled water, removed SiO_2 at the rate of 2Å/sec at 24.7°C. To insure accurate etch rates, the etchant was thermostated in a water bath at 24.7° ±0.2°C. Following the etching, the thickness of the remaining oxide was checked with an SiO_2 step gauge calibrated by the VAMFO technique (8). Finally, the wafer section was again counted as before, and the process was repeated until the oxide had been completely removed. Below 1000Å, where the gauge was ineffective, the etch rate alone was used as the thickness criterion. In some instances where greater accuracy was required, the VAMFO technique was used. Steps ranging in thickness from 100 to 500Å were used, depending on the initial thickness of the oxide. This counting method produced smooth and relatively scatter-free curves, but was greatly affected by attenuation of the low energy betas in thick oxide films. This problem will be discussed later.

The second method involved counting of the etchant. Fifteen 3-cm-long polypropylene tubes 1 cm in diameter fastened onto a metal base with epoxy cement were used to contain 2 ml of the etchant. This entire assembly was thermostated, and etching proceeded by dipping the wafer section into a vial for a predetermined length of time. Between etches, the section was rinsed and, if possible, the remaining thickness was measured. In some instances, the section was also counted between etches. When etching was complete, a 1-ml aliquot was pipetted from each etchant vial into 15 ml of scintillant and counted. Because the counting sensitivity was extremely low, particularly when small steps were used, it was necessary to use this small volume of etchant to reduce the dilution factor.

Calibration of the scintillation counter for the etchant counting was done by comparison of the experimental count rates with that of a tritium water standard. Because small quantities of water in the scintillant tended to quench the light produced by the betas, calibration curves were prepared with varying amounts of added water and etchant. Quenching produced by the etchant was much more severe than that produced by water alone.

For the profiling of the SiO_2 films, both counting methods were used and interpreted according to their relative merits.

In another set of experiments, the rate of out-diffusion of the protonic species was investigated by baking wafer sections at constant temperature and observing the decrease of count rate with time. For these measurements, the wafer counting technique alone was used. Baking was done in a conventional tube furnace with a dry nitrogen flow of 250 cm^3/min.

Finally, the response of the protonic species to an electric field was observed by evaporating an array of 20-mil-diameter aluminum electrodes on the oxide surface. The MOS devices thus formed were thermally biased at 200°C with a d-c field of 2 x 10^5 v/cm for ½ hr. Both positive and negative biases were used. Capacitance-voltage curves were measured before and after biasing. [For a more detailed description of these techniques see ref. (9) and (10).] Following the thermal-bias treatments, the electrodes were removed with a nitric acid aluminum etch, and the oxide was etched down to 1000Å or less with p-etch. Kodak KK x-ray film was then applied, and autoradiograms were made. The exposure times of these autoradiograms ranged from two weeks to one month.

Results and Discussion

For the profiling experiments, the greatest precision was obtained by the wafer counting technique. This method provided smooth scatter-free curves, as shown in Fig. 2 and 3. Because the tritium betas are of such low energies, attenuation becomes a serious problem in films thicker than 1000Å.

When the oxide is sufficiently thin, betas from the entire oxide contribute to the count and, consequently,

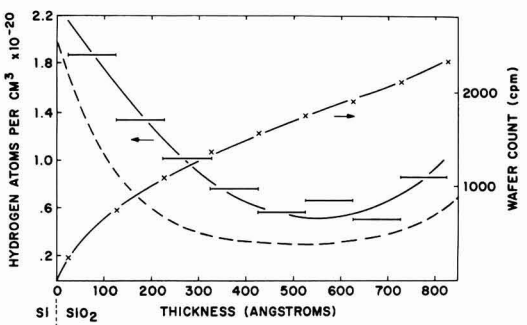

Fig. 2. Wafer count rate vs. thickness and etchant count profile for an 820Å SiO_2 film. The dashed line represents the derivative of the wafer count curve on an arbitrary scale.

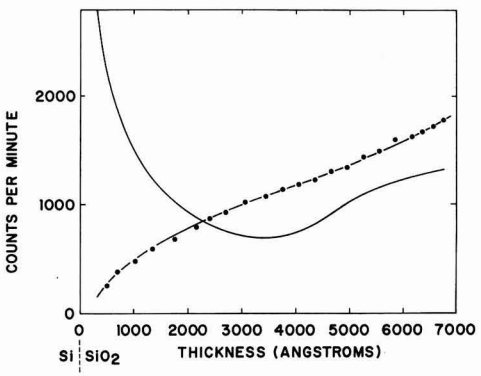

Fig. 3. Wafer count rate of a 6750Å SiO_2 film. The solid line represents the derivative of the count rate curve.

the derivative of the wafer count curve is proportional to the proton concentration in the removed section. To determine the maximum thickness of oxide in which attenuation effects are negligible, it was necessary to calibrate carefully the scintillation counter in terms of beta particle energies and to determine what portion of the beta energy spectrum the counter was capable of measuring. This was done by counting a solution of tritium-tagged water in scintillant at progressively widening energy windows. The lower limit of the energy window remained fixed. The count intensity difference between adjacent windows was taken to be representative of the density of betas having energies equal to those just above the energy maximum of the smaller window. As the window was gradually opened, the count rate increased with decreasing rapidity until finally further expansion of the window produced no more increase in count rate. At this width, betas of all energies were counted, including the highest energy, which was used as a reference calibration. This maximum energy is 18.6 kev (11). Figure 4 shows the beta energy spectrum as determined by this method. The voltage scale represents the counter discriminator voltages that are proportional to the beta energies by a constant determined from the maximum energy of 18.6 kev, which was taken to be at the position shown in Fig. 4. From this calibration, it was found that the lower cut-off limit of the counter was about 1.5 kev. An effort to locate the maximum energy by counting from a low voltage to infinity and continually raising the lower limit of the energies counted was unsuccessful because, as the lower limit was increased, it was necessary to use higher and higher concentrations of tritium in order to maintain a measurable counting rate. This increase, in turn, led to interference from coincidence counting.

It is obvious from Fig. 4 that an accurate energy calibration point for the scintillation counter could not be obtained by using the maximum beta energy of tritium alone. To verify the calibration, a sample of $_{27}Co^{57}$ was used to give another calibration point. This isotope decays to $_{26}Fe^{57}$ by electron capture and gamma emission. The electron capture results in the emission of a 6.4 kev x-ray (12). The three gammas released to relieve the nucleus from its excited state have energies of 14.4, 121.9, and 136.3 kev (13). By examining the spectrum of this isotope in the region of interest, peaks from the 6.4-kev x-ray and the 14.4-kev gamma could produce calibration points. The 14.4-kev gamma peak was found to yield a threshold energy of 1.7 kev for the tritium betas, which is in good agreement with the previous estimate.

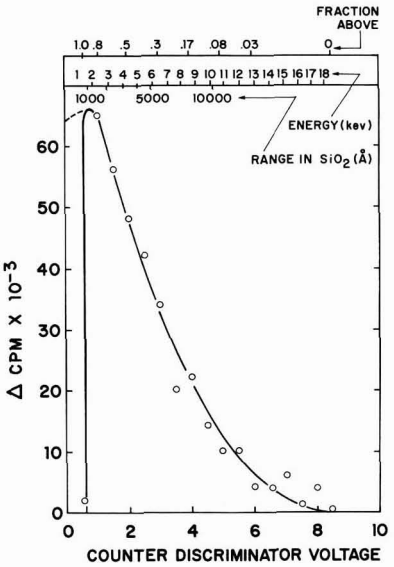

Fig. 4. Portion of the beta energy spectrum that was observed by the scintillation counter. The three scales at the top represent, respectively, the fraction of betas having energies above a certain point, the actual beta energy, and the effective range in SiO_2.

The fraction scale in Fig. 4 represents that portion of the total observed tritium betas which have energies greater than that indicated by the same point on the energy scale. This was obtained by integrating the area under the curve. Thus, for example, about 50% of the observed betas have energies greater than 4 kev.

The next problem to be considered is that of the effective range of monoenergetic electrons in silicon dioxide films. For this we refer to the work of Holliday and Sternglass (14), who have made range measurements and who also present data from other authors. In their Fig. 5 they show a nearly linear relationship of the logarithm of effective range (in mg/cm^2) and the logarithm of the primary electron energy from about 1 to 10 kev. Assuming this linear relationship and using a density of 2.2 g/cm^3 for silicon dioxide (15), one obtains a relationship between range in SiO_2 and initial electron energy of

$$d = 5 \times 10^{-6} E^{1.29} \quad [1]$$

where d is the range in cm and E the energy in kev. Recent measurements of effective range of monoenergetic electrons in SiO_2 films by the back-scatter technique indicate that the constant 5×10^{-6} in [1] is slightly low (16). The range in SiO_2 for various energies obtained by using [1] is shown by the range scale in Fig. 4. This scale takes into account the fact that a beta coming out of the SiO_2 film must have an energy of at least 1.5 kev to be counted. Examination of these scales indicates that about 90% of all the tritium betas are capable of penetrating a SiO_2 film 1000Å thick and being counted. Thus, the count rate profile for the 820Å film shown in Fig. 2 may be translated directly into concentration units by plotting the derivative of the curve. This derivative is shown in arbitrary units by the dashed line in the figure. What is immediately apparent from this figure is that the concentration of protonic species increases markedly very near the Si/SiO_2 interface.

The profile for this oxide, obtained by etchant counting, is also shown in Fig. 2. The thicknesses of the etch steps taken here were determined by the etch rate alone. For very thin oxide films, the etch rate is reputed to be somewhat faster than for thicker films (17). This factor was taken into account in determining the thicknesses of the very thin films. The appearance of hydrophobicity also served as an indication of oxide removal. Again, by etchant counting, it was found that the concentration of hydrogen increased near the Si/SiO_2 interface.

The wafer counting data for a thick oxide film (6750Å) is shown in Fig. 3. Also included in the figure is the derivative of the count curve which, of course, does not represent the concentration profile accurately. The increase of this curve toward the Si/SiO_2 interface does not represent an increase in tritium content in this direction but rather represents a decrease in attenuation effects. The etch count profile for this particular oxide is shown in Fig. 5 along with the corresponding profiles for 820 and 4400Å oxides. Note that in all cases we find what appears to be a normal in-diffusion profile over the bulk of the oxide. Assuming a complementary error-function diffusion profile, one may compute a diffusion coefficient. This coefficient, however, turns out to be much smaller than that obtained for water diffusion in SiO_2 (18). This may be due to the distortion of the profile during the cooling of the wafers following oxidation. Note that the hydrogen atom concentration near the outer surface of the oxides is about 8×10^{19} atoms/cm^3, which corresponds to 4×10^{19} water molecules/cm^3. This value is in good agreement with the value of 3.0×10^{19}

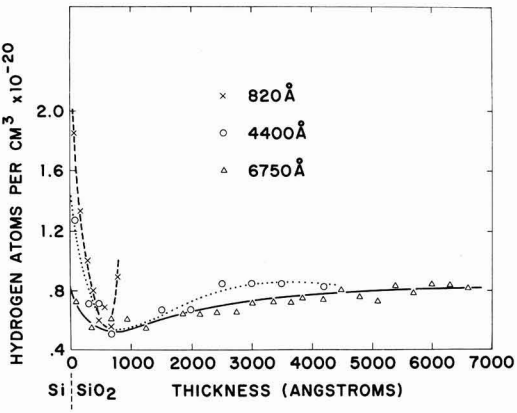

Fig. 5. Etchant count profiles for SiO_2 films of varying thickness

molecules/cm^3 obtained for the solubility of steam oxidizing species in SiO_2 at 1000°C by Deal and Grove (19). Moulson and Roberts' (18) infrared value, also given by Deal and Grove, is 3.4 x 10^{19} molecules/cm^3.

The data in Fig. 5 represent typical etch count profiles of oxides of various thicknesses. In all cases, the proton concentration began to rise again as the Si/SiO_2 interface was approached. The minimum always occurred in the neighborhood of 600Å no matter how thick the oxide was, indicating that the protonic species in this region was associated with the interface and not the diffusion. It is interesting to note here that the charged species observed by Olmstead *et al.* (3), which was responsible for producing n-channels in the silicon, was located in the region below 400Å. Possibly, it is an intermediate in the reaction between water and silicon. It thus remains near the reaction front until the reaction goes to completion and the product hydrogen then diffuses out rapidly. A potential gradient may also assist in confining the material in this region. This could also be affected by the doping. The steady-state amount of this intermediate behind the reaction front will depend on the rate at which the diffusant reacts with the silicon at the interface, which for practical purposes should be the same as the oxide growth rate. During the early stages of oxidation, the growth rate is very large and is determined by the concentration of oxidant in the gas phase. As the film thickens, the growth rate decreases parabolically. The amount of intermediate will then be greater in the thinner films, which were quenched when the growth rate was the greatest. Comparison of the three curves in Fig. 5 shows that this is indeed the case. The presence of a transition layer in the oxide at the Si/SiO_2 interface could also cause the segregation of the diffusant species in the region below 600Å as well as result in a greater concentration of hydrogen in this region for the thinner oxides. If this transition layer exists, other species could be made to segregate in this region.

A 5-min bake at 1000°C of a 4400Å oxide in a nitrogen ambient was sufficient to reduce the beta count to background level. To make sure that the protonic species near the Si/SiO_2 interface had been removed by this treatment, half of the oxide was etched off and the wafer recounted. No activity was detected. The lower limit of detection for these experiments was estimated to be about 10^{17} hydrogen/cm^3. To obtain some rate data on the removal of hydrogen containing species from the oxide film, a number of baking experiments were done in the temperature range of 500°-650°C. In this range, the wafer activity decayed at a conveniently measurable rate. The simplest physical process relating to this situation is the out-diffusion of material from a slab of thickness d into a large, well-stirred, ambient. The solution to this problem (20), where the initial concentration is uniform and one side of the slab is impermeable, is given by

$$M_t/M_o = 8/\pi^2 \sum_{n=0}^{\infty} \frac{1}{(2n+1)^2} \exp - \left[\frac{(2n+1)^2 \pi^2 Dt}{4d^2}\right] \quad [2]$$

where M_t is the amount of material remaining in the slab at time t, M_o the initial amount, and D the diffusion coefficient. For sufficiently long times, this series may be approximated by its first term, leading to an exponential decay of M_t/M_o with time.

The slope should yield the diffusion coefficient if the thickness is known. The situation which we encounter here deviates from the ideal case in two respects: (*i*) the concentration is not uniform, although it does not vary greatly, and (*ii*) the wafer counting method that had to be used does not measure all of the material in a thick film because of attenuation.

The data obtained by baking out oxides of various thicknesses did indeed follow the pattern suggested by [2]. If we consider only the first term in [2], we have

$$M_t/M_o = (8/\pi^2)\, e^{-t/\tau} \quad [3]$$

where

$$\tau \equiv (4d^2)/(\pi^2 D) \quad [4]$$

Figure 6 illustrates the data for a number of runs on different oxides plotted against t/τ. Normalizing the data to $1/\tau$ has the effect of eliminating dependence on D and d. However, from [3] it is expected that the intercept of the line in Fig. 6 should be at log $8/\pi^2$ = log 0.812, which is not the case. Instead the intercept occurs at the lower value of log 0.59. One explanation for this would be the presence of another protonic species which was in the oxide at time zero, but diffused out very rapidly during the first bake. This situation would lead to an anomalously high value for M_o. If this were the case, the fast species concerned could not be the species located near the Si/SiO_2 interface. The reason for this is that this species could not contribute significantly to M_o, particularly in the thicker oxides, because of attenuation. Efforts to remove any fast species by prebaking at 200°C for ½ hr had no significant effect on the intercept. Consequently, a second fast species must be ruled out as the cause of the intercept deviation. The fact that the distribution of protons is nonuniform will alter the boundary conditions of the diffusion problem, which might lead to a different intercept.

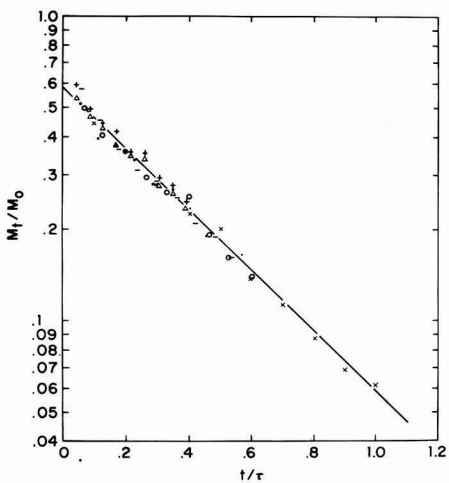

Fig. 6. Normalized kinetic data for baking out SiO_2 films

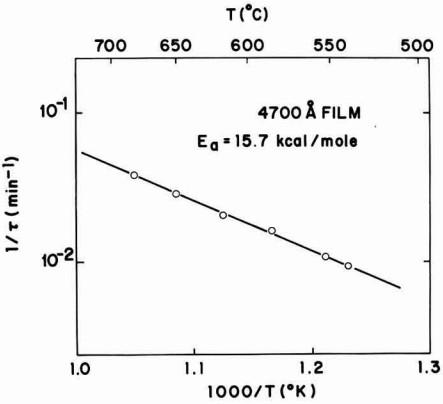

Fig. 7. Activation energy plot for a 4700Å SiO_2 film

From [4], one would expect an exponential temperature dependence of $1/\tau$ by virtue of the diffusion coefficient. The values of $1/\tau$ for a 4700Å oxide at various temperatures are presented in Fig. 7. The activation energy obtained from the slope of this line is 15.7 kcal/mole, which agrees well with that obtained by other authors. Table I gives the values of the activation energy and the pre-exponential of the diffusion coefficient obtained by several methods. The pre-exponential obtained by this work is some two orders of magnitude too low. This may be due in part to an isotope effect, especially if tritons are involved in the diffusion process.

The oxides which were electroded showed a large negative flat-band voltage from the C(V) trace corresponding to a negative surface charge in the silicon of 5×10^{12} charges/cm^2. Normally, oxides grown in a flow system with steam or by the dry-wet-dry method have surface charges of about 3×10^{11} per cm^2. We found that this initial large C(V) offset was characteristic of a capsule-grown steam oxide. Thermal biasing at 200°C for ½ hr showed a reduction of surface charge to about 1×10^{12} charges/cm^2 with negative bias on the aluminum electrode and only a very slight increase with positive bias. This indicates that a large amount of positive charge initially resides in the oxide near the Si/SiO_2 interface. During negative bias, this charge migrates away from the silicon. Positive bias has no significant effect.

It was expected that, if the migrating charge were associated with a hydrogen-containing species, the autoradiograms on the etched oxides would show the outlines of the electrodes for the negatively biased devices. However, the film appeared to be uniformly exposed, with no discernible electrode circles. This result suggests either that the positive charge initially in the oxide was not hydrogen associated or that it was initially on a proton, hydronium ion or some reaction intermediate and subsequently transferred to a silicon atom as follows

$$(\equiv Si - O - Si \equiv) + [RH]^+ \rightarrow (\equiv Si - OH) + [\equiv Si]^+ + R \quad [5]$$

Table I. Diffusion coefficient of water in silicon dioxide

Method	Author	E_a, kcal	D_o, cm^2/sec
Steam oxidation	Pliskin (21)	16.0	2×10^{-7}
Steam oxidation	Edagawa *et al.* (22)	23.0	1×10^{-6}
Wet oxygen oxidation	Deal (19)	16.3	2×10^{-7}
In-diffusion of H_2O	Moulson and Roberts (18)	18.3	1×10^{-6}
Out-diffusion of H_2O	Moulson and Roberts (18)	17.3	2.7×10^{-7}
Out-diffusion of T_2O	This work	15.7	2×10^{-9}

The formation and migration of the charged defect $[\equiv Si]^+$ is discussed in another paper (23).

Another method of charge transfer could be the replacement of a bound sodium ion by a proton, thereby rendering the sodium ion mobile. Such a possibility has been suggested (24) and can be described by

$$(\equiv Si - O - Na) + H^+ \rightarrow (\equiv Si - OH) + Na^+ \quad [6]$$

The presence of significant quantities of sodium in thermally grown SiO_2 films has been observed by neutron activation analysis (25).

Conclusions

The profiling experiments on steam-grown oxides of various thicknesses have suggested the possible existence of a reaction intermediate located in the oxide directly behind the reaction front. The concentration of this intermediate depends on the oxidation rate. Thus, the concentration is greater near the Si/SiO_2 interface in thinner films. Thermal biasing experiments suggest a positively charged species located near the Si/SiO_2 interface. Balk (4) has found that thinner oxides have greater surface charge than thicker ones, thus correlating the positively charged species with the hydrogen-associated species. Our autoradiograms suggested that the charged species which migrates at 200°C is not hydrogen associated. This could only be possible if (*i*) the positively charge species and the hydrogen associated species occur concurrently, as would be the case where a transition phase caused segregation of two species or (*ii*) the positively charged species and the hydrogen-associated species are initially one and the same and a charge transfer like that described by [5] or [6] takes place.

Burgess and Fowkes (26) have recently reported similar experiments using oxides grown with tritium-tagged steam in a flow system. They, too, have found that the hydrogen does not respond to an electric field. The results which are reported here for capsule-grown steam oxides are for the most part compatible with those of Burgess and Fowkes (26) for flow system oxides. There is a marked difference, however, with respect to the out-diffusion of hydrogen. Whereas we found an activation energy of 15.7 kcal/mole using the model described by [2], Burgess and Fowkes obtained an energy about twice as large from a first-order decay law.

Acknowledgment

The author wishes to express his gratitude to Dr. B. J. Masters for his assistance with the radiochemical techniques and to Mr. E. F. Roginsky for much of the experimental work.

Manuscript received May 25, 1966; revised manuscript received Sept. 28, 1966. This paper was presented at the Cleveland Meeting, May 1-6, 1966.

Any discussion of this paper will appear in a Discussion Section to be published in the December 1967 JOURNAL.

REFERENCES

1. M. M. Atalla, E. Tannenbaum, and E. J. Scheibner, *Bell Sys. Tech. J.*, **38**, 749 (1959).
2. A. B. Kuper and E. H. Nicollian, *This Journal*, **112**, 528 (1965).
3. J. Olmstead, J. Scott, and P. Kuznetzoff, *IEEE Trans. Elec. Dev.*, **ED-12**, 104 (1965).
4. P. Balk, Private communication.
5. Y. Nishi, *Japan. J. Appl. Phys.*, **5**, 333 (1966).
6. P. Balk, Paper presented at the San Francisco Meeting of the Society, May 9-13, 1965, Abstract No. 109.
7. W. A. Pliskin and R. P. Gnall, *This Journal*, **111**, 872 (1964).
8. W. A. Pliskin and E. E. Conrad, *IBM J. Res. Dev.*, **8**, 43 (1964).
9. D. R. Kerr, *ibid.*, **8**, 385 (1964).
10. A. S. Grove, B. E. Deal, E. H. Snow, and C. T. Sah, *Solid State Elect.*, **8**, 145 (1965).
11. F. T. Porter, *Phys. Rev.*, **115**, 450 (1959).

12. "Handbook of Chemistry and Physics," Chemical Rubber Pub. Co., Cleveland, Ohio, 45th Ed. (E-74).
13. D. Strominger, J. M. Hollander, and G. T. Seaborg, *Revs. Mod. Phys.*, **30**, 630 (1958).
14. J. E. Holliday and E. J. Sternglass, *J. Appl. Phys.*, **30**, 1428 (1959).
15. E. H. Snow and B. E. Deal, *This Journal*, **113**, 263 (1966).
16. R. Kontrimas, Private communication.
17. W. A. Pliskin, To be published.
18. A. J. Moulson and J. P. Roberts, *Trans. Faraday Soc.*, **57**, 1208 (1961).
19. B. E. Deal and A. S. Grove, *J. Appl. Phys.*, **36**, 3770 (1965).
20. See, for example, W. Jost, "Diffusion," pp. 35-42, Academic Press, New York (1952); J. Crank, "The Mathematics of Diffusion," pp. 52-56, Clarendon Press, Oxford (1956); H. Scholze and H. O. Mulfinger, *Glastechn. Ber.*, **32**, 381 (1959).
21. W. A. Pliskin, *IBM J. Res. Dev.*, **10**, 198 (1966).
22. H. Edagawa, Y. Morita, and S. Maekawa, *Japan. J. Appl. Phys.*, **2**, 276 (1963).
23. P. J. Burkhardt, *IEEE Trans. Elec. Dev.*, **ED-13**, 268 (1966).
24. G. Hetherington, K. H. Jack, and M. W. Ramsey, *Phys. Chem. Glasses*, **6**, 6 (1965).
25. E. Yon, W. H. Ko, and A. B. Kuper, *IEEE Trans. Elec. Dev.*, **ED-13**, 276 (1966).
26. T. E. Burgess and F. M. Fowkes, Paper presented at the Cleveland Meeting of the Society, May 1-6, 1965, Abstract No. 55.

Chemical Vapor Deposition of Mo onto Si

J. J. Casey, R. R. Verderber,[1] and R. R. Garnache[2]

Research and Development Laboratories, Sprague Electric Company, North Adams, Massachusetts

ABSTRACT

Molybdenum has been deposited on single crystal silicon substrates by the vapor phase decomposition of molybdenum chlorides. The thickness, alloy phase, and crystalline nature of the films were studied as functions of substrate temperature, substrate orientation, and source material, using electron microscopy and reflection electron diffraction.

The present study, which originated from work on the deposition of thin film metal layers for the base region of hot electron devices (1), describes the composition and structure of thin layers of molybdenum and molybdenum-silicon phases formed by chemical vapor deposition on single crystal silicon. The fabrication parameters investigated were source material, substrate temperature, and crystal orientation of the substrate.

Previous studies of the molybdenum-silicon system have been mostly concerned with the forming of the disilicide to obtain high temperature corrosion resistant coatings. A monograph (2) on the binary silicides is available which describes the uses, properties, and formation of molybdenum-silicon phases and includes an extensive literature survey.

Experimental

Three series of depositions were made at various substrate temperatures in the range from 600° to 1350°C. Two of these series used molybdenum pentachloride as the source for the molybdenum deposition on (111) and (100) oriented silicon single crystals. The other series utilized a molybdenum oxychloride (MoO_2Cl_2) source on a (100) oriented silicon substrate. The system used to deposit the films is shown in Fig. 1.

A lapped, mechanically polished, and cleaned silicon wafer was placed on the pedestal in the reaction chamber and the system was purged with nitrogen. The wafer was then heated 10 min at 1250°C in a purified hydrogen flow of 1.5 l/min to remove oxides. An epitaxial layer of silicon was then deposited at 1200°C by the hydrogen reduction of silicon tetrachloride. This presented a fresh silicon surface to the molybdenum deposit. The molybdenum was then deposited by the decomposition of the molybdenum pentachloride or oxychloride for 20 min at the various substrate temperatures. The source material was heated in the reservoir chamber to 35°C and transported to the reaction chamber by the purified hydrogen flowing at 1.5 l/min.

[1] Present address: Standard Telecommunications Laboratories, Harlow, Essex, England.

[2] Present address: Tibbitts Research Laboratories, Camden, Maine.

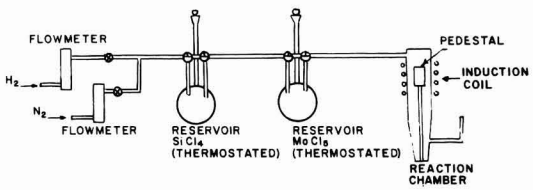

Fig. 1. Deposition system

Measurements

The crystal orientation of the substrates was known and the alloy phases and crystalline nature of each deposit were determined from the reflection electron diffraction data. For deposits that were single crystals, several diffraction patterns were taken at different azimuth angles to obtain the necessary data. Shadowed replicas were made of the surfaces to examine the morphology by electron microscopy.

The effective molybdenum thickness of the deposited molybdenum or molybdenum-silicon alloy was determined by the electron microprobe. The thickness was calculated from the ratio of intensities of MoL_α radiation measured for the film and for bulk molybdenum. The intensity ratio was corrected for x-ray absorption, the nonlinear trajectory of the primary exciting electrons, and the excitation by electrons backscattered from the substrate as described by Hutchins (3). The calibration factor was determined empirically by measurements of films of known thickness and also by interpolation of data for other elements.

For film thicknesses less than 10% of the total electron penetration depth, the corrections are small and the x-ray intensity is a nearly linear function of film thickness. The electron penetration may be controlled by adjusting the beam voltage. At 20 kv the MoL_α intensity is nearly linear up to a thickness of 1000Å of molybdenum.

The excellent sensitivity of the method is most easily demonstrated with an example of representative data (Table I). Relative accuracy depends primarily on counting statistics; absolute error depends primarily on the error in the calibration factor which may be as large as 10%. The measurement gives mass thick-

Table I. Representative data for molybdenum on silicon at 20 kv

Film thickness, Å	Peak counts/ 100 sec	Background counts/ 100 sec	Pk-bgd	Statistical error†	Calibration error*
100	31436	9074	22362	402 (1.8Å)	1118 (5Å)
2	9065	8614	448	265 (1.2Å)	22 (0.1Å)
500	124007	11842	112165	1166 (5.2Å)	5608 (25Å)

†Twice standard deviation 95% confidence.
* Estimated as 5%.

Table II. Properties of phases deposited on (100) Si substrate by H_2 reduction of an $MoCl_5$ source

Substrate temp, °C	Alloy phase	Structure	Thickness, Å, Microprobe
600	Mo	Polycrystalline	190 (as Mo)
700	Mo	Polycrystalline	147 (as Mo)
800	Mo + Mo_3Si	Polycrystalline	104 (as Mo)
900	Mo_3Si	Polycrystalline	52 (as Mo)
1000	Mo_3Si + $MoSi_2$	Polycrystalline and Monocrystalline	64 (as Mo)
1100	$MoSi_2$	Monocrystalline	21 (as $MoSi_2$)
1200	$MoSi_2$	Polycrystalline	16 (as $MoSi_2$)
1300	$MoSi_2$	Polycrystalline	32 (as $MoSi_2$)
1350	$MoSi_2$	Polycrystalline	26 (as $MoSi_2$)

ness; the theoretical bulk density has been used to calculate linear thickness in angstroms.

Results

$MoCl_5$ *Source and (100)* Si *Substrate.*—Table II lists the alloy composition, thickness, and crystalline nature of the layers deposited at the designated temperatures. At 800°C molybdenum-silicon alloys are formed which are molybdenum rich; at more elevated temperatures the deposited layers become more silicon rich until, at 1000°C, molybdenum disilicide is formed.

Deposits below 1000°C are all polycrystalline and have, at most, a small degree of orientation similar to a fiber aggregate (4). At 600°C the orientation is $(100)_{Mo} \parallel (100)_{Si}$ and at 700°C it is $(110)_{Mo} \parallel (100)_{Si}$. All other polycrystalline phases are randomly oriented. A single crystal phase appears at 1000°C and becomes highly developed at 1100°C, Fig. 2. The alloy phase of the 1100°C layer is molybdenum disilicide, and its orientation with respect to the silicon substrate can be described as $(001)_{MoSi_2} \parallel (100)_{Si}$ with $(110)_{MoSi_2} \parallel (010)_{Si}$. At 1200°C the film consists of large unoriented crystallites as evidenced by the occurrence of the diffraction spots on the diffraction rings of a molybdenum disilicide pattern, Fig. 2. These diffraction patterns also show Kikuchi lines typical of the silicon substrate.

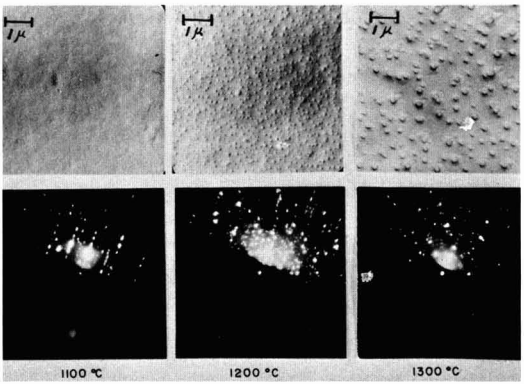

Fig. 2. Electron micrographs (X 10,000) and diffraction patterns of molybdenum deposited on (100) silicon substrate.

Table III. Properties of cylindrical growths obtained on (100) Si substrate using $MoCl_5$ source

Temperature, °C	Diameter, Å	Density, per cm^2	Height, Å	Avg. thickness of $MoSi_2$ (Å), Microprobe Calculated	Measured
1100	250	320×10^8	27	4	21
1200	500	42×10^8	41	3	16
1300	1000	8×10^8	68	4	32
1350	1500	4×10^8	130	9	26

Table IV. Properties of phases deposited on (111) Si substrate by H_2 reduction of an $MoCl_5$ source

Substrate temperature, °C	Alloy phase	Structure	Thickness, Å, Microprobe
800	Mo + $MoSi_{12}$(?)	Polycrystalline	191 (as Mo)
850	Mo + $MoSi_{12}$ (?) + $MoSi_5$ (?)	Polycrystalline	100 (as Mo)
900	Mo_5Si_3	Polycrystalline and Monocrystalline	24 (as Mo)
950	Mo_3Si	Monocrystalline and Polycrystalline	27 (as Mo)
1000	Mo_3Si	Monocrystalline and Polycrystalline	72 (as Mo)
1025	Unidentified	Monocrystalline	15 (as Mo)
1050	Unidentified	Monocrystalline	17 (as Mo)
1074	Unidentified	Monocrystalline	14 (as Mo)

The surfaces of the films are initially smooth and become rougher at higher substrate temperatures. From 1100° to 1350°C one observes cylindrically shaped growths protruding from a very smooth surface (Fig. 2). From the micrographs one can estimate the average size of the growths and the number per unit area can be counted. If one assumes that these growths represent the total $MoSi_2$ present, the average film thickness can be calculated and compared with the measured thickness. Pertinent data are presented in Table III.

The thickness data from the microprobe measurements are based on the assumption that all of the molybdenum determined by the probe is present as molybdenum disilicide, the equivalent thickness of which can be then calculated. Since the measured thickness values are several factors larger than the calculated ones, it must be assumed that either the growths do not represent all of the disilicide, or that some molybdenum has diffused into a thin surface layer of the bulk silicon, or that some other molybdenum-silicon phase is present, which does not contribute to the electron diffraction pattern under the experimental conditions. Insufficient data are available to allow unequivocal choice among these possibilities.

$MoCl_5$ *source and (111)* Si *substrate.*—The results from the experiments for the deposition on the (111) silicon substrate are listed in Table IV.

Molybdenum-silicon alloys initially form at 800°C. The alloys formed are metastable phases and have been tentatively identified as $MoSi_5$ and $MoSi_{12}$ by isomorphism (5) with the molybdenum-aluminum system (6). The structure of the phase tentatively identified as $MoSi_5$ has been determined from the diffraction pattern to be bcc with a_o equal to 7.6Å. The alloys formed become more molybdenum rich at higher substrate temperatures, finally becoming Mo_3Si. Above 1000°C the diffraction patterns (Fig. 3) become rather complex, and the corresponding alloy phases have not yet been identified.

The films deposited below 900°C are polycrystalline and randomly oriented. At 900°C epitaxial growth occurs and well-ordered single crystals are obtained at 950° and 1000°C (Fig. 3). However, a polycrystalline Mo_3Si phase is also present. The orientation of the single crystal phase with respect to the substrate can be described as $(110)_{Mo_3Si} \parallel (111)_{Si}$ with $[335]_{Mo_3Si} \parallel$

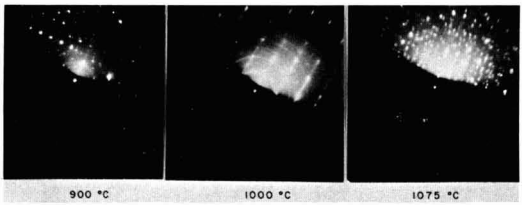

Fig. 3. Electron diffraction patterns of molybdenum deposited on (111) silicon substrate.

$[10\bar{1}]_{Si}$. At higher temperatures, the film consists of large crystals sufficiently disordered to result in a complex diffraction pattern (Fig. 3), and the alloy phase could not be determined.

The electron micrographs of these layers showed no peculiar growths as seen on the (100) silicon substrate and the layers could be described as having slightly rough surfaces.

MoO_2Cl_2 *source on (100) Si substrate.*—Table V lists the results for the series of depositions using the molybdenum oxychloride source material.

The deposits at 650° and 750°C were shown to contain molybdenum by microprobe analysis. Since they are amorphous, however, they cannot be positively identified. By analogy with the results in Table I, which show no silicide formation on (100) silicon at 600° and 700°C, it seems likely that these deposits are molybdenum, but this is not certain.

Discussion

The different alloy phases which are formed on the (100)- and (111)-oriented silicon substrates under similar experimental conditions indicate that the mechanism for alloy formation is different for the two orientations. At 850°C, a stable, molybdenum-rich alloy, Mo_3Si, is formed on the (100) surface, while unstable, silicon-rich alloys along with excess molybdenum are formed on the (111) surface. This difference can be accounted for by the different reactivities of the silicon surfaces which arise from the difference in atom densities. It is well known, for example, that the densely populated (111) silicon surface offers more resistance to chemical etching agents than the less populated (100) surface. A slow rate of reaction on the (111) surface could account for the initial formation of alloys deficient in molybdenum and for the presence of unreacted molybdenum in the deposited layer. In most cases 200Å films of molybdenum deposited at 800°C were found to be metallic, as determined by the attenuation of microwaves through the sample. These films, however, showed a 4-probe resistivity comparable to the silicon substrate. Furthermore, the line widths for the electron diffraction pattern for this specimen indicate that the molybdenum crystallite size is much less than 100Å. It is suggested that the phase tentatively identified as $MoSi_{12}$, unlike $MoSi_2$, Mo_3Si, and Mo_5Si_3, is nonmetallic, and that the whole layer consists of very small molybdenum crystallites in a $MoSi_{12}$ matrix. Further alloys are then formed with an excess of molybdenum available and become more molybdenum rich at the elevated temperatures. This explains the formation of Mo_3Si instead of the disilicide observed in the case of the (100) substrate. Studies of the kinetics of the formation of molybdenum silicides (7) show that Mo_3Si can be formed in a molybdenum-silicon system with excess molybdenum available by annealing at suitable times and temperatures.

Table V. Properties of phases deposited on (100) Si substrate by H_2 reduction of MoO_2Cl_2

Substrate temperature, °C	Alloy phase	Structure	Thickness, Å, Microprobe
650	Unidentified	Amorphous	85 (as Mo)
750	Unidentified	Amorphous	80 (as Mo)
850	Mo_3Si	Polycrystalline	77 (as Mo)
900	Mo_3Si	Polycrystalline	41 (as Mo)
1100	$MoSi_2$	Polycrystalline	10 (as $MoSi_2$)
1200	$MoSi_2$	Monocrystalline	21 (as $MoSi_2$)

The results show that the epitaxial growth is dependent on the substrate temperature, substrate orientation, and source material. As for any type of oriented overgrowth, a minimum temperature must be exceeded to obtain single crystal layers. The temperature is 1000°C for the $MoSi_2$-(100) silicon deposit-substrate pair and 900°C for the Mo_3Si-(111) silicon deposit-substrate pair. However, after a temperature is reached at which the films become well oriented, the orientation of films deposited at still higher temperatures deteriorates, and in the case of the (100) substrate the orientations are random. This indicates other factors are affecting the oriented growth.

The thickness data indicate a limiting deposit thickness at high substrate temperatures. Some clarification of this phenomenon was obtained when attempts were made to deposit molybdenum disilicides at 1200°C on the surface of silicon areas exposed by photoresist techniques on a thermally oxidized silicon surface.

Figure 4 is a photograph of a section of the surface polished on a bevel of 3°. The edge of the beveled section intersects two circular silicon areas on the otherwise oxidized surface. The surface of these areas, having a very thin layer of $MoSi_2$ after the reaction, is seen to lie below the level of the original silicon surface. It can be concluded that the silicon is slowly etched away by the hydrogen chloride and other chlorine-containing species in the reaction ambient. [The reaction of silicon with hydrogen chloride at elevated temperatures has been studied by many authors, among them Lang and Stavish (8).] The thin layer of disilicide deposited may be the result of a steady-state reaction, or it is possible that it is not deposited at all at the high temperature, but only during the cooling period as a result of the desorption of some molybdenum-containing species from the walls of the reaction chamber and subsequent reaction with the exposed silicon surface.

The occurrence of the cylindrical growths on the top (100) silicon surface and their variations in characteristics with temperature are interesting. The formation of a lower density of nuclei on the (100) surface than on the (111) surface is indicated, implying a high mobility of molybdenum atoms on the (100) surface compared to that on the (111) surface. This is particularly true at the higher temperatures, where the growths are larger and less numerous. These

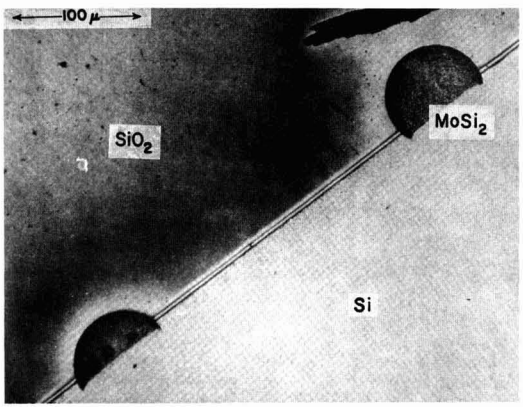

Fig. 4. Beveled section of molybdenum deposited on a masked silicon wafer showing the metal deposit below the initial silicon surface.

phenomena appear to be consistent with Haneman's (9) concepts of the atom arrangements and bonding characteristics on clean surfaces of semiconductors with the diamond structure, arrived at through interpretation of low energy diffraction studies of such surfaces after ion bombardment and vacuum anneal. Freshly formed epitaxial silicon surfaces such as those used as substrates in the present experiments can approach a high degree of perfection and cleanliness and might, therefore, be similar in character to the surfaces studied by Haneman, particularly at high temperatures, where a minimum of gaseous ambient would be adsorbed to the surface. Haneman's model of the (111) surfaces gives s-type bond character to the dangling bond on every other silicon atom in every other row of atoms, and also raises it slightly above the surface, while the dangling bonds on the remainder of the silicon atoms have p-character. Maximum overlap with the orbitals of approaching molybdenum atoms would be offered by the dangling s-bonds, providing a high uniform density of energy minima, which could tend to initiate a high density of nuclei and would result in a very smooth surface, as observed experimentally. The structural model proposed by Haneman for the (100) surface can be interpreted as resulting in dangling bonds which are mostly p-type in character, offering little overlap for the orbitals of approaching molybdenum atoms. The mobility of the molybdenum atoms would be unimpeded, and a smaller number of nuclei would be formed resulting in the type of growth observed in the (100) surface. The nucleation on these surfaces could arise more at the sites of impurity centers and micro-irregularities, which are generally accepted requirements for the initiation of epitaxial growth nuclei, and the high mobility would account for the growth of larger deposits at the higher temperatures. This model is in accord with concepts expressed by Pashley in his reviews on epitaxial growth (10, 11).

The effect of oxides on the crystalline growth is readily seen from the results using the molybdenum oxychloride source. The crystalline nature of the film is considerably poorer over the entire range of substrate temperatures, indicating that oxide contaminants inhibit the formation of a single crystal thin film.

Summary

This study shows that molybdenum can be deposited on a silicon substrate by the decomposition of $MoCl_5$ or MoO_2Cl_2. Under suitable conditions of temperature and source purity, highly oriented thin films can be grown. The process of alloy formation is critically dependent on the orientation of the substrate, and the thickness of the deposit is limited by an etching process occurring at high substrate temperatures.

Acknowledgments

The authors gratefully acknowledge the efforts of A. Harvin for her contribution in supplying the electron diffraction and electron microscopy data and determining the alloy phases, and Mrs. G. Hutchins for microprobe determination of film thicknesses.

This work was partially supported by government funds under Contract No. DA 28-043 AMC-00169(E).

Manuscript received Feb. 3, 1966; revised manuscript received Sept. 14, 1966.

Any discussion of this paper will apear in a Discussion Section to be published in the December 1967 JOURNAL.

REFERENCES

1. J. L. Sprague, J. Lindmayer, R. R. Garnache and J. J. Casey, 23rd Annual Conference Physical Electronics, March 1963, pp. 210-217, MIT, Cambridge, Mass.
2. A. S. Berezhnoi, "Silicon and its Binary Systems," (Academy of Sciences of the USSR, Kiev, 1958. English translation published by Consultants Bureau, New York, 1960) pp. 167-183.
3. G. A. Hutchins, "The Electron Microprobe," McKinley, Heinrich, Wittry, Editors, pp. 390-404, John Wiley & Sons, Inc., New York (1966).
4. J. M. Bijvoet, N. H. Kolkmeyer, and C. H. MacGillavry, "X-Ray Analysis of Crystals," Ist English Edition, translated by H. L. Furth, Interscience Publishers, New York (1951).
5. H. P. Klug and L. E. Alexander, "X-ray Diffraction Procedures," p. 405, John Wiley & Sons, Inc., New York (1954).
6. W. B. Pearson, "Lattice Spacings and Structure of Metals and Alloys," p. 376, Pergamon Press, New York (1958).
7. R. W. Bartlett, P. R. Gage, and P. H. Larssen, *Trans. Met. Soc. AIME*, **230**, 1528 (1964).
8. G. A. Lang and T. Stavish, *RCA Rev.*, **24**, 488 (1963).
9. D. Haneman, *Phys. Rev.*, **121**, 1093 (1961).
10. D. W. Pashley, *Advances in Physics*, **5**, 173 (1955).
11. P. W. Pashley, "Metallurgy of Adv. Elect. Mat.," **19**, pp. 175-207, John Wiley & Sons, New York (1962).

Technical Note

Gas Phase Etching of Sapphire with Sulfur Fluorides

H. M. Manasevit and F. L. Morritz

Autonetics, A Division of North American Aviation, Inc., Anaheim, California

The quality of epitaxial films of silicon grown on sapphire is greatly affected by the quality of the substrate surface (1-3). Processing with diamond has been, generally, a practical requirement for cutting and polishing sapphire substrates. Unless, however, stringent care is taken to polish the surface properly, various size scratches will remain. These scratches affect the nucleation mechanism and, consequently, the silicon overgrowth. Some success in "fine scratch" removal can be effected by a final alumina buff, but the fine powder frequently fills deep scratches and leaves a surface that appears optically to be scratch-free. The usual high-temperature etching prior to deposition can remove this material and expose a rather poor surface for the epitaxial growth of silicon.

Attempts at scratch removal using "wet" chemical techniques appear to have been only partially successful (3, 4). The usual etchants for sapphire (orthophosphoric acid, sodium borate, potassium carbonate, sodium hydroxide, potassium hydrogen sulfate, lead (II) fluoride, and potassium tetrafluoroaluminate) tend to be quite sensitive to orientation and temperature. Usually, polishing can be effected by these agents, but rates cannot be controlled sufficiently to provide the smooth, flat surfaces desired for epitaxial growth.

In addition, any residual surface contamination due to the etchants, even if not optically visible after polishing, can affect the epitaxial process. Furthermore, other wafers in the same system can be contaminated by transfer of residual material. For these reasons, it was thought advisable to study the feasibility of gas phase etchants for sapphire removal. Hydrogen gas has been used (1, 3, 5, 6) to treat sapphire in the reactor prior to deposition, but the etch rate is very low below 1500°C. Its "cleaning" capability is probably due, for the most part, to removal of the polycrystalline alumina residue remaining after optical polishing of the sapphire. Hydrogen chloride (HCl) reacts with sapphire (7) and was found to be a polishing etchant for sapphire at pedestal temperatures exceeding about 1400°-1450°C (8), but the low attendant etch rate of 0.1 μ/min may not be considered practical for removal of considerable surface work damage (or deep scratches).

This paper reports on the successful use of sulfur fluorides as polishing etchants for sapphire. Reactivity of the sulfur fluorides with other oxides had been established at room temperature and below (9, 10), but their use as etchants for aluminum oxide and other oxides at high temperatures has not been reported previously.

Experimental

Apparatus.—A vertical-reactor system similar to that used in our research laboratories for epitaxial growth (11) was used in performing the etching studies. Palladium-diffused hydrogen and a commercial grade helium were used in the studies. Sulfur tetrafluoride (nominally 90-94% pure) and sulfur hexafluoride (nominally 99.99% pure) were used without further purification.

The experiments were usually performed on 0.5-in. diameter sapphire windows, 0.010-in. thick, with $(1\bar{1}02)$ and $(11\bar{2}3)$ orientations. Substrates were heated indirectly while resting on a 3-mm thick alumina spacer which rested on an inductively heated carbon pedestal (except where indicated). The spacer minimized interaction between the substrate and pedestal and provided an even heat distribution. The etching gases were monitored on No. 600 Matheson flowmeters (a sapphire float for SF_4; a Pyrex float for SF_6), and the gases were introduced directly into the flowing H_2 or He ambient at approximately 1 atm total pressure. Carrier gas flow rates were arbitrarily set at 2.5 l/min. Pedestal temperatures were measured with an optical pyrometer, and uncorrected values are reported. They are estimated to be 50°-100° higher than the actual substrate temperature.

Results and Discussion

With SF_4.—Small amounts of SF_4 (less than 1 mole %), diluted with H_2 or He, effectively etched sapphire. After etching at silicon pedestal temperatures of about 1150°C (observed), fluorine compounds were detected on the sapphire surface by electron microprobe induced x-ray fluorescence. AlF_3 formation [presumably epitaxial because of its oriented nature on $(1\bar{1}02)$ sapphire] was suggested by the two-dimensional distribution of aluminum and fluoride which were obtained by electron microprobe techniques (Fig. 1). However, this growth was not observed when gas-phase etching was performed at about 1300°C. Presumably at this temperature the vapor pressure of the material was high enough so as not to interfere with the etching process. Etch rates of about 2 μ/min at carbon pedestal temperatures of 1450°C left highly polished scratch-free surfaces on good quality substrates. Major grain boundaries in sapphire were accentuated by the etching process (see Fig. 2).

With SF_6.—Since pyrolysis of the SF_4 produces sulfur and sulfur hexafluoride (10), the use of the latter was investigated to determine if, indeed, its *in situ* formation might be an important factor. It was found that SF_6 etched sapphire considerably when helium was the diluent gas and almost not at all when hydrogen was used as the carrier under otherwise comparable conditions. Representative removal rates with SF_6 are presented in Fig. 3 through 5 for different temperatures and concentrations. Figure 6 shows the effect of etch-polishing sapphire at 1350°C (ped. temp.) with different SF_6 concentrations so that equivalent amounts of sapphire were removed. The lower concentration produced a smoother sapphire surface.

Success in etching sapphire at reasonable rates by the above processes enhanced the possibility of applying the sulfur fluoride etch process to lapped sapphire surfaces as well as to diamond polished surfaces. The successful gas-phase polishing of lapped surfaces would minimize work damage attributed to mechanical polishing. Experience has indicated that a 10-min exposure of a polished sapphire to SF_6 at 0.22 mole %

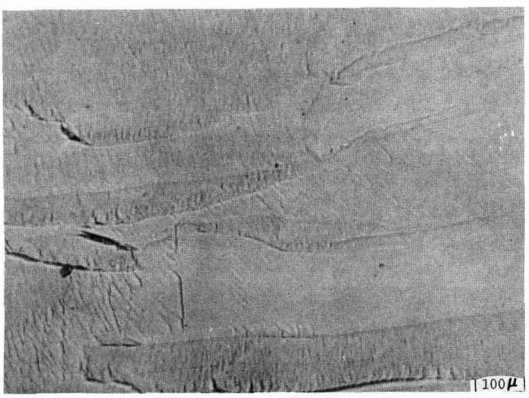

Fig. 2. Grain boundaries in sapphire as displayed by SF_4 etching

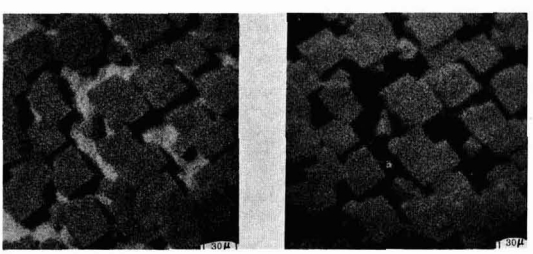

Fig. 1. X-ray photomicrographs as observed by electron beam scanning of the growth on sapphire obtained during etching with SF_4 at 1150°C: (a) (left) due to aluminum; (b) (right) due to fluorine.

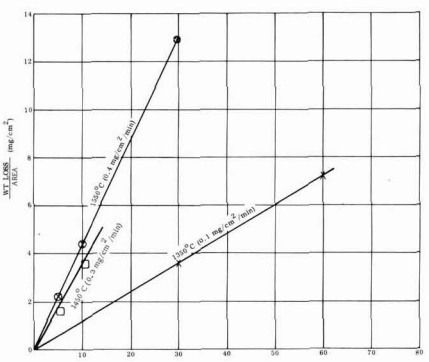

Fig. 3. Etching data with 0.22 mole % SF_6

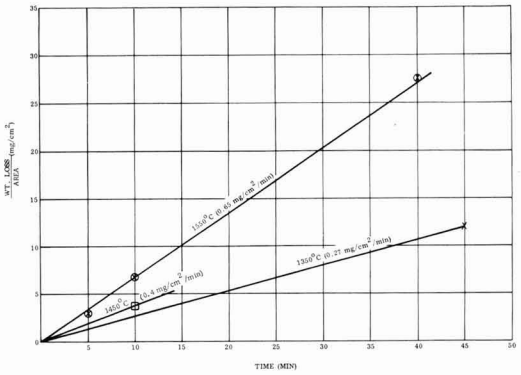

Fig. 4. Etching data with 0.34 mole % SF_6

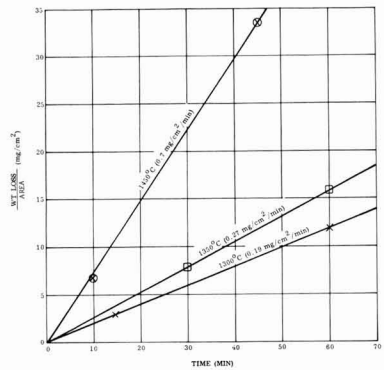

Fig. 5. Etching data with 0.60 mole % SF_6

in He flowing at 2.5 l/min at 1550°C (ped. temp.) will suffice to remove essentially all the surface scratches present due to normal optical polishing techniques. After a 30-min etch under the above flow and temperature conditions, a lapped ($1\bar{1}02$) sapphire slice had a reasonably smooth surface, as indicated in Fig. 7a. Figure 7b shows the surface of a sequential slice (from the boule) which was cut, mechanically polished and processed in the reactor simultaneously with the slice shown in Fig. 7a. The same grain boundary is depicted.

During preliminary experiments in which substrates rested directly on the heated pedestal, it was observed that the carbon pedestal was attacked by the sulfur fluorides. Examination of the substrate surface showed pitting of the type shown in Fig. 8, especially when low carrier gas flow conditions were used. The pits appear to have a definite orientation. Similar patterns are obtained after carbon particles were deliberately rubbed onto the sapphire surface which then was etch-polished. Molybdenum and silicon were also used as pedestal materials; however, a substantial amount of reaction occurred with the etching gases, producing deposits of undesirable byproducts throughout the reactor.

The results of the etching study with SF_6 indicate that it is selective in its etch-polishing capability for different orientations of sapphire. Under identical conditions, at relatively high SF_6 concentrations, optically polished ($1\bar{1}02$) sapphire will usually etch and roughen while ($11\bar{2}3$) sapphire will polish further. At very low concentrations of SF_6 (less than 0.2 mole %) ($1\bar{1}02$) sapphire seems to polish rather than etch at rather appreciable removal rates. Reasonably polished ($1\bar{1}02$) surfaces have been obtained on good quality

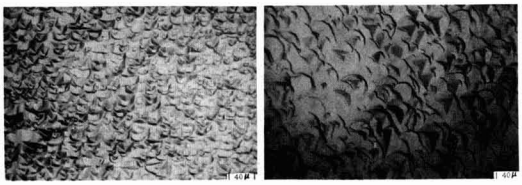

Fig. 6. Surface characteristics ($1\bar{1}02$) sapphire after SF_6 etching: (a) (left) for 30 min at 1350°C with 0.60 mole % SF_6; (b) (right) for 60 min at 1350°C with 0.22 mole % SF_6.

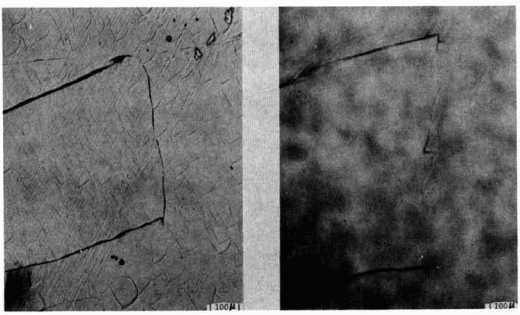

Fig. 7. Structure observed when SF_6 is used to etch ($1\bar{1}02$) sapphire with a (a) (left) lapped ($1\bar{1}02$) surface, and (b) (right) polished surface.

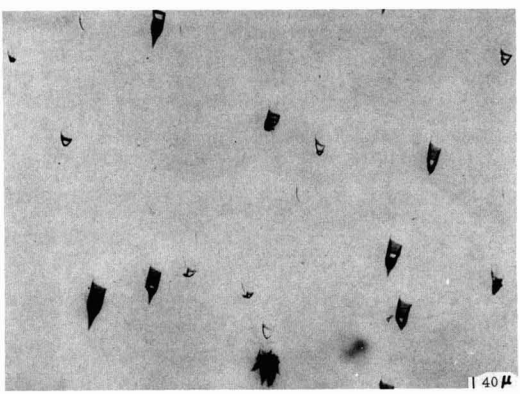

Fig. 8. Pits observed on ($1\bar{1}02$) sapphire after SF_6 etch (carbon pedestal used).

sapphire at removal rates of up to 0.4 mg/cm²/min at 1550°C (obs. ped. temp.) while optically polished surfaces oriented to the ($11\bar{2}3$) have retained a polish at etch rates of 0.7 mg/cm²/min at 1450°C. Single crystal silicon deposits were obtained on SF_4 or SF_6 polished sapphire surfaces.

Conclusion

The polishing of sapphire by the sulfur fluorides seems to offer a distinct advantage over the wet chemical techniques now available. Experience will dictate if the process is to be preferred over HCl polishing, which is considerably slower at comparable temperatures. Since it has been shown that SF_6 (or SF_4) will etch-polish a lapped (or ground) sapphire substrate, its potential as a means for eliminating optical polishing of sapphire is worth consideration.

Acknowledgments

The authors wish to express their appreciation to W. I. Simpson and J. E. Coker for their valuable as-

sistance in the etching studies, to C. C. Nealey and C. W. Laakso for the electron microprobe work, and to the Linde Company for their cooperation in supplying the Czochralski wafers used in the etching study.

Acknowledgment is hereby given to the Bureau of Ships for their support under Contract NObsr No. 93145.

Manuscript received Sept. 19, 1966; revised manuscript received Nov. 7, 1966. This paper was presented at the Cleveland Meeting, May 1-6, 1966.

Any discussion of this paper will appear in a Discussion Section to be published in the December 1967 JOURNAL.

REFERENCES

1. H. M. Manasevit and W. I. Simpson, *J. Appl. Phys.*, **35**, 1349 (1964).
2. H. M. Manasevit, Arnold Miller, F. L. Morritz, and R. L. Nolder, *Trans. AIME*, **233**, 540 (1965).
3. P. H. Robinson and C. W. Mueller, *ibid.*, **236**, 268 (1966).
4. "Single Crystal Silicon Films on Insulating Substrates," Contract NObsr 93145, Autonetics, Anaheim, Calif., First Interim Report, 1 May-31 July, 1965.
5. T. A. Voruz, R. P. Jewett, O. E. Accountius, *J. Amer. Ceram. Soc.*, **46**, 459 (1963).
6. D. W. Readey and G. C. Kuczynski, *ibid.*, **49**, 26 (1966).
7. J. V. Kerrigan, *J. Appl. Phys.*, **34**, 3408 (1963).
8. "Deposition of Silicon on Insulating Substrates," Contract AF19(628)-4220, Westinghouse Research Labs., Pittsburgh, Pa., Scientific Report No. 1, 1 July-31 Dec. 1964.
9. R. J. Brotherton, A. L. McCloskey, and H. M. Manasevit, *Inorg. Chem.*, **2**, 41 (1963).
10. E. L. Muetterties, E. I. du Pont de Nemours and Co., U. S. Pat. No. 2, 883,267, April 21, 1959.
11. H. M. Manasevit, D. H. Forbes, and I. B. Cadoff, *Trans. AIME*, **236**, 275 (1966).

Brief Communication

Travelling Solvent Defects on Silicon Wafers

E. Biedermann

IBM Laboratories, Boeblingen, Germany

In the usual planar silicon technology, the growth of an epitaxial Si layer on a single crystalline substrate wafer at a temperature of 1100°-1200°C is a basic process step. A variety of perturbations and defects can occasionally be observed on these epitaxial surfaces.

In Fig. 1, we show a special type of surface defect which occurs now and then, and which to our knowledge has not yet found its proper explanation. From its optical appearance in Fig. 1, we called it the "nail defect." These nails, achieving sometimes a length of a millimeter and more, can, under proper illumination, easily be observed even with the naked eye. The most obvious characteristic properties of these nails can be summarized as follows:

1. The distribution of the nails over the wafers is completely statistical.
2. Neighboring nails have almost identical length, shape, and orientation, without correlation to the crystal structure of the Si wafer, the orientation of the gas stream, or the direction of the gravitational force. (The exception of unusually short "incomplete" nails will be treated below.)
3. Length, shape, and orientation of the nails can vary strongly from one region of a wafer to another.
4. Under higher magnification (500X), head and shaft of the nails lose all their contrast, indicating that the nails consist of nothing but a slight profiling in the wafer surface (Fig. 2, 3)
5. Only in the uttermost tip of most of the nails, a sharp defect is found under high magnification. (Fig. 3)

These defects have been identified as small impurity pellets which, liquid at the temperature of the epitaxial process, travel over the wafer surface under the influence of the incidental temperature gradients thereon, just as does the liquid zone in the well-known travelling solvent processes (1). Thus the shafts of the "nails" are nothing but the traces of these traveling pellets. The small kinks in these traces can clearly be correlated to the change from preheating cycle to epitaxial growth period to postheating and cooling cycle. The behavior of the travelling pellets is apparently not much influenced by the epitaxial growth process itself, and the growth of a 10μ epitaxial layer

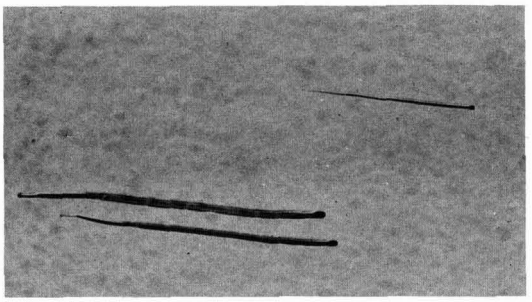

Fig. 1. Typical "nail" defect on epitaxial Si-surface. Magnification ca. 37X.

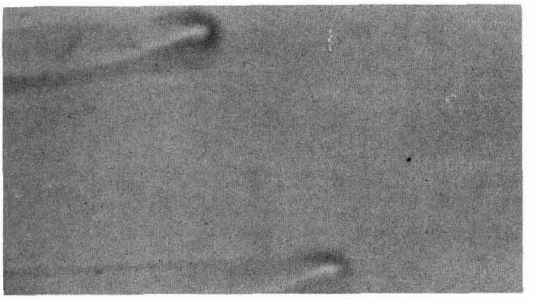

Fig. 2. Heads of nails from Fig. 1. The vanishing contrast as compared to Fig. 1 indicates the nails to consist of a rather smooth surface profiling. Magnification ca. 365X.

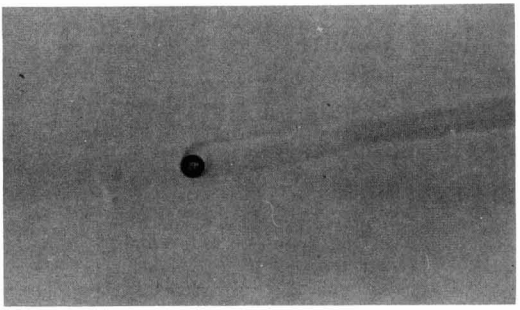

Fig. 3. Tip of nail from Fig. 1 with impurity pellet. Magnification ca. 365X.

does not effect a noticeable levelling out of these traces.

The occurrence of unusually short nails in the neighborhood of longer ones (like the one in Fig. 1) is also easily explained. They never contain a pellet in their tip. Here the impurity material has been used up before the end of the heating cycle by solution in the silicon wafer, respectively by evaporation.

By observation in a high-temperature microscope under pure H_2-atmosphere, the melting point of the pellets has been determined to be about 1000°C and the travelling direction and speed could qualitatively be correlated to the temperature gradient on the wafers.

Electron microprobe analysis showed the pellets to contain the elements Fe, Cr, and Ni in a ratio corresponding approximately to the composition of stainless steel: 70 pt Fe, 20 pt Cr, and 8 pt Ni. Besides these metals an appreciable content of Si was found in the pellets, as is to be expected from the formation of essentially the Fe-Si eutectic with about 25% Si.

Evidently, the vapor pressure of these metals over the eutectic melt and their solubility in the solid silicon are low enough to guarantee the astonishingly long lifetime of these pellets on the silicon surface even in the chlorine-containing ambient of the epitaxial process.

Quite similar nails are easily produced in a pure hydrogen atmosphere on a silicon surface by seeding it with small pellets of other metals such as Cu, Ag, Cr, Ni, Pd, Pt, and heating it in an inert atmosphere like hydrogen to a temperature somewhat above the respective eutectic point. All these metals also have a low solubility in solid silicon at the temperature of their eutectic melt with Si.

From these findings the nails on the Si wafers appear as one example of a quite basic process which may just as well be observed on any other solid surface under appropriate conditions.

Manuscript received Aug. 4, 1966; revised manuscript received Nov. 2, 1966.

Any discussion of this paper will appear in a Discussion Section to be published in the December 1967 JOURNAL.

REFERENCE

1. W. G. Pfann, *Trans. AIME*, **203**, 961 (1951).

ELECTROCHEMICAL
SOCIETY NEWS
FEBRUARY
1967

ECS Local Section News

Midland Section

The Midland Section held a meeting, December 7, 1966 in the Research Auditorium of The Dow Chemical Co. Professor Emmett Leith, Institute of Science and Technology, University of Michigan spoke on holography. He described how holograms are made, how they can be used to produce three dimensional images. He briefly showed the mathematical basis of this phenomena, and described some of the unusual properties of the images so formed. Possible uses of this process were discussed, such as the correction of spherical aberration, the study of vibration patterns, contour mapping, and the monitoring of changes in translucent substances. He ended the lecture with some demonstrations of virtual images produced from holograms using either a laser beam or white light.

R. E. Carr,
Secretary-Treasurer

Ontario-Quebec Section

On February 17, 1967 the Ontario-Quebec Section will hold their winter meeting at the Skyline Hotel, Toronto, Ont., Canada.

The following abstracts will be presented.

Thermodynamics of Vaporization of Salts

Daniel Cubicciotti, F. J. Keneshea, and J. W. Johnson, Stanford Research Institute, Menlo Park, Calif.

The determination of the thermodynamics of vaporization of fused salts allows the intercomparison of the thermal properties of the vapor and the condensed phase. Thus ΔH (formation of gas phase) can be obtained from ΔH (vaporization) and ΔH (formation of condensed phase) and similarly for the entropy (although the inverse process is more commonly applied to the entropy). This procedure is most useful when the molecular composition of the gas phase is known so that molecular properties can be related to those of the condensed phase. For high temperature systems the molecular composition of the equilibrium vapor is not generally as predictable as with low-boiling substances and so it is important that it be established.

The thermodynamics of vaporization of several fused salts has been studied in our laboratory to their critical points. For several salts whose critical temperatures are not too high, our studies of their vaporization indicate that on a corresponding states basis, their behavior is very similar to molecular fluids (H_2O, CO_2, Cl_4, Ar).

The Effect of Pressure on the Properties of Ionic Melts

D. J. Fray, Department of Metallurgy, Massachusetts Institute of Technology, Cambridge, Mass., and J. W. Tomlinson, Department of Chemistry, Victoria University, Wellington, New Zealand.

Experiments are described in which the effect of inert gas pressure on the conductances of fused KNO_3 and $NaNO_3$ is measured. From the results and the available compressibility data, the temperature coefficients of conductance at constant volume are calculated and discussed in relation to the current theories of transport in fused salts.

Electrochemical Properties of Molten Mixtures of Metal Sulfide-Metal Chloride Systems

S. Flengas, A. Garbee and W. Thompson, Department of Metallurgy, University of Toronto, Toronto, Ont., Canada

The liquidus curves, the densities and electrical conductivities of the binary systems, Cu_2S-CuCl, PbS-$PbCl_2$, and Ag_2S-AgCl, have been measured. The conductance of pure molten metal chlorides is of ionic nature, while pure molten metal sulfides are electronic conductors. Molten metal chloride-metal sulfide solutions show a spectrum of conductivities ranging from ionic to electronic.

The thermodynamic properties of Ag_2S in molten Ag_2S-AgCl solutions, indicating ionic behavior, have been investigated from emf measurements of the following formation cell

$$\mathrm{Ag} \;\Big|\; \begin{matrix}\mathrm{AgCl}\\ \mathrm{Ag_2S}\end{matrix} \;\Big|\; \begin{matrix}\mathrm{S_2}\\ \text{gas}\end{matrix} \quad (\mathrm{Pt_2\ or\ C})$$

The sulfur electrode was found to follow an exact Nernst relationship with respect to sulfur partial pressure, temperature, and silver sulfide concentration.

Behavior of Fluoride Mixtures in the Molten Salt Reactor Experiment

W. R. Grimes, Oak Ridge National Laboratory, Oak Ridge, Tenn.

The molten salt reactor experiment (MSRE) is fabricated from the special nickel, molybdenum, chromium, iron alloy Hastelloy N. The fuel, a molten ^7LiF, BeF_2, ZrF_4, enriched UF_4 mixture, is pumped, at about 1250°F, through the reactor core containing unclad moderator graphite and through an exchanger where the nuclear heat is transferred to a LiF-BeF_2 coolant mixture. Special features of the development program with emphasis on salt-graphite compatibility will be described. These findings will be compared with the similar, and generally gratifying, observations during the first several thousand megawatt hours of MSRE operation.

Molten Carbonates

G. J. Janz, Department of Chemistry, Rensselaer Polytechnic Institute, Troy, N. Y.

The deposition of carbon from molten electrolytes containing carbonates has frequently been reported both in fuel cell electrochemistry and in the oxygen-regenerative electrolysis for life support systems. This communication develops some aspects of molten carbonates as high temperature electrolytic solvents, with special reference to the carbon dioxide-oxide ion-carbonate ion equilibrium inherently present in such systems. Aspects of corrosion phenomena and the results of melt decomposition electrolysis are examined from this fundamental viewpoint.

Mechanisms for the Electrodeposition of Refractory Metals from Fused Salts

S. Senderoff, Union Carbide Corp., Parma, Ohio

Chronopotentiometric studies of the electrode reactions in the electrodeposition of niobium, tantalum, zirconium, chromium, molybdenum, and tungsten all show irreversible phenomena in the metal production step. The nature of

this irreversibility and its significance in the electrodeposition process will be discussed.

The Properties of Fused Oxide Mixtures Containing Vanadium Pentoxide

J. R. Wilson, Department of Metallurgical Engineering, Queen's University, Kingston, Ont., Canada

It is well-known that the presence of vanadium pentoxide in an oxide scale, whether from environmental contamination or from oxidation of vanadium contained in the metallic phase, produces catastrophic oxidation at temperatures above the fluxing temperature of the oxide. The exact mechanism of the greatly accelerated rate of attack in the presence of the liquid oxide is not well understood.

The emf of formation cells of the type

$$\text{vanadium or vanadium alloy} \,/\, \text{molten } V_2O_5 \,/\, \text{Pt, } O_2$$

has been measured with various cell geometries in an attempt to isolate some of the processes contributing to oxidation. In addition, conductivities and viscosity measurements have been made on melts of vanadium pentoxide under various environmental oxygen partial pressures and with various oxide additions to the melt. The results are interpreted in terms of the possible polymeric structure of pure molten V_2O_5 and its dependence on temperature and oxide composition. A mechanism of metal attack in the presence of molten oxides of this type is proposed.

C. B. Camplong,
Secretary-Treasurer

Pacific Northwest Section

As required by the bylaws of the Pacific Northwest Section, the Executive Committee has appointed Dr. Ned M. Lowry Vice-Chairman to replace the vacancy caused by the resignation of C. M. Botchek, former Vice-Chairman.

James R. Divine,
Secretary-Treasurer

San Francisco Section

The November meeting of the San Francisco Section was held on November 16, 1966 at the Men's Faculty Club, University of California at Berkeley. Chairman M. E. Sibert opened the meeting and presented Ernest Yim with the Past-Chairman's pin.

Vice-Chairman W. P. Cox introduced the speaker of the evening, Dr. Edward A. Grens, II, of the University of California, who presented a talk on "Porous Gas Electrodes," which is summarized in the following abstract.

An examination of the operation of porous gas electrodes commonly employed in aqueous fuel cell systems was described. The nature of the porous electrode is divided into three sections: (1) electrolyte, (2) electrode matrix, and (3) gas phase. The structure of the electrode is to hold the interface between electrolyte and the gas phase. This is done by: (1) pore size change, (2) lyophobic layer, e.g., teflon which restricts the amount of film formation, and (3) multiple porosity, the macro pores being filled with gas and micro pores with liquid.

The processes concerned are the kinetics of electrode reaction, transport of species in electrolyte, and of components in gas phase and of solubilities of gas in electrolyte.

Theories of operation based on the following models were described and evaluated: (a) flooded pore model, (b) surface diffusion model, (c) thin film model, and (d) multiple porosity model.

The application of these theories to typical electrodes was discussed. The first two were of academic interest only, and the third compared favorably when well defined electrodes are used. Some modification of the double pore model is necessary for highly active electrodes when precious metal catalyst is used with practice.

Joshyo Kinishita,
Secretary

Das Lied von der Hydrazin: luftsauerstoffbuelzellkraftanlage

(Seiner hochwohlgeboren, dem Herrn. Prof. Dr. K. Kordesch, g.m.b.H. gewidmet)

Der Kordesch, mit sei' Motorrad,
Läuft die Heiwehs, Krumm und grad.
Über, unter, vor und zwischen
(Fehs sogar an Televischen).
Mit e' Fiuelzell geschmückt,
Kann er rehssen wie verrückt.
Functioniert mit Hydrazine
(Fast so gut wie Kerosene)
Schur e' echtes Pauerhaus
Bei Galli! 's kommt kei schmohk heraus! !
Laster eine lange weil
(Kostet blos zwei Bocks e' Meil)
Daunhill geht es plenti schnell,
Aber opphill—pusch leik hell

Sol Neman
11-30-66

DIVISION NEWS

Battery Division

Howard R. Karas, Secretary-Treasurer of the Battery Division, has a new address, Aerospace Division, Clevite Corp., 540 East 105 St., Cleveland, Ohio, and has requested that all correspondence dealing with the Battery Division of the Society be sent to his new address.

Electrothermics and Metallurgy Division

The following slate of officers has been nominated to serve the Electrothermics and Metallurgy Division for the 1967-1969 term.

Chairman—Theodore D. McKinley, E. I. du Pont de Nemours, Wilmington, Del.

Vice-Chairman—Stanley Wlodek, Jones & Laughlin Steel Co., Graham Research Lab., 900 Agnew Rd., Pittsburgh, Pa.

Vice-Chairman—Joan B. Berkowitz, Arthur D. Little Inc., Cambridge, Mass.

Secretary-Treasurer—Walter W. Smeltzer, McMaster University, Department of Metallurgy and Metallurgical Engineering, Hamilton, Ont., Canada.

W. E. Kuhn, Chairman
Nominating Committee

Theoretical Electrochemistry Division

The Nominating Committee of the Theoretical Electrochemistry Division has suggested the following slate of officers to serve the 1967-1969 term.

Chairman—D. A. Vermilyea, General Electric Co., Schenectady, N. Y.

Vice-Chairman—Christie G. Enke, Department of Chemistry, Michigan State University, East Lansing, Mich.

Secretary-Treasurer—Robert E. Meredith, Chemical Engineering Department, Oregon State College, Corvallis, Ore.

Members-at-Large—Manfred Breiter, General Electric Co., P.O. Box 8, Schenectady, N. Y., and Alkis Makrides, Tyco Laboratories, Inc., Bear Hill, Waltham, Mass.

W. J. Hamer, Chairman
Nominating Committee

NEW MEMBERS

It is a pleasure to announce the following new members to The Electrochemical Society as recommended by the Admissions Committee and approved by the Board of Directors for December 1966.

Active Members

Albrethsen, A. E., South Plainfield, N. J.
Argano, E. S., Chicago, Ill.
Baker, C. T., Dallas, Texas
Barber, W. A., Stamford, Conn.
Bauer, H. H., Lexington, Ky.
Calvert, J. P., Chevy Chase, Md.

Davidson, S. H., Sidney, N. Y.
Deibert, M. C., Cambridge, Mass.
Gissy, J. L., Hannibal, Ohio
Halsall, Peter, Yorkshire, England
Hass, Karl, Troisdorf, Germany
Hill, L. H., Dallas, Texas
King, S. A., Millersville, Md.
Koening, John, Cleveland, Ohio
Kramer, H. G., St. Peters, Mo.
Lieberman, Robert, Murray Hill, N. J.
Llorens, R. L., Madrid, Spain
Marincic, Nikola, Burlington, Mass.
Marsh, R. A., Kettering, Ohio
McCandless, E. L., White Plains, N. Y.
Postal, R. H., Clifton, N. J.
Shuman, M. S., Forth Worth, Texas
Weich, S. R., Mountain View, Calif.
Witmer, W. H., Fullerton, Calif.

Associate Member

Gulla, Michael, Newton, Mass.

Student Associate Member

Womac, J. F., Brighton, Mass.

Transfers from Student to Active Membership

Graves, B. B., Louisville, Ky.
Kostiner, Edward, Ithaca, N. Y.
Newman, R. L., Minneapolis, Minn.

Reinstatement to Active Membership

Thomas, L. D., Toledo, Ohio

PEOPLE

H. B. Allport has been named manager of technical services in the marketing organization of Union Carbide Corporation's Carbon Products Division. In his new position, he will be located at the Division's Parma Technical Center near Cleveland, where he will manage the customer-oriented technical assistance programs provided by the various carbon and graphite product groups.

John C. Banter, for nine years senior chemist at Oak Ridge National Laboratory, is now on the faculty of Florida Atlantic University, Boca Raton, as associate professor of chemistry.

BOOK REVIEWS

"Physical Chemistry," by Frank T. Gucker and Ralph T. Seifert. Published by W. W. Norton and Co., New York, 1966. 824 pages; $10.00.

This book of introductory physical chemistry incorporates a greater degree of classical approach than texts by Moore, "Prentice-Hall"; Sheelan, "Allyn and Bacon"; and Castellan, "Addison Wesley." As a consequence, topics can be chosen so as to adapt to one semester courses requiring little or no background in calculus.

The first chapter provides a brief mathematical background which is of little value except for the emphasis on dimensional analysis and units which is, unfortunately, frequently lacking in the new physical chemistry texts.

Background for the study of atomic structure, thermodynamics, and kinetics is introduced through radiochemistry and nuclear reactions, Chapters 2 to 4. These chapters are well written and cover more material than most texts.

The chapters on atomic and molecular structure do not express wave mechanical concepts of structure and bonding as clearly and concisely as do the above mentioned texts and Coulson, "Valence," Oxford Press.

Chapter 7 on molecular properties presents the subject of spectroscopy very well. An extensive list of spectral source data is provided at the end of the chapter.

The remainder of the text contains the usual material such as is found in books like Glasstone and Lewis, van Nostrand. The chapter on solids is extremely limited. Little or no mention is made of defect structure, nonstoichiometry, magnetic structure, metallic bonding, band model of metals, neutron and electron diffraction, electrical properties of the solid state, etc. In short, there is a decided lack of modern concepts of solid state chemistry and theory for those who desire it.

The chapters on galvanic and electrolytic cells, surface chemistry, and kinetics are reasonably good and reflect recent research although the material on kinetics is not thoroughly and well expressed as in Castellan and Moore.

Overall, the text is good; there is a wealth of source data, the material is presented in logical order, and there are many problems (~600) of graded difficulty with some answers provided for typical problems. In addition several problems require the use of the literature.

The text is designed well but the cover of the book furnished the reviewer has parted from the binding in two months of careful handling.

William J. James
University of Missouri at Rolla

"Semiconductors and Semimetals, Vol. 2, Physics of III-V Compounds," R. K. Willardson and A. C. Beer, Ed. Published by Academic Press, New York, 1966. 432 pages; $16.50.

This is volume 2 (volume 1 has not yet been published) of a multivolume treatise providing "discussions of major developments, recent experimental techniques and theoretical advances in the study of III-V compounds." This volume contains chapters on physical properties (lattice constants, elastic properties, and low energy electron diffraction studies); thermal phenomena (thermal conductivity, thermal expansion and heat capacity, and Debye temperatures); magnetic resonances (nuclear magnetic resonance and electron paramagnetic resonance); photoelectric effects (photoconduction, quantum efficiency of the internal photoelectric effect in InSb, photoelectric threshold, and work function); and photon emission (nonlinear optics, radiative recombination and stimulated emission). The areas of most intense research activity on these compounds is indicated by the fact that the two chapters on radiative recombination and stimulated emission comprise about one-third of the book. This reviewer was disappointed that no section on microwave oscillation phenomena (Gunn effect) has been planned for the first three volumes of this series.

Two earlier books on the physics of these compounds have appeared; "Semiconducting III-V Compounds," Hilsum and Rose-Innes, and "Physics of III-V Compounds," Madelung. Willardson and Goeing, "Preparation of III-V Compounds," is also an excellent volume on the techniques of III-V compounds The editors of the present book apparently feel that, in a field growing at such a rapid rate, a sequence of books on the recent published literature is a necessity. This reviewer agrees. The editors have succeeded in obtaining contributions from recognized authorities on each topic. The chapters on radiative recombination and stimulated emission are outstanding.

This book is highly recommended as both a reference work and a survey of current efforts in the field for those scientists engaged in the field. The usefulness of this volume in graduate courses is somewhat doubtful.

Forrest V. Williams
Monsanto Co.

Gatos, Tobias, and Cherry Take Office in Dallas

H. C. Gatos

C. W. Tobias

H. H. Cherry

As a result of the recent annual election in which the voting was by mail ballot, Dr. Harry C. Gatos has been elected the new President (1967-1968) of The Electrochemical Society, Dr. Charles W. Tobias has been elected Vice-President (1967-1970), and Mr. H. Homer Cherry has been elected Treasurer (1967-1970). They will take office on Friday, May 12, 1967.

Dr. Gatos, Department of Metallurgical and Electrical Engineering, Massachusetts Institute of Technology, Cambridge, Mass., replaces Dr. Harold J. Read, who will continue as a Past-President on the Board of Directors.

Dr. Tobias, Department of Chemistry and Chemical Engineering, University of California, Berkeley, Calif., begins his first year of his three-year term as Vice-President.

Mr. Cherry, Research and Development Department, Leeds & Northrup Co., North Wales, Pa., begins his first year of his three-year term as Treasurer.

Other offices not affected by the election are those of the two Vice-Presidents and Secretary, Dr. Ivor E. Campbell, Mr. N. Corey Cahoon, and Dr. Richard F. Bechtold, respectively.

"Zone Melting," 2nd Edition by W. G. Pfann. Published by John Wiley & Sons, Inc., New York, 1966. 310 pages; $11.75.

There was a six-year interval between the first publication on zone melting and the publication of the first edition of this book. In this period zone melting techniques gained great acceptance and success in the electronics industry as a result of their effectiveness in the production of ultrapure materials and in the controlled distribution of solute in solid matrices. The first edition of this book summarized the theory of these techniques, presented the mathematical models on which they were based, and surveyed the then current practice and applications. The first edition was a sorely needed, timely, thoroughly comprehensive survey of the field. However, in the last eight years the value of zone melting techniques has become recognized by the scientific community as a whole and, as the author states, "the number of significant papers on zone melting has increased from about one hundred to one thousand." For this reason the first edition has become outdated and now inadequately represents the state of the art. The author, the inventor of zone melting, the most prolific contributor to the field, and the world's outstanding authority on zone melting has rectified this situation in the second edition.

The first three chapters deal with the principles of zone melting, its relation to the freezing process, and the theory and mathematical models of zone refining. The author has included many refinements made in the mathematical theory of zone refining such as the corrections to the basic equations when density is taken into account, the more complete solutions for multipass solute distributions, and the complete solutions for the ultimate distribution. In addition he has expanded his coverage on the relation of phase diagrams and zone refining and describes and discusses the newer techniques of zone chromatography, solid-vapor zoning, and liquid-vapor zoning. Chapter four describes the techniques of zone refining. The author has updated this chapter and has covered the many innovations and newer techniques which have been developed. Of particular interest are the expanded sections on floating zone techniques, electron beam zone melting, and the development of microscale zoning.

Chapter five, which deals with the applications of zone refining, contains the most significant addition to this book. The author has divided materials which have been purified by zone refining into four classes: (1) elements, (2) semiconducting and intermetallic compounds, (3) ionic compounds, oxides, etc., and (4) organic compounds. Substances in each class have been listed alphabetically in tables which include the pertinent references. In addition the zone refining of members of each class is discussed. This chapter contains the most complete available listing of materials that have been zone refined.

In chapters six and seven the author describes the latest continuous zone refining, zone leveling and crystal growth techniques, and discusses the latest mathematical contributions in these fields. Chapter eight is a completely new chapter and treats the zone melting of substances in which a volatile material is involved. Three categories are treated: "first, the zone refining of a substance containing volatile impurities; second, the addition of a desired volatile component via the gas phase; third, the zone melting for purification or crystal growth of a compound having a volatile constituent." This chapter will be of special interest to those concerned with the zone melting of materials such as compound semiconductors. Chapters nine and ten, concerned respectively with methods of perturbing solute concentrations via zone melting techniques, and temperature gradient zone refining, have also been revised in light of recent developments. The final chapter treats miscellaneous phenomena associated with zone refining such as the use of the Peltier effect field freezing and the vapor-liquid-solid growth mechanism.

As originally stated, the purpose of the second edition of this book was to revise and update the first edition in the light of the explosive growth sustained by zone refining in the last eight years. This end has been capably achieved and this book is highly recommended.

John K. Kennedy
Air Force Cambridge Research

"Zone Melting," by Hermann Schildkneckt. Published by Academic Press, Inc., New York, 1966. 222 pages; $9.00.

Zone melting is a technique of fractional crystallization first used by W. G. Pfann to purify germanium. Since its conception in 1952 when its use was primarily intended for the purification or controlled doping of the elemental materials for transistor or diode manufacture, it has become a valuable separations method for the purification of both inorganic substances and organic compounds.

The book "Zone Melting" written by Professor Hermann Schildkneckt of the Organisch Chemisches Institut der Universitat Heidelberg is a treatise on the principles, theory, and uses of this separations method. The book was published originally as "Zonenschmelzen" in the German language in July of 1964 by Verlag Chemie. Gm. H. Weinhein Bergstr. "Zone Melting" is a direct translation of the original "Zonenschmelzen" and is being handled by Academic Press, (New York, London). This edition is dated: Autumn, 1966. The translation was made by Express Translation Service of London and was well done. The captions and notations on all figures, charts and tables have been translated so there are no obstacles in its use. There are 360 references in the bibliography and an author index in addition to an extensive subject index.

The volume consists of 222 pages, 220 figures and 29 tables. The content is divided into three main parts, each comprised of about equal lengths. A general section treats theory and

method; an equipment section is devoted to apparatus and operations; and a special section deals with an extensive survey and description of the applications made of this technique.

Theory is handled in a well organized and scholarly manner and clearly sets forth the bases on which zone melting functions. The author makes extensive use of the general principles of heterogeneous equilibria to elucidate the phenomena of zone melting and normal freezing of mixed crystal systems. The significance of the distribution coefficient in terms of its determination and utility is adequately discussed. The theoretical discussion is well exemplified by illustrations and examples.

The section devoted to apparatus is quite complete. The author places emphasis on the principles involved rather than on the details of construction. Such details as might be needed by the reader will be available in the original articles to which, of course, reference is made. Individual treatment is given to each of the important functions or components of the apparatus such as heating, cooling, the container, and transport of the charge. Particular attention is given to apparatus for normal freezing of melts, micro and semimicro apparatus and special zone melting apparatus for large quantities.

The remainder of the volume is devoted to detailed discussion of the achievements made and reported for the zone melting process. Many published separations and purifications are reviewed for those materials which are amenable to this treatment. These include categories such as the semiconducting elements and their alloys, the semiconducting compounds, metals, oxides, salts, and a great variety of organic compounds. The concentration of organic substances from their solutions by normal freezing and ice zone melting is also described. Operating conditions and specific results or accomplishments are given.

In summary, the author presents in this volume an up-to-date assessment of the theory, practice, and recent technological developments of the zone melting process. The book should be equally useful to the expert in the field and to those just becoming interested in the potentials of this technique.

E. S. Perry
Eastman Kodak Co.

NEW BOOKS

"Chemistry and Physics of Carbon," Volume 2, Ed. by Philip L. Walker, Jr. Published by Marcel Dekker, Inc., New York, 1966. 384 pages; $14.50.

The contents of Volume 2 of this series of monographs are, "Electron Microscopy of Reactivity Changes near Lattice Defects in Graphite" by G. R.

Three $800 Electrochemical Society Summer Fellowships to be Awarded

The Board of Directors of The Electrochemical Society appropriated funds to support three 1967 Summer Fellowships for qualified graduate students. Each fellowship has a stipend of $800 and the purpose of the fellowship is to assist a student to continue his graduate work during the summer months in a "field of interest to The Electrochemical Society." These fellowships are known as the Edward Weston Fellowship, the Colin Garfield Fink Fellowship, and the ECS Fellowship Award.

Dr. James H. Bartlett, Chairman of the Honors and Awards Committee of the Society, has appointed Dr. Douglas N. Bennion as Chairman of a subcommittee to select the award winners.

Candidate Qualifications: "The award shall be made without regard to sex, citizenship or race, or financial need. It shall be made to a graduate student pursuing work between the degree of B.S. and Ph.D. who has received a nine months grant preceding the summer period and who will continue his studies after the summer period. A previous holder of the award is eligible for reappointment."

Qualified graduate students are invited to apply for these summer fellowships and should submit the following items:

1. a brief statement of educational objectives.
2. a brief statement of thesis research problems including objectives, work already accomplished, and work planned for the summer of 1967.
3. transcripts of undergraduate and graduate academic work.

The applicant should request his research advisor and one additional faculty member familiar with his work to write letters of recommendation. Application material and letters of recommendation should be sent to: Dr. Douglas N. Bennion, School of Engineering, University of California, Los Angeles, Calif.

Applications must be received by March 1, 1967 and award winners will be announced on May 1, 1967.

Hennig, "Porous Structure and Adsorption Properties of Active Carbons" by M. M. Dubinin, "Radiation Damage in Graphite" by W. N. Reynolds, "Adsorption from Solution by Graphite Surfaces" by A. C. Zettlemoyer and K. S. Narayan, "Electronic Transport in Pyrolytic Graphite and Boron Alloys of Pyrolytic Graphite" by C. A. Klein, and "Activated Diffusion of Gases in Molecular-Sieve Materials" by P. L. Walker, Jr., L. G. Austin, and S. P. Nandi. This second volume appears to maintain the high quality promised by the first volume in the series.

"Transition Metal Chemistry," Volume 2, Ed. by Richard L. Carlin. Published by Marcel Dekker, Inc., New York, 1966. 350 pages; $14.75.

The contents of Volume 2 of this series are "Reactions of Ligands Coordinated with Transition Metals" by J. P. Collman, "Transition Metal Ions as Reagents in Metallo-enzymes" by A. E. Dennard and R. J. P. Williams, and "Optical Activity in Inorganic and Organic Compounds" by A. D. Liehr. This volume appears to be an excellent series of reviews and monographs written by international experts in their particular field. The former volume was, and the proposed volumes seem to be of competent and thorough character. M. Dekker, Inc., a new publishing house, apparently likes to publish series of volumes. This is one way to perpetuate oneself. In many cases, the various series published by the above organization have filled a need and have provided both reference and up-to-date discourses in a number of fields. Occasionally they come up with a "blooper" but this can be excused as growing pains.

NEWS ITEMS

Power Sources for Electric Vehicles

The first conference in the nation designed to stimulate research and development of electrical power systems for automobiles, trucks, and buses as a major step in reducing air pollution will be held at Columbia University this Spring.

The three-day conference, which will be held April 6-8, 1967, is jointly sponsored by the Division of Air Pollution of the United States Department of Health, Education, and Welfare, the Polytechnic Institute of Brooklyn, and by Columbia University's School of Engineering and Applied Science.

Leading engineers and scientists from major universities, industry, and government will participate in the conference. Henry B. Linford, Columbia Professor of Chemical Engineering, will be the chairman assisted by cochairman Harry P. Gregor, Chemistry Professor at the Polytechnic Institute of Brooklyn, and by Dr. Bernard J. Steigerwald of the Laboratory of Engineering and Physical

Notice to Members
April 1 is Cut-off Date

Your attention is called to Article III, Section 9 of the Society Constitution which states: "Any member delinquent in dues after April 1 of each year shall no longer receive the Society's publications, and will not be allowed to vote in any Society election until such dues are paid. All members in arrears for one year after the first of April shall lose their membership status and can be reinstated only by action of the Board of Directors." Members who have not sent in 1967 payments will be mailed a second notice in February and are urged to make payment promptly in order to avoid delay in receipt of JOURNALS.

Sciences, Department of Health, Education, and Welfare.

Papers will be presented at the three-day affair covering the present status of the development of power systems for electric vehicles and the anticipated future development of such systems. Topics to be discussed will include the impact of the electric vehicles on urban problems such as air pollution, a high priority subject in the nation's search for remedies to control contamination.

Applications for those wishing to participate in the technical presentations or to attend the symposium are being handled by Professor Gregor, Polytechnic Institute of Brooklyn, Brooklyn, N.Y. 11201.

Symposium on Electrode Processes

The symposium will be held as part of the national meeting of the American Chemical Society in Miami Beach, Fla., April 9-14, 1967. The program consists of 18 invited papers plus 30 contributed research papers. The invited papers will review the present status of various aspects of electrochemistry with emphasis on recent developments. A session on Special Techniques in Electrochemistry has been organized as part of the symposium by Professor Ted Kuwana of Case-Western Reserve University. General chairman of the symposium is Professor Ernest Yeager, also of Case-Western Reserve.

Preprints of all symposium papers will be available in advance of the symposium. For further information concerning preprints, the following person should be contacted: Dr. R. A. Glenn, Bituminous Coal Research Association, Monroeville, Pa.

Joint with Divisions of Physical Chemistry and Analytical Chemistry, ACS, in cooperation with The Electrochemical Society, Inc.

Bold face type indicates ECS Member.

Electrochemical Reactions

Section A—**Ernest Yeager,** Presiding

Invited Papers

Ernest Yeager, Introductory Remarks
Roger Parsons, Some Problems of the Electrical Double Layer
Paul Delahay, The Essential Ideas of Electrode Kinetics
R. A. Marcus, Electron Transfers at Electrodes and in Solutions. Comparison of Theory and Experiment
Ernest Yeager and **Frank Ludwig,** Techniques for the Study of Electrode Processes

Section B—**J. O'M. Bockris,** Presiding

D. R. Turner, Electrochemical Reactions at Semiconductor Electrodes
A. C. Makrides, Passivation of Metals and Alloys
J. V. Petrocelli, Fundamentals of Electrodeposition
S. Senderoff, Electrode Reactions in Molten Salts

Section C—**Paul Delahay,** Presiding

Philip J. Elving, Organic Electrode Reactions: Approaches and Results
Charles N. Reilley, Survey of Modern Electroanalytical Methods
John S. Newman, Current Distribution and Mass Transfer in Electrochemical Systems
J. O'M. Bockris, A. Damjanovic, and R. J. Mannan, The Effect of Fundamental Properties of Electrode Materials on Electrocatalysis

Special Techniques in Electrochemistry

Section D—**T. Kuwana,** Presiding

T. Kuwana, Introductory Remarks
Fred C. Anson, George Lauer, and Arthur Hubbard, Electrochemistry in Thin Layers of Solution
Robert A. Osteryoung, Chronocoulometry: Application to the Study of Adsorption at an Electrode-Solution Interface
Ernest Yeager and **Ronald Zurilla,** Rotating Disk and Disk-Ring Techniques
Robert F. Nelson and Ralph N. Adams, EPR and Electrochemical Investigation of Tertiary Aromatic Amines
M. A. Genshaw, Ellipsometric Methods in Electrochemistry
Ted Kuwana and George Strojek, Optically Transparent Electrodes
Discussion

Section E—**Fred C. Anson,** Presiding

Contributed Papers

Charles A. Johnson and **Sidney Barnartt,** Generalized Theory of Electrode Kinetics at Constant Potential
Charles A. Johnson and **Sidney Barnartt,** Constant-Potential Reactions Simultaneously Controlled by Charge-Transfer and Mass-Transfer Polarization at Planar, Spherical, and Cylindrical Electrodes
Discussion
Robert H. Gibson, Derivative Chronopotentiometry of Multicomponent Systems
Discussion
Fred C. Anson, Applications of Charge-Step Chronocoulometry
Discussion
John R. Kuempel and Ward B. Schaap, Electrochemical Studies of the Rates of Chemical Reactions Coupled to Charge-Transfer Reactions
Discussion
Janet Jones and Fred C. Anson, Ligand Bridging in the Oxidation of Chromium (II) at Mercury Electrodes
Discussion
William M. Schwartz, The Electrochemical Reduction of Pentamminecobalt (III) Complexes. The Question of Ligand Bridging at Electrodes
Discussion
Peter E. Sturrock and Gibson W. Higgins, Polarographic Irreversibility of the Copper (II) Pyrophosphate System
Discussion

Section F—**H. A. Laitinen,** Presiding

Joseph S. DiGregorio and **Michael D. Morris,** Polarography of Diphenylthallium (III) Cation in Aqueous Solution
Discussion
A. L. Krivis and G. R. Supp, Polarographic Behavior of a Series of Substituted Hydrazines
Discussion
D. L. Manning, Gleb Manantov, and H. W. Jenkins, Voltammetric and EMF Measurements on the Nickel-Nickel (II) Couple in Molten Fluorides
Discussion
Gleb Manantov, H. W. Jenkins, and D. L. Manning, Exchange Current Measurements on the Nickel-Nickel (II) Couple in Molten Fluorides
Discussion
Robert A. Osteryoung, A Quantitative Study of Desorption in the Zinc (II)—Thiocyanate System
Discussion
John Lawrence, **Roger Parsons,** and Richard Payne, Adsorption of Halides at the Mercury-Water Interface
Discussion
George H. Nancollas and David S. Reid, Specific Adsorption of Alkali Metal Ions at the Mercury-Formamide Interface
Discussion

Section G—**Sidney Barnartt,** Presiding

V. S. Srinivasan and **T. Kuwana,** Interference Attenuated Total Reflection on Tin-Oxide Coated Glass Substrates
Discussion
B. S. Pons, L. O. Winstrom, J. S. Mattson, and **H. B. Mark, Jr.,** Application of Deposited Thin Metal Films as Optically Transparent Electrodes for the Internal Reflection Spectroscopic Observation of Electrode-Solution Interfaces
Discussion
S. P. Perone, J. R. Birk, H. E. Drew, and H. E. Stapelfeldt, Photo-Electrochemical Reactions in Solution
Discussion
Heinz W. Sternberg, Raymond E. Markby, and Irving Wender, Electrolytic Generation of Solvated Electrons in a Solvent of High Proton Donor Capability; Electrolytic Reduction of the Benzene Ring
Discussion
T. Freund and S. Roy Morrison, Mechanism of Cathodic Processes on the Semiconductor Zinc Oxide
Discussion
M. A. Genshaw, A. Damjanovic, and **J. O'M. Bockris,** The Role of Hydrogen Peroxide in Oxygen Reduction at Platinum, Rhodium, and Gold
Discussion
J. D. E. McIntyre and M. Salomon, Kinetic Isotope Effects in Oxygen Electrode Reactions, I. General Theory of Primary and Solvent H/D Isotope Effects in the Electrochemical Reduction of Oxygen
Discussion
Thomas C. Franklin, Donald H. McClelland, Phillip E. Hudson, and Jerry Barrett, The Use of the Potential of the Hydrogen Electrode to Determine the Mechanism of Reduction of Compounds
Discussion

Section H—**Ernest Yeager,** Presiding

Michael A. Aia and **Frederick P. Kober,** Methods for Determining the Structural and Stoichiometric Changes of $Ni(OH)_2$ Electrodes during Polarization in Alkaline Electrolytes
Discussion
John O'M. Bockris and **Boris D. Cahan,** The Finite Contact Angle in Porous Electrodes and Its Consequences
Discussion
Hilton A. Roth and William R. Lasko, Electrodeposited Platinum and Platinum-Lead Black Electrocatalysts
Discussion
Eugent Luksha and Eugene Y. Weissman, Oxidation of Multicomponent Hydrocarbon Fuels
Discussion
James F. Lennon, Eugene Luksha, and Eugene Y. Weissman, Long-Term Electrochemical Oxidation Studies of Multicomponent Fuels
Discussion
M. S. Foster, G. H. McCloud, and **Elton J. Cairns,** Electrochemical Studies of the Sodium-Bismuth System
Discussion
Ernest Yeager, Closing Remarks

Chicago Meeting Symposia Plans–Fall 1967

Battery Division Symposia Plans

The Battery Division is planning symposia on Nonaqueous Electrolyte Batteries and on Zinc Electrode Cells for the 1967 Fall Meeting to be held in Chicago, Ill., Oct. 15-20, 1967. A general session is also planned.

Nonaqueous Electrolyte Batteries

Papers dealing with properties of nonaqueous electrolytes and performance of primary and secondary cells utilizing nonaqueous electrolytes of the fused salt, organic-base, and ammonia-base electrolyte types are solicited. Inquiries and suggestions should be sent to the Symposium Chairman, Dr. M. Eisenberg, Electrochimica Corp., 1140 O'Brien Dr., Menlo Park, Calif. 94025.

Zinc Electrode Cells

Papers dealing with theory and technology of zinc electrodes are solicited. Dr. George Dalin, Yardney Electric Corp., 40-50 Leonard St., New York, N. Y., is Chairman.

Corrosion Division Symposium Plans

The Corrosion Division is planning a symposium on "Mechanical Properties of Oxide Corrosion Products" for the 1967 Fall Meeting to be held in Chicago, Ill., Oct. 15-20, 1967. There will be a number of invited papers, and contributed papers are also solicited.

Suggestions are most welcome, and should be directed to the Chairman, Dr. D. A. Vermilyea, General Electric Research and Development Center, Schenectady, N. Y. 12301.

Dielectrics and Insulation Division Symposia Plans

The Dielectrics and Insulation Division has planned three symposia and general sessions for the Chicago, Ill., Meeting, October 15-20, 1967.

Capacitor Technology

This symposium is divided into two separate sections. The first section will deal only with the Electrolytic Capacitor in all its forms, including liquid and solid electrolytic types.

Topics of interest are as follows:

(a) Properties of new capacitor materials as related to capacitor performance.
(b) Fundamentals of electrolytic capacitor behavior, equivalent circuits, failure mechanisms, etc.
(c) New or novel forms of electrolytic capacitors, advanced technology.
(d) New manufacturing processes and their impact on capacitor performance.

Triplicate copies of the usual 75-word abstract, as well as of an extended abstract 500-1000 words (see page 32C for typing instructions) are due at The Electrochemical Society, Inc., 30 East 42 St., New York, N.Y., 10017, not later than May 15, 1967.

The second section of this symposium proposes to provide broader coverage of the stated subject. Papers should deal with work that is either recent or fundamental. Subjects of interest are as follows:

(a) New materials and techniques in film capacitors.
(b) The physics of dielectrics and their properties.
(c) Life and environmental testing.
(d) Characteristics of breakdown and failure mechanisms.
(e) Film capacitors in microcircuit devices.
(f) New or novel capacitor fabrication techniques.

Contact Failure Arising from the Formation of Insulating Films

This symposium will deal with all aspects of its stated subject. Topics of interest therefore include:

(a) Failure mechanisms and mediums, tarnish films, and metal migration.
(b) Characteristic properties of formed films.
(c) Testing and evaluation contact performance and failure.
(d) Methods of preventing failure.
(e) Semiconductor device contact failure.

Electrets

This symposium proposes to provide a survey of current work in the field. It will therefore cover all phases of the electret phenomena. The basic categories of work to be presented are:

(a) New or recent theoretical studies.
(b) Experimental investigations, methods techniques, and results.
(c) Application or practical devices.

Electrodeposition Division Symposium Plans

The Electrodeposition Division plans a symposium on Dielectro-and Electrophoretic Deposition for the 1967 Fall Meeting to be held in Chicago, Ill., October 15-20, 1967.

Invited papers during the first half day of the symposium will survey the fundamental physics of dielectrophoresis and electrophoresis, as well as their biophysical and biochemical aspects. Another half day of invited papers will be directed to applied aspects, including equipment and techniques, metallic and inorganic coatings and deposits, organic coatings and deposits, and biological applications. The symposium will conclude with a half day of contributed papers.

The symposium Chairmen are Herbert A. Pohl, Oklahoma State University, and William F. Pickard, Massachusetts Institute of Technology.

Inquiries and suggestions about the symposium should be addressed to J. V. Petrocelli, Applied Research Office, Ford Motor Co., P.O. Box 2053, Dearborn, Mich. 48121.

Electrothermics and Metallurgy Division Symposium Plans

Protective Coatings

A symposium on Protective Coatings is being organized by the Electrothermics and Metallurgy Division as part of the 1967 Fall Meeting of the Society to be held in Chicago, Ill., October 15-20, 1967. Sessions are being planned on Coatings for Super Alloys, Coatings for Refractory Metals and Coated Steel Products. A general session is also planned. Additional sessions may be scheduled depending on the nature of the papers submitted for presentation.

In each of the above areas papers stressing applied or basic research investigations on methods of inorganic coating application, or relating the behavior of coated bodies to processing variables are desired. It is the purpose of this symposium to stress coating application technology rather than the properties of coated bodies. Papers which deal solely with the properties of coated products or structures will be considered for inclusion in the program only if the exact nature of the coating is specifically characterized.

General Sessions

General sessions on subjects that come within the scope of activity of the Division are also planned for the 1967 Fall Meeting. To assist potential contributors to decide whether their papers fall within the field of interest of the Division, the following paragraph from the Division's tentative statement of scope is reproduced:

In general, the purpose of the Divi-

SYMPOSIA PLANS continued

sion is to aid and encourage the advancement of electrochemical science and industry concerned with specialty materials and processes. As specific examples of field in which the Division has maintained interest and activity, there may be cited: materials such as refractory metals and compounds, intermetallics, graphite, fused salts, and rare earth metals; equipment for the utilization of electrical energy and materials synthesis; processes using arcs, vacua, plasma, and electron and ion beams; and phenomena such as melting, vaporization, reaction, sintering, diffusion or oxidation occurring at high-temperatures, high pressures or involving high temperature materials.

Papers of both fundamental and applied nature are welcome.

Inquiries and suggestions concerning this symposium or the general session program should be sent to the Symposium Chairman, S. T. Wlodek, Graham Research Laboratories, Jones & Laughlin Steel Corp., 900 Agnew Rd., Pittsburgh, Pa. 15230.

POSITIONS AVAILABLE

Please address replies to the box number shown c/o The Electrochemical Society, Inc., 30 East 42 St., New York, N. Y. 10017.

Chemist—Chemical Engineer with dry battery experience for expanding research and development position. Eastern location. Reply Box B-4.

Junior Physicist—Solid State Lab., Chemist—Integrated Circuits R&D, Metallization Engineer—silk screening and plating. Reply Box B-5.

Electrochemists, in the area of electrochemical study of corrosion and corrosion inhibition. Delaware Valley location. Reply Box B-6.

ADVERTISER'S INDEX

Extended Abstract Book Publication Program for the Society's 1967 Fall Meeting in Chicago, Ill.

The Board of Directors has provided that the National Office shall assist Divisions with the mechanics of publishing Extended Abstracts for sessions involving 15 or more papers at our National Meetings. The Divisions will handle the technical editing of the abstracts following which the Society Office will arrange for the printing and distribution of the books, thus relieving Division representatives of this responsibility. Each Division program will be the subject of a separate Extended Abstract Book. This means that each author who submits a paper for presentation at our meeting should do three things:

1—Submit *three* **copies of the usual 75-word abstract of the paper for publication in the printed program of the meeting;**

2—Simultaneously submit *three* **copies of an extended abstract of the paper of 500-1000 words (see instructions below); and**

3—Send the 75-word abstract and the 500-1000-word extended abstract to The Electrochemical Society, 30 East 42 St., New York, N. Y., 10017, *not later than May 15, 1967.*

Notification of acceptance for meeting presentation, along with scheduled time, will be mailed to authors with general instructions no earlier than two months before the meeting. Those authors who require more prompt notification are requested to submit with their abstract a self-addressed post card with full author-title listing on the reverse.

The Extended Abstract Books will be published by photo-offset reproduction *from typewritten copy submitted by the author.* Special care should therefore be given to the following typing instructions so as to establish uniformity in printing:

1—Abstracts are to be 500-1000 words in length (two pages single spaced), and are to contain (to whatever extent practical) all significant experimental data to be presented during oral delivery.

2—Please send an *original* **and** *two copies* **of the abstract typed SINGLE SPACE. Use white bond paper, size 8½ x 11 inches, with 1¼ inch margins on all sides.**

3—Title of paper should be in capital letters. Author(s) name and affiliation should be typed immediately below. It is not necessary in the heading or body to designate paper as "Extended Abstract," or to quote the Divisional Symposium involved.

4—All copy, including figures, symbols, and corrections, must be in black ink. No handwritten corrections, please. Submit graphs on onion skin without grids, or on graph paper specifically designed for offset reproduction; strip-on tape is acceptable.

5—Figures should be pasted in within the typing dimensions indicated. Submit only the important illustrations. Avoid use of half tones except where absolutely necessary. Captions should be typed not wider than figure dimensions and pasted in proper place in the abstract. Figure caption should appear at bottom of figure. Table title should appear at top of table.

6—Mail to The Electrochemical Society *unfolded.*

7—Please note that the extraordinarily low price, per volume, of Extended Abstracts is made possible only through your strict adherence to these instructions. Any deviation threatens this low cost.

Members and JOURNAL subscribers will receive notice of Extended Abstracts Books to be scheduled for publication. The notices will be accompanied by order blanks for the copies desired. Orders should be submitted with remittance. The advance orders will be necessary for estimating numbers of books to be printed and will be mailed to purchasers prior to the Chicago meeting. Some extra copies will be available at the meeting but the advance-paid order is the only way to be assured of getting copies.

Patron and Sustaining Members
of
THE ELECTROCHEMICAL SOCIETY

Patron Members

Aluminum Co. of Canada, Ltd., Montreal, Que., Canada

Dow Chemical Co.
Chemicals Dept., Midland, Mich.
Metals Dept., Midland, Mich.

General Electric Co.
Capacitor Dept., Hudson Falls, N. Y.
Chemical Laboratory, Knolls Atomic Power Laboratory, Schenectady, N. Y.
Chemical Systems and Processes Laboratory, Research and Development Center, Schenectady, N. Y. (3 memberships)
Direct Energy Conversion Operation, West Lynn, Mass
Lamp Div., Cleveland, Ohio
Materials & Processes Laboratory, Large Steam Turbine-Generator Dept., Schenectady, N. Y.

The International Nickel Co., Inc., New York, N. Y.

Olin Mathieson Chemical Corp.
Chemicals Div., Research Dept., New Haven, Conn.

Union Carbide Corp.
Divisions:
Carbon Products Div., New York, N. Y.
Consumer Products Div., New York, N. Y.

Westinghouse Electric Corp.
Electronic Tube Div., Elmira, N. Y.
Lamp Div., Bloomfield, N. J.
Molecular Electronics Div., Elkridge, Md.
Semiconductor Div., Youngwood, Pa.
Research Laboratories, Pittsburgh, Pa.

Sustaining Members

Air Reduction Co., Inc., New York, N. Y.

Allen-Bradley Co., Milwaukee, Wis.

Allied Chemical Corp.
General Chemical Div., Morristown, N. J.

Aluminum Co. of America, New Kensington, Pa

American Metal Climax, Inc., New York, N. Y.

American Potash & Chemical Corp., Los Angeles, Calif

American Smelting and Refining Co.,
South Plainfield, N. J.

American Zinc Co. of Illinois, East St. Louis, Ill.

American Zinc, Lead & Smelting Co., St. Louis, Mo

The M. Ames Chemical Works, Inc., Glens Falls, N. Y.

Ampex Corp., Redwood City, Calif.

Armco Steel Corp., Middletown, Ohio

Basic Inc., Bettsville, Ohio

Bell Telephone Laboratories, Inc., New York, N. Y. (2 memberships)

Bethlehem Steel Corp., Bethlehem, Pa. (2 memberships)

Boeing Co., Seattle, Wash.

Burgess Battery Co., Freeport, Ill. (2 memberships)

Burndy Corp., Norwalk, Conn.

Canadian Industries Ltd., Montreal, Que., Canada

Carborundum Co., Niagara Falls, N. Y.

Chrysler Corp., Detroit, Mich.

Consolidated Mining & Smelting Co. of Canada, Ltd., Trail, B. C., Canada (2 memberships)

Continental Can Co., Inc., Chicago, Ill.

Corning Glass Works, Corning, N. Y.

Diamond Alkali Co., Painesville, Ohio

Wilbur B. Driver Co., Newark, N. J.

E. I. du Pont de Nemours & Co., Inc., Wilmington, Del

Eagle-Picher Co., Chemical and Metals Div., Joplin, Mo.

Eastman Kodak Co., Rochester, N. Y.

Eltra Corp.
Prestolite Div., Toledo, Ohio
C&D Batteries, Conshohocken, Pa.

The Electric Storage Battery Co., Philadelphia, Pa. (2 memberships)

Engelhard Industries, Inc., Newark, N. J.

The Eppley Laboratory, Inc., Newport, R. I.

Esso Research and Engineering Co.
Engineering Technology Div., Florham Park, N. J.

Exmet Corp., Bridgeport, Conn.

Fairchild Semiconductor Corp., Palo Alto, Calif.

FMC Corp.
Inorganic Chemical Div., Buffalo, N. Y.
Inorganic Chemicals Div., South Charleston, W. Va.

Foote Mineral Co., Exton, Pa.

Ford Motor Co., Dearborn, Mich

General Motors Corp.
Allison Div., Indianapolis, Ind.
Delco-Remy Div., Anderson, Ind
Research Laboratories Div., Warren, Mich

General Telephone & Electronics Laboratories, Inc.,
Bayside, N. Y.

Globe-Union, Inc., Milwaukee, Wis

Sustaining Members (cont'd)

B. F. Goodrich Chemical Co., Cleveland, Ohio

Gould-National Batteries, Inc., Minneapolis, Minn.

Great Lakes Carbon Corp., New York, N. Y.

Harshaw Chemical Co., Cleveland, Ohio (2 memberships)

Hercules Powder Co., Wilmington, Del.

Hill Cross Co., Inc., West New York, N. J.

Hoffman Electronics Corp., Semiconductor Division, El Monte, Calif.

Honam Electric Industrial Co., Kwangju City, Korea

Honeywell, Inc., Minneapolis, Minn.

Hooker Chemical Corp., Niagara Falls, N. Y. (3 memberships)

HP Associates, Palo Alto, Calif.

Hughes Research Laboratories, Div. of Hughes Aircraft Co., Malibu, Calif.

International Business Machines Corp., New York, N. Y.

International Minerals & Chemical Corp., Skokie, Ill.

International Resistance Co., Philadelphia, Pa.

ITT Federal Laboratories, Div. of International Telephone & Telegraph Corp., Nutley, N. J.

Jones & Laughlin Steel Corp., Pittsburgh, Pa.

K. W. Battery Co., Skokie, Ill.

Kaiser Aluminum & Chemical Corp.
Metals Div. Research, Permanente, Calif.
Div. of Metallurgical Research, Spokane, Wash.

Kawecki Chemical Co., Boyertown, Pa.

Kennecott Copper Corp., New York, N. Y.

Leesona Moos Laboratories, Div. of Leesona Corp., Great Neck, N. Y.

Arthur D. Little, Inc., Cambridge, Mass.

Lockheed Aircraft Corp., Missiles & Space Div., Sunnyvale, Calif.

Mallinckrodt Chemical Works, St. Louis, Mo.

Metal Pumping Services, Inc., Cleveland, Ohio

P. R. Mallory & Co., Indianapolis, Ind.

Melpar, Inc., Falls Church, Va.

Miles Chemical Co., Div. of Miles Laboratories, Inc., Elkhart, Ind.

Monsanto Chemical Co., St. Louis, Mo.

M&T Chemicals Inc., Detroit, Mich.

Nalco Chemical Co., Chicago, Ill.

National Cash Register Co., Dayton, Ohio

National Lead Co., New York, N. Y.

National Steel Corp., Weirton, W. Va.

North American Aviation, Inc., El Segundo, Calif.

Northern Electric Co., Montreal, Que., Canada

Norton Co., Worcester, Mass.

Owens-Illinois Glass Co., Toledo, Ohio

Pennsalt Chemicals Corp., Philadelphia, Pa.

Phelps Dodge Refining Corp., Maspeth, N. Y.

Philco Corp., Research Div., Blue Bell, Pa.

Philips Laboratories, Inc., Briarcliff Manor, N. Y.

Pittsburgh Plate Glass Co., Chemical Div., Pittsburgh, Pa.

Potash Co. of America, Carlsbad, N. Mex.

Radio Corp. of America
Electronic Components and Devices, Lancaster, Pa.
RCA Victor Record Div., Indianapolis, Ind.

Republic Foil Inc., Danbury, Conn.

Reynolds Metals Co., Richmond, Va.

Shawinigan Chemicals Ltd., Montreal, Que., Canada

Socony Mobil Oil Co., Inc., Dallas, Texas

Sonotone Corp., Elmsford, N. Y.

Speer Carbon Co.
International Graphite & Electrode Div., St. Marys, Pa.

Sprague Electric Co., North Adams, Mass.

Stackpole Carbon Co., St. Marys, Pa.

The Standard Oil Company of Ohio, Cleveland, Ohio

Stauffer Chemical Co., Dobbs Ferry, N. Y.

Texas Instruments, Inc., Dallas, Texas
Metals and Controls Corp., Attleboro, Mass.

3M Company, St. Paul, Minn.

Titanium Metals Corp. of America, Henderson, Nev.

Tyco Laboratories, Inc., Waltham, Mass.

Udylite Corp., Detroit, Mich. (4 memberships)

United States Borax & Chemical Corp., Los Angeles, Calif.

United States Steel Corp., Pittsburgh, Pa.

Univac, Div. of Sperry Rand Corp., New York, N. Y.

Universal-Cyclops Steel Corp., Bridgeville, Pa.

Upjohn Co., Kalamazoo, Mich.

Varian Associates, Palo Alto, Calif.

Western Electric Co., Inc., Chicago, Ill.

Wyandotte Chemicals Corp., Wyandotte, Mich.

Yardney Electric Corp., New York, N. Y.